# Where stellar halos coexist with intracluster light: a case study of the giant Virgo-central galaxy M87

**Alessia Longobardi**

SIGILL·UNIVERSITAT·LUDOVIC·MAXIM·

München 2015

# Where stellar halos coexist with intracluster light: a case study of the giant Virgo-central galaxy M87

**Alessia Longobardi**

Dissertation
an der Fakultät für Physik
der Ludwig–Maximilians–Universität
München

vorgelegt von
Alessia Longobardi
aus Neapel, Italien

München, den 18 Juni 2015

Erstgutachter: Pr. Dr. Ortwin Gerhard
Zweitgutachter: Prof. Dr. Hans Böhringer
Tag der mündlichen Prüfung: 18 Juni 2015

*A zio*

*‘With hope faith and a little bit of luck’*
Alfred Doolittle, My fair lady

# Contents

**Zusammenfassung** **xv**

**Abstract** **xvii**

**1 Introduction** **1**
- 1.1 Optical properties of galaxy clusters . . . . . . . . . . . . . . . . . . . . . . . . . 2
- 1.2 The evolution of galaxies in clusters . . . . . . . . . . . . . . . . . . . . . . . . . 7
- 1.3 Intracluster light (ICL) . . . . . . . . . . . . . . . . . . . . . . . . . . . . . . 9
- 1.4 Physical morphology of Elliptical galaxies . . . . . . . . . . . . . . . . . . . . . . 12
- 1.5 The outer halos of elliptical galaxies . . . . . . . . . . . . . . . . . . . . . . . . 15
- 1.6 Planetary Nebulas (PNs) . . . . . . . . . . . . . . . . . . . . . . . . . . . . . 18
- 1.7 The Thesis: The Virgo cluster and its central cluster galaxy M87 . . . . . . . . . 24

**2 The Planetary Nebula population in the halo of M87** **27**
- 2.1 Introduction . . . . . . . . . . . . . . . . . . . . . . . . . . . . . . . . . . . 28
- 2.2 The Suprime-Cam M87 Planetary Nebula Survey . . . . . . . . . . . . . . . . . . 29
  - 2.2.1 Imaging and observations . . . . . . . . . . . . . . . . . . . . . . . . . 29
  - 2.2.2 Data Reduction, Astrometry and Flux Calibration . . . . . . . . . . . . . . 31
- 2.3 Selection of Planetary Nebula Candidates and Catalogue Extraction . . . . . . . 32
  - 2.3.1 Extraction of Point-Like Emission-Line Objects . . . . . . . . . . . . . . . 33
  - 2.3.2 Possible sources of contaminants in the Planetary Nebula sample . . . . . 36
  - 2.3.3 Comparison with previous Planetary Nebula samples in M87 . . . . . . . 39
- 2.4 The radial profile of the Planetary Nebula population . . . . . . . . . . . . . . 40
  - 2.4.1 The Planetary Nebula density profile . . . . . . . . . . . . . . . . . . . . 40
  - 2.4.2 The $\alpha$ parameter . . . . . . . . . . . . . . . . . . . . . . . . . . . . 43
  - 2.4.3 Halo and intracluster Planetary Nebula population . . . . . . . . . . . . 44
  - 2.4.4 Two component photometric model for M87 halo and intracluster light . 45
  - 2.4.5 Comparison with previously determined $\alpha_{2.5}$ values . . . . . . . . . . . . 47
  - 2.4.6 Implications of the measured $\alpha_{2.5}$ values . . . . . . . . . . . . . . . . . 47
- 2.5 Planetary Nebula Luminosity Function in the outer regions of M87 . . . . . . . . 48
  - 2.5.1 PNLF . . . . . . . . . . . . . . . . . . . . . . . . . . . . . . . . . . . 48
  - 2.5.2 Generalised analytical model for the Planetary Nebula luminosity function 50
  - 2.5.3 Comparison of the PNLF in the M87 halo and in the M31 bulge . . . . . 52

2.5.4 Planetary Nebula luminosity functions distance measurements for M87 . 54
2.6 Summary and Conclusions . . . . . . . . . . . . . . . . . . . . . . . . . . . . . 56

**3 Distinct stellar halo and intracluster light in the giant Virgo galaxy M87 59**
3.1 Introduction . . . . . . . . . . . . . . . . . . . . . . . . . . . . . . . . . . . . 60
3.2 The FLAMES M87 Planetary Nebula survey . . . . . . . . . . . . . . . . . . . . 62
3.2.1 Photometric sample . . . . . . . . . . . . . . . . . . . . . . . . . . . . . 62
3.2.2 Observations and data reduction . . . . . . . . . . . . . . . . . . . . . . 64
3.2.3 Spectroscopic success rates . . . . . . . . . . . . . . . . . . . . . . . . . 65
3.2.4 Classification of the extracted spectra . . . . . . . . . . . . . . . . . . . 66
3.2.5 Accuracy of the velocity measurements . . . . . . . . . . . . . . . . . . 68
3.3 Halo and intracluster Planetary Nebula components . . . . . . . . . . . . . . . 68
3.3.1 Projected Planetary Nebula phase-space diagram . . . . . . . . . . . . . 69
3.3.2 Robust separation of the M87 halo and intracluster light . . . . . . . . . 71
3.3.3 Spectroscopic validation of the Planetary Nebula subsample . . . . . . . 74
3.4 Halo and intracluster density profiles . . . . . . . . . . . . . . . . . . . . . . . 76
3.4.1 Completeness corrections . . . . . . . . . . . . . . . . . . . . . . . . . . 76
3.4.2 Density profiles of halo and intracluster component . . . . . . . . . . . 79
3.5 Halo and intracluster populations . . . . . . . . . . . . . . . . . . . . . . . . . 81
3.5.1 The $\alpha$ parameter . . . . . . . . . . . . . . . . . . . . . . . . . . . . . . 81
3.5.2 Planetary Nebula luminosity functions for halo and intracluster light . . . 83
3.6 Discussion . . . . . . . . . . . . . . . . . . . . . . . . . . . . . . . . . . . . . 85
3.6.1 The distinct halo and intracluster populations around M87 . . . . . . . . 85
3.6.2 Nature and number of the Virgo intracluster light progenitor galaxies . . 86
3.6.3 Is there an intracluster component of globular clusters around M87? . . . 87
3.6.4 Relation between brightest cluster galaxy and intracluster light and ICL . 88
3.7 Summary and Conclusions . . . . . . . . . . . . . . . . . . . . . . . . . . . . . 90

**4 The build-up of the cD halo of M87 Evidence for accretion in the last Gyr 93**
4.1 Introduction . . . . . . . . . . . . . . . . . . . . . . . . . . . . . . . . . . . . 93
4.2 Kinematic evidence for an accretion event in M87 . . . . . . . . . . . . . . . . 94
4.3 Localising the substructure with deep imaging . . . . . . . . . . . . . . . . . . 97
4.4 Physical properties of the accreted satellite . . . . . . . . . . . . . . . . . . . . 97
4.4.1 Luminosity and $\alpha$-parameter . . . . . . . . . . . . . . . . . . . . . . . 97
4.4.2 Colour and Mass . . . . . . . . . . . . . . . . . . . . . . . . . . . . . . . 99
4.5 Summary and Conclusion . . . . . . . . . . . . . . . . . . . . . . . . . . . . . . 99

**5 The kinematics of the outer halo of M87 as revealed by planetary nebulae 101**
5.1 Introduction . . . . . . . . . . . . . . . . . . . . . . . . . . . . . . . . . . . . 102
5.2 Kinematics of the smooth outer halo of M87 . . . . . . . . . . . . . . . . . . . 103
5.2.1 The main halo: identification of kinematical features . . . . . . . . . . . 103
5.2.2 Average two-dimensionsl halo kinematics . . . . . . . . . . . . . . . . . . 105
5.3 The kinematics of the M87 halo: ordered vs random motion . . . . . . . . . . . 106

5.3.1 $\lambda_{\mathrm{R}}$ parameter . . . . . . 106
5.3.2 Velocity dispersion profile of M87 . . . . . . 108
5.4 Discussion and Conclusion . . . . . . 112

**6 Summary and Conclusion 115**
6.1 Future Work . . . . . . 120

**A Spectroscopically confirmed Emission line objects: The Catalogue 123**

**Acknowledgements 191**

# List of Figures

1.1 Hubble scheme of morphological classification of galaxies . . . . . . . . . . . . . . . . . 4
1.2 Examples of galaxy morphologies. . . . . . . . . . . . . . . . . . . . . . . . . . . . . . 5
1.3 Boxy/disky isophote schematization . . . . . . . . . . . . . . . . . . . . . . . . . . . . 13
1.4 System of shells in NGC 474 . . . . . . . . . . . . . . . . . . . . . . . . . . . . . . . 15
1.5 Simulated velocity phase-space of accretion event . . . . . . . . . . . . . . . . . . . . . 16
1.6 Examples of Planetary Nebula optical image and spectrum . . . . . . . . . . . . . . . . . 18
1.7 Planetary Nebula detection techniques . . . . . . . . . . . . . . . . . . . . . . . . . . . 23
1.8 The Virgo cluster . . . . . . . . . . . . . . . . . . . . . . . . . . . . . . . . . . . . . 24

2.1 Positions of the Suprime-Camp fields super imposed on the Virgo cluster . . . . . . . . 30
2.2 Point-source test for colour selected sources . . . . . . . . . . . . . . . . . . . . . . . 35
2.3 Colour-Magnitude-Diagram for all sources in the M87 SUB1 and M87 SUB2 fields . . . 37
2.4 Colour-Magnitude-Diagram for a simulated Planetary Nebula population . . . . . . . . 38
2.5 Comparison of the photometric calibration for the $m_{5007}$ with other studies . . . . . . . 40
2.6 Spatial distribution of Planetary Nebula candidates . . . . . . . . . . . . . . . . . . . . 41
2.7 The M87 light profile and the logarithmic Planetary Nebula number density profile . . . 43
2.8 Modelled surface brightness profile from the two component photometric model . . . . 46
2.9 Luminosity function of the selected Planetary Nebulas . . . . . . . . . . . . . . . . . . 49
2.10 Empirical Planetary Nebula luminosity functions in three radial ranges . . . . . . . . . 51
2.11 M87 halo Planetary Nebula luminosity function . . . . . . . . . . . . . . . . . . . . . 52
2.12 Planetary Nebula luminosity functions for the bulge of M31 and the halo of M87 . . . . 53
2.13 Luminosity functions ofthe Planetry Nebula samples from this survey and other surveys . 55

3.1 Flames spectroscopic fields superposed on the Virgo cluster core . . . . . . . . . . . . 63
3.2 Spectra of single confirmed Planetary Nebulas . . . . . . . . . . . . . . . . . . . . . . 67
3.3 Spectra for background emission line galaxies . . . . . . . . . . . . . . . . . . . . . . 68
3.4 Planetary Nebula projected phase-space diagram . . . . . . . . . . . . . . . . . . . . . 69
3.5 Line-of-sight velocity distribution of the spectroscopically confirmed Planetary Nebulas . 70
3.6 Halo and intracluster Planetary Nebula projected phase-space diagram . . . . . . . . . 72
3.7 Combined spectra for the spectroscopically confirmed Planetary Nebulas . . . . . . . . 75
3.8 Sky positions of the spectroscopically confirmed halo and intracluster Planetary Nebulas 77
3.9 Halo and intracluster planetary nebula number density profiles . . . . . . . . . . . . . 80
3.10 NW and SE halo and intracluster planetary Nebuala number density profiles . . . . . . 81

3.11 Luminosity function of all spectroscopically confirmed Planetary Nebulas . . . . . . . 84
3.12 Luminosity function halo and intracluster Planetary Nebula system . . . . . . . . . . . . 84

4.1 Kinematic evidence for an accretion event in the M87 halo . . . . . . . . . . . . . . . . . 95
4.2 Spatial and colour distribution associated with the kinematic substructure . . . . . . . . 98

5.1 Two-dimensional velocity and and velocity dispersion maps for the M87 halo . . . . . . 104
5.2 Mean line-of-sight velocities as function of the position angle . . . . . . . . . . . . . 107
5.3 Radial $\lambda_R$ profile for the halo of M87 . . . . . . . . . . . . . . . . . . . . . . . . . . . . 107
5.4 Planetary Nebula projected phase-space: the impact of the intracluster component . . . 109
5.5 Combined velocity dispersion profile for the halo of M87 . . . . . . . . . . . . . . . . . . 111

A.1 Spectra of single confirmed halo PNs . . . . . . . . . . . . . . . . . . . . . . . . . . 131
A.2 Spectra of single confirmed IC PNs . . . . . . . . . . . . . . . . . . . . . . . . . . . 158
A.3 Spectra of single confirmed Ly$\alpha$ emitters . . . . . . . . . . . . . . . . . . . . . . . . 165
A.4 Spectra of single confirmed [OII] emitters . . . . . . . . . . . . . . . . . . . . . . . . 173

# List of Tables

1.1 Typical Properties of Clusters and Groups . . . . . . . . . . . . . . . . . . . . . . . . 3

2.1 Summary of the photometric Suprime-Cam survey . . . . . . . . . . . . . . . . . . . . 31
2.2 On-band and off-band limiting magnitudes. . . . . . . . . . . . . . . . . . . . . . . . . 32
2.3 Properties of the stellar populations in the bulge of M31 and in the halo of M87 . . . . . 54
2.4 Density profile for the Planetary Nebula candidates . . . . . . . . . . . . . . . . . . . . 57
2.5 Planetary Nebula luminosity function for the sample of emission line objects. . . . . . . 58

3.1 Flames Configuration and Exposure Times . . . . . . . . . . . . . . . . . . . . . . . . 64
3.2 Summary of the FLAMES spectroscopic survey . . . . . . . . . . . . . . . . . . . . . . 66
3.3 Properties of the combined Planetary Nebula spectra . . . . . . . . . . . . . . . . . . . 76

5.1 Amplitude and direction of rotation in the M87 outer regions . . . . . . . . . . . . . . . 106
5.2 Velocity dispersion estimates from the new Planetary Nebula sample . . . . . . . . . . . 110

A.1 Spectroscopically confirmed halo PNs . . . . . . . . . . . . . . . . . . . . . . . . . . . 124
A.2 Spectroscopically confirmed ICL PNs . . . . . . . . . . . . . . . . . . . . . . . . . . . 156
A.3 Spectroscopically confirmed $Ly\alpha$ PNs . . . . . . . . . . . . . . . . . . . . . . . . . 163
A.4 Spectroscopically confirmed OII PNs . . . . . . . . . . . . . . . . . . . . . . . . . . . 172

# Zusammenfassung

Diese Studie untersucht die Rolle der Akkretion kleinerer Galaxien in der Evolution der zentralen Galaxien in Galaxienhaufen. Kosmologische Simulationen erlauben uns die Entwicklung der Galaxienhalos in Galaxienhaufen genau zu untersuchen. Sie zeigen, dass die Bildung eines ausgedehnten Halos um die zentrale Galaxie eines Haufens und das ‘intracluster light’ (ICL) stark mit der morphologischen Transformation der Galaxien in den Haufen zusammenhängt. Auf Grund der sehr niedrigen Oberflächenhelligkeit der Komponenten ist es jedoch schwierig, diese Effekte in Beobachtungen zu bestätigen.

Diese Arbeit beschäftigt sich mit der Lichtverteilung und der Bewegung der Sterne im Halo der elliptischen Riesengalaxie M87 und mit der sie umgebenden IC Komponente im Zentrum des Virgo Haufens. Virgo ist die uns nächste großräumige Struktur, ein junger Haufen von Galaxien mit Substrukturen in der räumlichen Ausdehnung und der Geschwindigkeitsverteilung. M87 hat eine der ältesten Sternpopulationen im nahen Universum und einen Halo aus Sternen, welcher etwa 70% des gesamten Lichts der Galaxie bis $\mu_V = 27\,\mathrm{mag arcsec}^{-2}$ beinhaltet. Des Weiteren wurde in tiefen Bildern des Zentrums des Virgo Haufens ein ausgedehntes Netzwerk von Gezeiten-Strukturen entdeckt, welche darauf hindeuten, dass die Massenaufnahme der Galaxie durch Akkretion noch andauert. Daher eignen sich M87 und deren Umgebung hervorragend für die Untersuchung der hierarchischen Massenzunahme von Strukturen im Universum.

Diese Arbeit verwendet neue Photometriedaten des Suprime-Cam@Subaru Instruments und Spektroskopiedaten des FLAMES@VLT Instruments, um eine Fläche von ca. 0.5 $\mathrm{deg}^2$ im Übergangsbereich zwischen Galaxienhalo und ICL in M87 zu untersuchen. Dazu verwenden wir planetarische Nebel (PN), deren starke [OIII]$\lambda$5007 Å Emissionslinie sie zu hervorragenden photometrischen Indikatoren für die Kinematik in den Randgebieten der Galaxie macht.

Die photometrische Analyse der PN zeigt eine Überlagerung zweier Sternpopulationen von Halo und ICL. Dies wird durch spektroskopische Beobachtungen der PN bestätigt, deren Verteilung im Phasenraum auch zeigt, dass Halo und ICL zwei verschiedene Geschwindigkeitsverteilungen aufweisen. Die beiden Populationen haben sehr unterschiedliche räumliche Verteilungen und Vorgänger-Sternpopulationen. Dies geht aus den Eigenschaften ihrer PN-Population hervor, wie etwa dem $\alpha$-Parameter und der Steigung der PN-Leuchtkraftfunktion (PNLF). Die verschiedenen alpha Werte und PNLF Steigungen sind konsistent mit zunehmend blaueren Farben hin zu größerem Radius und mit einem Gradienten in der Metallizität mit höheren Werten im Halo als im ICL.

In dieser Arbeit liefere ich mit Hilfe von photometrischen und kinematischen Daten Evidenz für ein Akkretionsereignis, welches den äußeren Halo von M87 nachhaltig verändert hat. Die

andauernde Verschmelzung und Integration dieser Galaxie bei Radien grösser als 60 kpc spiegelt sich in der Kinematik der PN im Halo wieder. Dies zeigt wie komplex die Dynamik dieses ständig noch anwachsenden Systems ist.

Damit ist der Beweis mittels Beobachtungen geliefert, dass im Virgo Haufen sowohl die zentrale Galaxie als auch das ICL durch die Akkretion kleinerer Systeme weiter anwachsen. Jedoch handelt es sich bei Halo und ICL um dynamisch getrennte Komponenten mit verschiedenen Geschwindigkeits- und Dichteverteilungen und verschiedenen Vorgängersternpopulationen.

Ob diese Erkenntnisse über M87 auch für Galaxien in anderen Teilen des Virgo Haufens zutreffen, ist eine offene Frage und wird das Thema einer meiner zukünftigen Studien sein.

# Abstract

The work presented in this thesis studies the role that accretion events play in the evolution of galaxies in dense environments, such as galaxy clusters. Cosmological simulations allow us to study in detail the evolution of galaxies' halos in cluster environments and have shown that the formation of extended halos around central cluster galaxies and intracluster light (ICL) is closely correlated to the morphological transformation of galaxies in clusters. However, the extremely low surface brightness of these components makes it difficult to gather observational constraints.

This thesis studies the light and stellar motion in the halo of the giant elliptical galaxy M87 and its surrounding IC component at the centre of the Virgo cluster. Virgo is the nearest ($\sim$ 15 Mpc away) large scale structure, a young cluster characterised by both spatial and kinematic substructures. M87 has one of the oldest stellar populations in the local Universe and a stellar halo that contains $\sim 70\%$ of the galaxy light down to $\mu_{\mathrm{V}} = 27\,\mathrm{mag\,arcsec^{-2}}$. Moreover, deep images of the Virgo cluster core have revealed an extended network of tidal features suggesting that accretion events characterise its mass assembly. Thus, M87 and its host environment are prime targets to shed light on the hierarchical assembly of structure in the Universe.

This work uses new Suprime-Cam@Subaru photometry and FLAMES@VLT spectroscopy to study a $\sim 0.5\,\mathrm{deg}^2$ area around M87, in the transition region between galaxy halo and ICL. We use planetary nebulas (PNs) as tracers, whose strong [OIII] $\lambda$5007 Å emission line makes them excellent photometric and kinematic probes, also at large distances from the galaxy's centre.

The photometric analysis of the PN sample shows the superposition of two stellar populations, both halo and ICL. This is confirmed by spectroscopically detected PNs, whose velocity phase-space also reveals that halo and ICL split into two different kinematic components. They have very different spatial distributions and parent stars, as indicated by the properties of the PN populations they are associated with, such as the $\alpha$-parameter and the slope of the planetary nebula luminosity function (PNLF). The different $\alpha$ values and PNLF slopes are consistent with a gradient towards bluer colours at large radii and a gradient in metallicity with higher values associated to the halo with respect to the ICL. In this work I also give photometric and kinematic evidence for an accretion event that has caused an important modification of the outer halo of M87. The ongoing assembly of this galaxy at distances $R > 60$ kpc is also shown by the overall PN halo kinematics, reflecting the dynamical complexity of a still growing system.

In this thesis I give the observational proof that in Virgo the central galaxy and the ICL both evolve through the ongoing accretion of smaller systems. However, stellar halo and ICL are dynamically distinct components with different velocity and density distributions, and parent stellar populations. Whether or not these conclusions are true for different galaxies in different Virgo subclusters is still an open question and the topic of one of my planned future studies.

# Chapter 1

# Introduction

According to the current theory of structure and formation of the Universe, cosmologists place its formation ∼13.8 billion years ago, after which the Universe has been expanding ever since. Structure formation arises from gravitational instabilities amplifying perturbations in the cold dark matter (CDM)[1] density field in such an expanding system. At early times the perturbations were linear in amplitude, and well described by a Gaussian random field with a known power spectrum (the ΛCDM power spectrum[2]; Tegmark et al. (2004)). At later times, density perturbations became nonlinear and collapsed into gravitationally bound systems. The shape of the ΛCDM power spectrum is such that structure forms from the ”bottom up”, with smaller masses virialising first and subsequently growing by accretion and mergers(Peebles 1993; pea 1999). Thus, galaxy clusters correspond to the collapse of the largest gravitationally bound overdensities that happened rather recently (since z∼1), and are therefore unique laboratories to study the mechanisms leading to the evolution of galaxies and to test models of gravitational structure formation.

Only a small percentage of the total galaxy cluster mass is in the form of baryonic matter. Galaxy clusters are in fact embedded in extended DM halos, that directly influence the properties of the cluster itself such as mass function, that describes the number density of clusters above a threshold mass, and clustering properties. Hence, our understanding of the formation and evolution of baryonic matter depends on an understanding of the structure and formation of DM halos.

There are several models that have been adopted to describe the DM density profile. Assuming that the virialised halos resemble isothermal spheres the density profile, $\rho(r)$, can be modelled as:

$$\rho(r) \propto r^{-2}. \tag{1.1}$$

Although masses predicted by this model are in good agreement with studies of gravitational lensing phenomena[3] (Koopmans et al. 2006), deviations from this model may be expected when the hypothesis of spherical collapse is not verified. N-body simulations in a ΛCDM cosmology predict, indeed, that the DM density distribution deviates from a $r^{-2}$ law, i.e. shallower at small radii and steeper at larger radii. Hence, the DM density profile is better described by the so called NFW law (Navarro et al. 1996) of the form:

---

[1] CDM particles account for most of the matter budget in the Universe, they are non-relativistic (cold), and interact very weakly with the electromagnetic radiation (dark).

[2] ΛCDM is based on a cosmological constant, Λ, which is currently associated with a vacuum energy or dark energy in empty space that is used to explain the contemporary accelerating expansion of space against the attractive effects of gravity.

$$\frac{\rho(r)}{\rho_{crit}} = \frac{\delta_c}{(r/r_s)(1+r/r_s)^2}, \tag{1.2}$$

where $\rho_{crit} = \frac{3H^2}{8\pi G}$ is the critical density of an Einstein-de Sitter Universe, i.e. the amount of matter required for the Universe to be flat, $r_s$ is the scale radius, and

$$\delta_c = \frac{200}{3} c^3/[\ln(1+c-c/(1+c))] \tag{1.3}$$

is the characteristic density contrast (dimensionless) (Navarro et al. 1997). In addition, $H$ is the Hubble constant, G is the gravitational constant and $c$ is the concentration parameter. The concentration parameter is proportional to $r_{200}/r_s$, where $r_{200}$ is the radius within which $\rho(r < r_{200}) = 200\rho_{crit}$. The enclosed mass of a NFW profile is then given by:

$$M(r) = 4\pi\rho_{crit} r_s^3 \delta_c(c)\left[\ln(1+cx) - \frac{cx}{1+cx}\right], \tag{1.4}$$

where $x = \frac{r}{r_s}$. Masses derived assuming such a profile are in good agreement with X-ray and lensing mass estimates (Vikhlinin et al. 2005; Pratt 2006; Zhang et al. 2007; Mahdavi et al. 2008). Thus, the NWF model gives a consistent description of the dark matter halo density structure.

When not considering the DM component, baryonic matter constitutes only ∼16%-14% (Komatsu et al. 2011; Gonzalez et al. 2013) of the cluster content. The major baryonic component is in the form of hot, X-ray emitting gas, or intracluster medium (ICM), that permeates the cluster potential, while stars and galaxies cover only a few percent. Moreover the baryons distribution amongst the various components in a cluster can constrain models for cluster assembly and cluster galaxy evolution. For example, the partitioning between ICM and stars tell us about the efficiency with which baryons are converted to stars in massive halos (i.e., of star formation) and the role that the halo mass play in such efficiency (Bryan 2000; Lin et al. 2003). Finally, the relative contribution in light between satellite galaxies, brightest cluster galaxy (BCG) and intracluster light (ICL) provides stringent tests for models of cluster galaxy and galaxy luminosity function evolution (Conroy et al. 2007; Purcell et al. 2007; Behroozi et al. 2013; Watson et al. 2012).

## 1.1 Optical properties of galaxy clusters

### Classification schemes

The interest in the study of galaxy cluster properties in the last century led to the creation

---

[3] In a simplistic way this technique is based on the gravitational interaction between the radiation emitted by a source and the gravitation potential generated by a distribution of matter interposed between the source and the observer. The number and shape of the distorted images can be used to measure the mass of the lensing object

Table 1.1: Typical Properties of Clusters and Groups from Bahcall (1996) .

| Property$^{a}$ | Rich clusters | Groups and poor clusters |
|---|---|---|
| Richness | 30–300 galaxies | 3–30 galaxies |
| Radius | (1–2) $h^{-1}$ Mpc | (0.1–1) $h^{-1}$ Mpc |
| Radial velocity dispersion | 400–1400 km s$^{-1}$ | 100–500 km s$^{-1}$ |
| Radial velocity dispersion (median) | $\sim$ 750 km s$^{-1}$ | $\sim$ 250 km s$^{-1}$ |
| Mass ($r \leq 1.5h^{-1}$ Mpc) | $(10^{14}$–$\times 10^{15.3})h^{-1}\ \mathcal{M}_{\odot}$ | $(10^{12.5}$–$10^{14})h^{-1}\ \mathcal{M}_{\odot}$ |
| Luminosity ($B$) ($r \leq 1.5h^{-1}$ Mpc) | $(10^{11.7}$–$10^{12.7})h^{-2}\ L_{\odot}$ | $(10^{10.5}$–$10^{12})h^{-2}\ L_{\odot}$ |
| $\langle \mathcal{M}/L_{\mathrm{B}} \rangle$ | $\sim 300h\ \mathcal{M}_{\odot}/L_{\odot}$ | $\sim 200h\ \mathcal{M}_{\odot}/L_{\odot}$ |
| X-ray temperature | 2–14 keV | < 2 keV |
| X-ray luminosity | $(10^{42.5}$–$10^{45})h^{-2}$ erg s$^{-1}$ | $< 10^{43}h^{-2}$ erg s$^{-1}$ |
| Cluster number density | $(10^{-5}$–$10^{-6})h^{3}$ Mpc$^{-3}$ | $(10^{-3}$–$10^{-5})h^{3}$ Mpc$^{-3}$ |
| Cluster correlation scale | $(22 \pm 4)h^{-1}$ Mpc ($R \geq 1$) | $(13 \pm 2)h^{-1}$ Mpc |
| Fraction of galaxies in clusters or groups | $\sim$ 5% | $\sim$ 55% |

$^{a}$ The typical range in the listed property or the median value is given.
See Bahcall (1996) and reference therein for more details.

of several classification schemes based on optical surveys. The first morphological classification came from Abell (1958) which distinguished between *regular* and *irregular* clusters according to the degree of circular symmetry. He then distinguished between them based on their richness, where a rich cluster contains, within a radius of $r \simeq 1.5\ h^{-1}$ Mpc[4], at least 50 members brighter than $m_3 + 2^{\mathrm{m}}$, where $m_3$ is the magnitude of the third brightest cluster member (Abell 1958). Later on Zwicky et al. (1961) classified clusters as *compact*, *medium compact and open* according to the distribution of galaxies. A more specific classification scheme includes the Bautz-Morgan (BM) system (Bautz & Morgan 1970) in which clusters are classified based on the relative contrast of the brightest member galaxy (from Type I to Type III it goes from clusters with one dominant brightest cluster galaxy to clusters with no members significantly brighter than the general bright population); and the Rood-Sastry (RS) system (Rood & Sastry 1971) which classifies clusters based on the distribution of the ten brightest members. Finally, Oemler (1974) classified clusters by galaxy content in cD clusters, with one or two dominant cD galaxies (see next for the definition of cD galaxy), spiral rich and spiral poor clusters.

Several of the cluster properties are correlated with the associated classification type. Regular and cD clusters are characterised by a spatial distribution that is circular symmetric and smooth, with space density that increases rapidly towards the centre of the cluster. Spiral rich and irregular clusters are not symmetric and have no or little concentration. In addition to this, more physical quantities such as the line-of-sight (LOS) velocity dispersion, cluster mass, and amount and properties of the X-ray emission are associated to the different classification types. In Table 1.1 the main properties related to cluster's richness are summarised .

---

[4] This value correspond to the Abell radius $R = \frac{1.7}{z}$, where $z$ is the cluster redshift

### Galaxies in clusters: morphological types

Galaxies were first classified based on their single-colour morphological properties by Hubble in the 1920's. The classification, shown in Fig. 1.1, followed a sequence of increasing complexity from ellipticals (E0-E7) to lenticulars (S0), to spirals (Sa-Sc), to irregulars (Irr). Elliptical galaxies, lying on the extreme left hand part of this sequence are spherical or ellipsoidal masses of stars with smooth and featureless light distribution that to first approximation can be described by the Sérsic law (see Sect. 1.4 for more details),

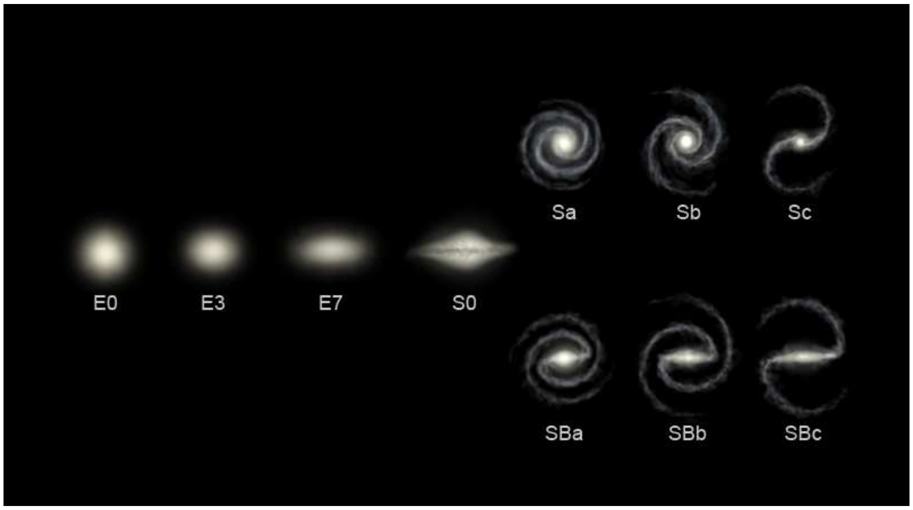

Figure 1.1: Hubble scheme of morphological classification of galaxies.

$$I(R) = I_e \exp(-R/R_e)^{1/n} - 1, \tag{1.5}$$

where $r_e$ is the effective radius within which half of the total light is contained, and $n$ is an index that controls the concentration of the light. Moving along the Hubble fork spiral galaxies are subdivided into Sa-Sc classes based on the prominence of the central bulge, the gas content and the wrapping of the spiral pattern. From the 'a' to the 'c' class it goes from systems with a large bulge component with respect to the disk, tightly wound and smooth arms, to systems with a small bulge compared to the disk, loosely wound and lumpy arms with star-forming regions. Spirals can present a barred structure and for an analogy with systems without a bar they are indicated with the labels SBa-SBc. As for the spiral galaxies S0s follow many trends along the Hubble sequence originally defined by morphological appearance, i.e. the bulge component getting less prominent and the disk component and spiral structure getting more pronounced from early to late-type galaxies. The light distribution of spirals and S0s' disks is observed to have an exponential profile of the form:

$$I(R) = I_0 exp(-R/R_s), \tag{1.6}$$

where $I_0$ is the central surface brightness (SB), and $r_s$ is a scale length. Galaxies that do not fit into the Hubble sequence are called Irregulars. Originally, Hubble interpreted (incorrectly) his diagram as an evolutionary sequence for galaxies, referring to galaxies towards the left of the diagram (E) as early-types and those towards the right (S and SB) as late-types [5]. This terminology is widespread today, with S0s and Es usually studied as one class of objects under the label of early-type galaxies (ETGs).

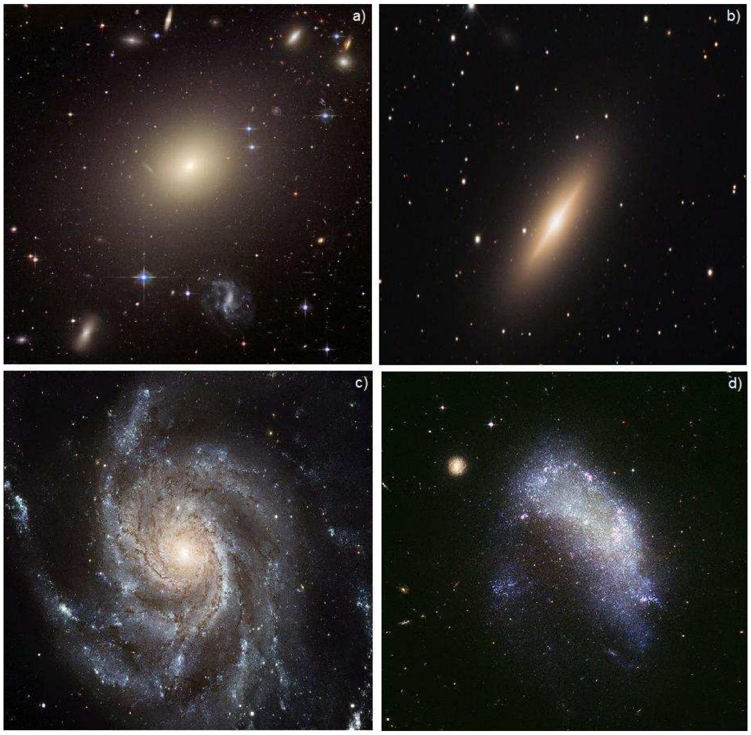

Figure 1.2: Examples of galaxies' morphologies. a) Hubble image of the giant elliptical galaxy ESO 325-G004 in Abell S740 cluster. North is left, East is bottom; b) LRGB image of lenticular galaxy NGC3115, 4.8° north of Lambda Hydrae. North is right, East is top; c) Hubble image of the spiral galaxy NGC 5457 that lies in the northern Ursa Major constellation. North is top, east is to the left; d) Hubble image of irregular galaxy NGC 1427A passing through the Fornax cluster. North is left, East is bottom.

---

[5] The adjectives 'early' and 'late' were used to describe the relative positions in the morphological sequence. The direction from simple to complex forms was chosen from the precedent of stellar spectral types, where early types (O+B stars) generally have more simple spectral features than late types (K+M stars). Ironically, the spectra of early-type galaxies are generally dominated by late-type stellar spectra and viceversa.

## Galaxy Luminosity Function

The relative fraction of ellipticals, S0s, and spirals in clusters is usually represented by the luminosity function (LF), that defines the number of objects in a particular range of luminosity. The total number of galaxies in a given cluster is then given by the sum over the individual luminosity functions of each Hubble type. The most common analytical formula used to fit the galaxy cluster luminosity function was proposed by Schechter (1976) and has the form:

$$\phi(L)dL \sim L^{\alpha} exp(-L/L^{*})d(L), \tag{1.7}$$

where $\alpha$ determines the faint end of the LF, and $L^{*}$ represents the characteristic luminosity of cluster galaxies (also quoted as the 'break' point in the LF). Different values of $\alpha$, $L^{*}$ and different steepnesses of the bright end of the luminosity function (Dressler 1978) are observed for different cluster morphologies, reflecting a dependence on the environment of the particular sample of galaxies. While a variation in $\alpha$ and $L^{*}$ may be related to variations in the condition of the cluster at its formation, variations in the steepening at the bright end may be the result of evolutionary changes. How different Hubble types are distributed in galaxy clusters led Melnick & Sargent (1977) to define the so called morphological segregation, according to which the inner regions of clusters are typically populated by ellipticals. Later Dressler (1980) found a correlation between the fraction of different morphological types and the local projected galaxy density, concluding that galaxy morphology is a function of local clustering rather than global conditions related to cluster environments. Several mechanisms have been proposed to explain the observed morphological segregation. Among them there are gravitational and hydrodynamical interactions that will be described in Sect. 1.2.

## Brightest cluster galaxies and cD galaxies

The most luminous galaxies in rich clusters, or brightest cluster galaxies (BCGs), are ellipticals, and some of these are classified as cD, i.e. they are characterised by an extra-large extended and diffuse envelope with a shallow brightness gradient (Matthews et al. 1964; Binggeli et al. 1988). They are located at the cluster centre, and they are among the most luminous and massive galaxies in the Universe. Being at the bottom of the cluster potential well, these objects are close to the peak of the X-ray emission (Rhee & Latour 1991; Lin et al. 2004; Rafferty et al. 2008). They are essentially at rest at their cluster centre (Zabludoff et al. 1990; Oegerle & Hill 2001), even though cases of central galaxies with peculiar velocities have been observed, suggesting that mergers of two clusters is in progress (Oegerle & Hill 2001). Despite their spheroidal morphology BCG/cD galaxies often lie off the physical relations that describe other ellipticals (Bernardi et al. 2007). Their extreme luminosity makes them too bright to be drawn by the same luminosity function as cluster ellipticals (Dressler 1978; Bernstein & Bhavsar 2001), and the observed velocity dispersions at larger radii are lower than what is predicted by Faber-Jackson-Kormendy relations (von der Linden et al. 2007; Bernardi et al. 2007; Desroches et al. 2007). Moreover, they are in general larger, more massive and have higher velocity dispersions than non-BCG/cD ellipticals (von der Linden et al. 2007). A recent analysis by Best (2007) showed that BCGs are also more likely to host active galactic nuclei than other galaxies of the same stellar mass, making them linked to the quenching of cooling flows[6] and star formation in clusters.

Their observed properties and their position at the bottom of the potential well of clusters, imply that the evolution of BCGs/cD might be different from galaxy evolution in general, and more tightly connected to the formation and evolution of the cluster as a hole (De Lucia & Blaizot 2007). Several formation mechanisms for BCGs have been proposed. In the next sections I will describe some of the processes that have been proposed as driving mechanisms of formation of the BCGs and of galaxies in general.

## 1.2 The evolution of galaxies in clusters

Galaxies formation scenarios are popularly divided into two different classes: the so-called monolithic collapse (Larson 1974), and hierarchical formation, usually inserted in the $\Lambda$CDM paradigm (Cole et al. 2000). The original model of monolithic collapse assumes that early in the Universe's history galaxies collapsed to form stars within a very short period of time ($\sim$100 Myr) with star formation rates of $10^2$-$10^3 M_\odot$ yr$^{-1}$. This would create massive galaxies that thereafter passively evolve in luminosity with no further star formation. This model is now ruled out as consequence of observational and theoretical constraints. Observationally, both the recent star formation observed in ellipticals and the varying ages of different components observed for example in our own Galaxy, reject the idea that all parts of the galaxies formed at the same time. Theoretically, $\Lambda$CDM cosmology predicts 'bottom-up' structure formation rather than 'top-down'.

In hierarchical models, structures form in a bottom up, hierarchical manner by which smaller fragments merge together to form more massive systems. The dominant signatures in the hierarchical scenario depend on the time evolution of the merging rate: if mergers were most frequent at high redshifts, as predicted by present-epoch cosmological models, signatures should be similar to those of dissipative (monolithic) collapse. More recent mergers and tidal disruptions would result in flatter metallicity gradients, and a significant fraction of young or intermediate-age stars. According to the hierarchical paradigm, most stars are thought to be born in disks while stellar spheroids arise as the remnants of subsequent merger events (Mihos & Hernquist 1996; Abadi et al. 2003). Gradual accretion of cooled gas from the hot gaseous halo will result in a newly formed disk around the spheroid. The 'anti-hierarchical' observations of younger ages for low mass galaxies are explained in modern theories of hierarchical merging by the use of feedback mechanisms (De Lucia et al. 2006). As well, concerns of too few disk-dominated systems in hierarchical predictions compared to observations can be improved by accounting for the role of gas in mergers (Hopkins et al. 2009).

In a Universe where hierarchical formation is predicted, several mechanisms have been proposed to drive the formation and/or evolution of different Hubble types in clusters, the most popular one involving galaxy-galaxy, galaxy-cluster potential well,and galaxy-ICM interaction. I give here a brief overview of the proposed processes.

---

[6] The quenching phenomenon describes the observational evidence that some galaxies reach a point in their lives when their star formation is turned off.

***Gravitational interactions:***

**Mergers** are gravitationally bound interactions between galaxies. When the masses of the merging galaxies are comparable, a major merger is occurring that will result in a remnant with properties significantly different from either progenitors. Such major-mergers are thought to be responsible for the formation of spheroidal galaxies from pre-existing galaxies, also disk-like. As a consequence of the fast fluctuations in the gravitational potential, the process of violent relaxation (Lynden-Bell 1967; Tremaine et al. 1986) can turn ordered motions seen in disks into random motions observed in spheroidals. However, spheroidals that derive from major mergers of purely stellar disk systems, are not ellipticals, and are characterised by too low phase-space densities (Hernquist et al. 1993). Mergers between gas rich galaxies, or wet mergers, are then required to explain the formation of higher phase space density, as the presence of gas allows for energy dissipation from gas friction (Robertson et al. 2006). However, very gas rich systems can lead to the formation of a disk after the merger is over (Springel & Hernquist 2005; Robertson et al. 2006). When one of the two galaxies is significantly more massive than the other, the process is called a minor merger. It has been shown (Bournaud et al. 2005; Somerville et al. 2008) that the higher the mass ratio, the more likely the process will destroy any disk involved in the interaction to leave a spheroidal object. Viceversa, the lower the mass ratio the more probable is that a disk remnant will be left in place. Numerical simulations predict that only very massive systems, like BCGs, are going to experience mergers up to ~5 times in their dynamical evolution history (De Lucia et al. 2006; De Lucia & Blaizot 2007). For galaxies with a mass $M \leq 10^{11} M_{\odot}$ mergers are more rare events that will happen at most once.

**Harassment** is another possible mechanism of galaxy evolution in clusters. Moore et al. (1998) proposed that the evolution of cluster galaxies is governed by the combined effect of multiple high speed galaxy-galaxy close encounters. The multiple encounters heat the stellar component increasing the galaxies' velocity dispersion and decreasing their angular momentum, meanwhile the gas sinks towards the central regions producing a starburst. During this process, a galaxy may lose an important fraction of its original disk stellar population. This mechanism is more effective in low-mass/low-surface brightness galaxies than in massive objects with strong disks and deeper potential wells. This process would then be responsible of the transformation of low SB systems into dwarf galaxies[7] (Moore et al. 1999; Mayer et al. 2006).

**Tidal Destruction** is a galaxy-galaxy or galaxy-cluster interaction, in which an orbiting satellite in the galaxy/galaxy cluster potential will experience tidal forces which may strip away its outer regions (Gnedin 2003). In extreme cases, the satellite is entirely distrupted resulting in tidal tails and debris (Toomre & Toomre 1972). In this type of interaction the key parameter is the tidal radius defined as the radius at which the stars within the satellite are stripped becoming bound to the host galaxy about which the satellites orbit. Recent numerical simulations have shown that the tidal radius depends not only on the potential of the host galaxy and on the potential and orbit of the satellite galaxy, but also on the orbits of the stars within the satellite. They show that particles on prograde orbits are more easily stripped than those on radial orbits which are in turn more easily stripped than those on retrograde orbits[8] (Read et al. 2006a).

---

[7] Each Hubble type galaxy has its dwarf counterpart, that is a much smaller system with similar physical properties.

***Hydrodynamical interactions:***

**Ram-pressure gas-stripping scenario** has been proposed as a possible path that could transform galaxies in clusters (Gunn & Gott 1972), for example spirals into S0s. When a galaxy passes from the field to the cluster environment, the pressure due to the hot ICM can remove the cold gas from the disk, producing a fast truncation of the star formation. On the other hand, galaxy-ICM interaction may also be responsible for a temporary increase of star formation particularly on the side where ram-pressure compresses galaxy gas clouds (Dressler & Gunn 1983).

## 1.3 Intracluster light (ICL)

### ICL formation mechanisms and physical properties

A fraction of the baryonic content in a cluster is represented by the ICL, i.e. a stellar component that is gravitationally unbound to cluster galaxies, but bound to the cluster potential. Even though the diffuse light was originally thought to come from the tidal forces that member cluster galaxies experience because of the cluster potential, several formation scenarios have been proposed as possible mechanisms that add stars to the diffuse light, and the role of interactions between member cluster galaxies in producing the IC component can be quite important. In addition to tidal interactions between galaxies and the cluster potential (Gnedin 2003), stripping due to high-speed interactions between cluster member galaxies (Moore et al. 1998), stripping during the first collapse of the cluster (Merritt 1984), and stripping within galaxy groups accreting onto the cluster (Rudick et al. 2006) are all processes that can contribute to the production of the IC component (Rudick et al. 2009; Watson & Conroy 2013; Laporte et al. 2013). Moreover, several recent studies have shown the importance of galaxy mergers in the building up of the ICL. Numerical simulations show that disrupted sub-halos can deposit up to ~50% of their stars into the ICL (Murante et al. 2007; Conroy et al. 2007; Lidman et al. 2012). Finally, a portion of intracluster light may come from in-situ star formation, wherein stars form in cold gas clouds stripped from infalling substructures (Puchwein et al. 2010; Yoshida et al. 2002). In a complex environment, such as a galaxy cluster, it is plausible that all these processes are involved in the building up of the ICL and that the IC component follows different paths of formation depending upon the dynamical evolution of that particular cluster (Willman et al. 2004; Rudick et al. 2009). Hence, the ICL is thought to be intimately linked to the dynamical history of the cluster, and its observable features, such as colour, metallicity, radial light distribution and kinematics, contain a great deal of information about evolutionary processes. Once IC stars have been built up predominantly by tidal stripping, a gradient in colour and metallicity is expected. The disruption of low mass satellites, which are metal-poor from the point of view of the mass-metallicity relation, can occur at larger radii than more massive systems. Moreover, if the satellite is characterised by a radial metallicity gradient the tidal forces will strip the most tightly bound stars (hence the reddest) at smaller cluster radii closer to the bottom of the potential well. Alternatively, if the ICL is the consequence of a merger event, the more massive the merging galaxy is the more metal rich the ICL component is expected to be, while the in-situ formation scenario would change the mean age of the IC component.

---

[8] Retrograde motion is the motion in opposite direction to the main system. On the contrary, particles on prograde motion, orbit in the same direction of the system.

## ICL fraction and distribution

Despite its dynamical definition the ICL is usually identified on the basis of its photometric properties. First identified by Zwicky (1937, 1952) in the form of faint and irregular distribution of stars, due to its low surface brightnesses (its peak in SB correspond to ∼ 1% of the brightness of the night sky (Vílchez-Gómez 1999) only the advent of CCD photometry allowed it to be studied in a more quantitative way. Nowdays, observational analysis implement mostly two methods to identify the ICL component. The first defines a fixed surface brightness limit (Feldmeier et al. 2004a; Mihos et al. 2005; Zibetti et al. 2005) and the optical light coming from the outside of such boundaries is attributed to the ICL. The second separates the ICL from the remaining galaxy component by modelling the SB with a two component fit, and identifying the ICL with the less concentrated profile (Gonzalez et al. 2005; Seigar et al. 2007). Moreover, the availability of individual stars in the ICL such as supernovae (Gal-Yam et al. 2003), red-giant branch (RGB) stars (Ferguson et al. 1998; Durrell et al. 2002) , and PNs (Arnaboldi et al. 1996; Feldmeier et al. 2004a; Arnaboldi et al. 2004; Gerhard et al. 2005; Aguerri et al. 2005; Ventimiglia et al. 2011) made it possible not only to analyse its photometric properties, but also to gather information on the kinematics of this diffuse component, that allow a less ambiguous definition to be made. Also, there is evidence that blue globular clusters (GCs) trace the IC stellar population (Richtler et al. 2004; Durrell et al. 2014), even though it is not clear how well they trace the light and hence its parent stellar population (Coccato et al. 2013).

Even though the ICL is now believed to be a common component of several structures of different sizes and richness, observed in both massive clusters and groups (Feldmeier et al. 2002, 2004a) a clear consensus on the fraction of stars that form the IC component has not been reached yet. Observational studies showed that the ICL can contain from a few percent up to 50% of the total optical light in the system (Gonzalez et al. 2000; White et al. 2003; Aguerri et al. 2005; Zibetti et al. 2005; Da Rocha et al. 2008). However whether the cluster mass influences this fraction is not clear. Lin et al. (2004) claim a positive correlation between ICL fraction and halo mass reaching up to half of the total light in very massive systems ($\sim 10^{15} M_{\odot}$); Zibetti et al. (2005) found that this fraction is uncorrelated to the cluster richness with an average value of ∼ 10%; while Krick & Bernstein (2007) find larger scatter of values of the ICL fraction (from ∼6% to ∼20%) with no evidence for any trend in mass. Differences from system to system have also been observed in its spatial distribution. Observational campaigns have shown that the ICL is present in the form of a smooth diffuse component among galaxies or extended halos around BCGs, and in the form of tidal features or plums. Of particular interest is the dynamical information that such distribution carries along: as material is stripped from the galaxy satellite, extended tidal streams are formed (Gregg & West 1998a; Feldmeier et al. 2004a; Mihos et al. 2005). Later on, further cluster accretion events and/or phase-mixing, can destroy such features leading to the observed smoothed and diffuse ICL distribution (Rudick et al. 2009). Hence, in dynamical young systems the ICL is found in the form of streams and shells, reflecting the recent interaction of the central galaxy with infalling material.

Up to now, the ICL component has been investigated at low to intermediate redshift. Several studies have been carried out for structure like the Coma cluster (Gregg & West 1998a; Trentham & Mobasher 1998; Adami et al. 2005; Gerhard et al. 2005, 2007), Fornax cluster (Theuns & Warren 1997a), Virgo cluster (Arnaboldi et al. 1996, 2002; Durrell et al. 2002; Feldmeier et al. 2004a; Aguerri et al. 2005; Mihos et al. 2005; Rudick et al. 2010), in other nearby clusters (Lin et al. 2004; Gonzalez et al. 2005; Krick & Bernstein 2007; Ventimiglia et al. 2011), and clusters at higher redshift (Zibetti et al. 2005; Toledo et al. 2011; Burke et al. 2012; Guennou et al. 2012; Presotto et al. 2014). In the near future, the lensing CLASH/VLT survey may allow the extension of the analysis to a statistically significant cluster sample up to a redshift $z = 0.6$. This will help in constraining the ICL formation scenarios given the theoretical agreement that most of the ICL has formed at relatively young epoch ($z \leq 1$) (Murante et al. 2007; Conroy et al. 2007; Dolag et al. 2010; Contini et al. 2014).

## ICL and BCG/cD galaxies

The central galaxies in clusters are often cD galaxies, characterised, as already pointed out, by an amount of extra-light at large radii that makes the SB profile deviate from a single de Vaucouleurs or Sérsic profile. An interesting question is to understand the nature of this extra light: is it dynamically bound to the main galaxy halo or it is floating in the cluster potential being a part of the ICL? In other words, where does the ICL begin and the galaxy halo end, or do we need to make a distinction at all? Analysing a large sample of clusters, Gonzalez et al. (2005) showed that the detected ICL components are often discernibly separate entities from the host BCGs, with well defined transitions in the surface brightness profile, axis ratio, and position angle. Interestingly, they interpreted such photometric differences as different physical components, emphasising that the evolution of the ICL is tied to the cluster as whole rather than to the central galaxy. Despite these results, in later works both observational and theoretical (e.g. Gonzalez et al. 2007; Cooper et al. 2014), the presence of an additional component is identified with the extra-light that causes the change of slope at large radii. However, the two components are treated as a continuum, for example in recent $\Lambda$CDM simulations by Cooper et al. (2014) the system BCG+ICL is treated as a single entity consisting of all stars which are not bound to any sub-halos. This is in contrast with a more sophisticated dynamical definition of the ICL, which identifies this component in terms of either binding energy (stars that are not bound to identified galaxies) (Murante et al. 2004) or velocity distribution (broader for the ICL than for the galaxy halo; Dolag et al. 2010; Contini et al. 2014). When such definitions are assumed, the authors find two well distinct stellar populations in terms of kinematics, spatial distribution and physical properties like age and metallicity.

## 1.4 Physical morphology of Elliptical galaxies

### Luminosity profiles

Galaxy luminosity profiles show how the surface brightness $I$[9] of a galaxy varies with radius $r$ from its center and provide fundamental information about galaxy morphology.
The radial distribution of stellar light in elliptical galaxies falls off smoothly with radius, historically described by the de Vaucouleurs law (de Vaucouleurs 1948):

$$\log\left(\frac{I}{I_e}\right) = -3.33\left[\left(\frac{R}{R_e}\right)^{1/4} - 1\right],$$

where the effective radius $R_e$ is the radius of the isophote[10] containing half of the total luminosity and $I_e$ is the surface brightness at $R_e$. Nevertheless, later works (Ciotti 1991; Caon et al. 1993) have shown that a generalised de Vaucouleurs or $R^{1/n}$ formula (Sérsic 1963)

$$I(r) = I_e \exp\left\{-b_n\left[\left(\frac{R}{R_e}\right)^{1/n} - 1\right]\right\},$$

where $b_n \sim 2n - 0.327$ (Capaccioli & Caon 1989), not only gives a better fit to the light profiles, but also provides an interesting correlation between shape ($n$) and total luminosity ($L \sim I_e R_e^2$).

How an E galaxy appears, hence its ellipticity and position angle, depend on the surface brightness used to define the isophotes. It has been found that isophotal shapes of early-type galaxies correlate with many of their important characteristics (Bender 1988; Bender et al. 1989; Faber et al. 1997; Mathieu et al. 2002). In order to measure the shape of the isophotes, ellipses are drawn from the best fitting isophote. The intensity along the ellipse is then expanded into a Fourier series,

$$I(R,\theta) = I_0(R) + \sum_n A_n(R)\sin n\theta + B_n(R)\cos n\theta,$$

with $n = 3$ and $n = 4$, and where

$$A_n(R) = \frac{1}{\pi}\int_0^{2\pi} I(R,\theta)\sin n\theta d\theta,$$

and

$$B_n(R) = \frac{1}{\pi}\int_0^{2\pi} I(R,\theta)\cos n\theta d\theta.$$

The amplitudes A3, B3, A4, and B4 , normalised by the semi-major axis length and the local intensity gradient, measure the isophote's deviations from perfect ellipticity. More specifically, the third-order moments (A3 and B3) represent isophotes with three-fold deviations from ellipses (that is, egg-shaped or heart-shaped), while the fourth-order moments (A4 and B4) represent four-fold deviations. Rhomboidal or diamond-shaped isophotes translate into a nonzero A4. For galaxies that are not distorted by interactions, B4 is the most meaningful moment: a positive B4 indicates ‘disky’ isophotes, while a negative B4 indicates ‘boxy’ isophotes. The effect of a non-zero B4 coefficient on the isophote shape is shown in Fig.1.3.

---

[9] Magnitude per unit of angular surface.

[10] Contour of equal surface brightness.

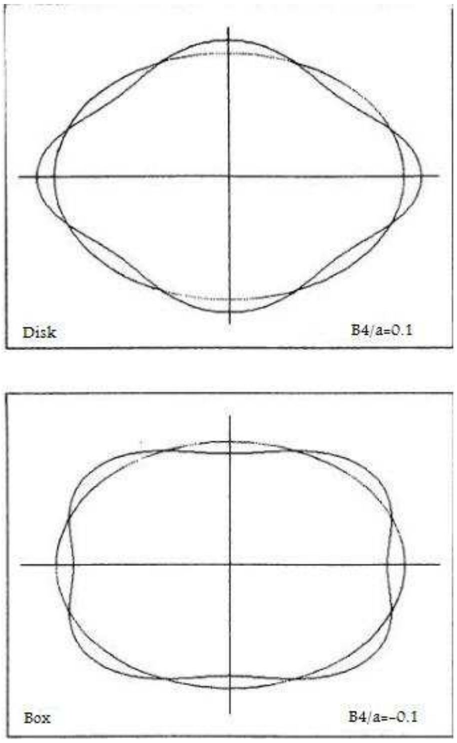

Figure 1.3: Schematic drawing illustrating the isophote deviation from a perfect ellipse. A disky isophote (top panel) is characterised by a positive B4. Viceversa, a negative B4 (bottom panles) indicates ‘boxy’ isophotes.

## Dynamical structure of elliptical galaxies

One of the main topics of interest in the study of ETGs is the evidence that correlations exist between the light distribution and the dynamical structure of a galaxy. For early-type galaxies and bulges of spirals the Faber & Jackson (1976) relation is one of the best known, for which the surface brightness, $I_e$ and the central velocity dispersion, $\sigma_0$ follows the scaling relation $I_e \propto \sigma_0$. Later on, a correlation between effective radius, $R_e$, and $I_e$ was found by Kormendy (1977) so that more luminous galaxies have larger $R_e$, and fainter $I_e$, and hence $R_e \propto I_e$.

The presence of intrinsic scatter in the Faber & Jackson (1976) relation led the astronomical community to hypothesise the necessity of a second parameter, later on identified as the effective radius. Observations of bulges and ellipticals showed that these objects lie on an inclined fundamental plane in the space of the observed parameters (Dressler et al. 1987; Faber 1987; Bender et al. 1992), such that:

$$R_e \propto \sigma^a I_e^b, \tag{1.8}$$

with a, and b constants. It is clear that the previous Faber & Jackson (1976), and Kormendy (1977) relations are projections of the fundamental plane.

The increasing accuracy at which the physical and photometric properties of galaxies could be studied led the astronomical community to consider classical classification schemes (see Sect. 1.1) as incomplete, mainly because of the lack of a physical significance.

Kormendy & Bender (1996) proposed a revision to Hubble's tuning fork, classifying galaxies according to whether they show boxy or disky isophote distortions. Based on the physical properties of galaxies, the classification scheme proposed by Kormendy & Bender (1996) emphasises the Elliptical-Elliptical dichotomy, so that ellipticals (and bulges) come in two varieties (Kormendy et al. 2009): (1) giant, slow-rotating, core galaxies with boxy distorted isophotes, and (2) normal/low luminosity, fast rotating disky and isotropic galaxies, with extra-light at the centre with respect to an inward extrapolation of the outer Sérsic profile.

A related modification to this scheme was recently proposed by Emsellem et al. (2007). They used the available full two-dimensional galaxy kinematics and defined a proxy for the baryons' projected specific angular momentum. In two dimensional spectroscopy this is measured as:

$$\lambda_R = \frac{\Sigma_1^N F_i R_i |V_i|}{\Sigma_1^N F_i R_i \sqrt{V_i^2 + R_i^2}}, \tag{1.9}$$

where $F_i$ is the flux inside the i$^{\text{th}}$ radial bin, $R_i$ its distance to the centre, and $V_i$ and $\sigma_i$ the corresponding mean stellar velocity and velocity dispersion. $\lambda_R$ is used to quantify the specific angular momentum in the stellar components of early-type galaxies, providing a way to examine their dynamical status as records of the galaxy's dynamical history. Using this parametrization the sample of early-type galaxies is divided in two classes: (1) slow rotators with $\lambda_R \leq 0.1$: more massive and brighter systems, nearly round with a significant photometric kinematic axis misalignment, that span a moderately large range of anisotropies. Almost all slow rotators contain a large kpc-scale kinematically decoupled core; and (2) fast rotators with $\lambda_R \geq 0.1$: rather flattened and low luminosity systems, without significant photometric/kinematic axes misalignment, and velocity twist, that span a larger range of anisotropies.

Numerical simulations have shown that fast rotators are formed preferentially through a series of minor mergers between systems where the gas component is not negligible (wet mergers) (Bournaud et al. 2005). Slow rotators instead, are thought to be the result of violent major mergers where the gas did not play an important role (dry mergers), and for which the extreme interaction caused the expulsion of baryonic angular momentum (Naab et al. 2006).

## 1.5 The outer halos of elliptical galaxies

### Cosmological build up of the outer stellar halos of elliptical galaxies

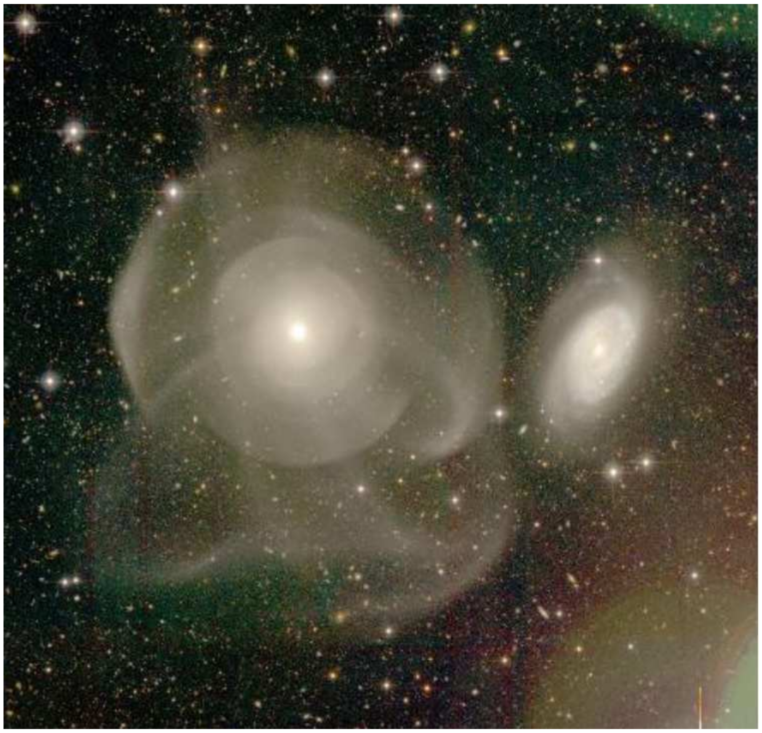

Figure 1.4: Left Panel: Example of early-type galaxy, NGC 474, exhibiting shells around it [credit Duc et al. (2015)]. North is up, East to the left.

In the hierarchical structure formation paradigm, galaxies grow by mergers and accretion of smaller subsystems (White & Rees 1978). These 'satellites' deposit their stars primarily in the outskirts of the main galaxy resulting in its size and mass growth. In a recent work, that used numerical simulations to analyse the origin and structure of the luminous halos surrounding elliptical galaxies, Abadi et al. (2006) introduced the concept of 'in-situ' and 'accreted' halo. In-situ stars are responsible for most of the stars in the main body of the galaxy, while the accreted halo is formed by stars shed by merging subunits during the many accretion events that characterise the hierarchical assembly of the galaxy. These make up preferentially the stellar halo component and dominate the outer regions of the galaxy. Semi-analytical models (De Lucia & Blaizot 2007), and hydrodynamical cosmological simulations (Naab et al. 2009) identified a two-phase scenario for the formation of massive spheroids. The first phase ($6 > z > 2$) is dominated by in-situ star formation from the inflow of cold gas that leads to the production of a massive and dense stellar system. The second phase ($3 > z > 0$) has little in-situ star formation, but significant accretion by stellar material that increases the size of the system with time (Oser et al. 2010). The two-phase formation scenario predicts then, that in the first dissipative phase (high redshift) stars form quickly and build the compact progenitor of the present day elliptical (with stars enriched in $\alpha$-elements); later on minor mergers events play an important role in the galaxy evolutionary process, and metal-poor stars are accreted from smaller stellar systems, resulting in a metallicity gradient.

On the observational front, van Dokkum et al. (2010) found that, within a radius of 5 kpc, the galaxy mass is nearly constant with redshift, whereas the mass of the outer envelope increases by a factor ∼4 since $z = 2$, with the effective radius evolving as $R_e \propto (1+z)^{-1.3}$ (see also Trujillo et al. 2011). Observations of blue colour gradient towards the outskirts of galaxies, mainly attributed to a gradient in metallicity, are also consistent with a late built up of the outer stellar halos. A case study comes from a work by Coccato et al. (2010). They constructed radial profiles of metallicity, [$\alpha$/Fe] abundances, and age from the centre out to ∼4 $R_e$ of the Coma BCG, NGC4889, and found that the inner regions are characterised by a steep metallicity gradient and high [$\alpha$/Fe] ratio, reflecting the rapid phase of formation. In the outer regions the metallicity gradient becomes shallower, and the [$\alpha$/Fe] ratio shows a strong negative gradient. This we would expect if the accreted systems had experienced a more extended star formation history. As I will discuss in Sect. 1.7, also for M87 colour, age and metallicity gradients support the hypothesis of hierarchical formation (e.g.Rudick et al. (2009); Montes et al. (2014)).

### Detecting substructure in elliptical galaxies

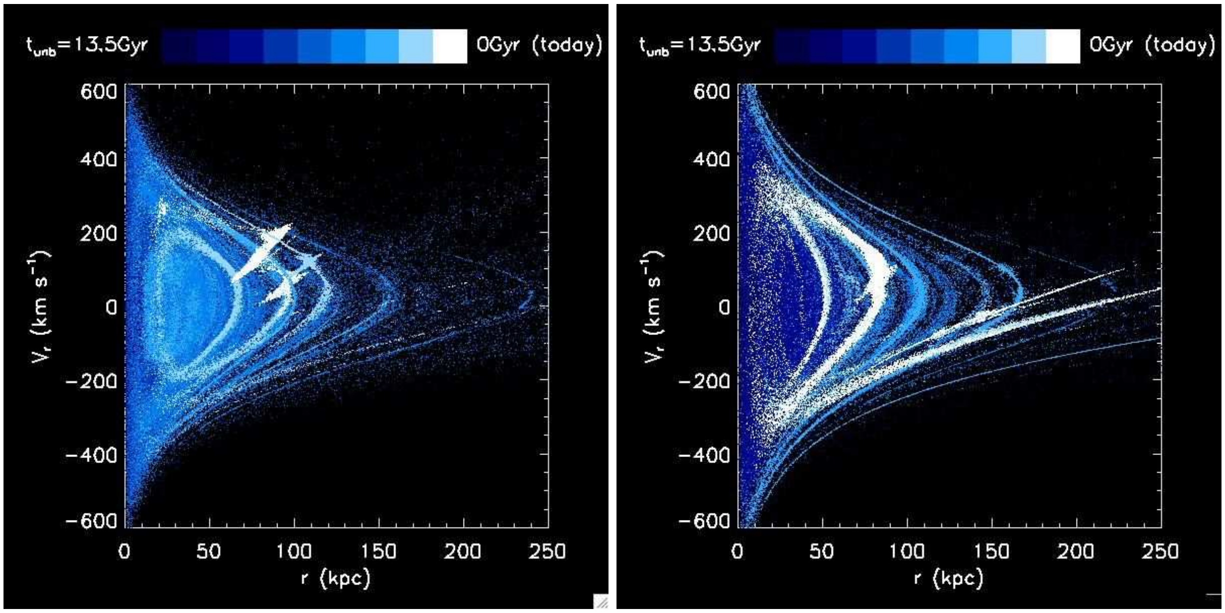

Figure 1.5: Left Panel: Radial phase-space diagrams (Radial velocity vs distance relative to the host halo centre) for semianalytic plus N-body simulations of a satellites being accreted by main halos. The colour code reflects the time each particle become unbound to its parent satellite Bullock & Johnston (2005)].

In a scenario where mergers and accretions are driving mechanisms in determining the current epoch characteristics of galaxies, we expect to find signatures of these accretion events that can be studied to trace the dynamical evolution of galaxies. Stars in the outer galaxy halos provide an important avenue for testing theories of galaxy formation because they have long orbital times. Records of accretion events are then revealed in the form of spatially extended low-surface brightness substructures (Mihos et al. 2005; van Dokkum et al. 2014; Duc et al. 2015), such as tidal streams and shells (Malin & Carter 1980; Tal et al. 2009) as evidence for the build-up of galaxy halos. In field galaxies, tidal tails and shells represent low surface brightness ($\mu_V > 26.5$mag arc$^{-2}$) tidal debris that formed during galaxy interactions and will survive over many Gyr (Hernquist & Spergel 1992; Gonzalez et al. 2005). While shell phenomena are consistent with mergers with lower mass companions (Quinn 1984), long and luminous tidal tails are the result of major mergers (Toomre & Toomre 1972). Fainter streams are more ambiguous and might come either from the accretion of smaller systems (Bullock & Johnston 2005) or from material at the base of a pre-existing tails that is falling back toward the merger remnant (Hibbard & Mihos 1995). For galaxies in a dense cluster environment the same substructures observed in field galaxies might have experienced tidal stripping by the cluster potential becoming spatial mixed and hence integrated in the diffuse ICL (Mihos 2004). Alternatively, the presence of such substructures can be indicative of a recent accretion event, not yet disrupted by the cluster tidal field. Fig.1.4 shows a great example of an early-type galaxy that experienced merger events.

These features are not only visible spatially but also in the kinematics. Halos that formed in this manner are expected to have a complex velocity phase-space, where the satellite stars are not in a phase-mixed equilibrium in the host galaxy potential (see Fig.1.5).

The finding of this type of structures can leave little doubt that accretion of satellites has been an important contributor of the formation of stellar halos, offering a direct test of whether cosmology is indeed hierarchical on small scale.

## Dark Matter and Dynamics

It is now well known that elliptical galaxies are luminous sources of X-ray radiation (Forman et al. 1985) due to the extensive atmospheres of hot, diffuse interstellar gas that they contain. X -ray observations provide a powerful tool to study the full isothermal potential, hence the shape of the dark matter distribution, and mass profile, using the hot gas as a tracer in assumed hydrostatic equilibrium in the gravitational potential (Nulsen & Bohringer 1995; Humphrey et al. 2006; Nagino & Matsushita 2009). Analysis of the hot X-ray emitting gas in X-ray bright ellipticals and comparison with dynamical mass determinations indicates that a contribution of non-thermal particles (~20-30%) to the gas pressure may be important in the inner ~10 kpc (Churazov et al. 2008a; Das et al. 2010). Das et al. (2010) also found that their entire galaxy sample is characterised by outer circular velocity curves that are rising, implying a density profile for the DM component steeper than an isothermal mass profile. In addition to X-ray gas profiles, mass distribution can be determined using gravitational lensing, and dynamics. Weak lensing allows mass estimates up to several hundreds of kiloparsec, while with strong lensing these measurements are constrained within the Einstein radius. Together with the velocity dispersion these data have shown that mass density are well represented by isothermal profiles. Dynamical models of nearby ellipticals in systems like Virgo, Fornax and Coma clusters (Gerhard et al.

2001; Cappellari et al. 2006; Thomas et al. 2007a) have shown that galaxies in these systems are usually DM dominated for distances larger than $2r_e$. In a later study Thomas et al. (2007b), demonstrated that the ellipticals in Coma have on average ~7 times larger DM densities than spirals with the same luminosity, and ~13 times higher DM densities than spirals with the same baryonic content, implying an earlier formation of the inner halos of ellipticals than those of spiral galaxies.

From what I have discussed about galaxy clusters and ICL it is clear that both the formation of extended galaxy halos and ICL are closely related to the morphological transformation of galaxies in clusters. Hence the study of the amount, distribution and kinematics of these stellar components provides information on the evolution of galaxies and their hosting clusters. The availability of bright stellar proxies such as PNs has made possible the study of the outer galaxy regions and diffuse light. These objects indeed are one of the few stellar probes that can be successfully measured and studied at such distances.

## 1.6 Planetary Nebulas (PNs)

### Physics of PNs

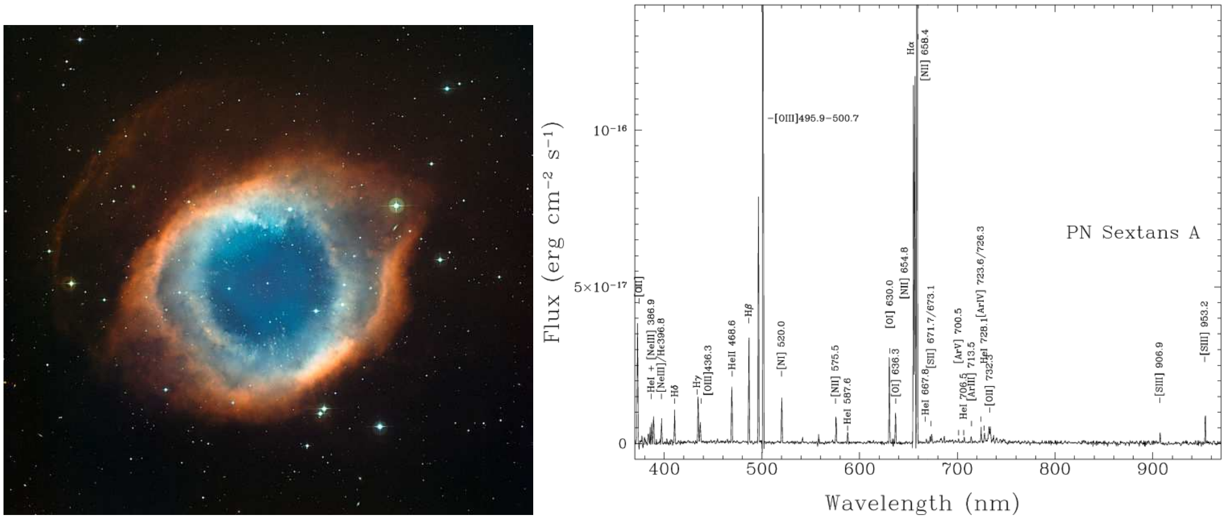

Figure 1.6: Left Panel: The Helix Nebula (NGC7293). The blue-green coloration is due to the $\lambda$5007/4959 forbidden lines of the [OIII] emission, while the red coloration comes from ionised hydrogen and nitrogen [credit: NASA] Right Panel: Example from a PN spectra from Magrini et al. (2005).

Stars in the mass range between 1 and 8 $M_\odot$ at the end of the asymptotic giant branch (AGB) phase go through the planetary nebula phase before they end their lives as a white dwarf. The formation mechanism of PNs is thought to be the following: during the AGB phase, the outer layers of the star are expelled via pulsations and strong stellar winds. Without these opaque layers, the ultraviolet (UV) radiation, emitted by the hot luminous core, escapes and causes the atoms in the outer shell to be excited or ionised. This energised shell radiates as a PN that emits in several strong emission lines from the UV to the near-infrared (NIR), the brightest of these being at the wavelength 5007 Å: Dopita et al. (1992) showed that up to 15% of the UV emitted energy by the central star is re-emitted in the forbidden [OIII]$\lambda$5007 Å line. In atomic physics a forbidden line is a spectral line that can only be seen in very low density conditions. In gas at extremely low densities, electrons can populate excited metastable energy levels in atoms and ions which at higher densities are rapidly de-excited by collisions. Electron transition from these levels to the double ionised oxygen gives rise to the [OIII]$\lambda$5007 Å line and other lines[11]. Thus, the observation of the [OIII]$\lambda$5007 Å emission line in a PN spectrum shows that PN are made of extremely rarefied gas. Characteristic temperatures of these emission objects are around $10^4$ K, i.e. in the range of the ionization temperature of the hydrogen. The PN expansion velocities, that are measured by the width of the spectral emission line, show that the gas is moving away from the central star with a typical speed between 10 and 30 kms$^{-1}$. When interpreted using dynamically evolving nebular models, PN shell expansion velocities provide estimates of PN dynamical ages (Schönberner et al. 2005). From the study of the luminosity specific PN number (see Sect.1.6), Buzzoni et al. (2006) estimated that their life-times go from a minimum of 1000 yr to a maximum of 30000 yr after which the PN will dissipate into the interstellar medium. Examples of an optical image of a PN and its typical spectrum are given in Fig. 1.6.

## PN as tracers of stellar populations

### PN Luminosity Function

The characteristic size of ~0.3 pc makes the PN shell and its [OIII] emission spatially resolved in our own Galaxy. Beyond the Milky Way, PNs appear as un-resolved sources of green light with a total flux in the [OIII] line, $F_{5007}$. Following (Jacoby 1989) the magnitudes, $m_{5007}$ are defined as:

$$m_{5007} = -2.5 \log F_{5007} - 13.74. \tag{1.10}$$

When these magnitudes are measured for a statistical sample of PNs, the count of objects as a function of $m_{5007}$ returns the PN luminosity function (PNLF). It has been shown that the PNLF can follow the analytical formula:

$$N(M) \propto e^{0.307 m_{5007}} [1 - e^{3(m^* - m_{5007})}], \tag{1.11}$$

where $m^*$ is the apparent magnitude of the brightest PN (Ciardullo et al. 1989). This empirical formula reproduces the high mass cut-off and the fading of a spherical gas cloud surrounding a non-evolving central star (Henize & Westerlund 1963). The total number of a PN population in a galaxy is then given by the integration of Eq. 1.11 down to 8 magnitude from $m^*$, where

---

[11] More generally forbidden lines are also observed as consequence of the electron transition from metastable levels to nitrogen and other oxygen ions (e.g, O+ and N+)

this magnitude range accounts for the faintest PN observed in the Galactic halo (Ciardullo et al. 1989). There are two aspects that can be addresses by analysing the shape of the PNLF.
(1) The bright cut-off is observed to be invariant between different stellar population systems, but the cause for it is not yet understood. The analysis of synthetic PN populations (e.g. Méndez et al. (2008)) shows indeed that the assumption of a constant, universal bright cut-off is in contrast with some physical and statistical arguments. It is reasonable to believe that the bright end of the PNLF must depend on i) the size of the sample, because the bigger the sample the higher the possibility of observing a very massive central star that will go through the PN phase producing a very bright PN; ii) the final post-AGB mass, because the presence of massive star formation would lead to the presence of more massive central stars than a population with no recent star formation history; iii) how optically thin are the brightest PNs, because the more ionising photons that are lost the fainter the PNs will result.

2) It is now believed that the function's faint end shape contains information about the parent stellar population the PN sample is associated with. Ciardullo et al. (2004) reported that star-forming systems are characterised by a shallower slope at ∼1.5 magnitude below $m^*$ when compared to older stellar populations. Thus the conundrum is: how can we explain such different behaviour in different stellar systems? To answer this question we need to take into consideration the different timescale regimes that control the PN evolution. In older stellar systems, for example, where the higher fraction of PNs is powered by low-mass, slowly evolving central cores, the predominant timescale will be the one tied to the expansion of the nebula, resulting in a LF with a higher fraction of PNs populating the faintest bins of magnitude. On the contrary, in a young stellar population system, where the probability of observing more massive central stars is higher, the time scale for the central star evolution is much shorter than for the nebular expansion and the resulting PNLF will show a deficit of PNs at intermediate magnitudes with an overall shape at the faint end consistent with a smaller fraction of fainter PNs. This has been confirmed with sophisticated analysis of PN evolution (Méndez et al. 2008) and can be summarised as following: relatively young stellar systems, dominated by high core mass PNs can present a dip in their PNLF. Dips in the PNLF are observed for PN populations detected in star forming galaxies such as the LMC, SMC, M33, and NGC 6822, and is absent in the PNLF associated with bulges or early-type galaxies. The magnitude at which the dip occurs varies in different PN populations from ∼ 1.5 to ∼ 4 magnitude below $m^*$ (Jacoby & De Marco 2002; Ciardullo et al. 2004; Hernández-Martínez & Peña 2009; Reid & Parker 2010). In a recent work Rodriguez et al. (2014) presented a new model for the PNLF that includes two populations in the distribution, based on the hypothesis that the non-monotonic PNLF is simply a reflection of the bimodal luminosity function expected from post-AGB stars.

### The $\alpha$-parameter

In a statistically complete sample, the total number of observed PNs, $N_{\mathrm{PN}}$ correlates with the sampled bolometric luminosity, $L_{\odot,\mathrm{bol}}$, of the system through the luminosity specific PN number, or $\alpha$-parameter for short, defined as:

$$\alpha = \frac{N_{\rm PN}}{L_{\odot,\rm bol}}. \tag{1.12}$$

In simple stellar populations (SSPs) theory, the stellar death rate is weakly dependent on the age, metallicity and star formation history of the underlying stellar populations that formed PNs (Renzini & Buzzoni 1986), so that the total number of PNs associated to a system with a given bolometric luminosity for a SSP can be written as:

$$N_{\rm PN} = B \times L_{\odot,\rm bol} \times \tau_{\rm PN}, \tag{1.13}$$

where $B$ is the specific evolutionary flux ( that approximates to $2 \times 10^{-11}$ in units of stars yrs$^{-1}$ $L_{\odot,\rm bol}$), and $\tau_{\rm PN}$ is the PN visibility lifetime in years. The luminosity-specific PN density then becomes:

$$\alpha = B\tau_{\rm PN}. \tag{1.14}$$

Due to the small variation of the specific evolutionary flux, different values of $\alpha$ correlate with different PN visibility lifetime associated to PNs with different parent stellar populations. In order to understand this, it needs to be said that the PN visibility lifetime is constrained by the post-AGB stellar core mass, that defines three different time regimes, i.e. the PN lifetime is driven by the nuclear, dynamical and transition timescales if the core masses are in the ranges $M_{core} \geq 0.57M_\odot$, $0.55M_\odot \leq M_{core} \leq 0.57M_\odot$ ,$0.52M_\odot \leq M_{core} \leq 0.55M_\odot$, respectively (Buzzoni et al. 2006). For low mass-core PNs, $M_{core} \leq 0.55$, the visibility lifetime can become shorter because the time required for the central star to produce ionising photons increases, and the surrounding nebula can be close to evaporation when the ionization/excitation process starts. Systems, characterised by old stellar populations that produce low mass core PNs will then be characterised by smaller values of $\alpha$. Observationally the values of $\alpha$ correlate with the integrated $(B-V)$ colour of the parent stellar populations. For redder galaxies with $(B-V) > 0.8$, the spread of the measured values increases by up to a factor of 7. Thus showing that the value of $\alpha$ may be strongly influenced by the morphological type of the host galaxy (Buzzoni et al. 2006), or on smaller scales by the different stellar populations that the PNs originated from.

### Kinematics with PNs

In addition to study the PNLF and the $\alpha$-parameter, PNs are also great kinematic tracers. As a consequence of their strong [OIII]$\lambda$5007 Å emission line PNs can be detected and the line-of-sight (LOS) velocity can be measured out to several $r_e$ from the galaxy centre, where the low surface-brightnesses make standard spectroscopy unavailable. PNs have been the target of several surveys aimed at tracing the motion of the stellar populations in the outer regions of early type galaxies (e.g. Hui et al. (1995); Arnaboldi et al. (1998); Méndez et al. (2001); Peng et al. (2004); Coccato et al. (2009); McNeil et al. (2010); Cortesi et al. (2013)), and of the IC component in nearby clusters (Arnaboldi et al. 1996, 2004; Gerhard et al. 2005; Doherty et al. 2009; Ventimiglia et al. 2011). Coccato et al. (2009) showed that absorption line spectroscopy and PN kinematics are in good agreement in the region where the data set overlap. The study of 2D PN

velocity fields in early-type galaxies (Coccato et al. 2009), shows that:
1) The slow-rotators/fast-rotators classification proposed by Emsellem et al. (2007) and based on inner data is preserved in the outer stellar halos. In particular, in the halo some fast rotators have a declining $\lambda_R$ profile, almost reaching the slow rotators regime. Viceversa, slow rotators have a slowly increasing $\lambda_R$ profiles which reach the fast rotators regime.

2) Velocity dispersion profiles can be divided into two groups: i) slowly decreasing profiles and steeply falling profiles. These two groups largely overlap with core and cusp ellipticals respectively (Kormendy et al. 2009).

3) Halo kinematics correlate with other galaxy properties such as luminosity, total mass and the V/$\sigma$ ratio.

## Extragalactic PN surveys

There are three techniques adopted to detect extragalactic PNs, a brief description is as follow with examples shown in Fig. 1.7.
**On-off technique**. As a result of their bright [OIII]$\lambda$5007 Å and faint continuum emission, extragalactic PNs can be identified as objects detected on a narrow-band image (centred on the redshifted wavelength of the $\lambda$5007 Å line at the distance of the observed object) but not detected on images taken through a broad/off-band filter centred on a nearby wavelength (V or R band mostly) (Jacoby et al. 1990). PNs are then detected by blinking the on-band vs the off-band image, or using selection criteria based on the distribution of the detected sources in a colour-magnitude diagram (Theuns & Warren 1997a; Arnaboldi et al. 2002). The highest source of contamination are background Ly-$\alpha$ galaxies at $z = 3.12$ and [OII] emitters at $z = 0.34$ that can mimic PN emission. The amount of contamination can be evaluated either by using pre-existing background emission galaxy surveys, or with additional observations with a H$\alpha$ narrow band filter. Eventually the sample of PN candidates can be followed-up spectroscopically.
**Counter-dispersed slitless spectroscopy technique**. The field of interest is imaged through a slitless spectrograph tuned to the [OIII] line. When this image is studied, the background light of the galaxy and foreground stars will be found to be blurred, while the PNs are recognisable as bright point-like images. This technique also allows to measure the PN LOS velocity when a second image is taken with the spectrograph rotated by 180°. The velocity of the detected emission line is in fact proportional to the separation between their position in the two spectral images. The two images can be either two consecutive, reversed exposures, or taken simultaneously using duplicate spectrograph arms (Douglas et al. 2002).
**Multi-slit Imaging spectroscopy technique**. This technique is based on the combination of a mask of parallel multiple slits with an [OIII] $\lambda$5007 Å narrow-band filter. As a result of the small width of a PN emission line, its entire flux is gathered in few pixels in the two-dimensional spectrum. The sky emission is instead dispersed in wavelength, reducing the sky noise by a factor 5-10, depending on the instrumental resolution. This is the adopted technique to survey galaxies at distanced $D > 25$ Mpc for which the level of the sky noise would be of the same order of magnitude as the [OIII] emission.

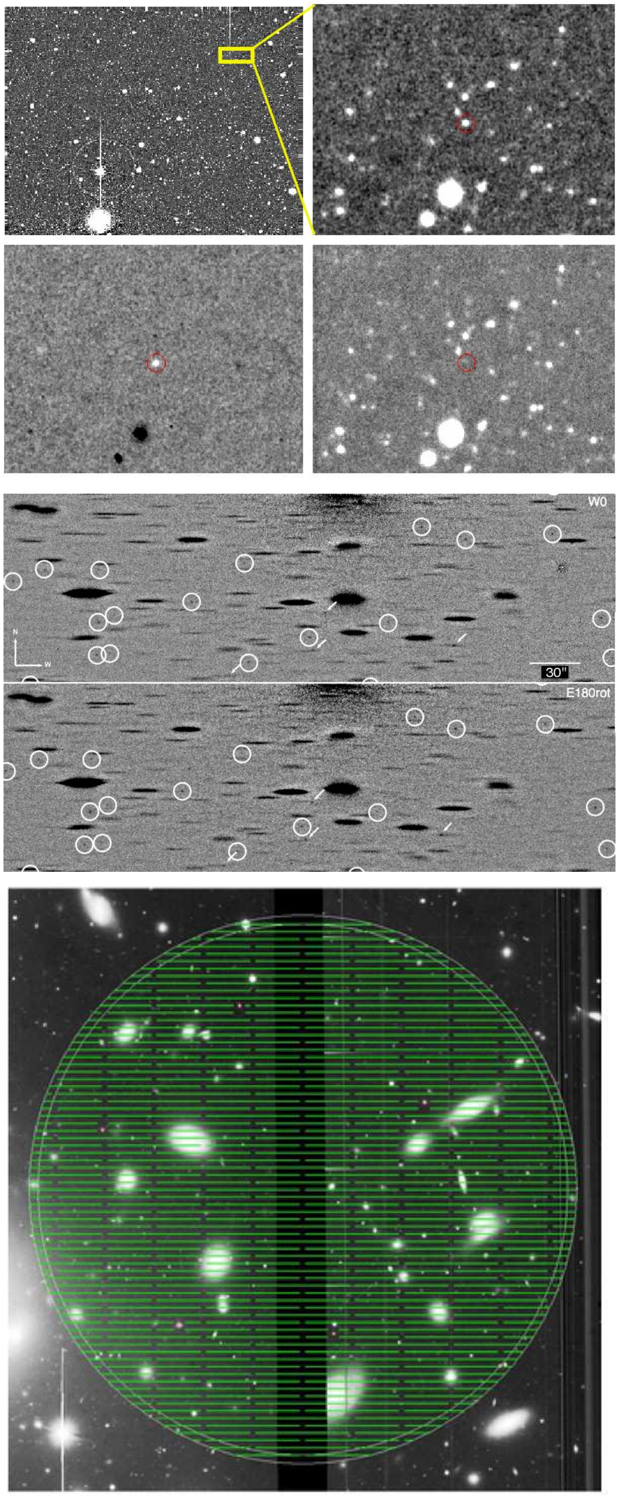

Figure 1.7: Top Panel: Example of a PN candidate (red circle) with detectable flux in the on-image (Top-top right panel), no measurable flux in the off-image (Top-bottom right panel), and positive flux in the colour image (top-bottom left) [credit Longobardi et al. (2013)]. Central Panel: Dispersed image at PA=0° (Central-top panel) and PA=180°. The stars appear as streaks in the x-direction (the direction of dispersion). Examples of PN candidates are circled. Notice that there is a small difference in the PNs x-positions in the images due to their velocity [credit McNeil et al. (2010)]. Bottom-Panel: Multi-Slit mask super imposed on the Coma cluster. The dispersion direction is horizontal and the spatial direction is vertical [credit Gerhard et al. (2005)].

## 1.7 The Thesis: The Virgo cluster and its central cluster galaxy M87

This work investigates the light in the outer regions of the Virgo central galaxy M87 in the region where the transition between galaxy halo and ICL occurs. To better understand the reason for choosing such a target, in what follows I describe the Virgo cluster and M87 physical properties, that will show that these are ideal targets for a survey aimed at detecting PNs in an extended halo when investigating halo and ICL stellar population properties.

### Virgo

Virgo is a medium rich cluster, the nearest to the Milky Way lying at a distance of approximately ∼15 Mpc[12]. Its structure is irregular, being characterised mainly by two components. There is a major subcluster A of galaxies around the giant E galaxy M87, made up predominantly of early-type galaxies and with a large velocity dispersion $\sigma$ ∼900 kms$^{-1}$ (Binggeli et al. 1993); and a smaller and less dense subcluster B around the brightest cluster galaxy M49 with mainly spiral galaxies and with a much smaller velocity dispersion $\sigma$ ∼400 kms$^{-1}$ (Binggeli et al. 1987). Since the advent of X-ray satellites, cluster subclusters can be observed and mapped in the intracluster gas. With a study of the X-ray structure of Virgo the different subclusters became evident by their extended X-ray halos, showing that the centre of Virgo lies close to M87 (Binggeli et al. 1987; Nulsen & Bohringer 1995; Churazov et al. 2008b), but it is slightly displaced towards M86, north-west with respect to M87. On the other hand M86, like M87 and M49 might identify the center of its own subcluster (Mei et al. 2007). The irregularity of Virgo in both configuration and velocity space shows that the core and the envelope are still forming. Studies of the ICL in Virgo suggest, in fact, a dynamically young structure: the IC component shows field to field variations (Feldmeier et al. 2004a) and a deep image of the Virgo cluster (Mihos et al. 2005; Rudick et al. 2010) revealed a complex network of extended tidal features suggesting that it is poorly mixed and not completely in equilibrium. From a study of intracluster RGB stars Durrell et al. (2002) observed that the IC population in Virgo is older than 2 Gyr, and moderately metal-rich, consistent with the building up of the IC component from the stripping of intermediate luminosity galaxies. Later on Williams et al. (2007) observed that

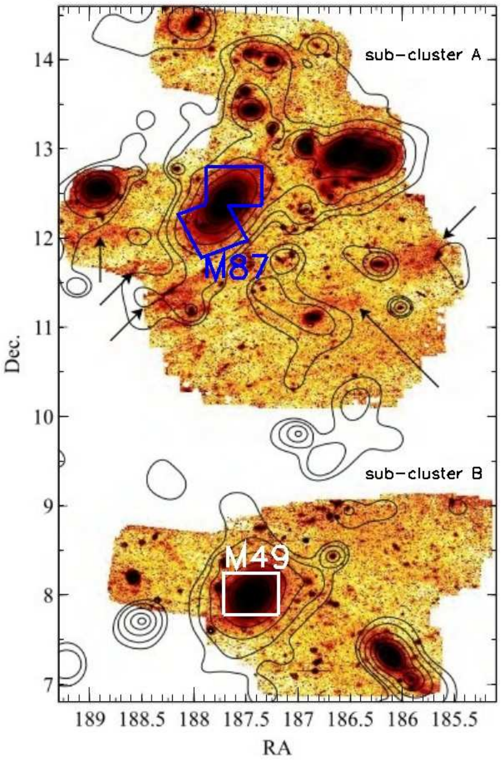

Figure 1.8: V-band image of the Virgo subcluster A/B (Mihos et al. 2005, 2013) depicting the area around M87 surveyed in this work (black rectangles), and in future works to study the region around M49 (white rectangle). Black contours are GC density contours (Durrell et al. 2014).

---

[12] For the Virgo distance we assume the one resulting from PNLF estimations.

stellar metallicities span a range of values, hinting at an ICL component that is a result of a larger variety of progenitors.

## M87

Close to the dynamical centre of the Virgo cluster, M87 is often the subject of investigation to understand the physics in dense cluster environment. Along the Hubble sequence M87 is catalogued as a peculiar E0 galaxy, where the peculiarity has to be attributed to the presence of a relativistic jet emerging from the core ejected by a supermassive black hole of few billion solar masses (e.g. Sargent et al. 1978; Walsh et al. 2013). M87 is considered a type-cD galaxy (Weil et al. 1997; Kormendy et al. 2009), where the outer envelope contributes a small amount of extra light. Kormendy et al. (2009), found that if the inner profile is well represented by a $n \simeq 9$ Sérsic profile, the whole light distribution outside the core can be well fitted by a $n \simeq 11.8$ Sérsic function, implying that the cD halo cannot conclusively be identified as a photometrically distinct outer component. The extended stellar envelope of this galaxy reaches a radius of about $\sim$ 150 kpc, beyond which it has been shown that the M87 halo could be truncated, possibly by an earlier interaction with another mass concentration (Doherty et al. 2009). Mergers play a prominent role in the hierarchical formation of galaxy such as M87. The presence of age and metallicity gradient in its inner regions (first 5 kpc from the galaxy centre) (Liu et al. 2005; Montes et al. 2014), and a blue colour gradient towards the outer regions (Rudick et al. 2010), as well as the recent finding of a kinetically decoupled core (Emsellem et al. 2014) support the hierarchical formation scenario for M87. This galaxy also has diffuse X-ray emission from hot gas. Hence, X-ray data (ROSAT X-ray observations by Nulsen & Bohringer (1995), and *Chandra* and $XMM-Newton$ X-ray observations by Churazov et al. (2010); Das et al. (2010)) have been used to determine the distribution of its gravitational mass. In addition to X-ray gas profiles, integrated stellar kinematics (Murphy et al. 2011, 2014), as well as single stellar tracers such as GCs and PNs (Zhu et al. 2014; Arnaboldi et al. 2004; Doherty et al. 2009) have been used to derive their matter distribution, showing that M87 is dark matter dominated beyond several $r_e$, and one of the most massive galaxy in the local Universe, with an estimated total mass $M \sim 10^{12} M_{\odot}$.

### Previous PN studies in Virgo and M87

Several large-scale [OIII]$\lambda$5007 Å surveys of intergalactic fields have been carried out with the goal of mapping the distribution, kinematics, and luminosity function of PNs in Virgo, starting from the discovery of ICPNs by Arnaboldi et al. (1996). The study of ICPNs constrained the fraction of the ICL to 10% in the Virgo core (Feldmeier et al. 2003), while Castro-Rodríguez et al. (2009) showed it is a non uniform distribution, higher in the core than in lower density regions. ICPN analysis has allowed a better understanding of the dynamical nature of Virgo. Aguerri et al. (2005) showed that PN numbers varies over different fields, suggesting that the ICL is poorly mixed. Arnaboldi et al. (2002) analysing the luminosity function of spectroscopically confirmed PNs at the north of Virgo cluster's core argued that the three-dimensional depth of the Virgo cluster put it at a 14% - 19% shorter distance than M87.

Interesting results also come from spectroscopic studies of PNs. Presenting measurements of the velocity distribution of ICPNs in three fields of the Virgo cluster Arnaboldi et al. (2004)

confirmed that Virgo is highly non uniform and an unrelaxed galaxy cluster. In addition, from the study of PNs in the outer regions of M87 by Doherty et al. (2009), there is evidence for the truncation of the luminous halo of M87 due to both the spatial distribution of the PNs with velocity near the systemic velocity of M87, and from the decreasing of velocity dispersion in the outer edge. Doherty et al. (2009) also show that by using their kinematics, PNs might be separable into components that are bound to either the potential of M87s halo or of that of the cluster.

To investigate and prove (or disprove) these initial hypotheses, I carried out work on a ~15 times larger, uniformly distributed PN sample, which I describe in more detail in the rest of this thesis.

The thesis is organised as follows: first, I present the PN Suprime-Cam Survey in Chapter2, and describe the automatic selection criteria that allowed me to acquire the largest, deepest, and most extended photometric catalogue of PNs in the outer regions of M87. I then outline how the study of this data showed the presence of two PN populations, one associated to the halo of M87 and one to the Virgo ICL, consistent with M87 halo being redder and more metal rich than the ICL.

Next, in Chapter3, I report the results of the wide and high-resolution FLAMES spectroscopic PN survey. Using the spectroscopically confirmed sample of PNs obtained with FLAMES, I investigated the halo-ICL dichotomy, confirming the presence of both a halo and a IC component. In addition, I show how the PNs spectroscopic information allows them to be distinguished, based on their velocity phase-space properties. Finally, I come to the conclusion, that in the Virgo cluster core, M87's halo and the ICL are two dynamically distinct components, that also differ in spatial distribution and physical properties.

In Chapter4, I present the discovery of an accretion event in the halo of M87, unknown until this work. With the combined use of PN kinematics and V/B-band photometry, I show that the accreted satellite can be traced both as a kinematic substructure in the velocity phase-space obtained by PNs, and as a spatial substructure in the optical light. This study emphasises the importance of the role that machine learning techniques (such as Gaussian Mixture Models) can play in astronomy.

Chapter5 is dedicated to the analysis of the overall kinematics of M87's halo, including the average velocity and velocity dispersion maps, point symmetry, and $\lambda(R)$ a proxy for the angular momentum profile. Then, I present the composite velocity dispersion profile of M87, tracing M87's stellar motions from the innermost regions out to 200 kpc along the major axis. I outline how the results show a dynamically complex system, which reflects that the halo is still assembling.

Finally, in Chapter6, I discuss and summarise the results and main conclusions obtained through the work described in this thesis.

# Chapter 2

# The planetary nebula population in the halo of M87

*This chapter is published as the study Longobardi et al. (2013)*

## Abstract

We investigate the diffuse light in the outer regions of the nearby elliptical galaxy M87 in the Virgo cluster, in the transition region between galaxy halo and intracluster light (ICL).

The diffuse light is traced using planetary nebulas (PNs). The surveyed areas are imaged with a narrow-band filter centred on the redshifted [OIII]$\lambda$5007 Å emission line at the Virgo cluster distance (the on-band image) and with a broad-band V-filter (the off-band image). All PNs are identified through the on-off band technique using automatic selection criteria based on the distribution of the detected sources in the colour-magnitude diagram and the properties of their point-spread function.

We present the results of an imaging survey for PNs within a total effective area of 0.43 deg$^2$, covering the stellar halo of M87 up to a radial distance of 150 kpc. We extract a catalogue of 688 objects down to $m_{5007} = 28.4$, with an estimated residual contamination from foreground stars and background Ly$\alpha$ galaxies, which amounts to $\sim 35\%$ of the sample. This is one of the largest extragalactic PN samples in number of candidates, magnitude depth, and radial extent, which allows us to carry out an unprecedented photometric study of the PN population in the outer regions of M87. We find that the logarithmic density profile of the PN distribution is shallower than the surface brightness profile at large radii. This behaviour is consistent with a model where the luminosity specific PN numbers for the M87 halo and ICL are different. Because of the depth of this survey we are also able to study the shape of the PN luminosity function (PNLF) in the outer regions of M87. We find a slope for the PNLF that is steeper at fainter magnitudes than the standard analytical PNLF formula and adopt a generalised model that treats the slope as a free parameter.

The logarithmic PN number density profile is consistent with the superposition of two components associated with the halo of M87 and with the ICL, which have different $\alpha$ parameters.

We derive $\alpha_{2.5,\mathrm{halo}} = (1.10^{+0.17}_{-0.21}) \times 10^{-8}\ \mathrm{N_{PN}L^{-1}_{\odot,bol}}$ and $\alpha_{2.5,\mathrm{ICL}} = (3.29^{+0.60}_{-0.72}) \times 10^{-8}\ \mathrm{N_{PN}L^{-1}_{\odot,bol}}$ for the halo and the intracluster stellar components, respectively. The fit of the generalised formula to the empirical PNLF for the M87 halo returns a value for the slope of 1.17 and a preliminary distance modulus to the M87 halo of 30.74. Comparing the PNLF of M87 and the M31 bulge, both normalised by the sampled luminosity, the M87 PNLF contains fewer bright PNs and has a steeper slope towards fainter magnitudes.

## 2.1 Introduction

Stars in the mass range between 1 and 8 $\mathrm{M_\odot}$ go through the planetary nebula (PN) phase before ending their lives as white dwarfs. The optical image of a PN is dominated by the luminous ionized envelope that is powered by the stellar core at its centre. The envelope emits in several strong lines from the UV to the NIR, and Dopita et al. (1992) showed that up to 15% of the luminosity of the central star is re-emitted in the forbidden [OIII] line at $\lambda$5007 Å.

PNs have been used as kinematic tracers of the stellar orbital distribution in the outer regions of galaxies, where the continuum from the stellar surface brightness is too low with respect to the night sky, both in nearby galaxies (Hui et al. 1993; Peng et al. 2004; Merrett et al. 2006; Coccato et al. 2009; Cortesi et al. 2013) and out to 50-100 Mpc (Ventimiglia et al. 2011; Gerhard et al. 2005). The outer regions of galaxies are particularly interesting because dynamical times are longer there, so they may preserve information of the mass assembly processes.

The observed properties of the PN population in external galaxies also correlate with the age and metallicity of the parent stellar population. These properties are the luminosity-specific PN number, $\alpha$-parameter for short, that quantifies the stellar luminosity associated with a detected PN, and the shape of the PN luminosity function (PNLF). We discuss these in turn.

Observationally the values of $\alpha$ correlate with the integrated (B-V) colour of the parent stellar population, with the spread in observed values for the reddest galaxies increasing significantly with respect to the constant value observed in bluer ($(B-V) < 0.8$) objects (Hui et al. 1993; Buzzoni et al. 2006). For the reddest galaxies, the value of $\alpha$ correlates with the (FUV-V) colour, with the lowest number of PNs observed in old and metal-rich systems (Buzzoni et al. 2006).

To describe the shape of the PNLF for extragalactic PN populations, the analytical formula proposed by Ciardullo et al. (1989) has generally been used, but see also models by Méndez et al. (1993, 2008). At the brightest magnitudes the PNLF shows a cutoff that is observed to be invariant between different Hubble types and has been used as secondary distance indicator (Ciardullo et al. 2004). From about one magnitude fainter than the PNLF cutoff, the analytical formula predicts an exponential increase, in agreement with the slow PN fading rate described by Henize & Westerlund (1963). Observationally, the PNLF slope correlates with the star formation history of the parent stellar population, with steeper slopes observed in older stellar populations and flat or slightly decreasing slopes in younger populations (Ciardullo et al. 2004; Ciardullo 2010).

The Virgo cluster, its elliptical galaxies, and intracluster light (ICL) were the targets of several PN surveys (Ciardullo et al. 1998; Feldmeier et al. 1998, 2004a; Arnaboldi et al. 2002, 2003, 2004; Castro-Rodríguez et al. 2003, 2009; Aguerri et al. 2005), aimed at measuring distances and the ICL spatial distribution. In this paper we report the results of a deep survey carried out with the Suprime-Cam at the Subaru telescope to study the PN population in the halo around M87, one of the two brightest galaxies in the Virgo cluster.

NGC 4486 (M87) is a giant elliptical galaxy situated at the centre of the subcluster A in the Virgo cluster (Binggeli et al. 1987), the nearest large scale structure in the local universe. According to current models of structure formation, M87 acquired its mass over a long period of time through galaxy mergers and mass accretion. The stars in M87 are old (Liu et al. 2005), and its stellar halo contains about 70% of the galaxy's light down to $\mu_V \sim 27.0$ mag arcsec$^{-2}$ (Kormendy et al. 2009). Thus M87 is an ideal target for a survey aimed at detecting PNs in an extended galaxy halo, when investigating the halo kinematics and stellar population.

The paper is organized as follows: in Section 2.2 we describe the Suprime-Cam PN survey and the data reduction procedure. In Section 2.3 we describe the PN catalogue extraction and validation. The relation between the spatial distribution of the PN candidates and the M87 surface brightness profile is investigated in Section 2.4. We present the PNLF measured in the M87 halo in Section 2.5 and discuss the comparison with the PNLF for the M31 bulge. Finally, we summarize our conclusions in Section 2.6. In the rest of the paper we adopt a distance modulus of 30.8 for M87, which means that the physical scale is 73 pc arcsec$^{-1}$.

## 2.2 The Suprime-Cam M87 PN Survey

### 2.2.1 Imaging and observations

In March 2010 we observed two fields with the Suprime-Cam 10k×8k mosaic camera, at the prime focus of the 8.2 m Subaru telescope (Miyazaki et al. 2002). The CCDs have a readout noise of 10 e$^-$ and an average gain of 3.1 e$^-$ ADU$^{-1}$. Each field of view covers an area of $34' \times 27'$, with a pixel size of $0''.2$; the two pointings cover the halo of M87 out to a radial distance of 150 kpc. Figure 2.1 shows a deep V-band image of the Virgo cluster core region and the two fields studied in this work overlaid. We label these fields as the M87 SUB1 and M87 SUB2 fields, respectively.

Both fields were observed through an [OIII] narrow-band filter (on-band filter), centred on $\lambda_c$=5029 Å with a band width $\Delta\lambda$=74 Åand a broad-band V-filter (off-band filter). The total exposure time for the on-band images was $\sim$ 3.7 hr and $\sim$ 4.3 hr, while for the off-band images it was 1 hr and 1.4 hr, for the M87 SUB1 and M87 SUB2 fields, respectively. Deep V-band images are needed for the colour selection of the PN candidates (see Sect. 2.3).

Our strategy for data acquisition was set up to achieve the best image quality. Narrow-band and broad-band images were taken close to each other during the observing nights to secure similar conditions in terms of scattered light and atmospheric seeing, while calibration images, such as dark sky[1], were taken in between the science images to have a similar S/N and image quality.

The nights were photometric with an overall seeing on the images less than $1''$. Airmasses were 1.01 and 1.06 for the reference M87 SUB1 [OIII] and V-band exposures, and 1.13 and 1.03

---

[1] Dark sky is an image of an empty field (off target) on the sky

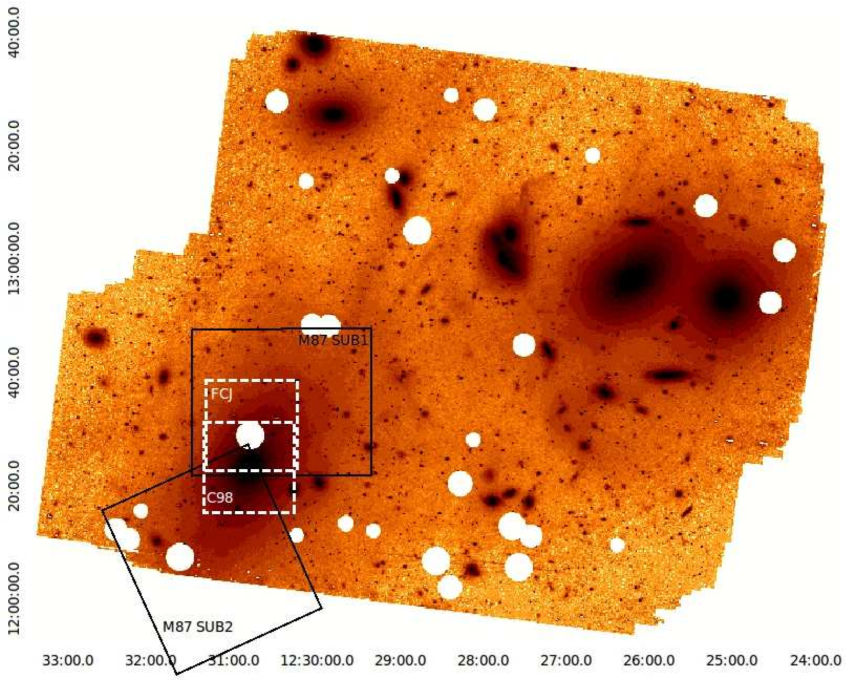

Figure 2.1: The core of the Virgo cluster (Mihos et al. 2005) with the positions of the fields studied in this work (black rectangles) and in previous surveys by Ciardullo et al. (1998) and Feldmeier et al. (2003) (dotted white squares). The region is dominated by the halos of 3 bright galaxies, M84, M86 and M87, with M87 covered by the Suprime-Cam fields. North is up, East is to the left.

for the reference M87 SUB2 [OIII] and V-band exposures[2]. We did not perform any measurements for the extinction coefficients. We adopted the mean value of X=0.12 mag/airmass, as listed for the [OIII] and V filters at the Mauna Kea summit web site[3], and in agreement with Buton et al. (2013).

The on-band filter bandpass was designed such that its central wavelength coincides with the redshifted $\lambda$5007 Å emission at the Virgo cluster. The Johnson V-band filter can be used as the off-band filter despite the fact that it contains the [OIII] line in its large bandpass ($\sim$ 1000 Å). The depth of the Suprime-Cam survey was chosen to detect all PNs brighter than $m^{*}$+2.5, where $m^{*}$ is the [OIII]5007 Å apparent magnitude of the bright cutoff of the PNLF for a distance modulus 30.8. Table 2.1 gives a summary of the field positions, filter characteristics and exposure times for the on-band and off-band exposures for the analysed area around M87.

---

[2] The reference [OIII] and V-band exposures are the one used as reference images for the final image combination.

[3] (http://www.jach.hawaii.edu/UKIRT/astronomy/exts.html)

Table 2.1: Summary of the field positions, filter characteristics, exposure times, and seeing for the narrow-band (on-band) and broadband (off-band) images.

| | | | [OIII] Filter | | | | V-band Filter | | | |
|---|---|---|---|---|---|---|---|---|---|---|
| Field | $\alpha$(J2000) | $\delta$(J2000) | $\lambda_c$ | FWHM | Exposure | S$_{FWHM}$ | $\lambda_c$ | FWHM | Exposure | S$_{FWHM}$ |
| | (hh mm ss) | ($^o$ ′ ″) | (Å ) | (Å ) | (s) | (″) | ( Å ) | (Å ) | (s) | (″) |
| M87 SUB1 | 12 30 25.230 | +12 35 03.85 | 5029 | 74 | 11 ×1200 | 0.96 | 5500 | 956 | 13×360 | 1.00 |
| M87 SUB2 | 12 31 15.581 | +12 07 22.33 | 5029 | 74 | 10 ×1200 | 0.98 | 5500 | 956 | 14 ×360 | 0.8 |

### 2.2.2 Data Reduction, Astrometry and Flux Calibration

The removal of instrumental signature, geometric distortion correction, background (sky plus galaxy) subtraction, a first astrometric solution and the final image combination were done using standard data reduction packages developed for Suprime-Cam data (sdfred software v2.0, from http://www.naoj.org/Observing/Instruments/SCam/sdfred). Cosmic rays identification and rejection were carried out with L.A.Cosmic (Laplacian Cosmic Ray Identification) algorithm (van Dokkum 2001). Because of the spectroscopic follow-up our aim was to derive accurate positions of the PN candidates. To do this we improved the astrometry of the images to get a relative positional accuracy with less than 0″.3 in the residuals. The astrometric solution was computed using image astrometry tasks in the IRAF[4] package **imcoords**, performing a geometrical transformation by 2nd order polynomial fitting. All images analysed in this paper are on the astrometric reference frame of the 2MASS catalogue[5].

We flux calibrated the broad-band and narrow-band frames to the AB system by observing standard stars through the same filters used for the survey. We used spectrophotometric standard star Hilt600 and Landolt stars for the [OIII]-band and V-band flux calibrations respectively, giving zero points for the [OIII] and V-band frames equal to $Z_{[\mathrm{OIII}]} = 24.29 \pm 0.04$ and $Z_{[\mathrm{V}]} = 27.40 \pm 0.17$, normalised to a 1 second exposure[6].

However, the integrated flux from the [OIII] line of a PN is usually expressed by the magnitude $m_{5007}$ using the relation introduced by Jacoby (1989):

$$m_{5007} = -2.5 \log_{10} F_{5007} - 13.74, \tag{2.1}$$

where $F_{5007}$ is in units of ergs cm$^{-2}$ s$^{-1}$. From this we determined the absolute flux calibration for the nebular flux in the [OIII] emission line, following Jacoby et al. (1987). This flux calibration takes the filter transmission efficiency at the wavelength of the emission line into account, due to the fact that the fast optics of wide-field instruments, such as the Suprime-Cam at the Subaru telescope can affect the transmission properties of the interference filter, especially for narrow-band imaging. This effect was quantified making use of the filter transmission curve described in Arnaboldi et al. (2003), representing the expected transmission of the [OIII] interference filter in the f/1.86 beam of the Suprime-Cam at the Subaru telescope.

---

[4] IRAF is distributed by the National Optical Astronomy Observatory, which is operated by the Association of Universities for Research in Astronomy (AURA) under cooperative agreement with the National Science Foundation.

[5] The astrometry accuracy of the [OIII] frames was improved by using the corresponding V-band image plate solution after being registered to the V-band image coordinate system. On/off images need to be registered on the same system due to the selection of PNs via colour excess (see Sect.2.3.1).

[6] These values of $Z_{[\mathrm{OIII}]}$ and $Z_{[\mathrm{V}]}$ are consistent with those obtained by Castro-Rodríguez et al. (2009) where they analyze data collected with the Suprime-Cam at the Subaru telescope through the same filters: [OIII] narrow-band filter ($\lambda_c$=5029 Å $\Delta\lambda$=74 Å), and broad-band V-filter ($\lambda_c$=5500 Å $\Delta\lambda$=956 Å).

The relation between the $m_{5007}$ and $m_{\rm AB}$ magnitudes for the narrow-band filter is given by:

$$m_{5007} = m_{\rm AB} + 2.49. \qquad (2.2)$$

A detailed description of the relation between AB and $m_{5007}$[OIII] magnitudes is given in Arnaboldi et al. (2002).

In this paper we will use the notation of $m_n$ and $m_b$ to refer to the narrow-band and broad band magnitudes of the objects in the AB system. We will use $m_{5007}$ to refer to the [OIII] magnitudes introduced by Jacoby (1989).

Table 2.2 gives the constant value for AB-to-$m_{5007}$ magnitude conversion, and limiting magnitudes in the on-band and off-band frames analysed in this paper.

Table 2.2: On-band and off-band limiting magnitudes.

| Field | $m_{lim,5007}$ | $m_{lim,b}$ | C |
|---|---|---|---|
| M87 SUB1 | 28.39 | 26.4 | 2.49 |
| M87 SUB2 | 28.39 | 26.6 | 2.49 |

**Notes**. C is the transformation constant between AB and 5007 magnitudes for the narrow-band [OIII] filter: $m_{5007} = m_{\rm AB}$+C

The final products for the M87 SUB1 and M87 SUB2 pointings consist of the stacked images in the [OIII] and V band, astrometrically and photometrically calibrated. As consequence of the observing strategy the seeing measured as the average FWHM of stellar sources is similar in both pairs of images, and less than $\mathrm{FWHM_{seeing}} < 1''$ (see Table2.1). A fit of the PSF with the IRAF task **psf** (in the digiphot/daophot package) shows that a Moffat analytical function with a $\beta$ parameter $\beta = 2.5$ (see IRAF/digiphot manual for more details) is the best profile to model the stellar light distribution of point sources in our images. Moreover, the PSF fit was computed in three different regions of the on-band and off-band images for both the M87 SUB1 and M87 SUB2 fields, covering the images from the centre to the edges: for all regions examined, the PSF fit gave the same best fit solution, showing that the PSF does not vary across the images.

## 2.3 Selection of PN Candidates and Catalogue Extraction

As a result of their bright [OIII] ($\lambda$5007) and faint continuum emission, extragalactic PNs can be identified as objects detected in images taken through the on-band [OIII] filter, but not detected in images taken through the off-band continuum filter. In our work, all PN candidates are extracted through the on-off band technique (Jacoby et al. 1990) using selection criteria based on the distribution of the detected sources in colour magnitude diagrams (Theuns & Warren 1997b). We used an automatic extraction procedure developed and validated in Arnaboldi et al. (2002, 2003) for the identification of emission line objects in our images. We give a brief summary of the selection procedure in the next section.

### 2.3.1 Extraction of Point-Like Emission-Line Objects

We employed the object detection algorithm SExtractor (Bertin & Arnouts 1996), that detects and measures flux from point-like and extended objects. Sources were detected in the on-band image requiring that 20 adjacent pixels or more have flux values $1 \times \sigma$ RMS above the background. Magnitudes were then measured in a fixed aperture of radius $R = 6$ pixels ($1.2''$, $\sim 3$ times the seeing radius) for sources in the on-band image, and then through the aperture photometry in the V-band image at the (x,y) positions of the detected [OIII] sources with SExtractor in dual-image mode. Candidates for which SExtractor could not detect a $m_b$ magnitude at the position of the [OIII] emitter were assigned a $m_b = 28.7$, i.e. the flux from an [OIII] emission of $m_n = m_{lim,n}$ seen through a V-band filter (Theuns & Warren 1997b). All objects were plotted in a colour magnitude diagram (CMD), $m_n$-$m_b$ vs. $m_n$, and classified according to their positions in this diagram. Based on their strong [OIII] line emission, the most likely PN candidates are point-like objects with colour excess corresponding to an observed EW greater than 110 Å, after convolution with photometric errors as function of the magnitude. The limit of completeness is defined as the magnitude at which the recovery fraction of an input simulated point-like population with a given luminosity function[7], drops below a threshold set to 50%. We find $m_{lim,5007}$=28.39; this is the limiting magnitude of our sample.

The colour selection of PN candidates requires off-band images deep enough so that the colour can be measured reliably at fainter magnitudes. As for the [OIII] images, we define the V-band limiting magnitude as the faintest magnitude at which half of the input simulated sample is retrieved from the image; we then derive $m_{lim,b} = 26.4$ and $m_{lim,b} = 26.6$ for the M87 SUB1 and M87 SUB2 fields respectively.

#### Colour selection

PN candidates are defined as objects with [OIII] magnitudes brighter than the [OIII] limiting magnitude and with a colour excess, $m_n \leq m_{lim,n}$ and $m_n - m_b < -0.99$, the latter representing the colour excess corresponding to $\mathrm{EW_{obs}} = 110$ Å. The relation between the observed EW and the colour in magnitudes is given by Teplitz et al. (2000): $\mathrm{EW_{obs}} \simeq \Delta\lambda_{\mathrm{nb}}(10^{0.4\Delta m} - 1)$, where $\Delta\lambda_{\mathrm{nb}}$ is the width of the narrow band filter and $\Delta m = m_b - m_n$ is the colour. A value of $\mathrm{EW_{obs}} = 110$ Å limits contamination from [OII]$\lambda$3726.9 emitters at redshift $z \sim 0.34$ (see Sect. 2.3.2).

Photometric errors may be responsible for continuum emission sources falling below the adopted colour excess, hence contaminating the emission object distribution. This effect is limited by defining regions in which 99% and 99.9% of a simulated continuum population would fall in this CMD. Below the 99.9% line, the probability to detect stars is reduced to the 0.1% level.

---

[7] In these simulations we adopted a Moffat $\beta = 2.5$ profile to define the PSF of unresolved sources (see Sect.3.2.2 for details) and an exponential LF similar to the one describing the PNLF in Ciardullo et al. (1998).

Theoretically a PN is a point-like source with no detected continuum, i.e. with no broad-band magnitude measured by Sextractor. Nevertheless we expect a continuum contribution in an aperture at the position of a [OIII] source in the halo of M87 because of crowding effects or residuals from the subtraction of the continuum light from the M87 halo. This is confirmed by the distribution of colours measured for a simulated PN population in the outer regions of M87, which we discuss in Sect.2.3.1.

### Point-like versus extended sources

At a distance of $\sim$ 15 Mpc, PNs are unresolved points of green light. We need to distinguish them from spatially extended background galaxies and, possibily, HII regions. Point-like objects in our catalogue are candidates that satisfy the following criteria:

1. we compare the SExtractor $m_n$ and $m_{core}$ magnitudes, where $m_{core}$ represents the measured magnitude in a fixed aperture of radius $R = 2$ pixels (0.4″). For point-like objects $m_n - m_{core}$ has a constant value as function of magnitude, while it varies for extended sources. We analyzed this difference for simulated point-like objects and determined the range of $m_n - m_{core}$ as function of $m_n$ where 96% of the simulated population fall. This range is narrow for bright magnitudes but it becomes wider towards fainter magnitudes due to the photometric errors.

2. we derive the distribution for the SExtractor half-light radius $R_h$, i.e. the radius within which half of the object's total flux is contained. For point-like objects this value should be constant but due to photometric errors it is confined to a range $1 \leq R_h \leq 4$ pixels that we determine as the range in which 95% of the simulated population lies.

These criteria for the selection of point-like sources are shown in Fig. 2.2. For the simulated population, 91% of the input sources are recovered as point-like objects. Therefore, applying these criteria to the observed objects excludes 9% of the PNs from the sample along with the extended objects.

### Masking of bad/noisy regions

The last step of our automatic selection is the masking of the areas where the detection and photometric measurements of sources are dominated by non-Poisson noise. These areas include diffraction and bleed spikes from the brightest stars, bad pixel regions and higher background noise regions, the latter mostly at the edges of the images because the dithering strategies lead to different exposure depth near the edges (we will discuss this further in Section 2.3.1). After these regions are excluded, the total effective area of our survey is $\sim 0.43$ deg$^2$.

The selection described above leads to a catalogue, hereafter called automatic sample, containing 792 objects classified as PN candidates. These sources are point-like objects with colour

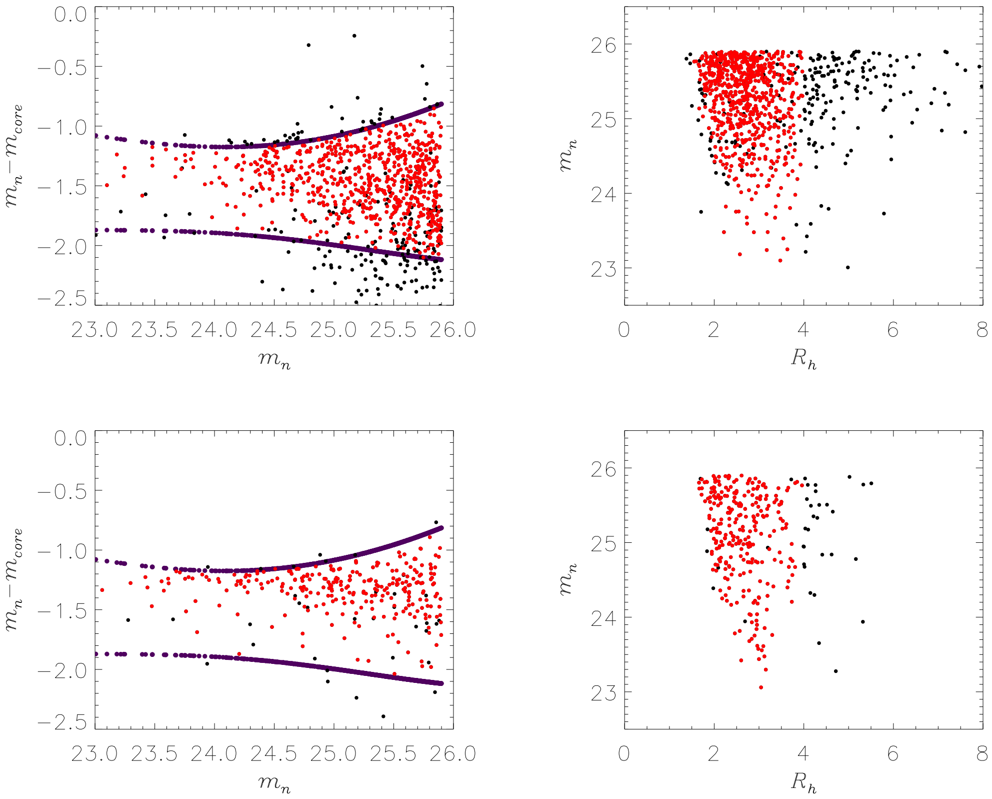

Figure 2.2: Point-source test, showing $m_n - m_{core}$ vs. $m_n$ (left) and $m_n$ vs. $R_h$ (right) for observed sources satisfying our colour restrictions in the M87 SUB1 field (top) and for modeled point-like emission objects (bottom). The dark lines in the left panels delimit the region within which 96% of the modeled point-like emission objects fall. Observed sources in the top panels are considered as point-like objects if they lie in this region and have a half light radius in the range $1 \leq R_h \leq 4$ pixels. This range of $R_h$ was chosen such that 95% of the modeled population was included. Red dots represent objects that satisfy both criteria and are thus selected as point-like objects. These criteria are also applied to sources in M87 SUB2 field.

excess, corresponding to an observed equivalent width $\mathrm{EW_{obs}} > 110$ Å and are located in regions of the colour-magnitude diagram where the contamination by foreground stars is below 0.1%.

Fig. 2.3 shows the colour selection for the M87 SUB1 and M87 SUB2 fields, with the PN candidates represented by asterisks.

#### Missing PNs in the photometric sample

The selection procedure based on flux thresholds is sensitive to photometric errors. At fainter magnitudes, PN candidates with intrinsic $\mathrm{EW_{obs}} > 110$ Å, or $m_n \leq m_{lim,n}$, can have smaller measured $\mathrm{EW_{obs}}$, or fainter $m_n$, because of photometric errors and are, therefore, excluded from our selection. We quantified this effect by simulating an [OIII] emission line population, with an exponential LF in the magnitude range $23 \leq m \leq 27.5$, randomly distributed on the on-band scientific image. No continuum emission was assigned to the objects. We then carried out the photometry as for the real sources: their CMD is shown in Fig. 2.4. We see that many simulated PNs have a measured continuum magnitude due to crowding effects or residuals from the galaxy background. This CMD shows also that for simulated sources brighter than the limiting magnitude, the percentage of PNs that we would miss due to photometric errors is 28.3% and 29.8% in the M87 SUB1 and M87 SUB2 fields respectively. This implies that our automatic procedure, within the magnitude range $23 \leq m_n \leq m_{lim,n}$, recovers 0.71 of the total sample.

#### Catalogue validation: visual inspection and joint candidates in both fields

Finally, the photometric catalogue obtained from the automatic selection described in the previous Sections was visually inspected, in particular for regions near bright stars or with a higher noise level. This visual inspection lead to a catalogue of 688 candidates, the removed spurious detections being ~11% of the automatic extracted sources.

In the final catalogue 18 candidates appear in both fields and their magnitudes are measured independently in the two pointings. Differences between the independent measurements are consistent with the errors.

### 2.3.2 Possible sources of contaminants in the PN sample

Following Aguerri et al. (2005), we examined the main contaminants and estimate their contributions to the final catalogue.

*Contamination by faint continuum objects*– At $m_{lim,n}$, the faint continuum objects can mimic an [OIII] emission line population, because they are scattered into the region where PN candidates are selected. We constrained this contribution by computing the 99.9% lines for the distribution of continuum objects. From the total number of the observed foreground stars, we determine the number of objects (0.1%) that would be scattered in the region of colour selected PNs. The resulting contribution from faint stars equals 9% and 11% of the total extracted sample for the M87 SUB1 and M87 SUB2 fields, respectively.

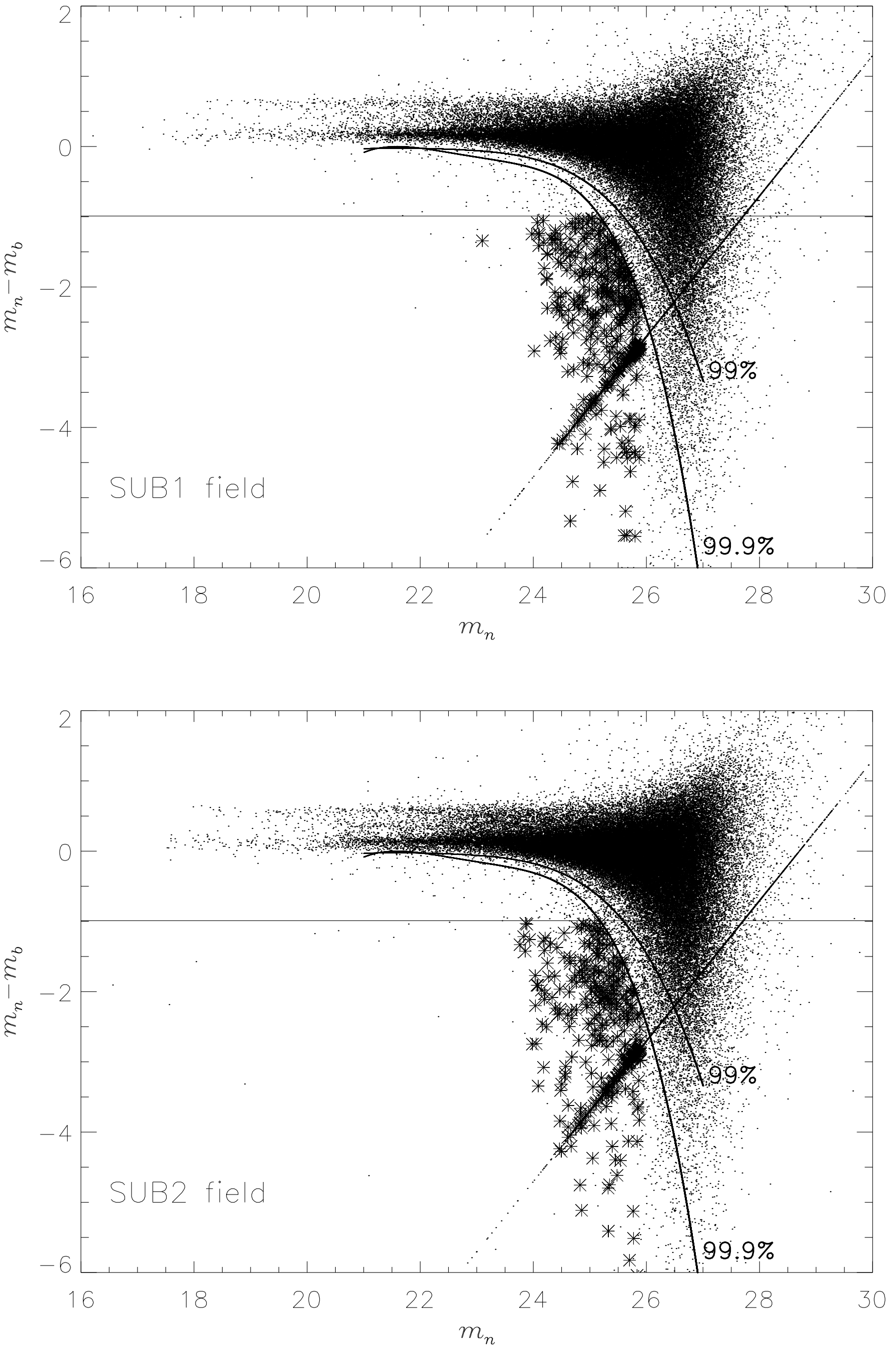

Figure 2.3: CMD for all sources in the M87 SUB1 (top panel) and M87 SUB2 (bottom panel) fields. The horizontal lines indicate the colour excess of emission line objects with an $EW_{obs}$ = 110Å. The curved lines delimit the regions above which 99% and 99.9% of the simulated continuum objects fall in this diagram, given the photometric errors. The set of points on the inclined line represents those objects with no broadband magnitude measured by SExtractor (see Sect. 2.3.1 for more details). Asterisks represent objects classified as PNs according to the selection criteria discussed in Sect. 2.3.1.

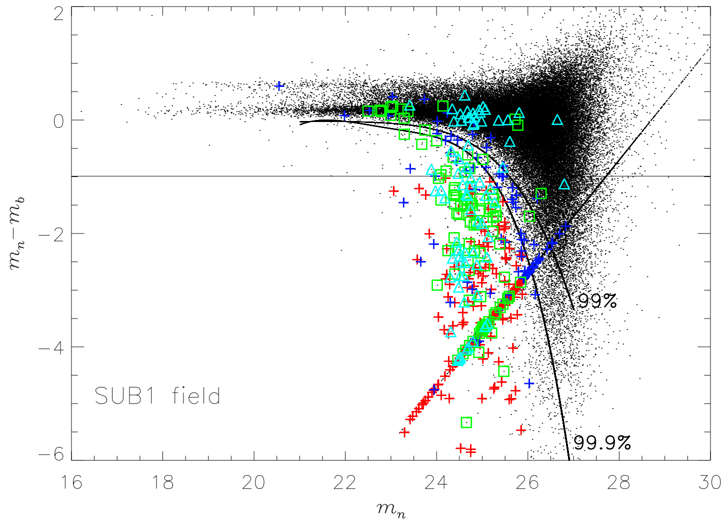

Figure 2.4: CMD for a simulated PN population in the M87 SUB1 field with intrinsic magnitudes $23 \leq m_n \leq m_{lim,n}$ (crosses). Because of photometric errors, our selection criteria would exclude 28.3% of the input sample (blue crosses). The remaining 71.7% would be selected as PNs (red crosses). Dots surrounded by green squares and cyan triangles are emission objects in common between our sample and the PN samples selected by Ciardullo et al. (1998) and Feldmeier et al. (2003), respectively. Solid lines as in Fig. 2.3.

*Contamination by background galaxies: Lyman $\alpha$ galaxies and [OII] emitters* – The strong [OIII] $\lambda$5007 PN emission with no associated detected continuum allows us to identify PNs as objects with negative colour (Theuns & Warren 1997b). This colour selection will also identify Ly$\alpha$ galaxies at redshift $z \sim 3.1$ as well as [OII] $\lambda$3727.26 emitters at redshift $z \sim 0.34$, whose emission lines fall within the bandpass of our narrow band filter.

The contamination by Ly$\alpha$ is quantified by using the number density of $z = 3.1$ Ly$\alpha$ galaxies from Gronwall et al. (2007) where their limiting magnitude of $m_{lim,n(G07)}(5007)=28.31$ for statistical completeness makes their survey as deep as ours. We consider their Ly$\alpha$ LF given by a Schechter function of the form:

$$\phi(L)d(L/L^*) \propto (L/L^*)^{\alpha} e^{-L/L^*} d(L/L^*), \tag{2.3}$$

with their best-fit values of $\log_{10} L^* = 42.66$ erg s$^{-1}$ and $\alpha = -1.36$, corrected for the effects of photometric errors and their filter's non-square transmission curve. At redshift $z = 3.1$, the surveyed area of 0.43 deg$^2$, observed through the Suprime-Cam narrow-band filter, samples $\sim 3.1\ 10^5$ Mpc$^3$ (Hogg 1999). However, as pointed out by Gronwall et al. (2007), when working with narrow band data taken through a nonsquare filter bandpass, the effective survey volume is ∼ 25% smaller than that inferred from the interference filter's FWHM. We thus compute the number of expected Ly$\alpha$ emitters by using a survey volume of $\sim 2.3\ 10^5$ Mpc$^3$. The Ly$\alpha$ population at $z \sim 3.1$ shows clustering over a correlation length of $r_0 = 3.6$ Mpc (Gawiser et al. 2007), corresponding to an angular size in the Virgo cluster of $r'_0 \sim 7.9'$. Hence we need to allow for the large-scale cosmic variance in the average Ly$\alpha$ density, which in our case is $\sim$ 20% (Somerville et al. 2004; Gawiser et al. 2007). From our effective sampled volume, we predict, then, that the number of expected Ly$\alpha$ contaminants is 25% ± 5% of our total catalogue.

The contribution from [OII] emitters is considerably reduced by selecting candidates with observed equivalent width, $\mathrm{EW_{obs}} > 110$ Å, corresponding to a colour threshold $m_n - m_b < -0.99$ (Teplitz et al. 2000). This is because no [OII] emitters with $\mathrm{EW_{obs}} > 95$ Å have been found (Colless et al. 1990; Hammer et al. 1997; Hogg et al. 1998). Note that in the Gronwall et al. (2007) sample of Ly$\alpha$ galaxies at $z = 3.1$, the fraction of [OII] contaminants is considered to be negligible because of their EW selection ($\Delta m_{(G07)} \sim -1$). This means that if there is a fraction of [OII] emitters with $EW_{\mathrm{obs}} > 110$ Å in our sample, then their contribution is accounted for by using the Ly$\alpha$ LF from Gronwall et al. (2007).

### 2.3.3 Comparison with previous PN samples in M87

Our survey area overlaps with those studied by Jacoby et al. (1990), Ciardullo et al. (1998, hereafter C98) and Feldmeier et al. (2003, hereafter F03); the locations of the C98 and F03 fields are over-plotted on Fig. 2.1.

We have a limited number of objects in common between Jacoby et al. (1990) and our catalogue ($\sim$ 14% of their catalogue), because of the high residual background in our images from the bright central regions of M87. These fractions are larger for the C98 and F03 catalogues, and we discuss them in turn.

C98 carried out an [OIII] $\lambda$5007 survey for PNs, covering a $16' \times 16'$ field around M87. They identified 329 PNs in the M87 halo, 187 of these in a statistically complete sample down to $m_{5007} = 27.15$. Of the 329 sources selected by C98, 201 fall within our surveyed area[8]. Of these sources, 91% are matched with [OIII] detected objects in our survey, but only $\sim$ 60% satisfy our selection criteria for PN candidates, see the CMD for the C98 candidates (green squares) in Fig. 2.4.

F03 carried out a survey of intracluster PNs (ICPNs) over several fields in the Virgo cluster region; the one overlapping with the current Subaru survey is a $16' \times 16'$ area north of M87, labeled "FCJ" field in F03 and Aguerri et al. (2005). 100% of the candidates in this field match with [OIII] sources in the M87 SUB1 field, but only 42% satisfy the selection criteria for PN candidates in our survey, see the CMD for the F03 candidates (cyan triangles) in Fig. 2.4.

On the basis of the common PN candidates with the largest S/N ratios, we can compare the photometric calibration for the $m_{5007}$ magnitudes and any variations with magnitude in the different samples. We find a constant offset that does not vary with magnitude between the C98, F03 samples and our survey, with our $m_{5007}$ system being $\sim$ 0.3 magnitudes fainter. In Fig.2.5 the F03 mags (corrected for $\sim$ 0.3 mag shift) are compared with ours.

In Section 2.5 we will compare the empirical PNLF for our PN sample with those for the C98 and F03 data, and based on this comparison will argue that there is a systematic effect in the C98 and F03 photometry, causing brighter $\mathrm{m}_{5007}$. In what follows, the calibration offset is therefore applied to the previously published data whenever we compare them with our PN magnitudes.

---

[8] This area does not include the regions affected by high background noise and bad pixels (see Sect. 2.3.1)

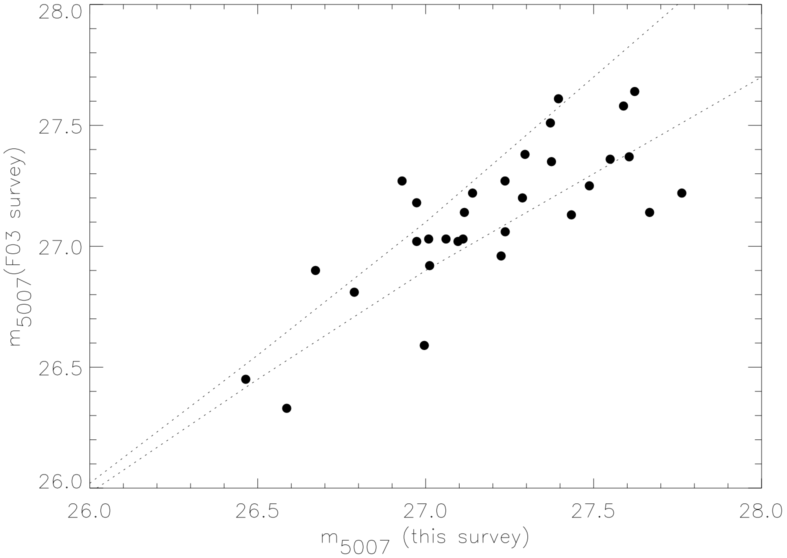

Figure 2.5: $m_{5007}$ for the F03 PN candidates (corrected for $\sim$ 0.3 mag offset) plotted against the $m_{5007}$ magnitudes measured in our survey. The dotted lines represent the $1\sigma$ uncertainty from the photometric errors of our survey. The two magnitude systems are consistent within the photometric errors with an offset that is constant with magnitude.

## 2.4 The radial profile of the PN population and comparison with the M87 surface brightness

In what follows we present the number density distribution from our PN sample, one of the largest both in number of tracers and in radial extent. Plotted in Fig. 3.8 is the position of our PN candidates together with the outline of our survey region.

### 2.4.1 The PN radial density profile

We now investigate whether the PN number density profile follows the surface brightness profile of the galaxy light. On the basis of the simple stellar population theory, the luminosity-specific stellar death rate is insensitive to the population's age, initial mass function, and metallicity (Renzini & Buzzoni 1986). Thus the probability of finding a PN at any location in a galaxy should be proportional to the surface brightness of the galaxy at that location.

In order to compare the surface brightness and PN number density profiles, we bin our PN sample in elliptical annuli, whose major axes are aligned with M87's photometric major axis and with ellipticities measured from the isophotes (see Fig. 3.8). We compute PN number densities as ratios between the number of PNs in each annulus and the area of the intersection of the annulus with our field of view. These areas, $A(R)$, are estimated using a Monte Carlo integration technique.

The PN number density profile must be corrected for spatial incompleteness because the

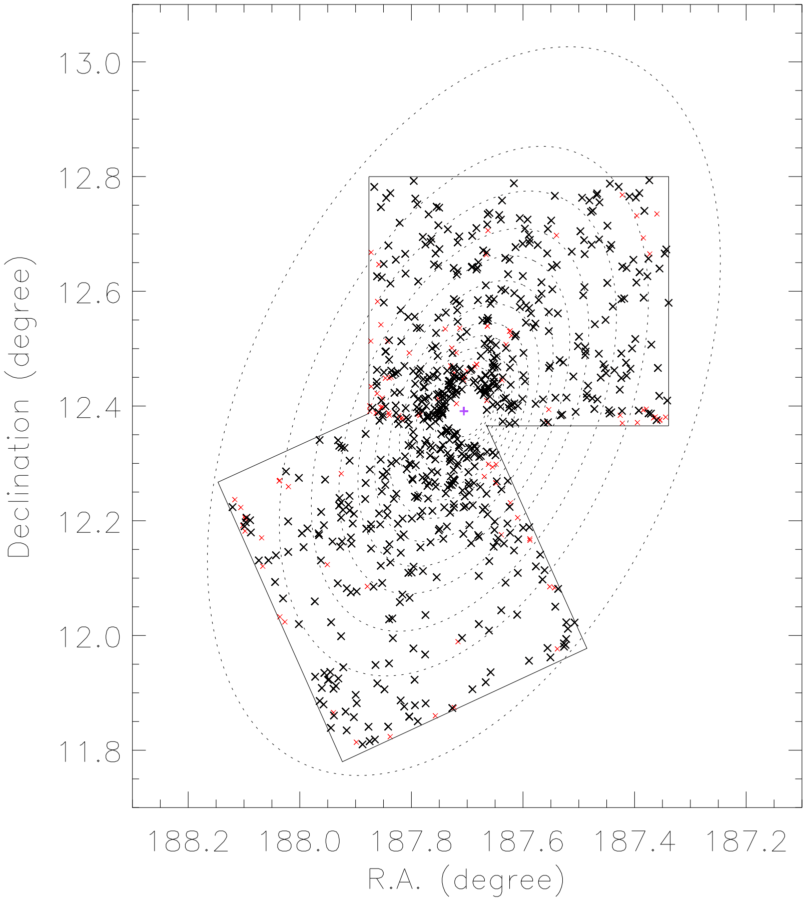

Figure 2.6: Spatial distribution of PN candidates (black crosses). Red crosses represent objects classified as spurious after visual inspection. The magenta cross indicates the centre of M87. Dotted ellipses trace the M87 isophotes from $R$ = 2.8 to $R$ = 40.7′ along the photometric major axis, at a position angle P.A.=-25.6° (Kormendy et al. 2009). The solid squares depict our survey area. North is up, East to the left.

bright galaxy background and bright foreground stars may affect the detection of PNs. We compute this completeness function, C($R$), by adding a PN sample modelled according to a Ciardullo et al. (1989) PNLF on the scientific image. C($R$) is then the fraction of simulated objects recovered by Sextractor in the different elliptical annuli vs the input modelled population, for PNs brighter than $m_{5007} = 28.3$ (values are given in Tab.2.4). The expected PN total number is then:

$$\mathrm{N_c}(R) = \frac{\mathrm{N_{obs}}(R)}{\mathrm{C}(R)0.71}, \tag{2.4}$$

where the value 0.71 accounts for the average colour incompleteness (see Sect. 2.3.1). In Fig. 3.9 we show the comparison between the major axis stellar surface brightness profile in the V band, $\mu_{\mathrm{K09}}$ (Kormendy et al. 2009), and the PN logarithmic number density profile, defined as:

$$\mu_{\mathrm{PN}}(R) = -2.5\log_{10}(\Sigma_{\mathrm{PN}}(R)) + \mu_0, \tag{2.5}$$

where

$$\Sigma_{\mathrm{PN}}(R) = \frac{\mathrm{N_c}(R)}{A(R)} \tag{2.6}$$

is the PN number density corrected for spatial and colour incompleteness, and $\mu_0$ is a constant value added to match the PN number density profile to the $\mu_{\mathrm{K09}}$ surface brightness profile. In the same plot, we also indicate radii that select three different regions in the halo of M87; these regions are for $R < \bar{R}/2$, $\bar{R}/2 \le R < \bar{R}$ and $R \ge \bar{R}$, where $\bar{R} = 13.5'$ represents the mean distance of the PN sample from the centre of M87. The innermost and the outermost number density points are at radii $R = 2.8'$ and $R = 27.6'$ respectively, and in Fig. 3.9 they are indicated with dotted red lines. The surface brightness and the logarithmic PN number density profile agree well in the innermost region, they slightly deviate in the intermediate region while in the outermost region the logarithmic PN number density profile flattens. The difference between the two profiles amounts to 1.2 mag at the outermost radii. This discrepancy would still be observed if we had used instead the candidates from the automatic selection procedure without any final inspection: the difference between the two number densities is too small to affect the slope at large radii (see Fig. 3.9, bottom panel). We also note that the flattening of the logarithmic number density profile is seen in both Suprime-Cam fields independently.

Empirically, the logarithmic PN number density profile follows light in elliptical (Coccato et al. 2009) and S0 (Cortesi et al. 2013) galaxies. However, these studies cover the halos out to typically only 20 kpc. The presence of Ly$\alpha$ background galaxies at $z \sim 3.1$ could also contribute to the flatter slope of the logarithmic PN number density profile, and so we need to evaluate their contribution to the number density at large radii. In Fig. 3.9 we show the contribution from Ly$\alpha$ contaminants (black dotted line) to the logarithmic number density (25% ± 5% of the total sample), assuming a homogeneous distribution in the surveyed area. We can make this assumption because the survey area 0.43 deg$^2$ extends over many correlation lengths of the Ly$\alpha$ population at $z = 3.14$ (see Sect. 2.3.2).

Hence we can statistically subtract the contribution of the Ly$\alpha$ backgrounds objects from the number of PN candidates in each annulus and obtain the corrected number density profile (filled circles in Fig. 3.9). Now the error bars also account for the expected fluctuation of Ly$\alpha$ density

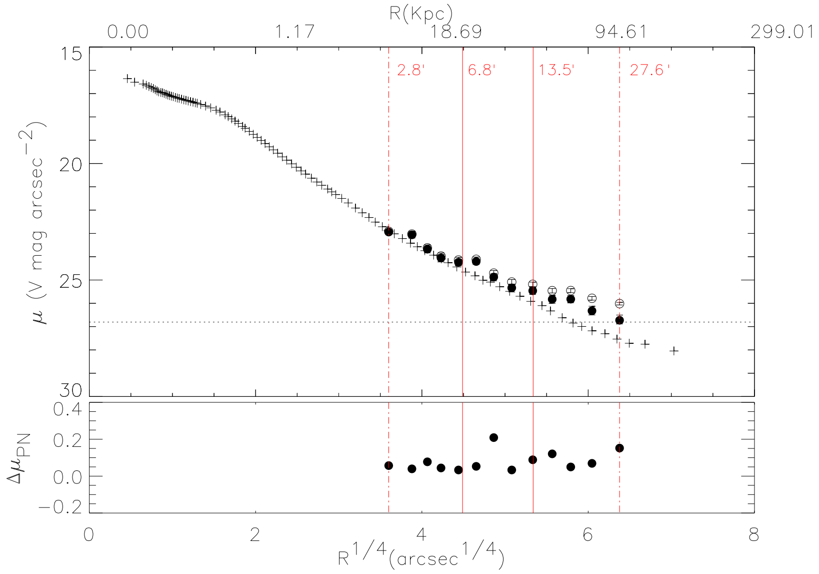

Figure 2.7: Top panel: comparison between surface brightness profile from Kormendy et al. (2009) (crosses) and logarithmic PN number density profile of the emission line candidates, brighter than $m_{5007}$ = 28.3, and corrected for spatial and colour incompleteness (open circles with error bars, see Table 2.4 for data), as function of the distance from the M87 centre. The black dotted line represents the contribution of Ly$\alpha$ emission objects to the logarithmic PN number density profile, assuming a homogeneous distribution over the surveyed area. Under the same hypothesis, filled circles show the logarithmic PN number density profile when the Ly$\alpha$ contribution is statistically subtracted. Red lines mark the inner, intermediate and outermost regions of the M87 halo (see text). Bottom panel: difference between the logarithmic PN number density profiles if we had used the automatically extracted sources without the final inspection: a value of zero would mean that no variation in the number of sources is implied in the annulus at a given radius.

(see Sect. 2.3.2 for details) and the flattening of the logarithmic PN number density profile is still observed. Using the derived $\alpha_{2.1}$ value for the halo from Sect. 2.4.4, the surface brightness profile translates to ~ 295 PNs down to $m_{5007}$ = 28.3. Down to this magnitude our catalogue contains ~420 estimated PNs. The excess, then, is ~ $3.6 \times \sigma_{\mathrm{Ly}\alpha}$, where $\sigma_{\mathrm{Ly}\alpha}$ is the standard deviation in the expected number of Ly$\alpha$ emitters from cosmic variance and Poisson statistics. Hence, the flattening can not be explained by fluctuations in the Ly$\alpha$ fraction. In what follows we investigate the physical origin of the flatter logarithmic PN number density profile.

### 2.4.2 The $\alpha$ parameter

The total number of PNs, $\mathrm{N_{PN}}$, is correlated with the total bolometric luminosity of the parent stellar population, $L_{\mathrm{bol}}$, through the so-called $\alpha$-parameter, that defines the luminosity-specific PN density: $\mathrm{N_{PN}} = \alpha L_{\mathrm{bol}}$.

From stellar evolution theory it is found that the luminosity-specific stellar death rate is insensitive to a stellar population's age, initial mass function, and metallicity (Renzini & Buzzoni

1986). Therefore, the total number of PNs associated with a parent stellar population can be computed from the bolometric luminosity using the formula:

$$\mathrm{N}_{\mathrm{PN}} = BL_{\mathrm{TOT}}\tau_{\mathrm{PN}}, \tag{2.7}$$

where $B$ is the specific evolutionary flux (stars yrs$^{-1}$ $\mathrm{L}_{\odot}^{-1}$), $L_{\mathrm{TOT}}$ is the total bolometric luminosity of the parent stellar population, and $\tau_{\mathrm{PN}}$ is the PN visibility lifetime. From Eq. 2.7, the luminosity-specific PN number, $\alpha$, is

$$\alpha = \frac{\mathrm{N}_{\mathrm{PN}}}{L_{\mathrm{TOT}}} = B\tau_{\mathrm{PN}}. \tag{2.8}$$

Observed values of the $\alpha$ parameter can then be interpreted as different values of $\tau_{\mathrm{PN}}$ for the PNs associated with different stellar populations, because variations of $B$ with metallicity or Initial Mass Function (IMF) slope are small(Renzini & Buzzoni 1986).

For any specific observation, the actual value of $\mathrm{N}_{\mathrm{PN}}$ depends on the flux limit of the survey in which the PNs are detected. Hence, for our survey depth we are interested in estimating $\alpha_{2.1}$, the number of PNs within $\Delta m = 2.1$ magnitudes of the bright cutoff, per given amount of bolometric luminosity emitted by the stellar population of the galaxy's halo or ICL. For any $\Delta m$, $\alpha_{\Delta m}$ is defined such that

$$\mathrm{N}_{\mathrm{PN},\Delta\mathrm{m}} = \int_{M^*}^{M^*+\Delta m} \mathrm{N}(m)\,\mathrm{d}m = \alpha_{\Delta m} L_{\mathrm{bol}}. \tag{2.9}$$

where $\mathrm{N}(m)$ is the PN luminosity function and $M^*$ is the bright cutoff magnitude.

### 2.4.3 Halo and Intracluster PN Population

When studying the PN population in the outer region of M87 out to 150 kpc from the galaxy's centre, we expect contributions from the halo PNs and from ICPNs. The presence of ICL in cluster cores is a by-product of the mass assembly process of galaxy clusters (Murante et al. 2004, 2007).

The existence of intracluster PNs in Virgo has been demonstrated on the basis of extended imaging surveys in the 5007 Å [OIII] line (Feldmeier et al. 1998; Arnaboldi et al. 2002; Feldmeier et al. 2003; Aguerri et al. 2005; Castro-Rodríguez et al. 2009) and spectroscopic follow-up (Arnaboldi et al. 1996, 2003, 2004). From the spectroscopic follow-up of Arnaboldi et al. (2004) we know the M87 halo and the Virgo core ICL to coexist for distances $R > 16'$ from M87's centre (the FCJ field). In fact, the projected phase space diagram from Doherty et al. (2009) (PN line-of-sight velocity vs. radial distance from M87 centre) shows the coexistence of the halo and ICL PN population out to 150 kpc.

To estimate the ICL luminosity in our two fields, we assume a constant surface brightness $\mu_{\mathrm{V}} = 27.7$ mag arcsec$^{-2}$ (Mihos et al. 2005), and a V-band bolometric correction $\mathrm{BC_V}$=-0.85 (Buzzoni et al. 2006), which then gives a total bolometric luminosity in the ICL of $L_{\mathrm{ICL}} = 1.66 \times 10^{10} L_{\odot,\mathrm{bol}}$. This amounts to about one quoter of the bolometric luminosity of the M87 halo.

### 2.4.4 Two component photometric model for M87 halo and ICL, and determination of their $\alpha_{2.5}$ parameters

Therefore we now investigate whether the observed discrepancy between the logarithmic PN number density profile and $\mu_{\mathrm{V}}$ surface brightness profile in Fig.3.9 may be explained by considering two PN populations associated with the M87 halo and ICL. The physical parameter that links a PN population to the luminosity of its parent stars is the luminosity-specific PN number, the $\alpha$ parameter, thus a discrepancy between $\mu_V$ and the measured logarithmic PN number density profile may come from different $\alpha$ values for the halo and ICL stellar population. This possibility is supported by Doherty et al. (2009) who measured two different values of $\alpha$ for the bound (M87 halo) and unbound (ICL) stellar component, which we are going to label $\alpha_{\mathrm{halo}}$ and $\alpha_{\mathrm{ICL}}$ in what follows. We can then define a photometric model with two components:

$$\tilde{\Sigma}(R) = [\alpha_{2.1,\mathrm{halo}} \mathrm{I}(R)_{\mathrm{halo,bol}} + \alpha_{2.1,\mathrm{ICL}} \mathrm{I}_{\mathrm{ICL,bol}}] \tag{2.10}$$

$$= \alpha_{2.1,\mathrm{halo}} \left[ \mathrm{I}(R)_{\mathrm{K09,bol}} + \left( \frac{\alpha_{2.1,\mathrm{ICL}}}{\alpha_{2.1,\mathrm{halo}}} - 1 \right) \mathrm{I}_{\mathrm{ICL,bol}} \right] \tag{2.11}$$

where $\tilde{\Sigma}$(R) represents the predicted PN surface density in units of $\mathrm{N_{PN}pc^{-2}}$, $\mathrm{I}(R)_{\mathrm{halo}}$ and $\mathrm{I_{ICL}}$ are the surface brightnesses for the halo and the ICL components, and $\mathrm{I_{K09}}$ from Kormendy et al. (2009) is the observed total surface brightness from M87 centre out to 40′, accounting for both halo and ICL components. These surface brightnesses are in units of $L_{\odot}\,\mathrm{pc^{-2}}$ and their bolometric values are computed from the measured profiles in units of mag arcsec$^{-2}$ via the formula:

$$\mathrm{I} = 10^{-0.4(\mathrm{BC_V} - \mathrm{BC_\odot})} 10^{-0.4(\mu - \mathrm{K})},$$

where $\mathrm{BC_V}$=-0.85 and $\mathrm{BC_\odot}$=-0.07 are the V-band and the Sun bolometric corrections, and K = 26.4 mag arcsec$^{-2}$ is a conversion factor from mag arcsec$^{-2}$ to physical units $L_{\odot}\mathrm{pc^{-2}}$ in the V-band. Assuming a fixed value of $\mathrm{BC_V} = -0.85$ for every galaxy type has a 10 per cent internal accuracy, i.e. ± 0.1 mag, for a range of simple stellar population (SSP) models ranging from irregular to elliptical galaxies (Buzzoni et al. 2006).

The surface brightness profile can be expressed in terms of PN surface density $\tilde{\Sigma}(R)$:

$$\tilde{\mu}(R) = -2.5 \log_{10} \tilde{\Sigma}(R) + \mu_0, \tag{2.12}$$

where $\mu_0$ is a function of the $\alpha_{2.1,\mathrm{halo}}$ parameter:

$$\mu_0 = 2.5 \log_{10} \alpha_{2.1,\mathrm{halo}} + \mathrm{K} + (\mathrm{BC_\odot} - \mathrm{BC_V}). \tag{2.13}$$

The value of $\mu_0$ is given by the value of the constant offset used in Eq. 3.5, and it can be fixed by fitting this offset between the observed logarithmic PN surface density and the surface brightness profile, $\mu_V$, at smaller radii ($R \leq 6.8'$). From the fitted offset of $\mu_0 = 16.0 \pm 0.1$ mag arcsec$^{-2}$, we compute the value for $\alpha_{2.1,\mathrm{halo}}$ (Eq. 2.13) resulting in $\alpha_{2.1,\mathrm{halo}} = (0.63 \pm 0.08) \times 10^{-8}$ PN $\mathrm{L}^{-1}_{\odot,\mathrm{bol}}$ . The error on the determined $\alpha_{2.1,\mathrm{halo}}$ is computed from the propagation of the errors on the variables $\mu_0$ and $\mathrm{BC_V}$, the latter having a 10% accuracy.

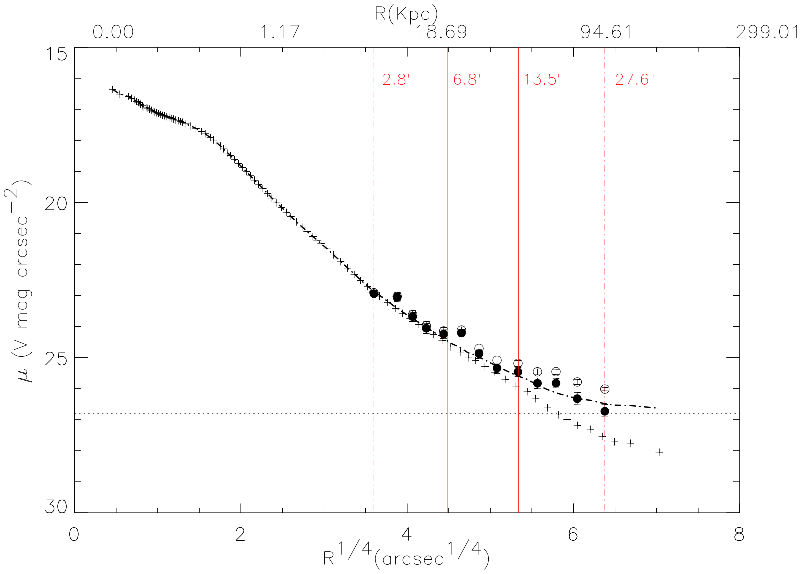

Figure 2.8: As in the top panel of Fig. 3.9 but with the modelled surface brightness profile from the two component photometric model superposed (dot-dashed black line). This modelled profile reproduces the flattening observed in the logarithmic number density well.

In Fig. 2.8 we show the fit of the two component PN model to the observed PN logarithmic number density profile for $\alpha_{2.1,\mathrm{ICL}}/\alpha_{2.1,\mathrm{halo}} = 3$ and a constant ICL surface brightness of $\mu_{\mathrm{ICL}} = 27.7$ mag arcsec$^{-2}$ (Mihos et al. 2005). The proposed model predicts a flatter slope for the PN logarithmic number density profile than the slope of the V-band surface brightness profile $\mu_{\mathrm{V}}$, as observed. The fitted value for $\alpha_{2.1,\mathrm{ICL}}$ is then $\alpha_{2.1,\mathrm{ICL}} = (1.89 \pm 0.29) \times 10^{-8}$ PN $\mathrm{L}_{\odot,\mathrm{bol}}^{-1}$.

Eq. 3.7 shows explicitly that when $\alpha_{2.1,\mathrm{halo}} = \alpha_{2.1,\mathrm{ICL}}$ then the logarithmic PN number density profile should closely follow light.

The measured values of $\alpha_{2.1,\mathrm{halo}}$ and $\alpha_{2.1,\mathrm{ICL}}$ correspond, down to the survey depth, to an estimated ∼ 390 halo PNs, and ∼ 310 ICPNs in the completeness-corrected sample, and to ∼ 230 halo PNs and ∼ 190 ICPNs in the observed sample.

To compute $\alpha_{2.5}$ for a PN sample which is not complete to $m^* + 2.5$, but only to a magnitude $m_c < m^* + 2.5$, then $\alpha_{2.5}$ is extrapolated by

$$\alpha_{2.5} = \Delta_{m_c} \times \alpha_{m_c} \tag{2.14}$$

where

$$\Delta_{m_c} = \frac{\int_{M^*}^{M^*+2.5} \mathrm{N}(m)\, \mathrm{d}m}{\int_{m^*}^{m_c} \mathrm{N}(m)\, \mathrm{d}m}, \tag{2.15}$$

If we use the derived M87 PNLF (see Sect. 2.5) to compute the cumulative number of PNs expected within 2.5 mag from the bright cut off, normalised to the cumulative number in the first 2.1 magnitudes, we obtain $\Delta_{2.1} \simeq 1.7$. As a result, the predicted values of $\alpha_{2.5}$, for the halo and ICL components are $\alpha_{2.5,\mathrm{halo}} = (1.10^{+0.17}_{-0.21}) \times 10^{-8}$ $\mathrm{N_{PN}L^{-1}_{\odot,bol}}$ and $\alpha_{2.5,\mathrm{ICL}} = (3.29^{+0.60}_{-0.72}) \times 10^{-8}$ $\mathrm{N_{PN}L^{-1}_{\odot,bol}}$ . The errors on the $\alpha_{2.5}$ values also take the uncertainty on the magnitude of the bright cutoff into account.

### 2.4.5 Comparison with previously determined $\alpha_{2.5}$ values

The $\alpha_{2.5}$ values for the M87 halo and ICL were measured in previous works by Durrell et al. (2002) and Doherty et al. (2009). There are several assumptions that are made when computing these values, hence is important to address them before the actual numbers are compared. As already pointed out in the previous section, when $\alpha_{2.5}$ is computed for a PN sample which is not complete to $m^* + 2.5$, then $\alpha_{2.5}$ is extrapolated by following Eq.2.14.

In the studies of Durrell et al. (2002) and Doherty et al. (2009), the PN samples were complete one magnitude down the bright cutoff of the PNLF. Then, $\alpha_{2.5}$ was computed using the extrapolation on the basis of the analytic formula for N($m$) by Ciardullo et al. (1989).

In Sect. 2.5 we derive the M87 PNLF in the brightest 2.5 mag range, which shows a steeper slope at $\sim 1.5$ mag below the cutoff than what is predicted by the analytical formula. If we use the observed PNLF then the cumulative number of PNs expected within 2.5 mag from the bright cut off, normalised to the cumulative number in the first magnitude, is about 2.7 times that predicted by the analytical PNLF. When comparing the actual values for the $\alpha_{2.5}$ measured by Durrell et al. (2002) and Doherty et al. (2009), they need to be rescaled by this fraction.

In the current work and in Doherty et al. (2009), $\alpha_{2.5}$ values were measured for the halo and ICL separately, using only the PNs associated with each component. In Doherty et al. (2009) the line-of-sight velocity of each PN was used to tag the PN candidate as M87 halo or ICL. In Durrell et al. (2002) this information was not available. Following Doherty et al. (2009), only 58% of the PN candidates considered by Durrell et al. (2002) are truly ICL. When this correction is applied, then the value measured by Durrell et al. (2002) for the ICPNs is $\alpha_{2.5,\mathrm{ICL}} = 1.3 \times 10^{-8}$ PN $\mathrm{L^{-1}_{\odot,bol}}$. If in addition we correct this $\alpha_{2.5}$ value for the ICL for the different shape of the PNLF, we get $\alpha_{2.5,\mathrm{ICL,DU02}} = 3.6 \times 10^{-8}$ PN $\mathrm{L^{-1}_{\odot,bol}}$. This value is $\sim 10\%$ greater than ours, but consistent within the uncertainties and the contamination from continuum sources in the F03 catalogue (see Sect.2.3.3).

When we correct the $\alpha_{2.5}$ values for halo and ICL from Doherty et al. (2009) by a factor 2.7, we obtain $\alpha_{2.5,\mathrm{halo,D09}} = 8.4{\times}10^{-9}$ PN $\mathrm{L^{-1}_{\odot,bol}}$ and $\alpha_{2.5,\mathrm{ICL,D09}} = 1.9{\times}10^{-8}$ PN $\mathrm{L^{-1}_{\odot,bol}}$. These values are smaller than ours, but consistent within the uncertainties and the colour/detection completeness corrections made here (see Sect. 2.4.1) but not in Doherty et al. (2009).

### 2.4.6 Implications of the measured $\alpha_{2.5}$ values

According to the analytical formula of Ciardullo et al. (1989) for the PNLF, $\alpha_{2.5}$ equals $\sim 1/10$ of the total luminosity-specific PN number $\alpha$ (see also Buzzoni et al. (2006)), assuming that PNs are visible down to 8 mags from the bright cutoff (Ciardullo et al. 1989). If we use this analytical function to extrapolate the total number of PNs from 2.5 to 8 magnitudes below the bright cutoff our measured values for $\alpha_{2.5}$ translate to total luminosity-specific PN numbers for the two components of $\alpha_{\rm halo} = 1.1 \times 10^{-7}$ PN $L^{-1}_{\odot,\rm bol}$ and $\alpha_{\rm ICL} = 3.3 \times 10^{-7}$ PN $L^{-1}_{\odot,\rm bol}$. We can recast these numbers in terms of the PN visibility lifetime $\tau_{PN}$ through Eq.3.5.1, assuming $B = 1.8 \times 10^{-11} L^{-1}_{\odot} yr^{-1}$ (Buzzoni et al. 2006). $\tau_{PN}$ is then $\simeq 6.1 \times 10^3$ yr and $\simeq 18.3 \times 10^3$ yr for the M87 halo and ICL PNs. Note, that these would be lower limits, because at this stage we do not know whether the extrapolation from 2.5 magnitudes below the cutoff to fainter magnitudes follows the analytical formula, or whether it is steeper.

Observationally there is some evidence that $\alpha$ is on average larger for bluer systems (Peimbert 1990; Hui et al. 1993). The measurements of the colour profile in M87 show a bluer gradient towards larger radii (Liu et al. 2005; Rudick et al. 2010): a fit of the colour profile along the major axis inside 1000″ has a slope of -0.11 in $\Delta(B-V)/\Delta \log(R)$ (Rudick et al. 2010). The observed PN logarithmic number density profile measured in this work is consistent with the empirical result of a gradient towards bluer colours at large radii. In the proposed model, the gradient is caused by the increased contribution of ICL at large radii, which is bluer than the M87 halo population.

One can ask whether the metallicity of the parent stellar population may influence the number of PNs associated with a given bolometric luminosity. We are interested in population effects in the advanced evolutionary phases of stellar evolution, as the [OIII] 5007 Å emission and its line width are weakly dependent on the chemical composition of the nebula (Dopita et al. 1992; Schönberner et al. 2010). For stellar populations with the same IMF and ages, Weiss & Ferguson (2009) computed models for the asymptotic giant branch (AGB) for stars between 1.0 and 6.0 $M_{\odot}$ with different metallicities. Their results show that the number of AGB stars varies with the chemical composition, because the latter effects the lifetime on the thermally pulsing AGB, with the longest lifetime obtained for metallicity between half and one tenth of $Z_{\odot}$. Given that the evolutionary path followed by a star from the end of the AGB to the beginning of the cooling phase of the central white dwarf corresponds to the planetary nebulae phase, it is suggestive to infer that stellar populations with metallicity -0.5 to -0.1 solar may have a larger number of PNs than stellar populations with solar metallicity or higher, for the same bolometric luminosity. The metallicities of ICL stars in the Virgo cluster core were measured by Williams et al. (2007) using colour magnitude diagrams to be between -0.5 to -0.1 solar. If the stars in the M87 halo have a higher metallicity, we might expect a variation of the luminosity specific PN number in the region of radii where the M87 stellar halo and the ICL are superposed along the line-of-sight (Doherty et al. 2009), as is quantified for the first time in this work.

## 2.5 Planetary Nebula Luminosity Function in the outer regions of M87

### 2.5.1 PNLF

We can now use our large PN sample in the outer regions of M87 to investigate the properties of the PNLF. To do this we need to take into account that the fraction of detected PNs on our scientific images can be affected by incompleteness, and that this incompleteness is a function of magnitude. As for the spatial completeness, we quantify this effect by adding a modelled sample

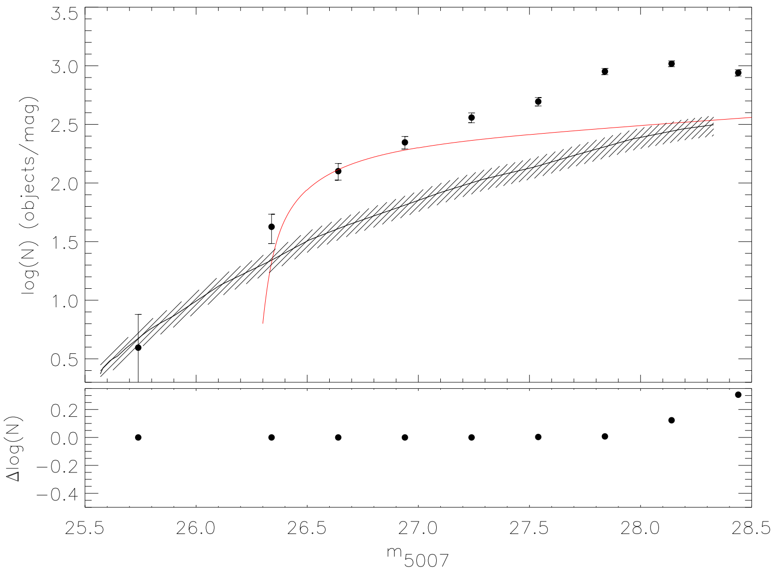

Figure 2.9: Top panel: luminosity function of the selected PNs in the outer regions of M87, corrected for colour and detection incompleteness. The error bars show the 1 $\sigma$ uncertainty from counting statistics. Data are binned into 0.3 mag intervals (see Table 2.5 for numerical values). The solid red line represents the analytical PNLF model for a distance modulus of 30.8, convolved with photometric errors. The black line shows the Ly$\alpha$ LF from Gronwall et al. (2007), scaled to the effective surveyed volume of the M87 SUB1 and M87 SUB2 fields, with the shaded area showing the cosmic variance due to Ly$\alpha$ density fluctuations (∼ 20%, see Sect. 2.3.2). Bottom panel: difference between the PNLF if we had used instead the automatically extracted sources without any final inspection. This plot shows that spurious detections affect mostly the two faintest magnitude bins.

of PNs on the scientific images and computing the fraction recovered by Sextractor of this input simulated PN population as function of magnitude (see Tab. 2.5 for values). In Fig. 3.12 we show the PNLF for the extracted candidates corrected for colour and detection incompleteness. We can compare this PNLF with the analytical formula by Ciardullo et al. (1989)

$$\mathrm{N}(M) = c_1 e^{c_2 M} \left\{1 - e^{3(M^* - M)}\right\} \tag{2.16}$$

where $c_1$ is a normalisation constant, $c_2 = 0.307$ and $M^*(5007)$=-4.51 mag is the absolute magnitude of the PNLF bright cutoff (Ciardullo et al. 1989). In Fig. 3.12 the red solid line shows the prediction from the analytical formula for a distance modulus of 30.8, after convolution with photometric errors and normalisation to the brightest observed bins. The comparison of the derived PNLF with the analytical formula shows two differences. First we detect one object with a $m_{5007} = 25.7$ that is ∼0.6 mag brighter than the expected cutoff for a distance modulus of 30.8. Second we measure a slope in the PNLF at ∼ 1.5 mag below the cutoff that is steeper than what is predicted by the analytical formula in this magnitude range (Ciardullo et al. 1989; Henize & Westerlund 1963).

We discuss the significance of these deviations in turn.

*Over-luminous source* – Fig. 3.12 also shows the comparison of the PNLF from our PN sample with the Ly$\alpha$ LF from Gronwall et al. (2007), scaled to our effective surveyed volume. The hatched range gives the uncertainty in the latter. We see that the bright end of the Ly$\alpha$ LF is consistent with the luminosity of the over-luminous object, within the photometric errors. Earlier suggestions that such overluminous objects could be due to a depth effect from Virgo ICL (Jacoby et al. 1990, C98) are not consistent with more recent studies of the ICL in Virgo; see Section 2.5.4. To definitively resolve the question of the nature of this object, whether it is a Ly$\alpha$ emitter or an object in the M87 halo, requires spectroscopic follow-up.

*Steeper PNLF 1.5 mag below the bright cutoff* – First, we carried out a Kolmogorov-Smirnov test to check whether our empirical PNLF can be drawn from the Ciardullo et al. (1989) analytical function, and this possibility is rejected. Next, because our sample covers 0.5° in the M87 halo, we can investigate the radial variation of the PNLF out to radii of 30′. We compute the PNLF for each of the three PN subsamples associated with the radial bins described in Sect. 2.4.1, correcting for colour and detection incompleteness, and subtracting the respective contribution from Ly$\alpha$ background objects. These are shown in the upper panel of Fig. 2.10, where the error bars also account for $\sim$ 20% cosmic variance in the Ly$\alpha$ density (see Sect. 2.3.2). We then compare the three PNLFs after normalisation to the total number of objects in each radial bin and carry out a Kolmogorov-Smirnov test to check whether they can result from the same underlying distribution. The probability that these three PNLFs are extracted from the same distribution is high, $P_{KS} > 99\%$.

These results are significant because the steepening of the PNLF is thus shown to be present in all three radial bins, while we know that the ICPN population contributes mostly to the outermost bin, see discussion in Sect. 2.4.3, and that any residual contamination of Ly$\alpha$ background emitters is also largest in the outermost radial region. We also checked that the PNLFs in the two Suprime-Cam fields are similar; both show the steepening at faint magnitudes. Hence we must conclude that the observed steepening of the PNLF is an intrinsic property of the PN population (halo and ICL) in the outer regions of M87.

### 2.5.2 Generalised analytical model for the PNLF and distance modulus of M87 halo

We determine the PNLF for the M87 halo as follows. From the colour and detection corrected PNLF, shown in the top panel of Fig. 3.12, we subtract the expected contribution from Ly$\alpha$ emitters. Using the measured values of $\alpha_{2.5}$ for the M87 halo and ICL PN population, we derive the fraction of PN in the M87 halo, using

$$\frac{\mathrm{N_{halo}}(m)}{\mathrm{N_{tot}}(m)} = \frac{\alpha_{2.5,\mathrm{halo}} L_{\mathrm{halo}}}{\alpha_{2.5,\mathrm{halo}} L_{\mathrm{halo}} + \alpha_{2.5,\mathrm{ICL}} L_{\mathrm{ICL}}} = \frac{1}{1 + 3\frac{L_{\mathrm{ICL}}}{L_{\mathrm{halo}}}} \tag{2.17}$$

where $L_{\mathrm{ICL}}$, $L_{\mathrm{L_{halo}}}$ are given in Table 2.3 and $\alpha_{2.5,\mathrm{ICL}}/\alpha_{2.5,\mathrm{halo}} = 3$. We show the PNLF of the halo of M87 in Fig. 2.11; error bars include Poisson statistics and a 20% cosmic variance of the Ly$\alpha$ density.

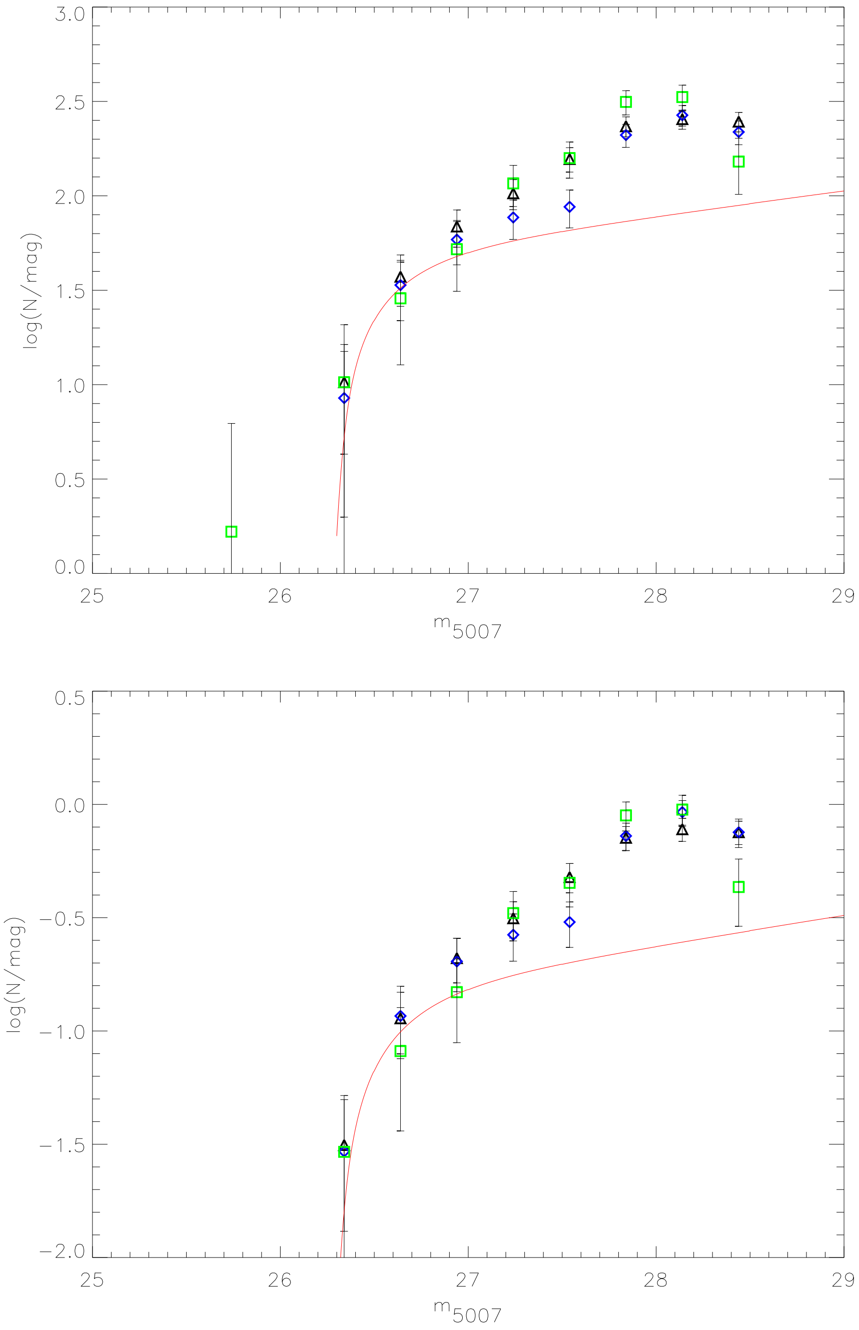

Figure 2.10: Top panel: empirical PNLFs in three radial ranges corrected for colour and detection incompleteness: PN candidates within 6.5′ from M87 centre - triangles, PN candidates between 6.5′ and 13.5′ from M87 centre - diamonds, PN candidates in the outermost region (distances greater than 13′) - squares.The respective Ly$\alpha$ contribution expected in each radial bin was subtracted. Magnitudes are binned in 0.3 mag bins and the error bars represent the 1 $\sigma$ uncertainty from counting statistics combined with the uncertainty from cosmic variance in the Ly$\alpha$ density (see text for details). As before, the red solid line is the convolved analytical formula of Ciardullo et al. (1989) for distance modulus 30.8. Lower panel: same as for the upper plot, but now the three PNLFs are normalised at the total number of objects in each radial bin. The three data sets are consistent with being drawn from the same underlying distribution.

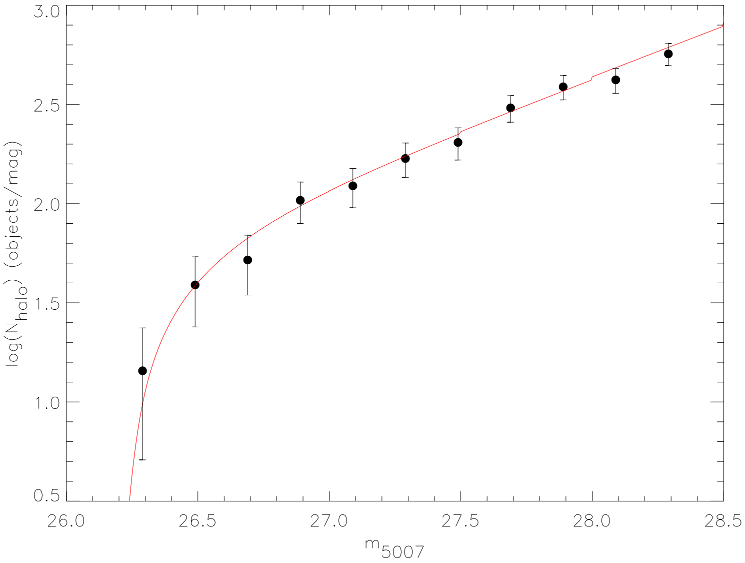

Figure 2.11: Completeness-corrected PNLF for the M87 halo (full dots) with magnitudes binned in 0.2 mag bins; error bars include Poisson statistics and 20% variance in the number of subtracted Ly$\alpha$ contaminants. The continuous line indicate the resulting fit of the generalised analytical formula Eq. 3.10, for the values of the free parameters given by $c_1 = 2017.2$, $c_2 = 1.17$ and a distance modulus of $m - M = 30.74$. The generalised PNLF is convolved with the photometric errors.

We now attempt to fit this PNLF with a generalised version of the analytical formula reported in Eq. 3.10. We continue to assume that the bright cutoff near $M^*$ is invariant for different PN populations, but we now allow for a free faint-end slope parameter $c_2$, in addition to varying the parameter $c_1$ equivalent to sample size. For the fit to the data we use robust non-linear least squares curve fitting, i.e., the IDL routine mpfit (Markwardt 2009), and account for the photometric errors. We derive the following values for the free parameters: $c_1 = 2017.2$, $c_2 = 1.17$ and $m^* = 26.23$, for a reduced $\chi^2 = 1.01$. Fig. 2.11 shows that this model is an excellent fit to the empirical PNLF for the halo of M87.

The fitted value of $m^* = 26.23$ corresponds to a nominal distance modulus for M87 of $m-M = 30.74$ mag, or $D = 14.1$ Mpc. Since the generalised PNLF formula has not been calibrated and our candidates are not spectroscopically confirmed, we regard this as preliminary and do not give an error on $m - M$. This value for the distance modulus is $\sim 0.4$ mag brighter than that measured with the surface brightness fluctuation method, $31.18 \pm 0.07$ mag (Mei et al. 2007), and with the tip of the red giant branch, $31.12 \pm 0.14$ mag (Bird et al. 2010), which correspond to distances of $17.2 \pm 0.5$ Mpc and $16.7 \pm 0.9$ Mpc.

### 2.5.3 Comparison of the PNLF in the M87 halo and in the M31 bulge

Here we compare the observed properties of the PNLF in M87 with the PNLF in the M31 bulge which was used to calibrate the analytical formula by C98. The PN population of the M31

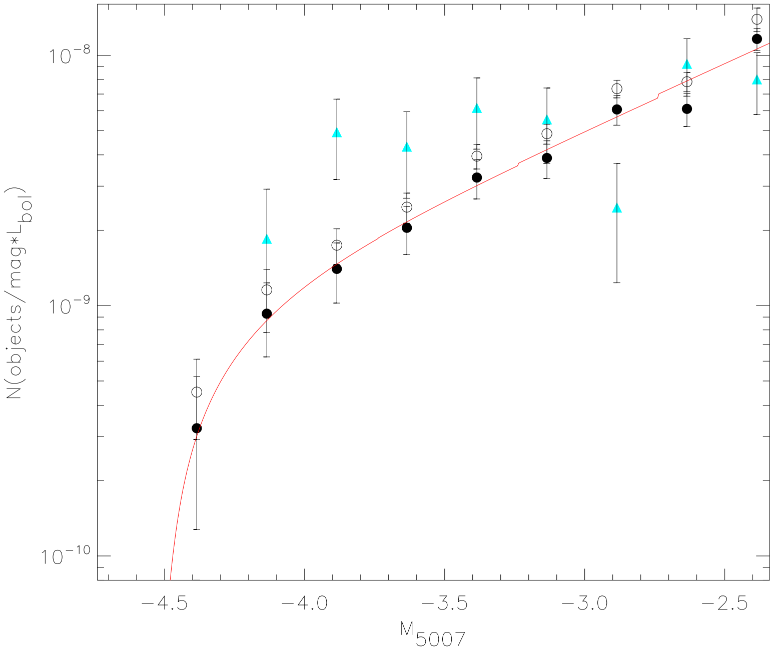

Figure 2.12: Luminosity-normalised PNLFs for the bulge of M31 (triangles) and the halo of M87 (circles). Open circles and filled circles represent, respectively, the PNLF of the halo of M87 before and after subtraction of the expected number of Ly$\alpha$ contaminants in each bin. Data are binned into 0.25 mag intervals. M87 has a higher number of faint PNs per unit bolometric luminosity and its PNLF has a steeper slope towards faint magnitudes than M31.

bulge was studied in detail by Ciardullo et al. (1989); it has similar depth to our PNLF, i.e. it is complete 2.5 mag down the bright cutoff of the PNLF. Also, the stellar population in the M31 has similar metallicity, colour and stellar population age as the population in the inner $\sim 6'$ of M87; see Tab. 2.3 for a complete list of the parameters.

We take the PN samples for M31 and the halo of M87 and normalise them by the sampled luminosity, then correct for the distance modulus. The results are shown in Fig. 2.12, where the PNLF for the halo of M87 is shown before and after the subtraction of Ly$\alpha$ contaminants. For the points where the Ly$\alpha$ contribution is subtracted the error bars take a $\sim$ 20% cosmic variance of the Ly$\alpha$ density (see Sect. 2.3.2) into account. Within 1 mag of the bright cutoff, the M87 PN population has fewer PNs than the PNLF of M31, i.e., the slope of the PNLF for the halo of M87 is steeper towards fainter magnitudes.

In old stellar populations, one expects the PN central stars to be dominated by low mass cores $M_{core} \leq 0.55 M_{\odot}$. Thus it is plausible that the slope of the PNLF should be steeper than predicted by modelling the fading of a uniformly expanding homogeneous gas sphere ionised by a non-evolving star in a single PN (Henize & Westerlund 1963). The comparison between the PNLFs of M87 and M31 may indicate that the M87 halo hosts a stellar population with a larger fraction of low mass cores with respect to the M31 bulge.

From observations, there is further evidence that the faint end slope of the luminosity function

Table 2.3: Properties of the stellar populations in the bulge of M31 and in the halo of M87

| Name | Distance | $L_{\odot,bol}$ | $(B\text{-}V)_0$ | $[Fe/H]^a$ | $\alpha_{2.5}$ | $Age^a$ | Ref |
|---|---|---|---|---|---|---|---|
| | (Mpc) | $L_{\odot,bol}$ | | | | Gyr | |
| M31 (bulge) | 0.76 | $6.5\times10^9$ | 0.95 | $\sim 0$ | $16.3\times10^{-9}$ | $> 10$ | (1) |
| M87 (halo) | 14.5 | $6.2\times10^{10}$ | 0.93 | $\sim 0$ | $8.2\times10^{-9}$ | $> 10$ | (2) |

**Notes**.[a] Ratio [Fe/H] and Age from Saglia et al. (2010) (M31) and Liu et al. (2005) (M87). M87 [Fe/H] and Age analysis covers the first 400″.

**References**. (1) Buzzoni et al. (2006); (2) This work.

may depend on the parent stellar population. Ciardullo et al. (2004) reported that star-forming systems, like the disk of M33 and the Small Magellanic Cloud (SMC), have shallower slopes ~ 1.5 mags below the bright cutoff when compared to older stellar populations such as NGC 5128 or M31. These shallower slopes correspond to lower values of $c_2$ in Eq. 3.10.

### 2.5.4 Comparison with previous PNLF distance measurements for M87

We already referred in Section 2.3.3 to the work of C98 who carried out a PN survey in an area of $16' \times 16'$ centred on M87, and investigated the properties of the PNLF. F03 studied the properties of ICPNs in the Virgo ICL, including an area of $16' \times 16'$ centred 14.8′ north of M87. Both surveys overlap with our current survey, but have a constant zero point offset $\Delta = 0.3$ mag relative to our measured magnitudes (see discussion in Section 2.3.3).

Fig. 2.13 compares the PNLFs of the matched subsamples common to our catalogue and those of C98 and F03, respectively. A residual zero point offset $\Delta = 0.3$ mag has been applied to the C98 and F03 subsamples. With this zero point shift, the empirical PNLFs agree very well within one magnitude of the bright cutoff, and are consistent with a distance modulus of 30.8. Without the zero point shift, the distance modulus obtained from the PNLFs of C98 and F03 would be 30.5. Thus the value obtained for our new M87 halo PN sample (30.75), which is closer to other determinations (Section 2.5.2), indicates a systematic effect in the C98, F03 photometry, in the sense of brighter $m_{5007}$ in these samples. This systematic effect can explain and resolve some of the tension between the assumptions and results of C98, F03, and more recent findings on the spatial distribution of ICPNs in the Virgo cluster and the radial extension of the M87 halo, as discussed now.

C98 find that their empirical PNLF deviates from the analytical formula and link the deviations with the presence of an ICPN population uniformly distributed in the Virgo cluster volume. C98 assume that all PNs at distances larger than $R_{iso} > 4.8'$ from the centre of M87 are ICPNs. Fitting a PNLF to this component, they derive that the ICPN population must extend 4 Mpc in front of M87; see Fig. 8 and its figure caption in C98 for further details. The depth effect, which

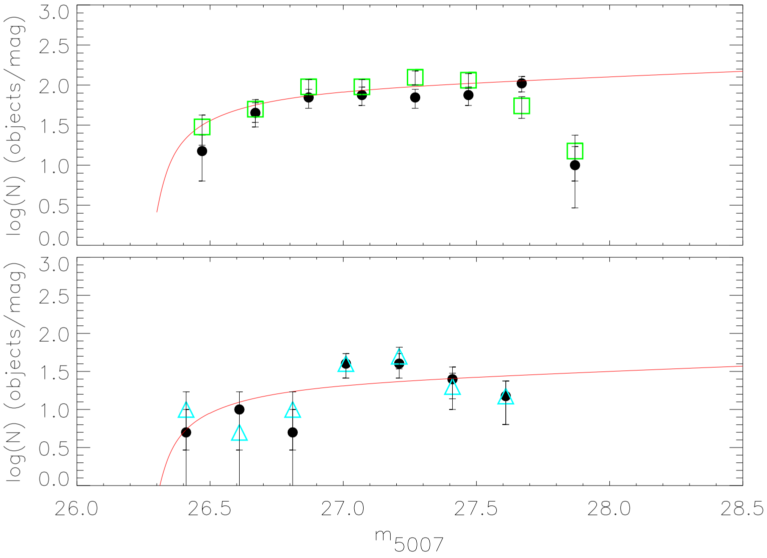

Figure 2.13: Luminosity functions of the matched PN samples from this survey (filled circles), from C98 (top panel, green squares), and from F03 (bottom panel, cyan triangles). The error bars show the 1 $\sigma$ uncertainty from counting statistics. Data are binned into 0.2 mag intervals. The solid red line represents the analytical PNLF model using a distance modulus of 30.8, convolved with photometric errors. The magnitude range is driven by the magnitude limit of the C98 sample (top panel) and F03 sample (bottom panel). A zero point shift $\Delta = 0.3$ mag relative to our sample was applied to both survey.

is equivalent to a brightening of the PNLF by foreground ICPNs, places the near edge of the ICL population at a distance modulus of 30.3, corresponding to a distance of 11 Mpc.

The assumptions of C98 on the membership of PNe at $R_{iso} > 4.8'$ from M87 to the ICL and on the spatial distribution of the ICL are not supported by the results of the spectroscopic follow-up of Arnaboldi et al. (2004) and the wide area ICPN survey by Castro-Rodríguez et al. (2009). The spectroscopic follow-up by Arnaboldi et al. (2004) showed that in the FCJ field of F03 at 14.8′ from the M87 centre 87% of the PNs are bound to the M87 halo, and only 13% are ICPNs. Thus the fraction of ICPNs in regions that are even closer to the centre, as in the C98 $R_{iso} > 4.8'$, sample, will be down to a few %. The wide area survey for ICPNs carried out by Castro-Rodríguez et al. (2009) shows that the ICL is associated with only the densest regions of the Virgo cluster, ~ 0.4 Mpc around M87. Hence the brightening of the PNLF expected due to foreground ICPNs is < 0.1 mag. These results indicate that the C98 PNs at $R_{iso} > 4.8'$ are bound to the M87 halo, with very limited contamination by ICL: thus they are at the distance of M87 and the brightening of the C98 sample is not caused by volume effects or a contamination by ICPNs. Similar arguments apply to the F03 PN sample.

We therefore conclude that the magnitudes for the C98, F03 PNs sample must be systematically too bright by 0.3 mag, and that our new photometry is reliable.

## 2.6 Summary and Conclusions

We carried out a deep survey for planetary nebulas (PNs) in two wide fields of $34' \times 27'$, covering the halo of the cD galaxy NGC 4486 (M87) in the Virgo cluster with Suprime-Cam at the Subaru telescope. Both fields were imaged through a narrow-band filter centred at the redshifted [OIII]$\lambda$5007 Å emission and a broad-band V filter. The surveyed area covers the halo of M87 out to a radial distance of 150 kpc. This is the largest survey so far for PNs in the M87 halo in terms of number of detected PN candidates, depth and area coverage.

PN candidates were identified via the on-off band technique on the basis of automatic selection criteria using their narrow-band colours and their two-dimensional light distributions. The final photometric catalogue contains 688 objects, with a magnitude range extending from the apparent magnitude of the bright cutoff at Virgo distance down to 2.2 magnitude deeper.

We studied the radial number density profile of the PN candidates and compared it with the V-band surface brightness profile of the stellar light in the M87 halo. The logarithmic PN number density profile shows good agreement with the $\mu_{\rm V}$ surface brightness profile within $13'$ from M87's centre, but flattens at large radii. At the most distant point the difference to the prediction from the light profile is 1.2 mags. We investigated whether contributions from background Ly$\alpha$ emitters at redshift $z = 3.1$ can be responsible for the flatter distribution. By using the Ly$\alpha$ LF from Gronwall et al. (2007) scaled to our effective surveyed volume, we constrained the Ly$\alpha$ contribution to be $25\% \pm 5\%$ of the total sample over the whole surveyed area, and we concluded that it cannot explain the factor 3 more sources in the outer regions that are responsible for the flatter profile.

Stimulated by the early finding of Doherty et al. (2009) who determined different luminosity specific PN numbers for the M87 halo light and the ICL, we propose a two component model for the PN population, with the ICL contributing a larger number of PNs per unit light. This composite model is consistent with the observed flattening of the logarithmic PN density profile when the luminosity specific PN numbers are $\alpha_{2.5,\rm halo} = (1.10^{+0.17}_{-0.21}) \times 10^{-8}\ \rm N_{PN} L^{-1}_{\odot,bol}$ and $\alpha_{2.5,\rm ICL} = (3.29^{+0.60}_{-0.72}) \times 10^{-8}\ \rm N_{PN} L^{-1}_{\odot,bol}$, for the M87 halo and ICL population respectively.

Because of the large magnitude range of this PN survey, we were able to study the shape of the PNLF in detail and measured a steeper slope at faint magnitudes than what is expected from the analytical formula of Ciardullo et al. (1989). The fit of the generalised PNLF formula (Eq. 3.10) to the empirical PNLF of the M87 halo population gives faint-end slope of $c_2 = 1.17$ and a nominal distance modulus of 30.74.

The depth of the current survey allowed us to carry out a comparison with the benchmark for PNLF studies, the M31 bulge. The comparison of the M87 halo PNLF with the M31 bulge PNLF, when both are normalised by the sampled bolometric luminosity, shows that the former has fewer PNs at bright magnitudes, and a steeper slope towards the faint end. The steepening of the PNLF at fainter magnitudes is consistent with a larger fraction of PNs with low mass cores. PN evolution models and stellar population measurements at large radii will be needed to understand the stellar population effects that shape the PNLF of the M87 halo.

Table 2.4: Number density and logarithm number density profile for the colour and spatial corrected sample of emission line objects.

| R | $\frac{N_c}{A}$ | $-2.5\log_{10}\left(\frac{N_c}{A}\right)+\mu_0$ | C($R$) |
|---|---|---|---|
| (arcsec$^{1/4}$) | (N/arcsec$^2$) | mag/arcsec$^2$ | |
| 3.6 | $1.7\times10^{-3}$ | 22.9 | 0.55 |
| 3.9 | $1.5\times10^{-3}$ | 23.1 | 0.84 |
| 4.1 | $8.4\times10^{-4}$ | 23.7 | 0.91 |
| 4.2 | $6.0\times10^{-4}$ | 24.0 | 0.87 |
| 4.4 | $5.0\times10^{-4}$ | 24.2 | 0.87 |
| 4.6 | $5.2\times10^{-4}$ | 24.2 | 0.85 |
| 4.9 | $2.8\times10^{-4}$ | 24.9 | 0.86 |
| 5.1 | $1.8\times10^{-4}$ | 25.3 | 0.83 |
| 5.3 | $1.6\times10^{-4}$ | 25.5 | 0.86 |
| 5.6 | $1.2\times10^{-4}$ | 25.8 | 0.88 |
| 5.8 | $1.2\times10^{-4}$ | 25.8 | 0.88 |
| 6.0 | $7.4\times10^{-5}$ | 26.3 | 0.88 |
| 6.4 | $5.1\times10^{-5}$ | 26.7 | 0.91 |

**Notes.**The term $C_R$ is the spatial completeness factor as function of the distance from M87's centre.

Table 2.5: Planetary Nebula luminosity function for the sample of emission line objects.

| $m_{5007}$ | $\log_{10}(N/bin)$ | *ColourCompleteness* | *DetectionCompleteness* |
|---|---|---|---|
| 25.7 | 0.6 | 100% | 85% |
| 26.0 | — | 75% | 85% |
| 26.3 | 1.6 | 70% | 90% |
| 26.6 | 2.1 | 88% | 90% |
| 26.9 | 2.3 | 85% | 90% |
| 27.2 | 2.6 | 85% | 90% |
| 27.5 | 2.7 | 98% | 90% |
| 27.8 | 2.9 | 81% | 80% |
| 28.1 | 3.0 | 66% | 80% |
| 28.4 | 2.9 | 43% | 40% |

**Notes**.The term *ColourCompleteness* represents the percentage of simulated PNs that we retrive with our colour selection, as function of the magnitude.

The term *DetectionCompleteness* represents the recovery fraction of an input simulated PN population as function of magnitude.

# Chapter 3

# The outer regions of the giant Virgo galaxy M87. Kinematic separation of stellar halo and intracluster light

*This chapter is accepted on A&A as the study Longobardi et al. (2015a)*

## Abstract

We present a spectroscopic study of a sample of 287 Planetary Nebulas (PNs) around the brightest cluster galaxy (BCG) M87 in Virgo A, of which 211 are located between 40 kpc and 150 kpc from the galaxy center. With these data we can distinguish the stellar halo from the co-spatial intracluster light (ICL) and study both components separately.

PN velocities were obtained with a high resolution FLAMES/VLT survey targeting eight fields in a total area of $\sim 0.4$ deg$^2$. PNs were identified from their narrow and symmetric redshifted $\lambda$5007Å [OIII] emission line, the presence of the second $\lambda$4959Å [OIII] emission line, and the absence of significant continuum. We implement a robust technique to measure the halo velocity dispersion from the projected phase-space to identify PNs associated with the M87 halo and ICL. Using photometric magnitudes, we construct PN luminosity functions (PNLFs), complete down to $m_{5007}$=28.8.

The velocity distribution of the spectroscopically confirmed PNs is bimodal, containing a narrow component centered on the systemic velocity of the BCG and an off-centred broader component, that we identify as halo and ICL, respectively. We find that 243 PNs are part of the velocity distribution of the M87 halo, while the remaining subsample of 44 PNs are intracluster PNs (ICPNs). Halo and ICPNs have different spatial distributions: the number density of halo PNs follow the galaxy's surface brightness profile, whereas the ICPNs are characterised by a shallower power-law profile, $I_{ICL} \propto R^{\gamma}$ with $\gamma$ in the range $[-0.34, -0.04]$. No evidence is found for an asymmetry in the halo and ICPN density distributions when the NW and SE fields are studied separately. Study of the composite PN number density profile confirms the superposition

of different PN populations associated with the M87 halo and the ICL, characterised by different PN specific numbers $\alpha$. We derive $\alpha_{\mathrm{halo}} = 1.06 \times 10^{-8}$ $\mathrm{N_{PN}L^{-1}_{\odot,bol}}$ and $\alpha_{\mathrm{ICL}} = 2.72 \times 10^{-8}$ $\mathrm{N_{PN}L^{-1}_{\odot,bol}}$, respectively. The M87 halo PNLF has fewer bright PNs and a steeper slope towards faint magnitudes than the ICPNLF, and both are steeper than the standard PNLF for the M31 bulge. Moreover, the ICPNLF has a dip at ~ 1-1.5 mag fainter than the bright cutoff, reminiscent of the PNLFs of systems with extended star formation history such as M33 or the Magellanic clouds.

The BCG halo of M87 and the Virgo ICL are dynamically distinct components with different density profiles and velocity distributions. Moreover, the different $\alpha$-parameter values and PNLF shapes of the halo and ICL indicate distinct parent stellar populations, consistent with the existence of a gradient towards bluer colours at large radii. These results reflect the hierarchical build-up of the Virgo cluster.

## 3.1 Introduction

Galaxy halos are faint stellar components made of stars gravitationally bound to the individual galaxies. In galaxy clusters these halos may be surrounded by intracluster stars. The existence of a diffuse population of intergalactic stars was first proposed by Zwicky (1937, 1952). Due to its low surface brightness it was only with the advent of CCD photometry that this diffuse stellar component could be studied in a quantitative way, thus becoming a topic of interest for observational and theoretical studies.

The formation of intracluster light (ICL) and of the extended halos around the brightest cluster galaxies (BCG) is closely related to the morphological transformation of galaxies in clusters. Two of the main physical processes describing the gravitational interaction between galaxies during cluster formation and evolution are dynamical friction (Ostriker & Tremaine 1975; Merritt 1985; Taffoni et al. 2003; Boylan-Kolchin et al. 2008; De Lucia et al. 2012) and tidal stripping (Gallagher & Ostriker 1972; Moore et al. 1996; Gregg & West 1998b; Willman et al. 2004; Read et al. 2006b). Depending on its mass, central distance and orbit, these processes determine the fate of a cluster galaxy. Dynamical friction is the primary mechanism dragging a massive satellite towards the host halos centre, where it will merge with the BCG. On the other hand, tidal forces strip stars from satellite galaxies which will end up orbiting the cluster as unbound ICL (Gnedin 2003; Murante et al. 2004, 2007; Mihos 2004; Rudick et al. 2006). In the ICL and the outer regions of BCGs where the dynamical time-scales are long, fossil records of accretion events can be preserved over extended periods (Willman et al. 2004; Rudick et al. 2009; Cooper et al. 2014). Hence, the study of the luminosity, distribution and kinematics of galaxy halos and ICL may provide information on the evolution of galaxies and their host clusters.

In the last ten years the analysis of simulated galaxy clusters has shed light upon the nature and origin of the diffuse stellar component and its connection with the BCG (Napolitano et al. 2003; Murante et al. 2004, 2007; Willman et al. 2004; Rudick et al. 2006, 2009; Puchwein et al. 2010; Laporte et al. 2013; Contini et al. 2014). In the framework of cosmological hydrodynamical simulations, Dolag et al. (2010) and Cui et al. (2014) separated stars bound to the cluster potential from those bound to the BCG by adopting a dynamical definition of the main galaxy halo and the diffuse light. Tagging particles as galaxy or intracluster component based on their different velocity distributions, they identified two distinct stellar populations in terms of kinematics, spatial distribution, and physical properties like age and metallicity. Other studies do not adopt such a dynamical definition of the two components and treat the BCG and ICL as a single system at the centre of the cluster, consisting of all stars that are not bound to any satellite subhalos in the cluster (e.g., Murante et al. 2004; Cooper et al. 2014).

Galaxy halos, diffuse ICL, and their connection with galaxy evolution in clusters have been the subject of many observational studies. Deep imaging of individual objects (Bernstein et al. 1995; Gonzalez et al. 2000; Feldmeier et al. 2004b; Mihos et al. 2005; Krick & Bernstein 2007; Rudick et al. 2010) has shown that the faint ICL around BCGs often has irregular morphology, consistent with predictions from simulations. From stacking images for a large number of objects (Zibetti et al. 2005; D'Souza et al. 2014), average photometric properties were obtained, showing that the ICL extends to many 100s of kpcs from the cluster centre. In the Virgo cluster, Kormendy et al. (2009) analysed a sample of ellipticals and spheroidal galaxies and studied their halos through the light profiles. Comparing their results with the earliest simulations of van Albada (1982), they argued that light profiles with a large Sersic index ($n > 4$) are common in many giant ellipticals whose origin can be associated with merger processes.

Kinematics and stellar population parameters have been measured only in a small number of BCG halos, such as NGC 4889 in the Coma cluster (Coccato et al. 2010), which shows a change of stellar population at large radii, the central galaxy NGC 3311 in Hydra I (Ventimiglia et al. 2010; Arnaboldi et al. 2012) where the kinematics as well as the morphology of the outer halo signal on-going accretion events, and NGC 6166 in Abell 2199 (Kelson et al. 2002; Bender et al. 2014) whose velocity dispersion profile blends smoothly into the cluster. ICL kinematics in the Coma cluster suggest an on-going merger of two cluster cores (Gerhard et al. 2007). All these studies aimed at understanding the role of tidal disruption and merger events as the main processes involved in the formation and evolution of central cluster galaxies and the ICL.

In the nearest clusters, single stars can be used to study the stellar populations associated with the outer halos and the diffuse stellar component (Ferguson et al. 1998; Durrell et al. 2002; Williams et al. 2007; Yan et al. 2008). Globular clusters (GCs) have been used to obtain kinematic information in the outer regions of nearby early-type galaxies (Côté et al. 2001; Schuberth et al. 2010; Strader et al. 2011; Romanowsky et al. 2012; Pota et al. 2013). Planetary Nebulas (PNs) have been targeted in several surveys aimed at tracing the light and motions in galactic halos (Hui et al. 1993; Méndez et al. 2001; Peng et al. 2004; Coccato et al. 2009; McNeil et al. 2010; McNeil-Moylan et al. 2012; Cortesi et al. 2013), the Virgo cluster IC component (Arnaboldi et al. 1996, 2003, 2004; Aguerri et al. 2005; Doherty et al. 2009; Castro-Rodríguez et al. 2009; Longobardi et al. 2013), and the Hydra I and Coma clusters, out to 50-100 Mpc distance (Ventimiglia et al. 2010, 2011; Gerhard et al. 2005). It was found that the observed properties of the PN population, such as the $\alpha$ parameter which quantifies the stellar luminosity associated with a detected PN, and the PN luminosity function (PNLF) correlate with the age, colour and metallicity of the parent stellar population (Hui et al. 1993; Ciardullo et al. 2004; Ciardullo 2010; Buzzoni et al. 2006; Longobardi et al. 2013). Thus PNs can be used to trace these physical quantities of their parent stellar populations at surface brightnesses too faint for other techniques.

The giant elliptical galaxy M87 has one of the oldest stellar populations in the local Universe

(Liu et al. 2005), and a stellar halo containing 70% of the galaxy light down to $\mu_{\rm V}$ =27.0 mag arcsec$^{-2}$ (Kormendy et al. 2009). It is close to the centre of sub-cluster A in the Virgo cluster (Binggeli et al. 1987), the nearest galaxy cluster, and it is expected to have transformed over larger time scales due to galaxy mergers (De Lucia & Blaizot 2007). Deep imaging (Mihos et al. 2005; Janowiecki et al. 2010) has revealed a complex network of faint, extended tidal features around M87, suggesting that it is not completely in equilibrium. Thus, M87 and the surrounding Virgo cluster core are prime targets to address the formation and evolution of galaxy clusters, ICL, and BCGs. Indeed, M87 has been the subject of many dynamical studies with X-ray measurements (Nulsen & Bohringer 1995; Churazov et al. 2010), integrated stellar kinematics (Murphy et al. 2011, 2014), GC kinematics (Côté et al. 2001; Strader et al. 2011; Romanowsky et al. 2012; Zhu et al. 2014), and PN kinematics (Arnaboldi et al. 2004; Doherty et al. 2009), to estimate its mass and derive the dark matter distribution. Using PN kinematics, Doherty et al. (2009) identified M87 halo and IC PNs and showed the coexistence, at radii > 60 kpc, of a stellar halo bound to the galaxy potential and a surrounding unbound Virgo ICL.

In this work, we report the results of a wide and high resolution spectroscopic survey covering the outer regions of M87 out to a distance of 150 kpc from the galaxy centre. The aim of this project is to investigate the halo-ICL dichotomy, making use of a large spectroscopic sample of PNs (approximately fifteen times larger than the previous sample of Doherty et al. (2009)). The paper is structured as follows: in Sect. 5.2 we describe the spectroscopic survey together with the data reduction procedures and the classification of PN spectra. In Sect. 5.3 we study the PN phase-space distribution and dynamically separate the halo and IC populations. Spatial density distributions are derived in Sect. 5.4, and in Sect. 4.5 we present the properties of the halo and IC PN populations in terms of their $\alpha-$parameters and the morphology of their PNLFs. Finally we discuss our results in Sect. 3.6 and give our conclusions in Sect. 3.7.

In this study we adopt a distance modulus of 30.8 for M87 (Ciardullo et al. 2002; Longobardi et al. 2013), implying a physical scale of 73 pc arcsec$^{-1}$.

## 3.2 The FLAMES M87 PN survey

### 3.2.1 Photometric sample

The photometric candidates targeted by our spectroscopic survey come from an earlier imaging survey (Longobardi et al. 2013), covering a 0.43 deg$^2$ region centred on M87. Images were taken through a narrow band filter centred on the redshifted [OIII]$\lambda$5007Å emission line at the Virgo cluster distance (on-band image), and through a broad-band V-filter (off-band image). Because of their bright [OIII]$\lambda$5007Å emission, extragalactic PNs can be identified as unresolved emission sources with positive flux on the on-band [OIII] image and no detection on the off-band image.

Spectra were obtained in two observing campaigns. For the first spectroscopic campaign, we selected emission line candidates as objects with positive flux on the colour [OIII]-V band image[1] (hereafter difference method, see Feldmeier et al. (2003) for more details). The *visual*

---

[1] Before the subtraction the continuum off-band image was scaled to the on-band image by a multiplicative scaling factor found measuring fluxes from several bright, isolated stars on both images.

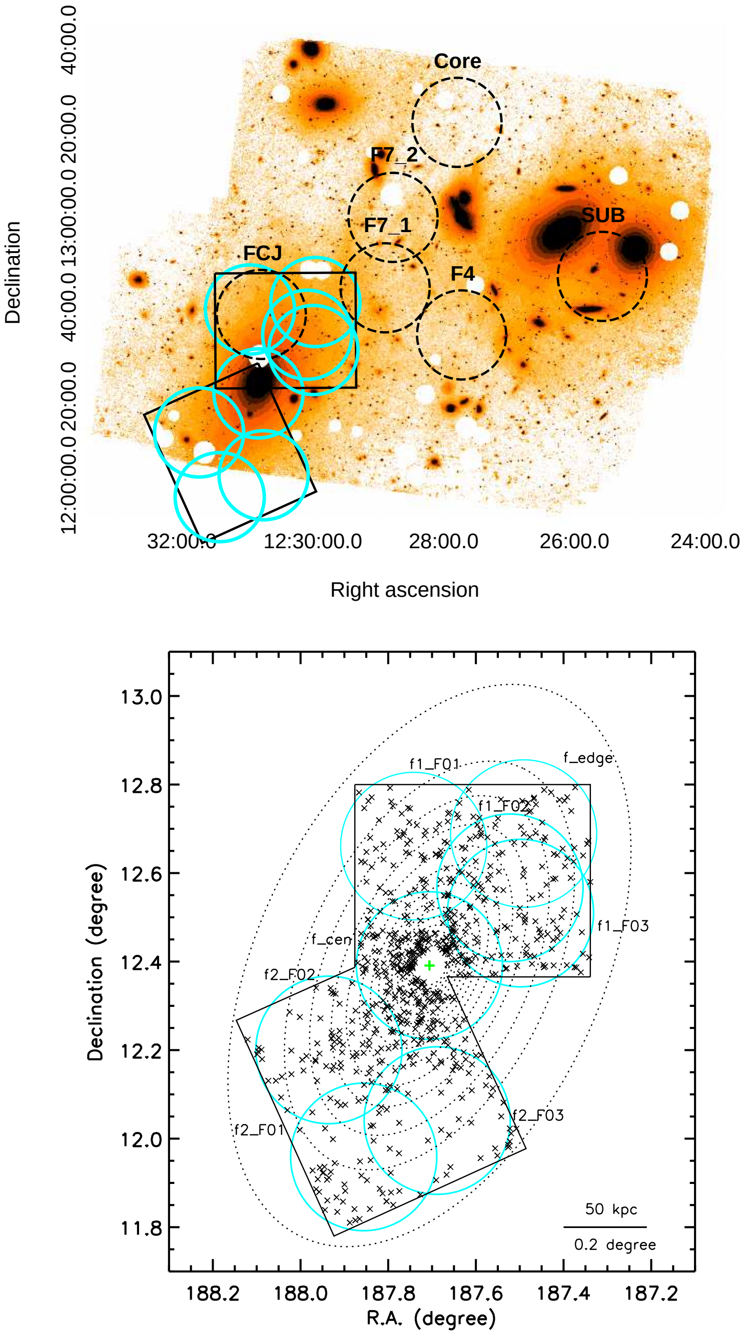
Core
F7_2
F7_1
FCJ
F4
SUB
Declination
12:00:00.0 20:00.0 40:00.0 13:00:00.0 20:00.0 40:00.0
32:00.0 12:30:00.0 28:00.0 26:00.0 24:00.0
Right ascension
f1_F01
f_edge
f1_F02
f1_F03
f_cen
f2_F02
f2_F01
f2_F03
50 kpc
0.2 degree
Declination (degree)
13.0 12.8 12.6 12.4 12.2 12.0 11.8
188.2 188.0 187.8 187.6 187.4 187.2
R.A. (degree)

Figure 3.1: *Top panel*: Image of the core of the Virgo cluster (Mihos et al. 2005) with the positions of the FLAMES fields studied in this work (cyan circles) and in previous surveys by Arnaboldi et al. (2004) and Doherty et al. (2009) (dotted black circles). Black squares represent the Suprime-Cam survey fields used for the extraction of the photometric PN candidates (Longobardi et al. 2013). *Bottom panel*: Schematic zoom-in of the surveyed area (black rectangles). FLAMES pointings (cyan circles) and PN candidates from the photometric survey (black asterisks; Longobardi et al. 2013) are plotted over the isophotes of the M87 halo surface brightness (Kormendy et al. 2009). The green cross depicts M87's centre. North is up, East is to the left.

Table 3.1: Flames Configuration and Exposure Times. Column 1: ID of FLAMES plate. Columns 2 & 3: FLAMES plate Right Ascension and Declination. Column 4: Total exposure time. Column 5: Single exposure time × number of exposures.

| FLAMES Conf | RA h:m:s | DEC degrees | Total Exposure time (s) | Single Exposure time × # of exposures (s) |
|---|---|---|---|---|
| M87SUB1 Bright F01 | 12:30:58.015 | +12:39:39.28 | 2700 | 1350 × 2 |
| M87SUB1 Bright F02 | 12:30:05.332 | +12:34:00.08 | 2700 | 1350 × 2 |
| M87SUB1 Bright F03 | 12:29:59.574 | +12:30:34.49 | 2700 | 1350 × 2 |
| M87SUB1 Norm F01 | 12:30:58.015 | +12:39:39.28 | 8100 | 2700 × 3 |
| M87SUB1 Norm F02 | 12:30:05.332 | +12:34:00.08 | 8400 | 2800 × 3 |
| M87SUB1 Norm F03 | 12:29:59.574 | +12:30:34.49 | 8400 | 2800 × 3 |
| M87SUB2 Bright F01 | 12:31:25.426 | +11:57:31.43 | 2700 | 1350 × 2 |
| M87SUB2 Bright F02 | 12:31:44.477 | +12:12:01.55 | 2700 | 1350 × 2 |
| M87SUB2 Bright F03 | 12:30:45.170 | +12:02:27.20 | 2700 | 1350 × 2 |
| M87SUB2 Norm F01 | 12:31:25.426 | +11:57:31.43 | 8400 | 2800 × 3 |
| M87SUB2 Norm F02 | 12:31:44.477 | +12:12:01.55 | 8400 | 2800 × 3 |
| M87SUB2 Norm F03 | 12:30:45.170 | +12:02:27.20 | 8400 | 2800 × 3 |
| M87SUB FEDGE | 12:29:57.854 | +12:41:20.90 | 6800 | 1700 × 4 |
| M87SUB FCEN | 12:30:50.019 | +12:20:48.88 | 6800 | 1700 × 4 |

*catalogue* extracted on the basis of the difference method consisted of 1074 objects that covered a magnitude range $23 \leq m_{5007} \leq 29.8$, and is statistically complete down to $m_{5007} \simeq 28.8$[2].

For the second spectroscopic campaign, we carried out a more stringent selection procedure described in Longobardi et al. (2013). In this procedure, the PN candidates were selected using automatic selection criteria, based on the distribution of the detected sources in the colour-magnitude (CM) diagram and the properties of their point-spread function (PSF) (for more details see Arnaboldi et al. 2002; Longobardi et al. 2013). This *automatic catalogue* is complete within the magnitude range $26.3 \leq m_{5007} \leq 28.4$.

The combined total input sample for the spectroscopic survey (*visual catalogue* plus *automatic catalogue*) consisted of 1484 emission line candidates.

### 3.2.2 Observations and data reduction

The spectra were acquired in service mode with the FLAMES spectrograph on the VLT-UT2 telescope, in the GIRAFFE+MEDUSA mode. This observing mode allows up to 132 separate fibres that can be allocated to targets in one plate configuration, covering a circular area of 20′ diameter. The total emission line sample was observed in two observing runs (24h, 088.B-0288(A); 11h, 093.B-0066(A); PI: M.Arnaboldi) which were characterised by clear conditions and seeing better than 0.9″. We used the high-resolution grism HR08, covering a wavelength range of ∼ 250 Å centred on 5048 Å with a spectral resolution of $R = 22500$. With this setup, the instrumental broadening of the arc lines has a FWHM of 17 km s$^{-1}$ and the statistical error on the wavelength measurements is 150 m s$^{-1}$ (see Royer et al. 2002). We refer to Sect. 3.2.5 for discussion of the velocity accuracy estimated from repeat observations of the same emission line candidates.

---

[2] The transformation between the AB and 5007 magnitudes for the photometric narrow band filter is given by $m_{5007} = m_{\rm AB} + 2.49$ (Longobardi et al. 2013).

Because the [OIII] emission lines from PNs are only a few km $s^{-1}$ wide, high resolution spectra are also desirable to reduce the sky contamination, making the FLAMES spectrograph the ideal instrument for LOS velocity measurements of extragalactic PNs.

For our first spectroscopic campaign, the *visual catalogue* was divided into a bright ($m_{5007} < 27.2$) and a normal ($m_{5007} > 27.2$) sample. The FLAMES plate configurations and exposure times were then optimised in order to reach the maximum number of fibres allocated, as well as optimal signal-to-noise ratio (S/N) for both samples. Based on the FLAMES/GIRAFFE/HR08 configuration, for a $10^4$ sec exposure, the monochromatic [OIII]$\lambda$5007Å emission of a PN with [OIII] flux of $F_{5007} = 1.0 \times 10^{-17} \mathrm{erg\,cm^{-2}\,s^{-1}}$ ( $m_{5007} = 28.8$ ) is detected with S/N=10 per resolution element (0.29 Å).

In total we defined 12 FLAMES plate configurations, labelled as M87SUB1 Bright F01-F03, M87SUB1 Norm F01-F03 and M87SUB2 Bright F01-F03, M87SUB2 Norm F01-F03 for the NW (SUB1) and SE (SUB2) Suprime-Cam fields respectively. The layout of the FLAMES pointings on the sky, together with the coverage of the photometric Suprime-Cam survey, is shown in Fig. 3.1.

In the second spectroscopic campaign we added two FLAMES plate configurations covering the very central region of M87 and the NW edge of the Suprime-Cam imaging survey, in addition to completing the observations of the 12 FLAMES configurations from the first campaign. These two additional FLAMES configurations are shown in Fig. 3.1 with the labels FCEN and FEDGE, respectively. Table 3.1 provides an overview of the FLAMES field configurations and the total exposure times.

The spectroscopic data were reduced using the GIRAFFE pipeline[3]. The reduction procedure included bias subtraction, flat-fielding, identification of the fibre locations on the CCD, geometric distortion correction, wavelength calibration and extraction of the one-dimensional spectra. The calibrated one-dimensional spectra were then corrected to the heliocentric velocity using the IRAF[4] task *dopcor*. Finally, we combined spectra from single exposures using the IRAF task *scombine* to get the targeted S/N for each spectrum (see above).

### 3.2.3 Spectroscopic success rates

We define the nominal success rate as the ratio between the number of spectra with detected emission line and the number of fibres allocated for a given FLAMES plate configuration. For our observations, it varies from field to field, in a range of values between ~ 20% and ~ 60%. These values are similar to those obtained in the spectroscopic follow-up of GCs in the outer halo of M87 (see Sect. 3 in Strader et al. (2011))[5]. The low success rates for some of the fields (mostly

---

[3] https://www.eso.org/sci/software/pipelines/giraffe/giraf-pipe-recipes.html

[4] IRAF is distributed by the National Optical Astronomy Observatory, which is operated by the Association of Universities for Research in Astronomy (AURA) under cooperative agreement with the National Science Foundation.

[5] In Strader et al. (2011) the 'nominal' success rate is defined as the ratio between number of slit/fibres allocated to candidates and the number of identified GCs.

Table 3.2: Summary of the total number of allocated fibres, nominal success rate, detected number of PNs, and spectroscopic completeness in all fields. Numbers in brackets refer to sources in common with the automatic sample.

| FLAMES Conf. | # of targets with fibres allocated | Nominal success rate | Confirmed PNs | $\mathbf{C}_{\rm spec,fb}$ |
|---|---|---|---|---|
| M87SUB1 Bright F01 | 33 (12) | 52% (42%) | 8 (3) | 0.6 |
| M87SUB1 Bright F02 | 41 (19) | 23% (32%) | 4 (4) | 0.5 |
| M87SUB1 Bright F03 | 33 (14) | 42% (71%) | 8 (8) | 0.9 |
| M87SUB1 Norm F01 | 125 (58) | 47% (57%) | 49 (26) | 0.9 |
| M87SUB1 Norm F02 | 130 (65) | 52% (62%) | 55 (35) | 0.9 |
| M87SUB1 Norm F03 | 127 (56) | 53% (64%) | 54 (31) | 0.9 |
| M87SUB2 Bright F01 | 23 (8) | 61% (75%) | 5 (3) | 0.8 |
| M87SUB2 Bright F02 | 31 (16) | 26% (25%) | 5 (4) | 0.6 |
| M87SUB2 Bright F03 | 26 (7) | 54% (57%) | 5 (3) | 0.8 |
| M87SUB2 Norm F01 | 104 (40) | 16% (17%) | 10 (6) | 0.3 |
| M87SUB2 Norm F02$^{a}$ | 144 (71) | 42% (51%) | 44 (27) | 0.6 |
| M87SUB2 Norm F03 | 117 (50) | 24% (30%) | 23 (14) | 0.4 |
| M87SUB CEN | 130 (94) | 54% (60%) | 63 (51) | 0.9 |
| M87SUB FEDGE | 131 (60) | 27% (30%) | 30 (16) | 0.8 |

**Notes.** Fibre configuration was modified between different exposures.

M87SUB2 fields) are caused by guide star proper motions which were not correctly accounted for in the FLAMES astrometry input file for the fibre allocation. We were also able to estimate the fraction of fibre-object misalignments, from the repeat observations of the emission objects in common between adjacent FLAMES plate configurations. From this we determine the *spectroscopic completeness* $\mathrm{C}_{\rm spec,fb}$. The success rates are affected by the spectroscopic completeness as well as by the presence of stars in the catalogue of candidates to which the fibres are allocated. In Table 3.2 we report the total number of allocated fibres together with the nominal success rate, the number of spectroscopically confirmed PNs, and the spectroscopic completeness $\mathrm{C}_{\rm spec,fb}$ for all of the FLAMES fields.

Because success rates are also dependent on the absence of stars in the submitted catalogue, candidates from the more stringent *automatic sample* have higher success rates than candidates from the *visual catalogue*, reaching $> 70\%$ in M87SUB1 BrightF03 and M87SUB2 BrightF01 (see Table 3.2). On the other hand, about 30% of the confirmed spectra come from targets in the *visual catalogue*: this is consistent with the results of the simulations by Longobardi et al. (2013) for the fraction of missed true line emission sources with automatic selection criteria.

### 3.2.4 Classification of the extracted spectra

The colour selection criteria are based on the strong [OIII] $\lambda$5007Å emission of a PN, with faint or no continuum. Nonetheless, background galaxies like Ly$\alpha$ emitters at $z \sim 3.1$ and [OII] $\lambda$3727.26Å emitters at $z \sim 0.34$ have relatively strong lines that fall within the bandpass of the narrow-band filter. Thus, the extracted spectra were classified on the basis of the shape of the

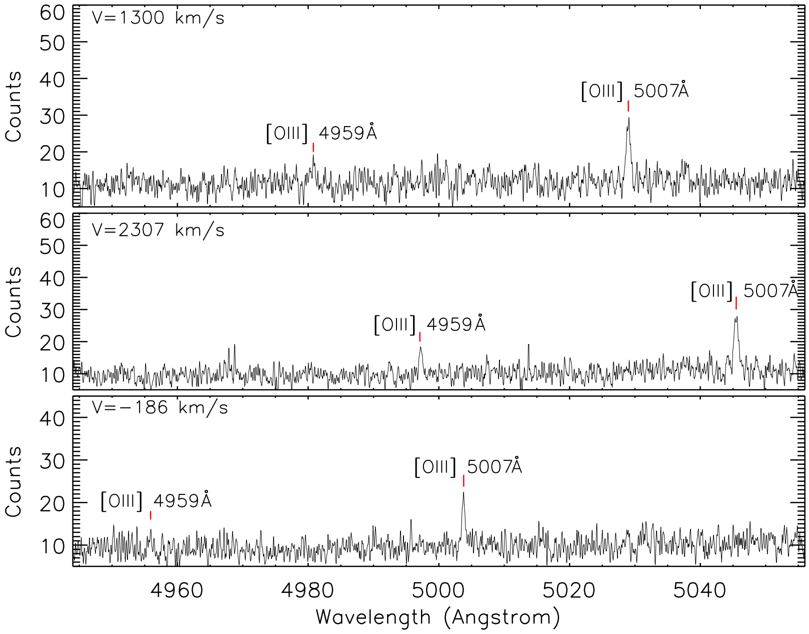

Figure 3.2: Spectra of single confirmed PNs. The top panel shows the spectrum for a PN dynamically bound to the halo component. The middle and bottom panels show spectra for PNs dynamically unbound to the halo (see Sect.5.3), with higher (middle panel) and lower (bottom panel) velocity than the M87 systemic velocity. Red vertical lines mark the positions of the two oxygen lines at their red-shifted wavelengths. Spectra have been smoothed to 0.015 nm per pixel.

line profile of the strongest emission. The extracted spectra fall into these categories:

- PN spectra: the [OIII]$\lambda$5007Å emission of a PN is characterised by a narrow and symmetric line shape and very low continuum. In high S/N spectra, we detected the redshifted [OIII] $\lambda$4959/5007Å doublet. Typical S/N ratios for the spectroscopically confirmed PN [OIII]]$\lambda$5007Å cover a range of $2.5 \leq S/N \leq 8.5$ per resolution element. In Fig. 3.2 we show examples of single PN spectra with different $V_{\rm LOS}$.

- Ly$\alpha$ spectra: the emission line of a Ly$\alpha$ emitter has a broader and more asymmetric line profile, characterised by a steep drop-off at bluer wavelengths. Such a signature comes from the forest absorption bluewards of Ly$\alpha$: the symmetric emission line is truncated below the object redshift by Ly$\alpha$ scattering in the intergalactic medium. Fig. 3.3 shows an example of an extracted FLAMES spectrum for a Ly$\alpha$ emitter.

- [OII] spectra: the [OII]$\lambda$3727Å emitters are characterised by the redshifted, resolved and broad emission lines of the oxygen doublet at $\lambda$3726-3729Å. Fig. 3.3 shows an example of an extracted FLAMES spectrum for an [OII] line emitting galaxy.

The final sample of emission line objects consists of 380 sources, of which 287 were classified as PNs and the remaining as background emission line galaxies, either as Ly$\alpha$ or as [OII]

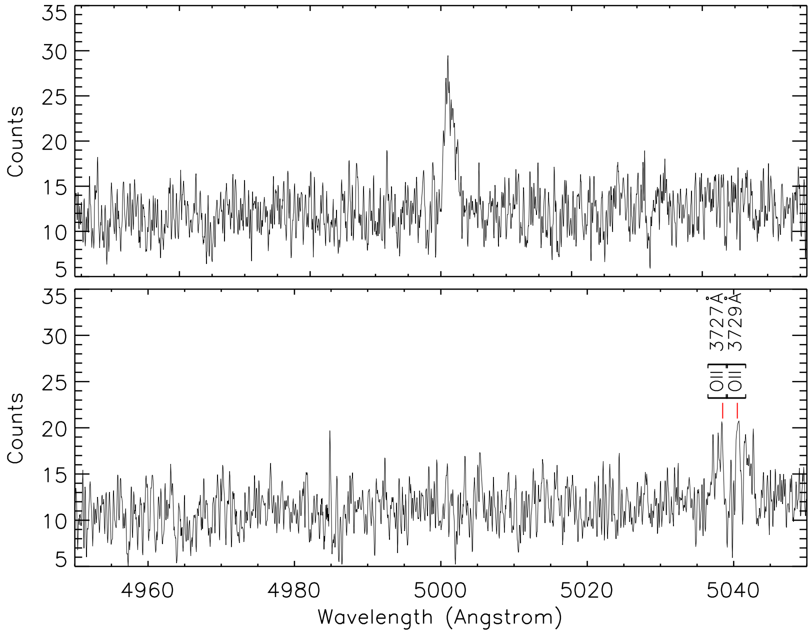

Figure 3.3: Spectra for background emission line galaxies: Ly$\alpha$ emitter at $z \sim 3.1$ (top panel) and [OII] emitter at $z \sim 0.34$ (bottom panel). Red vertical lines mark the positions of the two components of the $\lambda$3726+3729Å emission. Spectra have been smoothed to 0.015 nm per pixel.

emitters. This is the largest sample of spectroscopically confirmed PNs around M87 thus far, about a factor 15 larger than the sample of Doherty et al. (2009).

The fraction of background emitters is consistent within one $\sigma$ with the estimate in the photometric study of Longobardi et al. (2013). They estimated that ∼ 25% of the total imaging sample would be background emission galaxies. Here we find that the same fraction of the *automatic catalogue* is in fact L$\alpha$ or [OII] emitters.

### 3.2.5 Accuracy of the velocity measurements

From the repeat observations of the same candidates in areas where different FLAMES plate configurations overlap (see Fig. 3.1) we obtained independent velocity measurements for a subsample of PNs. The median deviation of these measurements is 4.2 $\mathrm{kms}^{-1}$, and the whole distribution covers a range of $0.6 \leq \Delta V_{\mathrm{LOS}} \leq 16.2\ \mathrm{kms}^{-1}$. The largest errors occur when a cosmic ray falls near the wavelength of the [OIII]$\lambda$5007Å emission in one of the exposures.

## 3.3 Halo and IC PN components

When studying the outer regions of M87 out to a distance of ∼ 150 kpc from the galaxy centre, we are tracing the light in the radial range where the M87 halo blends into the ICL. Arnaboldi et al. (2004) showed that the M87 stellar halo and the Virgo core ICL coexist for distances > 60 kpc from the galaxy centre, and Doherty et al. (2009) showed that the two components overlap out

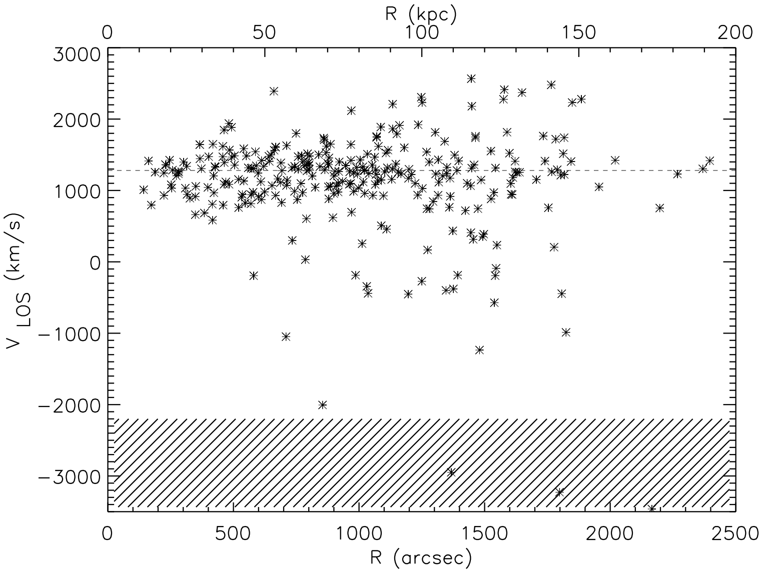

Figure 3.4: Projected phase-space diagram showing $V_{LOS}$ vs. major axis distance $R$ from the centre of M87, for all spectroscopically confirmed PNs (black asterisks). The major axis distance is given both in arcsec (bottom axis), and in kpc (top axis), where 73 pc = 1″. The dotted horizontal line shows M87's systemic velocity $V_{sys}$ = 1275 $kms^{-1}$ from Sect.3.3.2. The shaded area represents the region of the projected phase-space where the blue-shifted [OIII] 4959Å emission line would fall below the wavelength of the blue edge of the FLAMES sort ordering filter HR08.

to 150 kpc. Longobardi et al. (2013) showed that the observed slope of the PN number density profile is consistent with the superposition of two PN populations associated with the M87 halo and ICL, respectively.

In the following subsections, we show that the distribution of LOS velocities obtained from the FLAMES spectra shows evidence for two dynamically distinct PN populations at large radii, confirming this interpretation.

## 3.3.1 Projected PN phase-space diagram

For each confirmed PN spectrum, we measured $V_{LOS}$ and computed the major axis distance via the formula $R^2 = {x_{PN}}^2/(1-e)^2 + y_{PN}^2$, where e is the isophote's ellipticity from Kormendy et al. (2009) and $x_{PN}, y_{PN}$ are the PN coordinates measured in a reference frame centered on M87, where the y axis is aligned with the major axis of the outer elliptical isophotes at P.A. = −25.6 (Kormendy et al. 2009). In Fig. 3.4, we show the projected phase-space diagram $V_{LOS,PN}$ vs. $R$ for the spectroscopically confirmed PNs in the M87 survey (black asterisks).

In this projected phase-space, PN velocities show a concentration around the systemic velocity of M87 ($V_{sys}$ = 1275 $kms^{-1}$; see Sect. 3.3.2), in addition to a scattered distribution at higher and lower velocities. In Fig. 3.5, we show the histogram of the velocities for the entire sample. It has two very strong and quite asymmetric wings around the main peak. The wing (or tail) at low velocities is more extended than the tail at high velocities with respect to the peak.

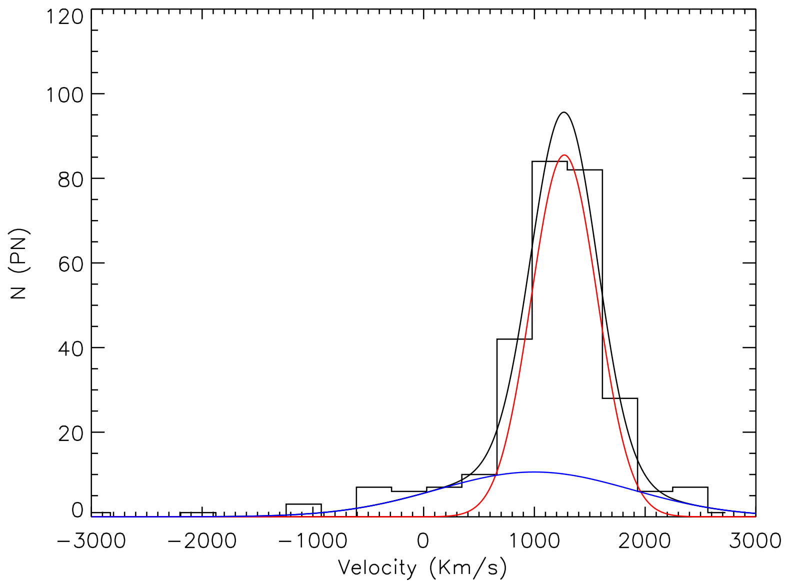

Figure 3.5: Histogram of the line-of-sight velocities of the spectroscopically confirmed PNs (black histogram) fitted with a double Gaussian (black curve). Red and blue lines represent the two Gaussians associated with the M87 halo and the IC components.

These extended tails are very different from those measured in the LOS velocity distributions (LOSVDs) of isolated early-type galaxies, which are well described by single Gaussian distributions to within ∼ 1% (e.g., Gerhard 1993; Bender et al. 1994). The total velocity distribution is well fitted by a double Gaussian, while a single Gaussian is a poor fit to the observed LOSVD. The reduced $\chi^2$ of a double Gaussian fit is 1.1, while for a single Gaussian it is 2.0. Therefore, we fit the LOSVD in Fig. 5 with the sum of two Gaussians. The fit to the data returns a narrow component centred on $V_{\mathrm{LOS,n}} = 1270.4$ kms$^{-1}$ with velocity dispersion of $\sigma_{\mathrm{n}} = 298.4$ kms$^{-1}$, and a broad component, centred on $V_{\mathrm{LOS,b}} = 999.5$ kms$^{-1}$ with a larger velocity dispersion $\sigma_{\mathrm{b}} = 881.0$ kms$^{-1}$.

The broad component is shifted from the M87 systemic LOS velocity: both $V_{\mathrm{LOS,b}}$ and $\sigma_{\mathrm{b}}$ are consistent with those values determined for the LOSVD of galaxies in the main sub-cluster region *A* of the Virgo cluster (Binggeli et al. 1993; Conselice et al. 2001). The LOSVD around M87 is thus bimodal, containing a narrow component associated with the systemic velocity of the galaxy plus a broader component associated with the ICL.

Different LOSVDs for the halo and ICL are predicted by cosmological analysis of structure formation. Using hydrodynamical cosmological simulations, Dolag et al. (2010); Cui et al. (2014) study the LOSVD of star particles at the centre of their clusters. These authors find that this LOSVD is well-described by the sum of two Gaussians, with similar average velocities but different $\sigma$. One component is gravitationally bound to the galaxy and more spatially concentrated; the other is more diffuse and its high velocity dispersion reflects the satellites' orbital distribution in the cluster gravitational potential. It is plausible that the halo stars are spatially confined as a consequence of merging processes that led to the formation of the BCG (Murante et al. 2007; Contini et al. 2014).

### 3.3.2 Robust separation of the M87 halo and ICL

We have seen that the overall LOSVD of the PNs in M87 is characterised by a narrow component associated with the M87 halo, superposed on a broad IC component with a shifted mean velocity and much larger velocity width. We are now interested in separating halo and IC PNs based on their different LOSVDs. In this analysis we combine our PN sample with that of Doherty et al. (2009). We concentrate on those PNs that have a major axis distance $R \leq 190$ kpc, to study the transition between the M87 halo and the Virgo ICL. The combined total sample consists of 299 PNs with measured positions and velocities within $R \leq 190$ kpc; the PNs from Doherty et al. (2009) further out are classified as ICPNs and will not be discussed further.

In order to separate halo and IC components we use a sigma clipping algorithm in elliptical radial bins, corresponding to vertical strips in the projected phase-space diagram in Fig. 3.6. The idea is to separate the velocities in the narrower Gaussian (see Fig. 3.5) from those in the high and low velocity wings of the distribution. By tagging our sources depending on whether their $V_{LOS}$ belongs to the narrower or wider Gaussian, we assign PNs to either the M87 halo or the ICL.

*The velocity dispersion profile of the M87 halo: a robust sigma estimate*– We binned the PN velocity sample in elliptical annuli and, for each bin, we determined the standard deviation of the LOSVD for the PNs in this bin. A $2\sigma$ limit with respect to the systemic velocity of M87, $V_{sys} = 1275 \pm 24$ kms$^{-1}$, is applied[6] and the dispersion is calculated for all PNs with $|V_{LOS}\text{-}V_{sys}| < 2\sigma$ kms$^{-1}$. This dispersion is then scaled by a numerical factor determined from Monte Carlo simulation to correct to the dispersion of a complete Gaussian distribution (see McNeil et al. (2010)). Since we expect the initial estimate for the $2\sigma$ to be influenced by the ICPNs, we repeat this process until the dispersion value stabilises.

*Separating M87 halo and IC PNs: sigma clipping* – We now identify the two components using a sigma clipping algorithm. We begin by classifying as ICPNs all velocity outliers that deviate from the M87 systemic velocity $V_{sys} = 1275$ kms$^{-1}$ by more than $2\sigma$. To obtain the required $\sigma$ value at the radius of each PN, we took the robust estimates of the velocity dispersions in the elliptical radial bins, and fitted these data with a fourth-order polynomial. This takes into account radial gradients and at the same time reduces the effects of binning and scatter in the dispersion profile on the separation of the components. Using the $2\sigma$ threshold from the interpolated polynomial, we identify 243 objects as M87 halo PNs.

Two further steps are still needed. The $2\sigma$ criterion accounts for $\sim$ 95.5% of a complete Gaussian distribution; hence we expect it to have missed 11 halo PN candidates. To include these, we considered all outliers within $3\sigma$ from the M87 $V_{sys}$ and from those selected the 11 with the smallest $|V_{LOS}\text{-}V_{sys}|/\sigma$ ratios. This leads to a final sample of 254 M87 halo PNs and 45

---

[6] The systemic velocity of M87 is taken as the median value of the entire sample of velocities within two sigma of the original median. Our value $1275 \pm 24$ kms$^{-1}$ is consistent with those obtained by Binggeli et al. (1987) ($V_{sys} = 1258 \pm 10$kms$^{-1}$) , and Cappellari et al. (2011) ($V_{sys} = 1284 \pm 5$kms$^{-1}$).

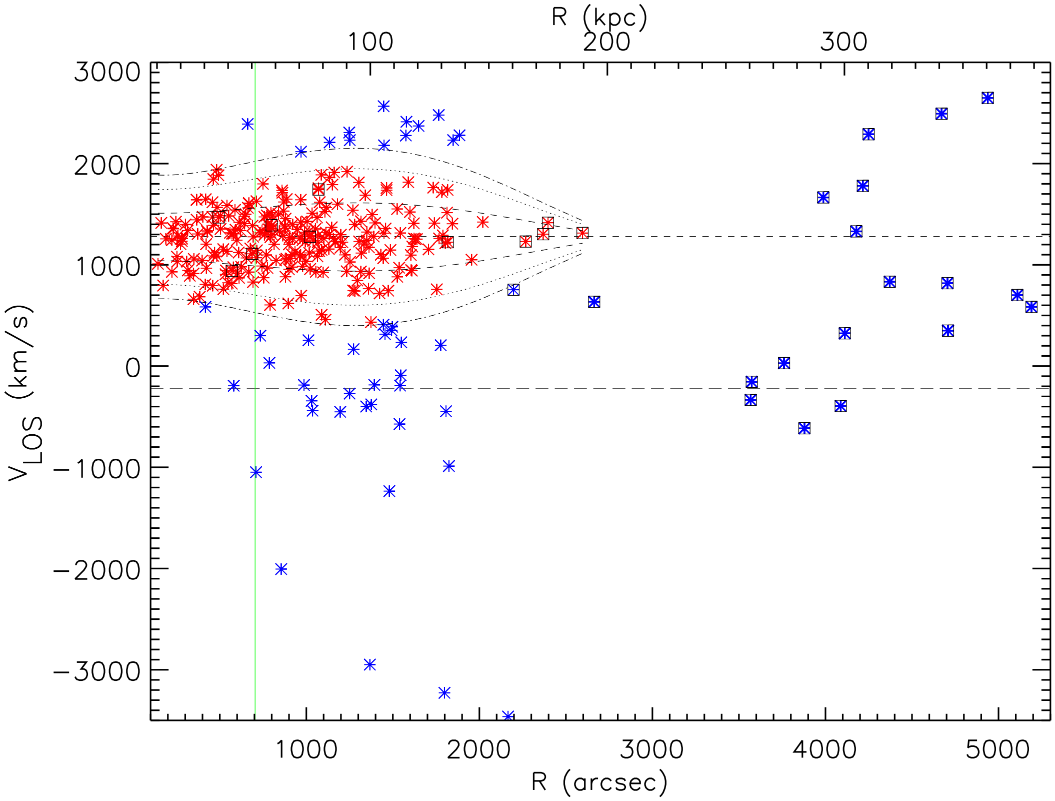

Figure 3.6: Projected phase-space diagram, $V_{LOS}$ vs. major axis distance from the centre of M87, for all spectroscopically confirmed PNs from this work and Doherty et al. (2009).The major axis distance is given both in arcsec (bottom axis), and in kpc (top axis), where 73 pc = 1″. The PNs are classified as M87 halo PNs (red asterisks) and ICPNs (blue asterisks), respectively; see text. Black squares identify spectroscopically confirmed PNs from Doherty et al. (2009). The smoothed 1,2 and 2.5 $\sigma$ thresholds are represented by the dashed, dotted and dot-dashed lines, respectively. The dashed horizontal line shows the M87 systemic velocity $V_{sys}$ = 1275 $kms^{-1}$ as computed in Section 3.3.2, while the continuos green line shows the effective radius $R_e = 703.914''$ determined by Kormendy et al. (2009). At $V_{LOS} = -220\,kms^{-1}$ we plot the M86 systemic velocity (long dashed line).

ICPNs. In this final sample, 11 halo PNs and 1 ICPN came from Doherty et al. (2009).

Secondly, as can be seen in Fig. 3.5 the ICL and halo velocity distributions overlap, and as result, when using the sigma-clipping algorithm, the ICPNs at low velocities relative to $V_{sys} \sim 1275\,\mathrm{kms}^{-1}$ will be considered as part of the halo component. To statistically quantify this effect, we compared the halo and IC velocity distributions in each radial bin (or slice in the phase-space). We approximated the halo distribution in the bin as a Gaussian centred on the systemic velocity of M87 with a dispersion equal to the average value for that bin, and for the IC component we used the same Gaussian in all radial bins using the parameters as in Fig. 3.5. We then calculated the fraction of ICPNs that lie inside the halo distribution as the area of overlap between the two curves. With this analysis we obtain a statistical estimate of the number of ICPNs contained in the halo velocity distribution in each bin. For all bins combined we find that a further ~17% of the halo sample, i.e., ~ 44 PNs, are to be associated with the IC component.

In Fig. 3.6, we show the projected phase-space distribution of our PNs as in Fig.3.4, with velocities colour-coded to show the membership to the halo (red) and ICL (blue). Since we only know statistically but not individually which PNs in the halo velocity range are ICPNs, these are also shown with the red halo colour.

In Fig. 3.6 we also show $1/2/2.5\sigma$ limit contours for the halo PNs, obtained by fitting a polynomial to the $\sigma$ values from the robust estimation. The velocity dispersion profile increases from $250''$ to $1200''$, and then decreases, showing a colder component at radii $R > 1200''$. A more detailed analysis of the dispersion profile will be carried in a separate paper (Longobardi et al., in preparation).

We now enquire whether any ICPNs could be associated with other galaxies in the cluster. The first to consider is M86, because it is bright, has the most extended halo, and is relatively close to M87 (~ 1.2° away). Extrapolating the Sersic fit from Janowiecki et al. (2010) we compute the total luminosity associated with the M86 halo in our surveyed area to be $L_{V,bol} \sim 8.0 \times 10^{8} L_{\odot,bol}$. We adopt a similar PN specific number as for M87, $\alpha_{2.5} = 1.01 \times 10^{-8} \mathrm{PN}/L_{\odot,bol}$ (see Sect.3.5.1), but correct for the fact that we can only sample the brightest 2.3 mag of the PNLF because of the larger distance to M86 (Mei et al. 2007). This leads to a predicted number of 7 M86 PNs that could be counted as IC component, i.e., only ~ 2.5% of the completeness-corrected ICPN sample (see Sect.3.5.1), or 2 out of a total of 88 ICPNs.

Other fainter galaxies have less extended halos and contribute less to the sampled ICPNs around M87 unless they are very near or in the survey area. Moreover, from the shape of the ICPNLF (see Sect.3.5.2) the majority of ICPNs is likely to have been stripped from low luminosity star forming galaxies such as M33 and the LMC. ICPNs still bound to dwarf galaxies would be correlated with their position and velocity. Only 3 PNs with velocity V~350 km/s out of the ICPN sample seem correlated with the position and systemic velocity of a dwarf galaxy, IC3549, which has $V_{LOS} = 375\,\mathrm{kms}^{-1}$ (Adelman-McCarthy & et al. 2009). Hence we can state that the contribution from other nearby galaxies to the ICPN sample is negligibile and does not affect any of the results presented in this work.

Finally, we comment that a few ICPNs are characterised by extraordinary blue shifts relative to M87 ($V_{LOS} < -1000\,\mathrm{kms}^{-1}$). Such (hyper-) velocities of $|V_{LOS}\text{-}V_{sys}| > 2300\,\mathrm{kms}^{-1}$ relative to M87, corresponding to several $\sigma_{Virgo}$, could be due to infall from the outskirts of the Virgo cluster, perhaps associated with the infall of the M86 group, or they could be tracers of three-body interactions, as previously hypothesised for the extreme globular cluster observed at a projected distance of $\sim$ 80 kpc from M87 with a velocity of $V_{\mathrm{LOS}} < -1025$ $\mathrm{kms}^{-1}$ (Caldwell et al. 2014).

### 3.3.3 Spectroscopic validation of the PN subsample

In Section 3.2.4 we classified 287 spectra as PNs on the basis of the line profile of the strongest emission. We will now strengthen this earlier classification based on the detection of the weaker 4959Å line of the [OIII] doublet in the PN spectra.

In 114 out of the 287 spectra, nearly 40% of the sample, we are able to detect the Doppler-shifted [OIII]$\lambda$4959Å line with the expected 1:3 ratio of the [OIII]$\lambda$4959/5007Å line fluxes. In the rest of the sample, the single spectra do not have the required S/N ($S/N > 3$) for the main [OIII]$\lambda$5007 Å emission line to allow the detection of the weaker 4959Å line. However, following Arnaboldi et al. (2003) we can achieve the required S/N by stacking these spectra, after shifting their [OIII]$\lambda$5007Å emission to a common reference wavelength. By measuring the [OIII]$\lambda$5007/4959Å line ratio of the coadded spectrum we can statistically constrain the fraction of misclassified PN spectra: if the stacked spectrum contains misclassified PN candidates, the ratio [OIII] $\lambda$5007/4959Å will be larger than 3.

The 287 spectra are further grouped in three classes: M87 halo spectra, IC high-velocity and IC low-velocity spectra. We have respectively 254, 13, and 31 PN in each category. Three sources in the IC low-velocity class are not included, because their Doppler shifted [OIII]$\lambda$4959Å emission would fall at a shorter wavelength than the blue edge of the FLAMES HR08 filter (see Fig. 3.4). The spectra are shifted so that the main [OIII]$\lambda$5007Å emission falls at the same nominal wavelength for all spectra of a given class. For the halo and IC high-velocity class, we adopt the nominal wavelength of 5029Å for [OIII]$\lambda$5007Å, i.e. the redshifted wavelength at the systemic velocity of M87. For the IC low-velocity class, the adopted nominal wavelength is 5000Å. We shifted the single spectra for each class, and obtained three coadded spectra. These are plotted in Fig. 3.7. The [OIII] doublet is visible in all spectra, with the [OIII]$\lambda$4959Å line visible at the correspondent shifted wavelength. In all three spectra, the FWHM of [OIII]$\lambda$5007Å is FWHM=0.6Å (Table 3.3), somewhat smaller than the typical FWHM of single spectra, FWHM=0.8 Å. Because of filter edge effects, together with the shifting and alignment of the spectra with reference to the stronger line, the weaker [OIII]$\lambda$4959Å emission is broader in the IC low-velocity spectrum than in the single PN spectra.

The fluxes and FWHMs of the [OIII]$\lambda$4959/5007Å emissions in the coadded spectra are measured via a Gaussian fit to the lines with the IRAF task *splot*. The errors on the line fluxes were calculated using the relation (Pérez-Montero & Díaz 2003):

$$\sigma_1 = \sigma_c N^{1/2}[1 + EW/(N\Delta)]^{1/2}, \tag{3.1}$$

where $\sigma_1$ is the error in the line flux, $\sigma_c$ is the standard deviation in a box near the measured line and represents the error in the definition of the continuum, $N$ is the number of pixels used to measure the line flux, $EW$ is the equivalent width of the line, and $\Delta$ is the wavelength dispersion in Å $\mathrm{pixel}^{-1}$. In Table 3.3 we give a summary of the observed properties of the [OIII] doublet of the coadded spectra.

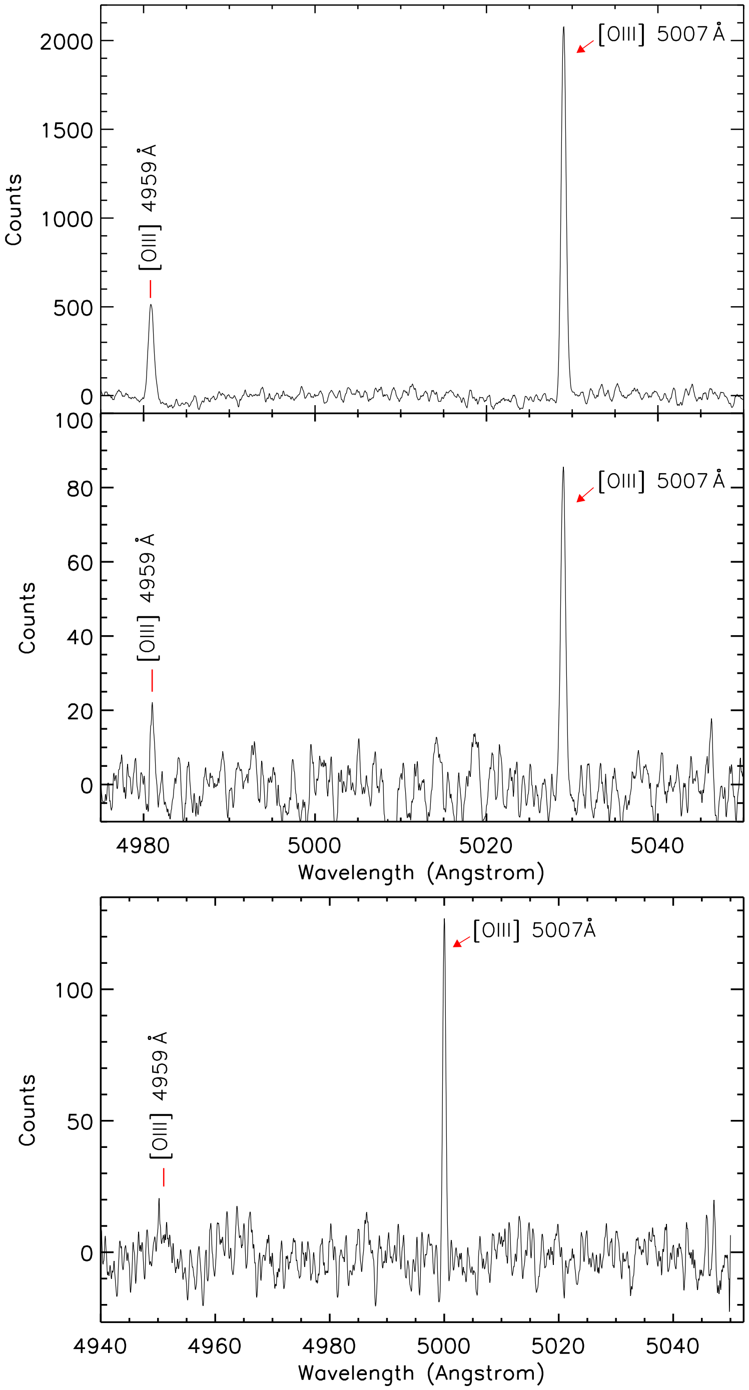

Figure 3.7: Combined spectra for the spectroscopically confirmed subsamples of PNs belonging to the halo (upper panel), IC high-velocity (central panel) and IC low-velocity (bottom panel) classes. As expected from atomic physics, the [OIII]$\lambda$4959/5007Å doublet is detected with a flux ratio 1:3 confirming that the large majority of our candidates are true PNs (see text for more details).

Table 3.3: Fluxes, FWHMs and line ratios of the [OIII] $\lambda$5007/4959Å doublet for halo, high-velocity and low-velocity IC PNs sub samples.

| IDs PN subsample | Line Flux$_{5007}$ ( Counts ) (1) | Line Flux$_{4959}$ ( Counts ) (2) | FWHM$_{5007}$ ( Å ) (3) | FWHM$_{4959}$ ( Å ) (4) | Line Ratio (5) |
|---|---|---|---|---|---|
| halo | 1528.0±0.2 | 506.9±0.3 | 0.60±0.08 | 0.76±0.1 | 3.01±0.02 |
| IC high-velocity | 64.1±3.0 | 20.6±1.2 | 0.60±0.07 | 0.6±0.09 | 3.1±0.2 |
| IC low-velocity | 106.3±3.0 | 33.9±3.7 | 0.60±0.08 | 1.4±0.1 | 3.1±0.3 |

**Notes.** Columns (1) and (2): fluxes for the [OIII] main and second emission line, respectively. Errors are calculated following Eq.3.1.

Columns (3) and (4): emission line FWHMs from Gaussian fitting of the spectral lines. Errors represent $1\sigma$ uncertainties from sampling statistics.

Column(5): flux ratio between the [OIII] doublet emission lines. Errors are propagated from the flux errors.

The [OIII] doublet is visible in the three spectra from the different classes, with approximate flux ratio of 3:1, as expected from atomic physics. Given the uncertainties on the measured fluxes, the spectral validation shows that at $1\sigma > 99\%$ of the halo and $> 90\%$ of the IC high-velocity spectra are true PNs. This implies that only 2 and 1 PNs of the halo and high-velocity ICPNs could be misclassified. For the IC low-velocity PNs the line ratio of the [OIII]5007/4959 Å is 3.1 ± 0.3 from Table 3.3. Hence up to 13% of the spectra could be misclassified, i.e. 4 ICPNs. On the total sample of 287 spectroscopically confirmed PNs, at most 7 candidates might have been misclassified, i.e. only 2% of the whole sample.

## 3.4 Halo and IC density profiles

By tagging PNs according to their $V_{LOS}$, we differentiated between halo and IC PNs in the last section. We are now interested in recovering the spatial distribution of these two components and in studying their number density profiles separately.

In Fig. 3.8 we show the sky positions of the spectroscopically confirmed halo and IC PNs. If the halo and ICL are characterised by different evolutionary histories, their radial distributions may be different. If so, this can be seen in the PN density profile. Because PNs follow light, the presence of a single parent stellar population would be reflected in a PN number density distribution proportional to the surface brightness profile at each radius. Deviations of the PN number density from the light profile would trace the presence of more than one stellar population in the surveyed region (Longobardi et al. 2013).

### 3.4.1 Completeness corrections

To construct a PN density profile we require a spatially complete sample hence we must correct the detected PN number using a completeness function, $C_{tot}(x_{PN}, y_{PN})$, which accounts for the

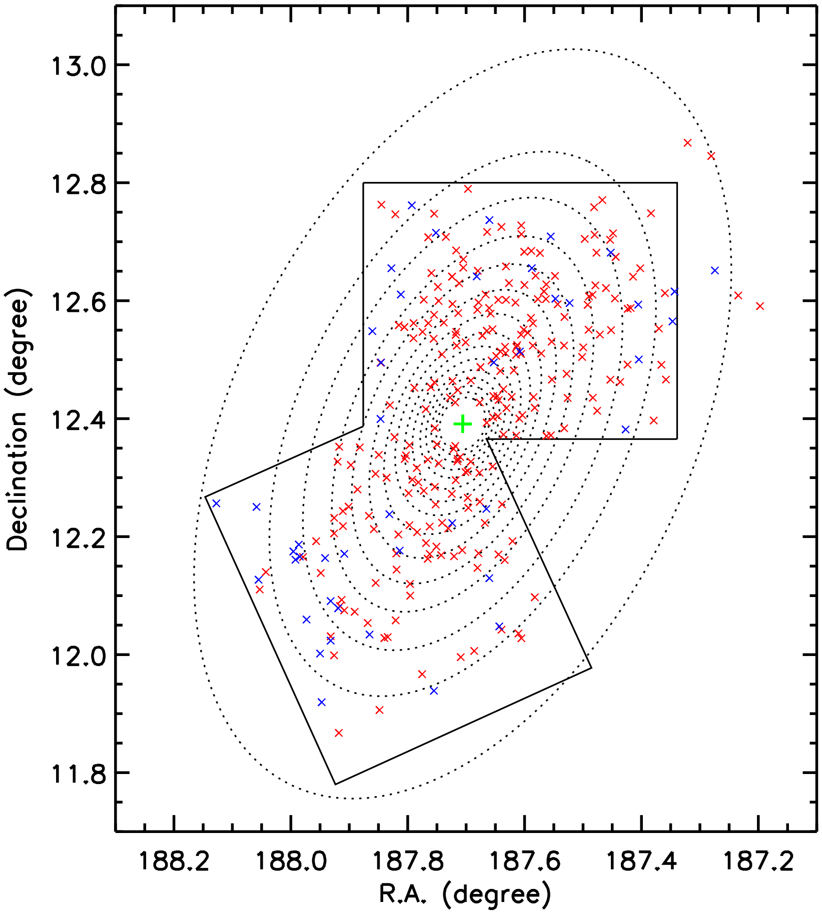

Figure 3.8: Sky positions of the spectroscopically confirmed halo (red crosses) and IC PNs (blue crosses). The green plus sign indicates the centre of M87. The ellipses *(dotted lines)* trace the M87 isophotes between photometric major axis radii $R = 2.'8$ and $R = 40.'7$, for position angle P.A.=-25.6°, from Kormendy et al. (2009). The solid squares depict the area covered by our narrow band imaging survey (Longobardi et al. 2013). North is up, East to the left.

selection function of the sampled PNs over the surveyed area. Our PN sample is affected by four different kinds of incompleteness, that are related to the photometric identification of the candidates and the selection effects in the spectroscopic observations. These are:

**Photometric incompleteness**, characterised by:

i) $C_{\rm phot,sp}(R)$ - Spatial incompleteness due to the high galaxy background and foreground stars that affect the detection of PN candidates in the images. This was estimated in Longobardi et al. (2013) by adding a simulated PN population to the scientific images and determining the fraction of simulated objects recovered by SExtractor in the different elliptical annuli shown in Fig. 3.8.

ii) $C_{\rm phot,col}$ - Colour incompleteness due to the colour criteria adopted for the automatic selection of PN candidates. This colour incompleteness was computed by analysing the properties of the recovered simulated PN population in the colour-magnitude diagram (see Longobardi et al. 2013, for more detail). This incompleteness affects only the M87SUB FCEN and M87SUB FEDGE fields, where the photometric candidates were selected through colour criteria (see Sect. 5.2). $C_{\rm phot,col}$ is magnitude-dependent but for constructing the density profile we use an average value, computed for the whole sample down to 2.5 magnitudes below the bright cutoff, which amounts to 0.7.

**Spectroscopic incompleteness**, characterised by:

iii) $C_{\rm spec,sp}(R)$ - Spatial incompleteness due to the limited number of fibres (up to 132) that can be allocated for each FLAMES field. This was estimated by computing the ratio between the number of allocated fibres and the total number of photometric candidates in each elliptical annulus shown in Fig. 3.8.

iv) $C_{\rm spec,fb}(x_{\rm PN}, y_{\rm PN})$ - Incompleteness due to fiber-target misalignment. This incompleteness was estimated from the detection statistics of objects in common between overlapping FLAMES plate configurations, whose [OIII] emission was detected in spectra taken with both or only one of the two plate configurations (see Sect. 3.2.3).

Our spectra are sufficiently deep that we found no dependence of the spectroscopic incompleteness on the magnitude of the PN candidates.

The total completeness function, $C_{\rm tot}(x_{\rm PN}, y_{\rm PN})$, is the product of the photometric and spectroscopic incompleteness:

$$\begin{aligned} C_{\rm tot}(x_{\rm PN}, y_{\rm PN}) &= C_{\rm phot,sp}(R) * C_{\rm phot,col} \\ &* C_{\rm spec,sp}(R) * C_{\rm spec,fb}(x_{\rm PN}, y_{\rm PN}), \end{aligned} \tag{3.2}$$

with

$$C_{\rm phot,col} = \begin{cases} C_{\rm phot,col} & \text{for M87SUB FCEN, M87SUB FEDGE,} \\ 1 & \text{elsewhere.} \end{cases}$$

The completeness-corrected number of PNs in each bin of major axis distance $R$ is then

$$\mathrm{N_c(R)} = \Sigma_i^{N_{\mathrm{obs}}} k_i(R), \tag{3.3}$$

where the sum extends over all PNs of the halo or IC component in the bin, respectively, and $k_i(R) = 1/\mathrm{C_{tot}}(\mathrm{x_{PN_i}}, \mathrm{y_{PN_i}})$ is the completeness-corrected specific weight of each observed PN at its position.

### 3.4.2 Density profiles of halo and IC component

In order to construct the PN number density profile and compare it to the galaxy's surface brightness profile, we bin our PN sample in elliptical annuli. The radial range of the elliptical annuli is chosen such that they include the major axis distance of the innermost and outermost PN candidates in the photometric sample of Longobardi et al. (2013). Their P.A.s and ellipticities are taken from Kormendy et al. (2009). The sizes of the annuli are determined separately for the halo and IC components, such that for each component all bins contain at least 10 spectroscopically confirmed PNs. In each annulus and for each component, we compute the completeness-corrected PN number density as the ratio of the completeness-corrected number of PN (Eq. 3.3) and the area of the portion of the annulus intersecting our FOV[7],

$$\sigma_{\mathrm{PN}_j}(R) = \frac{\mathrm{N}_{\mathrm{c},j}(R)}{A(R)}. \tag{3.4}$$

Here we consider all the spectroscopically confirmed PNs whose magnitudes are within 2.5 mag below the bright cut-off. The subscript $j$ indicates the two different PN components, halo and ICL. The major axis distances $R$ in Eq. 3.4 are determined by computing the average major axis distance of all PNs falling within each elliptical annulus.

In Fig. 3.9 we show the comparison between the V-band M87 surface brightness profile $\mu_{\mathrm{K09}}$ from Kormendy et al. (2009), with the logarithmic PN density profiles for the halo (red triangles) and IC (blue diamonds) PNs, defined as:

$$\mu_{\mathrm{PN_j}}(R) = -2.5\log_{10}\left(\sigma_{\mathrm{PN_j}}(R)\right) + \mu_0. \tag{3.5}$$

The value $\mu_0$ is a constant to be added so that the PN number density profile matches the $\mu_{\mathrm{K09}}$ surface brightness profile. As described in Sect. 3.3.2, the kinematic decomposition of the halo and IC components does not identify ICPNs in the velocity range of the halo, and their contribution must be evaluated statistically for each bin. Averaged over the bins, ~10% of the halo PN sample is thus estimated to be associated with the ICL, in addition to the ICPNs identified from their large velocities. For each of the radial bins, we subtract the estimated contribution from the halo component and add it to the IC component. In Fig. 3.9, the PN number densities for halo and ICL account for this effect. Furthermore, the profiles shown in Fig. 3.9 are computed using all PNs whose magnitudes are within 2.5 magnitude from the bright cutoff. However, the halo

---

[7] These areas are estimated using Monte Carlo integration.

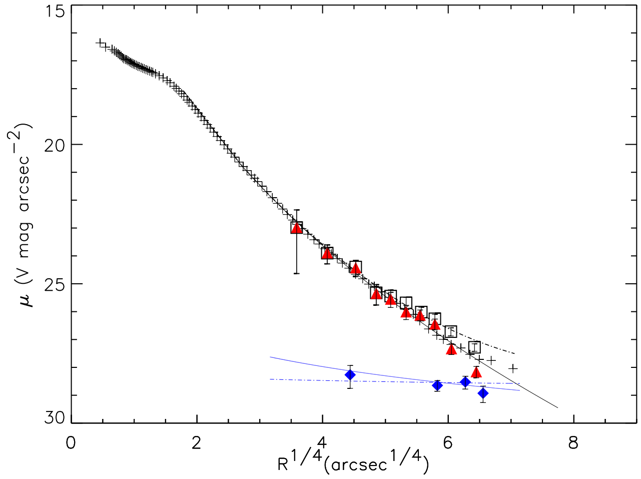

Figure 3.9: Logarithmic PN number density profiles for the M87 halo (red triangles) and the IC PNs (blue diamonds), corrected for incompleteness. The error bars include counting statistics and completeness correction. The halo PN profile compares well with the surface brightness profile from Kormendy et al. (2009, (plus signs)). The continuous black line shows their Sersic fit with $n = 11.8$. The ICPN number density decreases towards larger radii as $I_{ICL} \propto R^{\gamma}$ with $\gamma$ in the range $[-0.34; -0.04]$ (full and dashed-dotted blue lines). Black squares show the combined halo and IC PN number density profile which is well modelled by the two-component photometric model (dot-dashed black line, see Section 4.5).

and IC number density profiles do not change significantly when the fainter spectroscopically confirmed PN are also included.

We find that the $\mu_{PN_{halo}}$ agrees well with the surface photometry: the halo PN logarithmic number density profile follows the surface brightness profile. The ICPN logarithmic number density has a flatter profile, also concentrated towards M87; it decreases towards larger radii as $I_{ICL} \propto R^{\gamma}$ with $\gamma$ in the range $[-0.34; -0.04]$, depending on the choice of binning. These results are consistent with predictions from hydro-dynamical simulations, where the radial density profile of the bound component, i.e. the halo, is observed to be much steeper than that of the diffuse IC component (Murante et al. 2004; Dolag et al. 2010).

Finally, we compute density profiles for the PNs for the NW and SE sides of M87 independently, to search for an NW-SE-asymmetry in the spatial distribution. For this test we now use the total sample of PNs including very faint PNs, in order to increase the statistics in each half annulus (this also changes the binning). Fig. 3.10 shows the four number density profiles; each pair of profiles are consistent with each other and the halo profiles are consistent with the galaxy surface brightness profile. Thus within the statistical uncertainties, the stellar halo density is NW-SE symmetric and the PN number density follows the light on both sides. The ICPN density profile pair are again flatter than the halo, and consistent with the previous surface brightness profile $I_{ICL} \propto R^{\gamma}$ with $\gamma = [-0.34; -0.04]$; no asymmetry is evident. In Fig. 3.10 we also plot the differences between the NW and SE logarithmic densities as function of radius (bottom panel). For both the halo (red filled circles) and the ICL (blue filled circles), these differences are

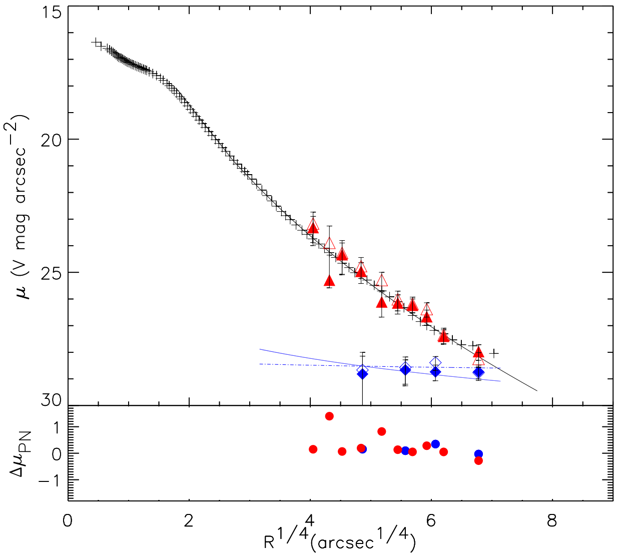

Figure 3.10: Top panel: Same as in Fig. 3.9, but here the halo and IC number density profiles are computed separately for the NW (filled symbols) and SE (open symbols) sides of M87. Bottom panel: Difference between the logarithmic PN number density profiles of the halo (red dots) and IC (blue dots) PNs in the NW and SE M87 regions: a value of zero indicates no difference in the number of sources on opposite sides at a given major axis distance.

consistent with zero within the uncertainties (see further discussion in Sect. 3.6).

## 3.5 Halo and IC populations

### 3.5.1 The $\alpha$ parameter

The total number of PNs, $N_{PN}$, is proportional to the total bolometric luminosity of the parent stellar population through the luminosity-specific PN density, or $\alpha$-parameter for short, such that $N_{PN} = \alpha L_{bol}$. The $\alpha$-parameter determined for this PN sample will be an estimate of the total number of PNs within 2.5 magnitudes of the bright cutoff of the PNLF, because of the magnitude limit of this survey at $m_{5007}$=28.8 and the bright cutoff at $m^{*}_{5007}$=26.3 (see Section 3.5.2). The measured value of $\alpha$ will be derived from the scaling factor required to match the PN number density profile to the surface brightness profile in the V band and then taking into account the appropriate bolometric correction.

In Fig. 3.9, we showed the total PN number density profile for the spectroscopically confirmed PNs sample within 2.5 magnitudes from the bright cutoff, together with the halo and IC PN number densities separately. The total PN number density profile flattens at large radii compared to the V-band surface brightness profile: as already shown in Longobardi et al. (2013) this effect is due to a superposition of stellar populations with different PN specific frequencies. The flattening for the spectroscopocally confirmed PN number density profile provides independent support for these results. Following Longobardi et al. (2013) we can model it by two components such that

$$\tilde{\sigma}(R) = [\alpha_{\rm halo}\mathrm{I}(R)_{\rm halo,bol} + \alpha_{\rm ICL}\mathrm{I}(R)_{\rm ICL,bol}] \tag{3.6}$$

$$= \alpha_{\rm halo}\left[\mathrm{I}(R)_{\rm K09,bol} + \left(\frac{\alpha_{\rm ICL}}{\alpha_{\rm halo}} - 1\right)\mathrm{I}(R)_{\rm ICL,bol}\right] \tag{3.7}$$

where $\tilde{\sigma}(R)$ represents the predicted total PN surface density in units of $\mathrm{N_{PN}pc^{-2}}$; $\mathrm{I}(R)_{\rm halo}$ and $\mathrm{I}(R)_{\rm ICL}$, with and without subscript bol, are the bolometric and V-band luminosities for the halo and the IC components respectively, in $L_{\odot}\mathrm{pc}^{-2}$; $\mathrm{I_{K09}}$ is the M87 luminosity profile in the V band in $L_{\odot}\mathrm{pc}^{-2}$, from Kormendy et al. (2009). $\mathrm{I}(R)_{\rm halo}$ and $\mathrm{I}(R)_{\rm ICL}$, respectively, are given by the Sersic fit to the observed M87 surface brightness data ($n = 11.8$, Kormendy et al. 2009), and by the scaled power-law fit to the IC surface density data from Sect. 5.4. They satisfy the relation $\mathrm{I_{K09}} = \mathrm{I}(R)_{\rm halo} + \mathrm{I}(R)_{\rm ICL}$ which determines the normalisation of the IC surface brightness profile. In the surveyed area over a radial range $7\mathrm{kpc} < R < 150\mathrm{kpc}$ these profiles give total V-band luminosities $L_{\rm halo} = 4.41 \times 10^{10} L_{\odot}$ and $L_{\rm ICL} = 0.53 \times 10^{10} L_{\odot}$, and after the bolometric correction (see below), total bolometric luminosities for the sampled halo and ICL of $L_{{\rm halo},bol} = 9.05 \times 10^{10} L_{\odot,\rm bol}$ and $L_{{\rm ICL},bol} = 1.1 \times 10^{10} L_{\odot,\rm bol}$.

The surface luminosity $\tilde{\sigma}(R)$ can be related to the bolometric surface brightness through the formula :

$$\tilde{\mu}(R) = -2.5\log_{10}\tilde{\sigma}(R) + \mu_0, \tag{3.8}$$

where $\mu_0$ is given by the analytical function:

$$\mu_0 = 2.5\log_{10}\alpha_{\rm halo} + \mathrm{K} + (\mathrm{BC}_{\odot} - \mathrm{BC_V}). \tag{3.9}$$

In Eq. 3.9, $\alpha_{\rm halo}$ is the specific PN number for the halo, $\mathrm{K} = 26.4$ mag arcsec$^{-2}$ is the V-band conversion factor from mag arcsec$^{-2}$ to physical units $L_{\odot}\mathrm{pc}^{-2}$, $BC_{\odot} = -0.07$ is the V-band bolometric correction for the Sun, and $BC_V$=-0.85 is the bolometric correction for the V-band (Buzzoni et al. 2006). According to their simple stellar population (SSP) models for irregular, late and early-type galaxies this value can be used with 10% accuracy.

From the offset value $\mu_0 = 16.56 \pm 0.08$ mag arcsec$^{-2}$ determined from the density profile in Fig. 3.9, we compute $\alpha_{\rm halo} = (1.06 \pm 0.12) \times 10^{-8}$ PN $\mathrm{L_{\odot,bol}^{-1}}$. From Eqs. 3.6 and 3.7, the derived value for $\alpha_{\rm ICL}$ is then $(2.72 \pm 0.72) \times 10^{-8}$ PN $\mathrm{L_{\odot,bol}^{-1}}$, using the steeper slope -0.34 for the ICL, but the difference for the shallower slope is only 5%. The difference in $\alpha$-parameters is then $\sim 2.3\sigma$.

These luminosity specific PN $\alpha$ values are consistent with those obtained by Longobardi et al. (2013) from the photometric sample, and are now independently validated on the basis of the spectroscopically confirmed PNs. Moreover, they also agree within the uncertainties with the preoviously determined values by Durrell et al. (2002); Doherty et al. (2009) (see Longobardi et al. 2013). The consistency of the spectroscopic and photometric values confirms the accuracy of the estimated contamination by Ly$\alpha$ background objects in the photometric sample.

We can now compare the $\alpha_{\rm halo}$ and $\alpha_{\rm ICL}$ values determined in this work with the known $\alpha$ values for PN populations in nearby galaxies. Galaxies with integrated $(B - V)$ colours smaller than 0.8 are empirically characterised by similar values of the $\alpha$ parameter, $\alpha \sim 3{\times}10^{-8}\mathrm{N_{PN}L_{\odot,bol}^{-1}}$, with a scatter of a factor of two. For redder galaxies with $(B-V) > 0.8$, the spread of the measured values increases, spanning a range from $\alpha \sim 10^{-9}\mathrm{N_{PN}/L_{\odot,bol}}$ to $\sim 6 \times 10^{-8}\mathrm{N_{PN}/L_{\odot,bol}}$. For these redder galaxies, there is an empirical inverse correlation of the $\alpha$ values with the $FUV - V$ integrated colours of the parent stellar population, such that smaller $\alpha$ values are associated with galaxies with larger FUV-V excess. Hence, observationally, the $\alpha$ values are linked to the metallicity and star formation history of the parent stellar population of the PNs (Peimbert 1990; Hui et al. 1993; Buzzoni et al. 2006; Longobardi et al. 2013).

Our result that the IC component contributes more PNs per unit bolometric luminosity than the M87 halo light therefore signals a change in the stellar populations from halo to ICL, consistent with the existence of a gradient towards bluer colours of the M87 stellar light at large radii (Liu et al. 2005; Rudick et al. 2010). We interpret this gradient as the result of the gradual transition from the redder halo light to the bluer ICL with decreasing surface brightness.

### 3.5.2 PNLFs for halo and ICL

The PNLF of [OIII]$\lambda$5007Å emission line fluxes is often empirically described via the truncated exponential formula (Ciardullo et al. 1989):

$$\mathrm{N}(M) = c_1 e^{c_2 M}\left\{1 - e^{3(M^* - M)}\right\} \tag{3.10}$$

where $c_1$ is a normalisation constant, $c_2 = 0.307$ and $M^*$(5007)=-4.51 mag is the absolute magnitude of the PNLF bright cutoff. This analytical formula is designed (i) to reproduce the high mass cutoff observed for the PN central stars in nearby galaxies, and ii) to model PNs as uniformly expanding homogeneous spheres ionised by a non-evolving central star (Henize & Westerlund 1963).

Our deep and extended imaging survey of PNs in the outer regions of M87 showed that the PNLF for this galaxy has significant deviations from Eq. 3.10 in the faint magnitude bins (Longobardi et al. 2013): its slope ~1-2 magnitudes below the bright cutoff is steeper than expected from the Ciardullo et al. (1989) formula. This is also true for the spectroscopically confirmed PN sample, as we show in Fig. 3.11 where we compare the total PNLF with the analytical formula for a distance modulus of 30.8.

Our data allow us to analyse separately and compare the PNLFs of the two spectroscopically confirmed PN samples for the M87 halo and ICL, from the bright cutoff down to 2.5 mag below. In the upper panel of Fig. 3.12, we show the PNLF for the spectroscopically confirmed sample of halo PNs, corrected for detection incompleteness as a function of magnitude. The data points trace a smooth function, and the fit of the generalised analytical formula (Eq. 3.10) to the observed PNLF within the 2.5 mag limit results in $c_2 = 0.72$ and a bright cutoff at $m^*_{5007} = 26.3$ (overplotted on the data). With $M^* = -4.51$ this corresponds to a distance modulus $(m-M)$=30.8.

In the central panel of Fig. 3.12, we present the ICPNLF (full blue circles), corrected for incompleteness. As for the M87 halo PNLF, the ICPNLF is consistent with the same distance modulus as for M87. However, it shows an overall shallower gradient than the M87 halo PNLF: the best fit of Eq. 3.10 to the empirical PNLF returns $c_2 = 0.66$.

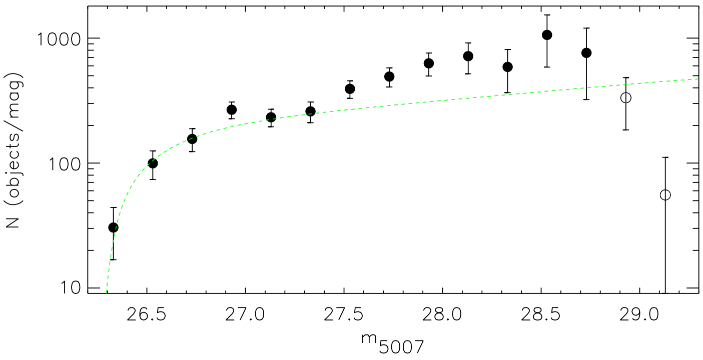

Figure 3.11: Luminosity function of all spectroscopically confirmed PNs corrected for incompleteness (full dots). The dashed green line represents the Ciardullo et al. (1989) formula for a distance modulus of 30.8, convolved with photometric errors and normalised to the data at the bright end. The spectroscopically confirmed PNLF shows an excess of fainter PNs with respect to the analytical formula, similar to the photometric PNLF (Longobardi et al. 2013). Open circles represent magnitude bins were the sample is not completeness-corrected. The error bars show the uncertainties from counting statistics and completeness correction.

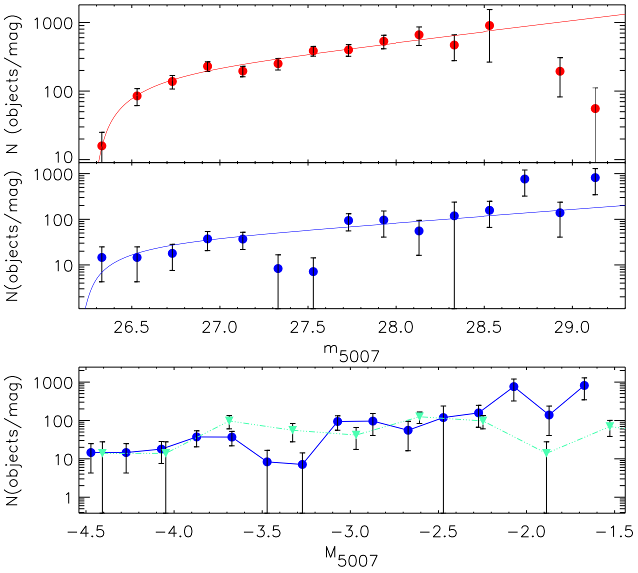

Figure 3.12: *Top panel*: Luminosity function of the spectroscopically confirmed halo PNs, corrected for incompleteness (red circles). The red line shows the fit of the generalised analytical formula (Eq. 3.10) to the halo PNLF, with $c_2 = 0.72$ and bright cutoff at 26.3 mag, corresponding to a distance modulus $m - M = 30.8$. *Central panel*: Completeness-corrected PNLF for the ICPNs (blue circles). The blue line shows the fit of the generalised analytical formula (Eq. 3.10) to the ICPNLF, with $c_2 = 0.66$. The ICPNLF shows a dip 1-1.5 mag fainter than the bright cutoff. *Bottom panel*: PNLFs in absolute magnitude for the spectroscopically confirmed Virgo ICPNs (blue circles) and for the outer disk of M33 (Ciardullo et al. 2004, cyan triangles) matched at the first bin. For this comparison, the data are corrected for line-of-sight reddening (see text). Absolute magnitudes are determined using a distance modulus of 30.8 for the ICL and 24.86 for M33 (Ciardullo et al. 2004).

In addition to the shallower gradient at fainter magnitudes, the ICPNLF shows a clear dip at 1-1.5 mag fainter than $m^*_{5007}$. This feature is statistically significant: the difference between the number of PNs in these bins with respect to the magnitude bins before and after the dip is $> 3\,\sigma_{\rm dip}$ on both sides, where $\sigma_{\rm dip}$ is the uncertainty from Poisson statistics in the magnitude bins where the dip occurs.

Dips in the PNLF are observed for PN populations detected in star forming galaxies (irregulars/disks), and are absent in the PNLFs of bulges or early-type galaxies. The magnitude below the bright cutoff at which the dip occurs varies between different PN populations, from ~ 2 to ~ 4 mag below $M^*$ (Jacoby & De Marco 2002; Ciardullo et al. 2004; Hernández-Martínez & Peña 2009; Reid & Parker 2010). We discuss this issue further in Section 3.6.1. In the bottom panel of Fig. 3.12 we compare the PNLFs for the Virgo ICPNs and for the spectroscopically confirmed sample of PNs for the outer disk of M33 (Ciardullo et al. 2004). Both LFs are corrected for foreground Galactic extinction, adopting reddening values of $E(B-V)_{\rm ICL}$=0.02 (Ciardullo et al. 1998) and $E(B-V)_{\rm M33}$=0.04 (Ciardullo et al. 2004) for the Virgo ICL and M33, respectively[8]. Absolute magnitudes are determined using a distance modulus of 30.8 for the ICL and 24.86 for M33 (Ciardullo et al. 2004). Both PNLFs show dips relative to the smooth luminosity function: the ICL at 1-1.5 mag fainter than $M^*$, the outer disk of M33 at ~ 2.5 mag fainter than the bright cutoff.

Finally, we recall that about 17% of the PNs contained in the M87 halo PNLF shown in Fig. 3.12 are ICPNs whose velocities fall in the same velocity range of the M87 halo PNs, and can therefore not be individually identified. The hint of a slight dip in the halo PNLF at ~ 1 mag below the bright cutoff may be due to these ICPNs.

To summarise, the observed properties of the M87 halo and Virgo ICPN populations, i.e., their $\alpha$-parameters and PNLFs, show significant differences. Because these quantities depend on the physical properties of the parent stellar populations, these differences imply that the M87 halo and ICL consist of different populations of stars. To understand this better, more work is clearly required for a better theoretical understanding of how metallicity, age and different star formation histories affect the post-AGB phases of stellar evolution and the resulting PN populations.

## 3.6 Discussion

### 3.6.1 The distinct halo and IC populations around M87

In Sect. 5.3 we presented the projected phase-space distribution of the spectroscopically confirmed PNs in our M87 fields (Fig. 3.6). With a robust procedure we showed that the PN velocity distribution splits into two kinematically very different components, the M87 halo (with mean velocity $V_{\rm LOS,n} = 1275$ kms$^{-1}$ and velocity dispersion $\sigma_{\rm n} \simeq 300$ kms$^{-1}$) and the ICL (with $V_{\rm LOS,b} \simeq 1000$ kms$^{-1}$ and $\sigma_{\rm b} \simeq 900$ kms$^{-1}$). In Sect. 4.5 we furthermore found that the halo and IC components were characterised by specific PN numbers ($\alpha$ parameters) that differed by a factor of three, and by different shapes of their PNLFs.

---

[8] We used the relation of Cardelli et al. (1989) with $R_V = 3.1$ to go from reddening to extinction at 5007Å.

These results demonstrate the coexistence of two distinct PN progenitor stellar populations in this region of the Virgo cluster core: the M87 halo and the ICL. These two populations have very different surface density distributions, with the M87 halo described by an $n = 11.8$ Sersic law, while the ICL follows a shallow power-law $\propto R^{\gamma}$ with $\gamma$ in the range $[-0.34, -0.04]$. We also have external information on the metallicities and ages of both components. At $R \sim 35$kpc, the mean metallicity of the M87 halo obtained with population synthesis models from multi-colour photometry is $\sim 0.7$ solar, with a shallow outward gradient, and the mean age is $\sim 10$Gyr (Liu et al. 2005; Montes et al. 2014). On the other hand, the metallicity and age distributions of ICL red giants in a field at $R \sim 190$ kpc from HST ACS star photometry are dominated by metal-poor ($[M/H] \leq -1$), $\geq 10$Gyr old stars (Williams et al. 2007). Because of the large velocities and shallow surface density profile of the IC stars, these IC population parameters are likely to be similar in the radial range probed by our observations, $R \sim 50 - 140$ kpc, whereas the M87 halo stars might reach $\sim 0.5$ solar in the outer regions if the outward gradient continues as inferred by Liu et al. (2005).

Currently there is no good theoretical understanding of how the properties of a PN population are related to the metallicity and age of a stellar population. Observationally, star forming and bulge populations have $\alpha$ numbers such as we find for the ICL, while only the most massive early-type galaxies have $\alpha$ numbers as low as we find for the M87 halo (Buzzoni et al. 2006; Cortesi et al. 2013). The primary driver is believed to be increased mass loss at high metallicities. PNLFs are empirically found to steepen from star forming to old metal-rich populations (Ciardullo et al. 2004; Longobardi et al. 2013). The PNLFs of Local Group star forming galaxies such as the SMC (Jacoby & De Marco 2002), LMC (Reid & Parker 2010), M33 (Ciardullo et al. 2004), and NGC 6822 (Hernández-Martínez & Peña 2009) furthermore show a ’dip’ 2-2.5 mag down from the PNLF cutoff for the LMC, M33, and NGC 6822, and 4 mag down from the cutoff for the SMC. A tentative model for this feature is the superposition of a faint PN population with a brighter population of more massive cores from a younger stellar population (Rodríguez-González et al. 2014). We can speculate that as the brighter population fades in older and/or more metal-rich populations, the dip might move towards brighter magnitudes. This could explain why in the Virgo IC population we find the dip 1-1.5 mag down from the cutoff. No other PN population with this PNLF is known; however, PNLFs as deep as for M87 have only been obtained in the Local Group so far. Clearly, more observational and theoretical work on the nature and location of the dip in the PNLF is needed.

### 3.6.2 The ICL in Virgo: nature and number of its progenitor galaxies

The combined properties of the Virgo ICPN population - the fairly small inferred bolometric luminosity, the relatively large $\alpha$ parameter, and the dip in the PNLF - as well as the low mean metallicity from Williams et al. (2007), appear to be most readily explained if this population derives from a faded population of low-luminosity, low-metallicity, star forming or irregular galaxies, such as M33 or the LMC, very different from M87 itself.

In Section 3.5.1, we determined the total V-band and bolometric luminosities of the IC component sampled by our survey fields: $L_{\mathrm{ICL}} = 0.53 \times 10^{10} L_{\odot}$, and $L_{\mathrm{ICL,bol}} = 1.1 \times 10^{10} L_{\odot,\mathrm{bol}}$. Using the total V-band luminosities for M33 and the LMC listed in NED, $L_{\mathrm{M33}}=3.65\times10^{9} L_{\odot}$ and

$L_{\rm LMC}$=1.26×10$^9 L_\odot$, we find that the IC stars sampled in our survey fields corresponds to ∼ 1.5 M33-like galaxies or ∼ 4 LMC-like galaxies[9].

We can now also check whether the Virgo ICL associated with the ICPN population could be related with the blue GC population that is found around M87, with a shallower and more extended surface density profile than the red GCs which trace the stellar halo light (Côté et al. 2001; Tamura et al. 2006; Strader et al. 2011; Forte et al. 2012; Durrell et al. 2014). To do this, we need to estimate the total number of GCs associated to M33 and LMC-like systems. Harris et al. (2013) studied GC populations in a large sample of galaxies and analysed the correlation of the total number of GCs, $N_{\rm GC}$, with global galaxy properties and type. They find that $N_{\rm GC}$ increases roughly in direct proportion to host galaxy luminosity, with a scatter of a factor of ∼ 2.5. For an LMC-like system with luminosity $\rm L_{LMC}$=1.3×10$^9$L$_\odot$ the expected mean number of GCs is $N_{\rm GC}$ ∼ 20, while for an M33-like galaxy with $\rm L_{M33}$=3.7×10$^9$L$_\odot$ the expected mean number of GCs is $N_{\rm GC}$ ∼ 60. This leads to an estimated number of blue GCs associated to the sampled ICL of $N_{\rm GC,ICL}$ ∼ 80 − 90, with a scatter of a factor ∼ 2.5. If a fraction of the ICL is due to the accretion of even lower luminosity galaxies, the estimated number of GCs would increase (Harris et al. 2013; Coccato et al. 2013).

The recent survey of the GC population in the Virgo cluster around M87 by Durrell et al. (2014) showed the presence of an ICGC population, mostly associated with blue GCs (see further discussion in Sect. 3.6.3). This intracluster component has a density equal to $\Sigma_{bGC,tot} = 0.2^{+0.13}_{-0.08}\rm arcmin^{-2}$. In our surveyed region this would lead to a total number of 100-430 ICGCs. This is larger than but consistent within the uncertainties with the value estimated above, suggesting that a substantial fraction of the blue GC population around M87 could have been accreted with the galaxies which we now see in the ICL.

### 3.6.3 Is there an intracluster component of globular clusters around M87?

There has been some controversy in the recent literature about the existence of intracluster GCs in the halo of M87. The most extensive photometric study of the distribution of GCs in the Virgo cluster so far was carried out by Durrell et al. (2014) as part of the NGVS. They studied density maps of the GC population, selected using colour criteria, and statistically accounted for the contamination to the GC sample by subtracting a modelled map for the expected background, from both Milky Way stars and background galaxies[10]. The blue GCs in their map have a shallower and more extended profile than the red GCs. Durrell et al. (2014) also found that the total GC (blue plus red) density profile is in good agreement with the number density profile of photometrically selected PNs from Longobardi et al. (2013), including a change of slope and a flatter profile at large radii. They suggested that their blue GCs at distances > 215 kpc are part of the intracluster component of Virgo. Cosmological simulations (Dolag et al. 2010; Cui et al. 2014; Cooper et al. 2014) predict that the density of this component would then increase inwards.

---

[9] The *total* luminosity at all radii corresponding to the detected IC stars will be much larger; their large measured velocity dispersion implies that the orbits of these IC stars will reach to much larger radii in the cluster.

[10] We note here that the M87 PN sample cannot be contaminated by Milky Way halo PNs, as these would have [OIII]$\lambda$5007Å fluxes about 12 mag brighter than M87 PNs.

Durrell et al. (2014) also found evidence for a spatial asymmetry of GCs surrounding M87 for major axis distances larger than 20′, with an excess of tracers in the NW region (mostly the blue population). In Sect. 5.4 we studied the distribution of M87 halo and IC PNs separately for the NW and SE. We find no clear evidence of asymmetry in either the halo and ICL within major axis distance $\sim 20'$ (Fig. 3.10). Inside this radius, both PN and GC number density profiles are consistent with a symmetric halo and IC distribution. For the halo component this result is significant, given the number of tracers and radial extent, and indicates that if the halo was the subject to accretion events these were not recent. For the ICL, we may expect asymmetries, given the longer time-scales involved in IC accretion events, but we may not have a large enough sample of ICPNs to see them.

Strader et al. (2011) carried out a spectroscopic study of the GCs around M87, using colour criteria to select their candidates. In the same colour and magnitude range populated by globular clusters, $0.55 \leq (g' - i') \leq 1.15$ and $20 \leq g' \leq 24$, there is however a large contribution from foreground Milky Way halo stars. To mitigate this effect Strader et al. (2011) used a combination of photometry, radial velocity and HST imaging information. However, they considered all objects with velocity $\mathrm{V_{LOS}} < 150\,\mathrm{kms^{-1}}$ to be stars, and in the most ambiguous range, i.e. $150\mathrm{kms^{-1}} < \mathrm{V_{LOS}} < 350\mathrm{kms^{-1}}$, they classified all uncertain objects, for which a clean separation between contaminants and GCs could not have been done, as stars. Based on the remaining sample, they reported that the number density profile of the spectroscopically confirmed GCs showed no evidence for a transition between a halo and IC component, either as a sharp truncation of the halo, or a flattening of the GC number density profile at large radii. From the sample kinematics, they observed that their GCs around M87 have velocity dispersion in the range $300 \leq \sigma \leq 500$ $\mathrm{kms^{-1}}$ out to 190 kpc, with $\sim$ 500 $\mathrm{kms^{-1}}$ for the GCs population at 190 kpc significantly smaller than the velocity dispersion of Virgo cluster galaxies (Binggeli et al. 1993; Conselice et al. 2001). However, from the PN phase-space distribution $(\mathrm{V_{LOS,PN}}, R_{\mathrm{PN}})$ in Fig. 3.6, we see that a large fraction of IC stars near M87 have velocities $\mathrm{V_{LOS}} < 350$ $\mathrm{kms^{-1}}$. This suggests that the lack of evidence for the IC component reported by Strader et al. (2011) could be caused by the velocity threshold $\mathrm{V_{min}} = 350$ $\mathrm{kms^{-1}}$ imposed on the GC sample, which is needed to prevent the contamination from Milky Way halo stars, but may also remove many of the ICGCs from their analysis.

### 3.6.4 Relation between BCG and ICL

When studying central galaxies in clusters, one of the main question is to establish where the ICL begins and where the associated BCG ends, or whether any distinction is to be made at all.

For M87, the differences in the density profiles and velocity distributions of the halo and ICPN populations, as well as in their $\alpha$-parameters and PNLFs, are sufficient to argue that the two components must be considered as separate stellar populations with different metallicities and star formation histories, and not as a continuum. As discussed above, published stellar population data suggest that the halo stars are older and more metal-rich than the ICL (see Sects. 4.5, 3.6.1 for more details).

In more distant BCGs where a kinematic decomposition between BCG halo and ICL is not available, the presence of an additional dynamical component in BCGs is usually inferred from a change of slope at large radii in the SB profile (Zibetti et al. 2005; Gonzalez et al. 2007; D'Souza et al. 2014). Photometric properties or colours are obtained by treating the two components as a continuum, because no differentiation between the underlying stellar populations is normally possible.

Using a particle tagging method to analyse galaxy clusters in $\Lambda$CDM simulations, Cooper et al. (2014) consider the BCG and ICL as a single entity consisting of all stars which are not bound to any cluster subhalos. They then split the BCG stars into *accreted stars* and *in situ stars*, and find that the large majority of BCG stars are accreted stars. They find double-Sèrsic surface density profiles in their simulated BCGs, where the inner component ($R < 200$kpc) is dominated by 'relaxed' accreted components, and the outer component by 'unrelaxed' accreted components. Cooper et al. (2014) argue that the accreted/in situ separation is physically meaningful and that the ICL should be naturally considered as a continuation of the BCG to low surface brightness, because both components are formed by similar mechanisms.

In contrast, a dynamical approach based on the velocity distributions of diffuse light particles in hydrodynamic cosmological simulations (Dolag et al. 2010; Cui et al. 2014) is found to separate these stars into two components, one bound to the cluster potential, and the other bound to the BCG. The resulting BCG and diffuse ICL are formed on different time scales, and the simulated stars associated with the two components are different in terms of spatial distribution, ages and metallicities. Cui et al. (2014) showed that it is possible to dynamically differentiate between halo and IC particles by using the particles' binding energies. Stars with high binding energy that end up belonging to the BCG were subjected to relaxation and merging processes such that the gravitational potential changed so quickly that these stars lost memory of the kinematics of their progenitors (Murante et al. 2007; Dolag et al. 2010). On the other hand, stars with lower binding energy, that belong to the diffuse component, still reflect the dynamics of the satellite galaxies. Both Dolag et al. (2010) and Cui et al. (2014) observed also that the slope of the surface brightness profile associated with the two components change, with the halo profile being steeper than the ICL profile.

It is likely that the distinct BCG and IC components found in the hydrodynamical simulations are related to the relaxed and unrelaxed accreted components in the particle tagging analysis, but the inclusion of baryonic processes in the former may accentuate the differences found between BCG and ICL. If we associate the BCG and ICL of Dolag et al. (2010); Cui et al. (2014) with the relaxed and unrelaxed accreted components of Cooper et al. (2014), the progenitors of the stars in the steeper Sèrsic (relaxed) component would be accreted from more massive systems at higher redshifts, while the stars in the shallower and more extended ICL (unrelaxed) component would come from the accretion of less massive systems at lower redshifts. More massive progenitors dominate the diffuse light in simulated clusters close to the center (Murante et al. 2007; Puchwein et al. 2010) because they move inwards further by dynamical friction. They cause stronger relaxation of the gravitational potential, and if accreted early they have more time to relax.

To summarise, recent simulations show that a distinction can be made between stars that trace the cluster potential and stars bound to the BCG, based on the physical properties and binding energies of the accreted progenitors. From the study of the PN population around M87, we have shown the coexistence of two discrete components in the Virgo cluster core, tracing different stellar populations, in agreement with these predictions. While the PN population for the IC component around M87 indicates low-mass dwarf and star-forming galaxy progenitors, the stellar halo has higher metallicity, $\sim 0.7$ solar, indicating more massive progenitors. This bimodality in the progenitors may be the root of the bimodality in the kinematics and density profiles of the M87 halo and the ICL.

However, we note that such a bimodality need not occur in every cluster of galaxies. For example, it is plausible that, for a more continuous distribution of progenitor masses and a more uniform distribution of binding energies of the debris stars, the final BCG plus ICL system would show continuous radial gradients in kinematics and stellar population properties, rather than appear as the sum of several discrete components. It is possible that NGC 6166 in the Abell 2199 cluster is closer to this situation: the velocity dispersion in the high-surface brightness halo of this BCG was recently measured to increase up to the cluster velocity dispersion of $\sim 800 \mathrm{km} s^{-1}$ at 100" from the galaxy center (Bender et al. (2014); see also Kelson et al. (2002)).

## 3.7 Summary and Conclusions

We obtained spectra for 287 PNs in the outer regions of the nearby elliptical galaxy M87, of which 211 are located between distances 40 kpc to 150 kpc from the galaxy centre. Spectra were acquired with the FLAMES spectrograph in the GIRAFFE+MEDUSA configuration, with spectral resolution of $R = 22500$. We observed 14 different FLAMES plate configurations, using candidates from the catalogue described in Longobardi et al. (2013). The spectroscopic survey aimed at measuring the LOS velocities of PNs in the transition region between the galaxy's stellar halo and the ICL. PNs were identified through their narrow and symmetric, redshifted [OIII]$\lambda$5007Å emission line, with no or negligible continuum, and verified with the second [OIII]$\lambda$4959Å emission line. Spectra were measured for PNs in the magnitude range from $m_{5007}$=26.3 down to 28.8. This is the largest spectroscopic sample of PNs at such galactic radii for a central galaxy, in the number of tracers and magnitude depth.

The area covered by the survey allowed us to trace the transition between the M87 halo and ICL in the Virgo cluster core. The coexistence of these two components is shown by the bimodality of the LOSVD, whose strong asymmetric wings make it deviate from the near-Gaussian LOSVD typical of early-type galaxies. We separated halo and ICPNs by studying the projected phase-space distribution. We implemented a robust technique to measure the velocity dispersion of the M87 halo, separating its velocity distribution from the broader component, the ICL. We identified 243 PNs for the M87 halo and 44 ICPNs. We found that the logarithmic number density profile for the halo PNs follows the V-band SB profile from Kormendy et al. (2009), while the IC number density profile decreases towards large radii as a power-law $I_{\mathrm{ICL}} \propto \mathrm{R}^{\gamma}$ with $\gamma$ in the range $[-0.34, -0.04]$.

The total PN surface density profile at large radii is flatter than the surface brightness profile, because of the presence of the IC component (see also Longobardi et al. 2013) which contributes ~3 times more PNs per unit luminosity than the halo population. We find luminosity-specific PN numbers $\alpha_{\mathrm{halo}} = (1.06 \pm 0.12) \times 10^{-8}\ \mathrm{N_{PN}} L^{-1}_{\odot,\mathrm{bol}}$ and $\alpha_{\mathrm{ICL}} = (2.72 \pm 0.63) \times 10^{-8}\ \mathrm{N_{PN}} L^{-1}_{\odot,\mathrm{bol}}$ for the M87 halo and IC PN population, respectively. This is consistent with the known existence of a gradient towards bluer colours at large radii, due to the increased contribution of ICL at large distances and its lower metallicity compared to the halo population.

The spectroscopically confirmed PNLFs for both the halo and IC PNs have a steeper slope towards faint magnitudes than is predicted by the analytical formula of Ciardullo et al. (1989), confirming the result from the photometric sample (Longobardi et al. 2013). This steepening is consistent with an old stellar population dominated by PNs with low mass cores. The PNLF of the ICPN population has a slightly shallower gradient than the M87 halo PNLF, and in addition shows dip at about ~ 1 - 1.5 magnitudes from the bright cutoff. Such a dip is an evolutionary feature observed in star-forming systems, such as M33 and the Magellanic clouds, and may be related to rapidly evolving PNs with massive central cores. The presence of the dip in the ICPNLF but not in the M87 halo PNLF provides additional evidence for intrinsic differences between the halo and IC parent stellar populations.

Using PNs as tracers we showed in this work that the stellar halo of the BCG galaxy M87 is distinct from the surrounding ICL in its kinematics, density profile, and parent stellar population, consistent with the halo of M87 being redder and more metal-rich than the ICL. We note that the ICL in our surveyed fields corresponds to about four times the luminosity of the LMC, spread out over a region of ~ 100 kpc diameter. It is remarkable that population properties can be observed for such a diffuse component.

In the Virgo cluster, BCG halo and ICL cannot be considered as component with a gradual transition in their kinematics. This supports results from analysis of galaxy cluster simulations, which suggest that the IC component in Virgo consists of unrelaxed accreted stars bound to the cluster potential, while the stellar halo of M87 appears to be described as a relaxed accreted component bound to the galaxy itself. Based on its PN population properties, we propose that the progenitors of the Virgo ICL were low-mass, star-forming galaxies, which may also have brought with them a significant fraction of the blue GC population seen in the outer regions of M87.

# Chapter 4

# The build-up of the cD halo of M87 Evidence for accretion in the last Gyr

*This chapter is submitted on A&A as a Letter to the editor, Longobardi et al. (2015b)*

## Abstract

We present kinematic and photometric evidence for an accretion event in the halo of the cD galaxy M87 in the last Gyr.

Using velocities for ∼ 300 planetary nebulas (PNs) in the M87 halo, we identify a chevron-like substructure in the PN phase-space. We implement a probabilistic Gaussian mixture model to identify PNs that belong to the chevron. From analysis of deep V-band images of M87, we find that the region with the highest density of chevron PNs is a crown-shaped substructure in the light.

We assign a total of $N_{\mathrm{PN,sub}} = 54$ to the substructure, which extends over ∼50 kpc along the major axis where we also observe radial variations of the ellipticity profile and a colour gradient. The substructure has highest surface brightness in a 20kpc × 60kpc region around 70 kpc in radius. In this region, it causes an increase in surface brightness by $\gtrsim$60%. The accretion event is consistent with a progenitor galaxy with a V-band luminosity of $L = 2.8 \pm 1.0 \times 10^{9} L_{\odot,V}$, a colour of $(B - V) = 0.76 \pm 0.05$, and a stellar mass of $M = 6.4 \pm 2.3 \times 10^{9} M_{\odot}$.

The accretion of this progenitor galaxy has caused an important modification of the outer halo of M87 in the last Gyr. By itself it is strong evidence that the galaxy's cD halo is growing through the accretion of smaller galaxies as predicted by hierarchical galaxy evolution models.

## 4.1 Introduction

According to the current theory of hierarchical formation and evolution of structures, accretion events are believed to have an important role in the cosmological build up of stellar halos in elliptical galaxies (De Lucia & Blaizot 2007), responsible for their growth at relatively low redshifts

($z < 2$; Oser et al. 2010). In dense environments accretion is even more dramatic, such that close to the dynamical centre of the cluster, central cluster galaxies are expected to have the majority of their stars accreted (Laporte et al. 2013; Cooper et al. 2014).

On the observational front, the outer stellar envelopes are observed to increase in mass by a factor of $\sim 4$ since $z = 2$ (van Dokkum et al. 2010). The presence of an accreted component is usually identified as an excess of light over the extrapolation of the galaxy's inner profile (Zibetti et al. 2005; Gonzalez et al. 2007; D'Souza et al. 2014), or by high Sersic indexes ($n > 4$; Kormendy et al. 2009). Observations of blue colour gradients from the centres of early-type galaxies towards their outskirts (Peletier et al. 1990; Liu et al. 2005; Rudick et al. 2010), mainly attributed to a gradient in metallicty (Tamura et al. 2000; Loubser & Sánchez-Blázquez 2012; Montes et al. 2014) are also in agreement with a change in stellar properties driven by the accretion of smaller systems. Records of accretion events are also revealed in the form of spatially extended low-surface brightness features in the outskirt of stellar halos (Mihos et al. 2005; van Dokkum et al. 2014; Duc et al. 2015). These *substructures* are not in a phase-mixed equilibrium in the host galaxy potential and, therefore, can in principle be traced as kinematic features in velocity phase-space.

M87 is one of the nearest central galaxies (at an adopted distance of 14.5 Mpc; Ciardullo et al. 2002; Longobardi et al. 2015a), close to the dynamical centre of the Virgo cluster (Binggeli et al. 1987). It is considered a type-cD galaxy (Weil et al. 1997; Kormendy et al. 2009) with an extended stellar envelope that reaches $\sim 150$ kpc in radius. A blue colour gradient towards its outskirts (Rudick et al. 2010) has been interpreted as age and metallicity gradients (Liu et al. 2005; Montes et al. 2014), consistent with a late build-up of its halo. The orbital properties of globular clusters (GCs) (Agnello et al. 2014) and ultra compact dwarfs (Zhang et al. 2015) also favour accretion onto the halo. M87 has been the target of several deep imaging surveys (Mihos et al. 2005; Rudick et al. 2010), and its close proximity has made it possible to identify hundreds of planetary nebulas (PNs), and to measure their line-of-sight velocities (LOSVs; Doherty et al. 2009; Longobardi et al. 2015a).

In this letter we use the synergy between PN kinematics and deep imaging to identify an ongoing accretion event in the outer halo of M87, which we find to be a non-negligible perturbation of the galaxy properties at the distances where it is traced.

## 4.2 Kinematic evidence for an accretion event in M87

We acquired kinematic data from the FLAMES/VLT spectroscopic survey for a large sample of PNs in the outer regions of M87 (Longobardi et al. 2013, 2015a). The total sample consists of 254 objects classified as M87 halo PNs and 44 intracluster PNs, for which we have obtained LOSVs with an estimated median velocity accuracy of 4.2 $\mathrm{kms}^{-1}$ . We concentrate here on the M87 halo PNs that cover a range of radii from $\sim 15 - 150$ kpc.

We see a notable chevron (or "V" shape) structure in the projected phase-space of the PN sample as shown in Fig. 4.1 (top left). To isolate this kinematical substructure we utilise a three-component Gaussian mixture model to identify high-density, narrow features on top of a broader distribution. We note that there is not enough data to statistically favour this model over

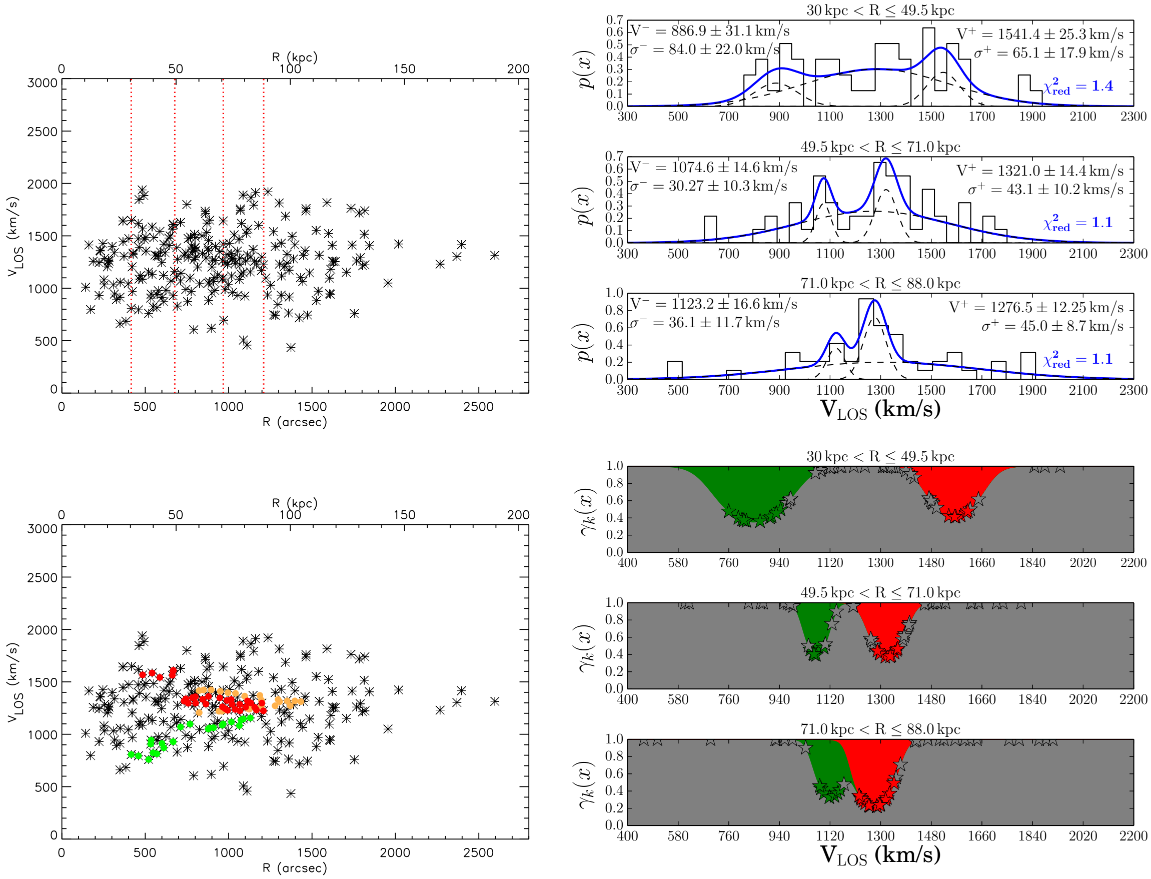

Figure 4.1: Top-left: Projected phase-space, $V_{LOS}$ vs. major axis distance (*R*), for all spectroscopically confirmed PNs (black asterisks) in the halo of M87. Red-dashed lines indicate three elliptical annuli where cold components associated to the substructure were identified. Top-right: Histograms of the LOSVD in the three elliptical annuli. In each panel, the blue lines show the best-fit model computed as a combination of three Gaussians. Black-dashed lines show the relative contribution of each component to the LOSVD, with parameters for the cold components given in the plot. Bottom-left: As in the top-left panel, however, the green and red circles show the PNs associated with the cold secondary peaks in the LOSVD. Orange circles show a kinematically selected GC substructure from Romanowsky et al. (2012). Bottom-right: Probability that a PN is drawn from the halo component (dark grey area) or from the chevron (green, red areas). Coloured stars represent chevron PNs and probabilities at their measured $V_{LOS}$.

simpler models with BIC or AIC; however, it is visually indicated and we will confirm it with photometry in Sec.5.4. A brief description of the technique is given in the following paragraph; for more details we refer the reader to Pedregosa et al. (2011).

A Gaussian Mixture Model (GMM) is a probabilistic model, which assumes that a distribution of points can be described as a linear combination of $K$ independent Gaussian probability density functions (PDFs), or components, expressed by:

$$p(x) = \sum_{k=1}^{K} p_k(x\,|\,\mu_k, \sigma_k) P_k, \tag{4.1}$$

where, $x$ is a data vector (here the LOSVs), $P_k$ is the mixture weight that satisfies the conditions $0 \leq P_k \leq 1$ and $\sum_{k=1}^{K} P_k{=}1$, and $p(x\,|\,\mu_k, \sigma_k)$ are the individual Gaussian PDFs, with mean $\mu_k$, and dispersion $\sigma_k$. The GMM classifier implements the Expectation-Maximization (EM) algorithm, i.e. an iterative process that continuously updates the PDF parameters until convergence is reached. At the end of the EM procedure, the posterior probabilities, $\gamma_k(x)$ for a data value to belong to each of the $k$ Gaussian components are returned. These are described by:

$$\gamma_k(x) = \frac{p_k(x\,|\,\mu_k, \sigma_k) P_k}{p(x)}. \tag{4.2}$$

To apply the GMM to our LOSV distribution (LOVSD) we bin the PN M87 halo sample into seven elliptical annuli, or stripes in phase-space, covering the entire PN velocity phase-space. The LOSVD in each annulus is analysed as a combination of three Gaussians, where the centres ($\mu_k$), widths ($\sigma_k$), and weights ($P_k$) are treated as free parameters in the EM algorithm, and have uncertainties $\sigma_{\mu_k} = \sigma_k/\sqrt{S}$, $\sigma_{\sigma_k} = \sigma_k/\sqrt{2S}$, and $\sigma_{P_k} = P_k/\sqrt{S}$, with $S = [\sum_n \gamma_k(x_n)]$ (MacKay 2003).

We find cold components in three out of seven elliptical bins, for which we show the histogram of the data, along with the best-fit GMM and reduced $\chi^2$ in Fig. 4.1 (top-right panel). We also plot (bottom-left panel) the LOSV phase-space for the 254 PNs in the halo of M87: black crosses represent PNs of the smooth halo LOSVD of M87, while red and green dots are PNs that have a higher probability (see eq. 4.2) to belong to the chevron. Finally, we show the probability that a given PN is drawn from each of the components as a function of its velocity (bottom-right panel). The GMM assigned a total of 54 PNs to the chevron substructure, which covers $700''$ ($\sim$ 50 kpc) for major axis distances $500'' < R < 1200''$. The separation, $\Delta$V, between the two peaks of the cold components becomes smaller at larger distances. For the three elliptical bins, it is $\Delta\mathrm{V} = 654.5 \pm 40.1$, $246.4 \pm 20.5$, and $153.3 \pm 20.6\,\mathrm{kms}^{-1}$, respectively. At $R \sim 1200''$ ($\sim$ 90 kpc) the width of the chevron goes to zero with LOSVs close to the galaxy's systemic velocity ($\mathrm{V}_{\mathrm{sys}} = 1275\,\mathrm{kms}^{-1}$; Longobardi et al. 2015a)[1]. PNs on the arms of the chevron are seen on both the northern and southern sides of the galaxy as is shown in Fig. 4.2 (see Sect. 5.3). The broad Gaussian with average mean velocity $\sim 1290\,\mathrm{kms}^{-1}$ and dispersion $\sim 320\,\mathrm{kms}^{-1}$ in the three bins traces the M87 halo.

---

[1] The stability of the fitted parameters and the measured distance of the chevron edge were tested with 100 GMM runs for different mock data sets and initialisation values.

The search for kinematic features in the phase-space of GCs has resulted in the discovery of a similar chevron-like structure (Romanowsky et al. 2012), shown in Fig.4.1 above as orange dots. Though the morphology in the phase-space is similar it differs in a number of physical properties: the width goes to zero at $R_{\rm GC} \sim 1500''$ with $\rm V_{LOS,GC} = 1307\,kms^{-1}$, versus $R \sim 1200''$ and $\rm V_{LOS} \sim 1250 \pm 21\,kms^{-1}$ for the PNs. Moreover, the 27 chevron GCs show a very different spatial distribution with the highest density of points on the NE photometric minor axis (Romanowsky et al. 2012; D'Abrusco et al. 2015), and few GCs near the crown substructure traced by the PNs.

## 4.3 Localising the substructure with deep imaging

In Fig. 4.2 (left), we show the position of the chevron PNs overplotted on $1.6 \times 1.6$ deg$^2$ V-band image of M87, with an estimated surface brightness limit of $\mu_{\rm V} = 28.5\,\rm magarcsec^{-2}$ (Mihos et al. 2015). Here we see the large spatial extent of the substructure associated with the chevron PNs. Because of its shape on the image we will refer to it as the *veil of M87.* Now we are interested to see if this feature is also visible in the optical light.

To this end, we constructed an unsharped masked image, which is the difference between the original image and a smoothed image. We utilised the IRAF task **fmedian** to smooth the original image by using a window with a size of $1450'' \times 1450''$. This window size was chosen so that it contained the large scale extension of the substructure. By looking at the highest concentration of PNs, in the NW region of M87, it can be seen to extend over many hundreds of arcseconds ($\sim 800''$). Thus, the adopted box size is $\sim 1.8$ times larger than the long side of the feature.

The results of the unsharped masking can be seen in Fig. 4.2 (top-central panel), where the high frequency structures are now clearly visible. A previously unknown debris structure, with a crown-like shape, can be seen on top of M87 at the NW side. This we refer to as the *crown* of M87's veil. It has a characteristic width of $\sim 300''$, an extension of $\sim 800''$, and is almost perpendicular to M87's photometric major axis. Just as the PN spatial distribution showed, the edge of this feature is found at $R \sim 1200''$ ($\sim 90$ kpc).

Over the same major axis distances at which the substructure is located, we also observe variations in the M87 ellipticity profile. Between $300'' < R < 800''$ the ellipticity increases and then flattens to a value of $e \sim 0.43$ for $R > 800''$ (Kormendy et al. 2009). In particular, the region at which the gradient flattens reflects the crown-like overdensity.

## 4.4 Physical properties of the accreted satellite

### 4.4.1 Luminosity and $\alpha$-parameter

To understand the physical origin of this structure, we compute its total luminosity. We do it in a region with size $\sim 800'' \times 300''$, after the subtraction of the local background, determined using a region photometry method (for more details see Rudick et al. 2010). We find a total luminosity in the range of $\rm L_{crown} = 3.7 \pm 0.9 \times 10^8 L_{\odot,V}$. When compared to the luminosity determined in

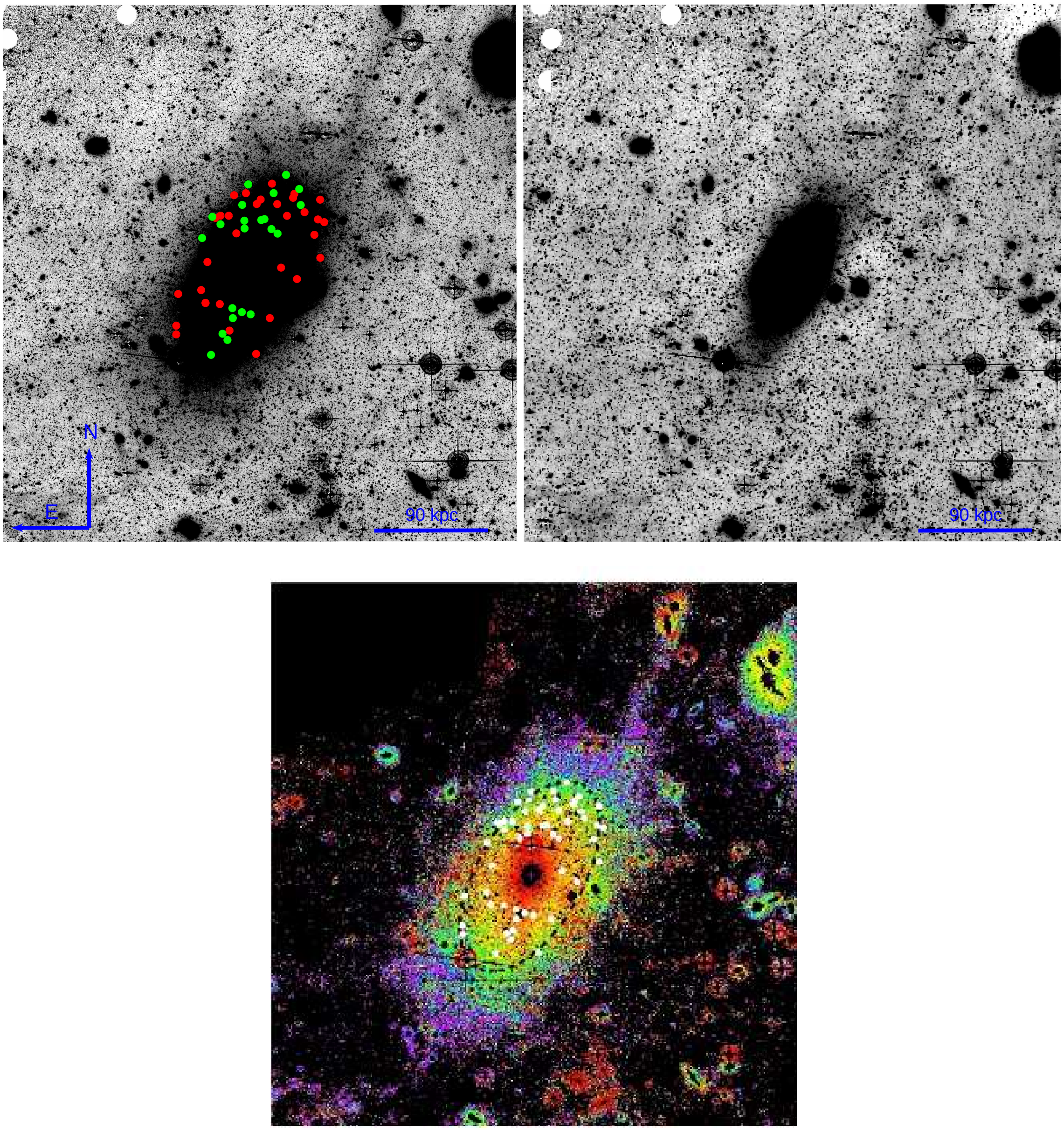

Figure 4.2: Spatial and colour distribution associated with the kinematic substructure identified in the phase-space of the M87 halo PNs. **Top-Left panel**: V-band image of a 1.6 × 1.6 deg$^2$ centred on M87 from Mihos et al. (2015). Full circles indicate the spatial position of the M87 halo PNs in the chevron substructure. Red and green colours indicate PN LOSVs above and below $V_{LOS} = 1254\,\mathrm{kms}^{-1}$, the LOSV at the end of the chevron. **Top-Central panel**: Unsharped masked image of M87 median binned to enhance faint structures. The crown-shaped substructure is visible at distance of 800″-1200″($\sim 60-90$ kpc) along the major axis, NW of M87. Details are given in Section 5.3. The blue line measures 90 kpc. **Bottom panel**: (B-V) colour image of M87 from Mihos et al. (2015) with chevron PNs overplotted (white dots). The dashed ellipse indicates the isophote at a major axis distance of 1200″. The crown is found in a region where the (B-V) colour is on average 0.8, bluer than on the minor axis.

the same region from the original image, $L \sim 5.9 \times 10^8 L_{\odot,V}$, it is clear that at these distances the substructure represents a significant fraction, $\sim 60\%$, of the total light.

In the region of the crown we count $N_{PN,crown} = 12 \pm 3$ PNs, while we find a total of $N_{PN,chevron} = 54 \pm 7$ PNs associated to the entire chevron (see Sect. 5.2). By correcting these numbers for incompleteness factors as in Longobardi et al. (2015a) these become 19 and 142, respectively. Hence, by scaling $L_{crown}$ to the total number of PNs associated to the chevron we obtain the total luminosity associated to the progenitor of the M87 veil to be $L \sim 2.8 \pm 1.0 \times 10^9 L_{\odot,V}$.

The total number of PNs is proportional to the total bolometric luminosity of the parent stellar population, and the proportionality is quantified with the luminosity-specific PN density, or, $\alpha-$parameter (Buzzoni et al. 2006). Utilising the computed luminosity, and the completeness-corrected estimate for $N_{PN,chevron}$, we can calculate the $\alpha$-parameter for the progenitor of the substructure. Considering that the typical probability of the $N_{PN,chevron}$ PN to belong to the chevron is $\sim 0.7$ (Fig. 4.1), we obtain $\alpha_{2.5} = 1.8 \pm 0.7 \times 10^{-8} N_{PN} L^{-1}_{\odot,bol}$. Here $\alpha_{2.5}$ is 2.5 mag down the luminosity function as in Longobardi et al. (2015a), and we have assumed a bolometric correction for the V-band of $BC_V$=0.85 (Buzzoni et al. 2006) and $BC_{\odot}$=-0.07 for the Sun.

### 4.4.2 Colour and Mass

In Fig. 4.2 (bottom panel) we show the chevron PNs overplotted on the B-V colour image of M87, that combines the V-band data (see Sect. 5.3) with deep B-band photometry with a surface brightness limit of $\mu_B = 29\,\mathrm{mag\,arcsec^{-2}}$. It is interesting to notice that close to $R \sim 1200''$ the colour shows an azimuthal variance, such that along the photometric minor axis the measured values are redder (Mihos et al. 2015). This feature correlates with the spatial number density of the chevron PNs, showing a deficit in number along the photometric minor axis. This suggests that the bluer regions are the result of the accreted material on top the light from M87's halo. In particular, the crown structure is measured to have integrated colour $(B - V) = 0.76 \pm 0.05$.

(B-V) colour is a good estimator of the mass-to-light-ratio, $\Upsilon^{\star}$, of the underlying stellar population. By adopting $\Upsilon^{\star}_V = 2.3$ for (B-V)=0.76 (McGaugh & Schombert 2014), the total stellar mass associated to the disrupted galaxy is then $M = 6.4 \pm 2.3 \times 10^9 M_{\odot}$.

From the distribution and velocities of chevron PNs in Fig. 4.2 a possible interpretation of the satellite orbit could be that it was first disrupted entering M87 from the South (along the green dots), with the debris then moving up North, turning around in the crown region, and coming back down on both sides across M87 (the veil, red dots). The velocities would then imply that the northern side of M87 is closer to the observer. The dynamical time for such an orbit is of order $\leq 1$ Gyr (Weil et al. 1997).

## 4.5 Summary and Conclusion

In this letter we have presented kinematic and photometric evidence for an accretion event in the halo of the cD galaxy M87. This event is traced by PNs whose velocity phase-space shows a distinct chevron-like feature, which is a result of the incomplete phase-space mixing of a disrupted galaxy. At major axis distances of $R \sim 60 - 90\,\mathrm{kpc}$, where the width of the chevron goes to zero, a deep optical image shows the presence of a crown-like substructure that contributes $\gtrsim 60\%$ of the total light in this area.

The *crown* of M87's *veil* is the densest part of the entire substructure, which covers $\sim 50\,\mathrm{kpc}$ along the major axis. In this region also a radial variation in M87's ellipticity profile is observed. Looking at the spatial distribution of all the chevron PNs, it traces the azimuthal variation observed in the colour of M87, showing a deficit in number of tracers along the photometric minor axis where the galaxy is redder, and a higher fraction where the substructure is strongest and the colour is bluer.

We determined several physical properties of the disrupted satellite: a total luminosity of $\mathrm{L} = 2.8 \pm 1.0 \times 10^{9} \mathrm{L}_{\odot,\mathrm{V}}$, colour (B-V)=0.76±0.05, and total stellar mass of $\mathrm{M} = 6.4 \pm 2.3 \times 10^{9}\,\mathrm{M}_{\odot}$. The inferred value for the $\alpha$-parameter is $\alpha = 1.8 \pm 0.7 \times 10^{-8}\ \mathrm{N}_{\mathrm{PN}} \mathrm{L}_{\odot,\mathrm{bol}}^{-1}$. The similar colours of the accreted satellite and ICL suggest that the cD halo of M87 is presently growing by the accretion of similar star-forming systems as those that originate the diffuse IC component.

The evidence for on-going accretion in the outer halo of M87 is consistent with the observed size growth of giant elliptical galaxies and with predictions by theory. The presence of the newly discovered substructure within the halo of M87 demonstrates, that beyond a distance of $\sim 60\,\mathrm{kpc}$, its halo is still assembling.

# Chapter 5

# The kinematics of the outer halo of M87 as revealed by planetary nebulae

*This chapter is based on the study Longobardi et al. (2015), in prep.*

## Abstract

We present a kinematic study of a sample of ~300 planetary nebulas (PNs) in the outer halo of the central Virgo galaxy M87. The PN kinematics is used to explore the rotation of the halo and constraint the orbital distribution of the stars at these large radii.

We used a probability weighted estimation of the velocity and velocity dispersion to minimise the contribution from a previously identified substructure and measure the main halo kinematics, including velocity map, point symmetry, and $\lambda(R)$ parameter (proxy for the angular momentum).

The averaged PN two-dimensional velocity field is consistent with no rotation for major axis distances $R < 90\,\mathrm{kpc}$, while it shows a small amount of rotation, $\mathrm{V_{MAX}} = 37.3 \pm 23.3\,\mathrm{kms^{-1}}$ for larger major axis distances. This kinematical transition is also mapped by the $\lambda(R)$ profile that slowly increases to a value of $\lambda(R) = 0.13$ at $R \sim 110$ kpc. The velocity dispersion profile is observed to rise between $20\,\mathrm{kpc} < \mathrm{R} < 90\,\mathrm{kpc}$ to a value $\sigma = 362.6 \pm 30.4\,\mathrm{kms^{-1}}$, and then sharply decline to $\sigma = 126.8 \pm 36.6\,\mathrm{kms^{-1}}$ at $R \sim 170\,\mathrm{kpc}$. The comparison with previously published velocity dispersion profiles predicted from the X-ray inferred mass distribution and light distribution via inversion of Jeans equations show the the M87 dynamics is more complex than the one predicted by spherical symmetrical models based on the assumption of dynamical equilibrium.

The increase of angular momentum, as well as the first rise and then decline of the velocity dispersion in the outer region of the M87 halo support the hierarchical scenario, consistent with a late build-up of its halo. The new velocity dispersion data set the base for more sophisticated dynamical analysis that need to trace the transition from the smoothed halo to the still assembling halo.

## 5.1 Introduction

One of the most interesting question in extragalactic astronomy is how galaxy form and evolve. In a hierarchical Universe, where mergers are believed to play a predominant role in galaxy assembly (De Lucia & Blaizot 2007), a two phase-formation scenario (Naab et al. 2009), predicts that the innermost regions of massive galaxies formed the majority of their stars at high redshifts and on short time-scales (Thomas et al. 2005), while the stars in the outermost regions are assembled as a consequence of accretion events (Oser et al. 2010). As a result, the outermost regions of galaxies, where the growth is expected to occur and dynamical scales are longer, represent unique laboratories of study towards the understanding of galaxy formation and evolution.

A tight correlation between average photometrical properties and the formation history of the galaxy does exist: the presence of accreted component is usually inferred from the change of slope of its light profile at large radii (Zibetti et al. 2005; Gonzalez et al. 2007; D'Souza et al. 2014), by high Sersic indexes ($n > 4$ Kormendy et al. 2009), and by variation in the ellipticity profile (Tal & van Dokkum 2011; D'Souza et al. 2014; Longobardi et al. 2015b). However, when galaxy stellar kinematics is available the galaxy dynamical history can be directly traced, reflected in a specific orbital structure, and signatures in the velocity moments (Hernquist & Barnes 1991; Hoffman et al. 2010; Emsellem et al. 2004, 2014).

Recent surveys of bright, discrete stellar probes such as globular clusters (GCs) (Côté et al. 2001; Schuberth et al. 2010; Strader et al. 2011; Romanowsky et al. 2012; Pota et al. 2013) and Planetary Nebulas (PNs) have allowed a systematic study of the physical properties of early type galaxy halos, reaching regions where the galaxy surface brightness is too low for usual absorption line spectroscopy. In particular, PNs, as a consequence of their strong [OIII] emission line, whereby ∼15% of the luminosity of the central star is re-emitted in the forbidden [OIII] line at $\lambda5007$ Å (Dopita et al. 1992), have been targeted in several surveys, allowing to trace the light and the motion in nearby clusters (Hui et al. 1993; Méndez et al. 2001; Peng et al. 2004; Coccato et al. 2009; McNeil et al. 2010; McNeil-Moylan et al. 2012; Cortesi et al. 2013; Longobardi et al. 2013, 2015a,b), and out to 50-100 Mpc distance (Ventimiglia et al. 2010, 2011; Gerhard et al. 2005).

M87 is the central galaxy in the Virgo subcluster A (Binggeli et al. 1987). It is considered a type cD-galaxy, well described by a single Sersic fit with $n \sim 11$ (Kormendy et al. 2009; Janowiecki et al. 2010), and with an extended halo that reaches $R$ ∼200 kpc . M87 is usually presented as system dominated by random motion, with the lack of any significant rotation (van der Marel 1994a; Sembach & Tonry 1996; Gebhardt et al. 2011). However, in more recent studies, this galaxy has been shown to present a low-amplitude kinematically distinct core (Emsellem et al. 2014), as well as low rotational components (Murphy et al. 2011; Emsellem et al. 2014), and rising stellar velocity dispersion at large radii (Murphy et al. 2011). Many tracers were used to probe the M87 mass distribution: X-ray measurements (Nulsen & Bohringer 1995; Churazov et al. 2010), integrated stellar kinematics (Murphy et al. 2011, 2014), GC kinematics (Côté et al. 2001; Strader et al. 2011; Romanowsky et al. 2012; Zhu et al. 2014), and PN kinematics (Arnaboldi et al. 2004; Doherty et al. 2009). All these studies identify M87 as one of the most massive galaxy with a total mass $M \sim 10^{12} M_{\odot}$.

In this study we present the kinematics of the outer regions of M87 using a sample of PNs that is ~ 15 times larger than the one previously available (Doherty et al. 2009), covering major axis distance from ~ 20 kpc to ~ 175 kpc. The kinematic data were acquired from the FLAMES/VLT spectroscopic survey (Longobardi et al. 2013, 2015a). The total sample consists of 254 objects classified as M87 halo PNs and 44 intra cluster (IC) PNs, for which we have obtained line-of-sight velocities (LOSVs) with an estimated median velocity accuracy of 4.2 $\mathrm{kms^{-1}}$ .

The paper is structured as follows: in Sect.5.2 we present the M87 halo kinematics, i.e. averaged velocity and velocity dispersion maps. The $\lambda(R)$ profile and M87 composite velocity dispersion profile are given in Sect.5.3 together with a dynamical interpretation of it. Finally we give our conclusion in Sect.5.4.

In this work we adopt a distance modulus of 30.8 for M87 (Ciardullo et al. 2002; Longobardi et al. 2015a), implying a physical scale of 73 pc $\mathrm{arcsec^{-1}}$

## 5.2 Kinematics of the smooth outer halo of M87

### 5.2.1 The main halo: identification of kinematical features

In this work we study the kinematical properties of the 254 PNs bound to the halo of M87 (Longobardi et al. 2015a). To characterise its average kinematical properties we must take into account the presence of substructures that may imprint on the halo LOSV distribution (LOSVD). In the recent study by Longobardi et al. (2015b), photometric and kinematic evidence are given for an accretion event in the outer halo of M87. Using Gaussian Mixture Models on the PN LOSVD, they statistically assigned PNs to either the main smooth halo or to the colder substructure, identifying 54 PNs with a small probability $\gamma_P \sim 0.3$ to be part of the main smooth halo. In this study the contribution of each PN to the average kinematical properties is weighted by its membership probability, as we discuss in more details in Sect5.2.2.

Furthermore, in Fig. 5.1, where we show the sky position of the spectroscopically confirmed PNs, colour coded based on their LOSVs, we see two groups of two PNs each close in positions and velocities, with values in the tail of the LOSVD (red circles), in an overall system clearly dominated by random motions. Small galaxies around M87 could contribute to the sampled halo PNs, however we note that the above identified PNs do not correlate with the position and systemic velocity of any of the low luminosity galaxies present in the surveyed area. Hence, we enquire how likely such velocity configurations are by using conditional probability theory, following which the probability of event $V_i$ and event $V_j$ equals:

$$\mathrm{P(V_i \text{ and } V_j) = P(V_i) \times P(V_j|V_i)}, \tag{5.1}$$

i.e. the probability of event $V_i$ times the probability of event $V_j$ given that event $V_i$ is occurred. If the two variables are independent, Eq. 5.1 reduces to

$$\mathrm{P(V_i \text{ and}V_j) = P(V_i) \times P(V_j)}. \tag{5.2}$$

Assuming a halo velocity distribution represented by a Gaussian centred on $V_{sys} = 1275 \mathrm{kms^{-1}}$, and with dispersion $\sigma \sim 300 \mathrm{kms^{-1}}$ (Longobardi et al. 2015b), then the probabilities to observe such groups of velocities are $P_1 \sim 0.9\%$ and $P_2 \sim 0.1\%$, respectively. These 4 PNs, are then classified as kinematical outliers and will not be considered further.

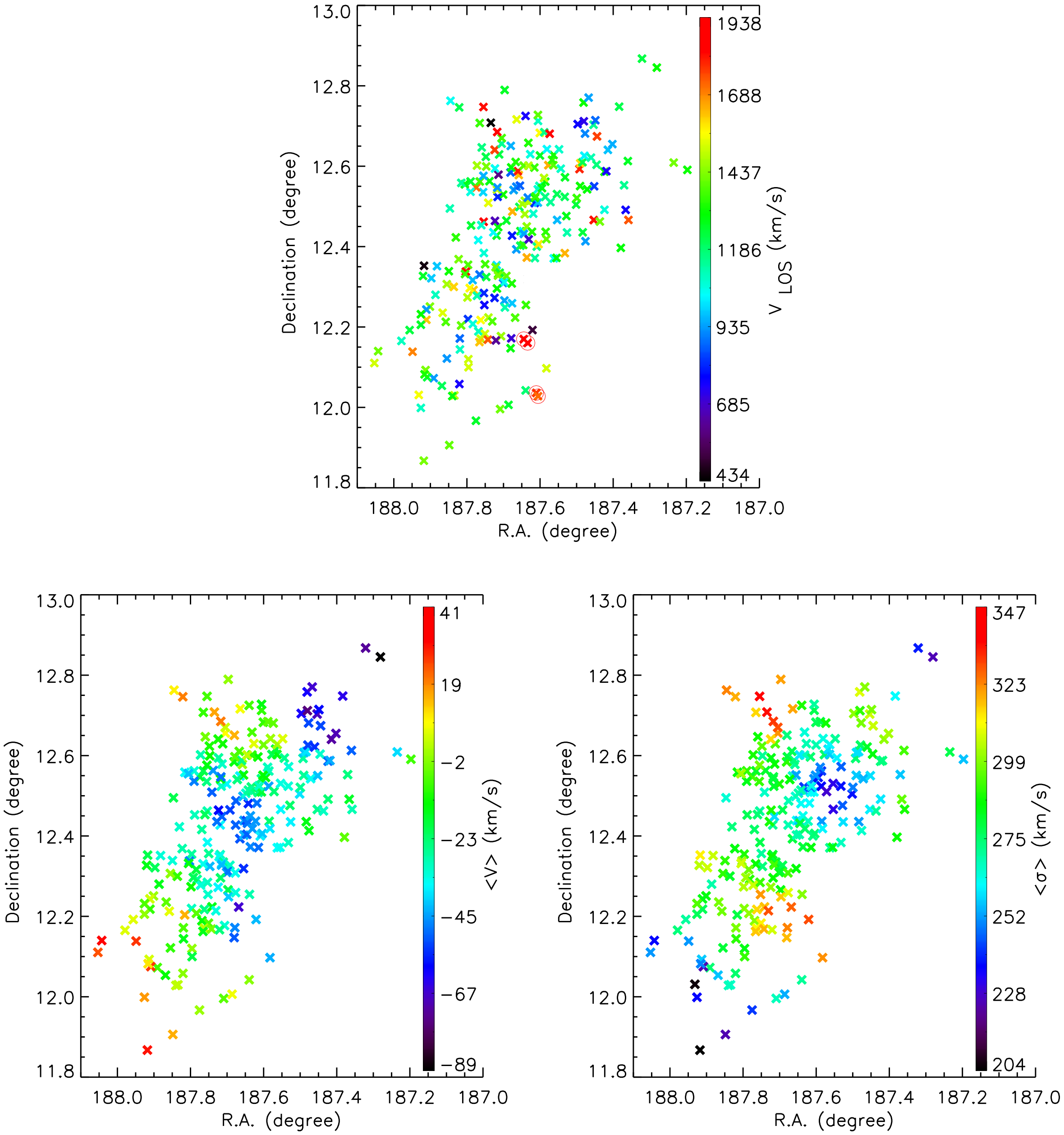

Figure 5.1: **Top Panel:** Spatial distribution of the 254 spectroscopically confirmed PNs in the halo of M87, colour coded according to their $V_{LOS}$. This figure shows a system dominated by random motion. Red circles identify two groups of PNs, close in velocity and in space, with high probability (> 99%) to be kinematic outliers from the smooth component (see text for more details). **Bottom Panels:** Smoothed PN velocity and velocity dispersion fields for M87 from the sample of PNs without the 4 kinematical outliers. The maps indicate that the kinematics becomes more rotational supported at large radii. North is up, East to the left.

### 5.2.2 Average two-dimensionsl halo kinematics

In order to quantify deviations from the mean stellar velocity structure, we build an average two-dimensional velocity field computed using an adaptive Gaussian kernel that defines the spatial resolution (Coccato et al. 2009). Simultaneously we weight each PN velocity by its membership probability, $\gamma_P$, to belong to the smooth halo components (see Sect.5.2.1). At the position of each source $(x_P, y_P)$ the mean velocity and velocity dispersion are:

$$< \mathrm{V}(x_P, y_P) >= \frac{\sum_i \mathrm{V}_{\mathrm{LOS,i}} w_{P,i}}{\sum_i w_{P,i}}, \tag{5.3}$$

and

$$< \sigma(x_P, y_P) >= \left[ \frac{\sum_i \mathrm{V}^2_{\mathrm{LOS,i}} w_{P,i}}{\sum_i w_{P,i}} - < \mathrm{V}(x_P, y_P) >^2 - \Delta V^2 \right]^{1/2}, \tag{5.4}$$

where $\mathrm{V}_{\mathrm{LOS,i}}$ is the ith PN LOSV, and $\Delta V$ is the instrumental error, given by the median uncertainty on the velocity measurements, i.e. $\Delta V = 4.2\,\mathrm{kms}^{-1}$; $w_{P,i}$ is the ith PN weight given by:

$$w_{P,i} = \exp - \frac{D_i^2}{2k(x_p, y_p)^2} \times \gamma_{P,i}, \tag{5.5}$$

where $D_i$ is the distance of the ith PN to $(x_P, y_P)$ , and $k$ is the amplitude of the kernel. Following Coccato et al. (2009) $k$ is defined to be dependent on the local tracers density $\rho(x, y)$ via:

$$k(x, y) = A \sqrt{\frac{M}{\pi\rho}} + B, \tag{5.6}$$

with $M = 20$ representing the number of nearest neighbours considered in the smoothing technique, and $A$ and $B$ chosen by processing simulated sets of PNs for a given density, velocity gradient and velocity dispersion as deduced from the data. The simulations resulted in the $A = 0.25$, and $B = 20.4$ kpc. Thus, each PN is assigned a weight that depends on the distance, on the amplitude of the kernel (in turn depending on the local tracer's number density[1]), and on its probability to belong to the smooth halo component.

In Fig. 5.1 we show the mean two-dimensional velocity field for the M87 halo. The kinematics is dominated by random motion with no or negligible rotation in the innermost region, while at larger distances a small rotational component starts being visible. In Fig. 5.1 (bottom panels) we also notice the presence of a group of PNs (NW region) characterised by higher mean velocities. This is likely to be driven by the high velocity dispersion values measured at the same positions.

The amplitude and direction of rotation is then computed by modelling the total rotation as function of the position angle with a simple rotation model of the form:

$$< \mathrm{V} > (\phi, \mathrm{R}) = \mathrm{V}_{\mathrm{sys}}(\mathrm{R}) + \mathrm{V}_{\mathrm{rot}}(\mathrm{R}) \cos[\mathrm{PA} - \mathrm{PA}_{\mathrm{kin}}(\mathrm{R})], \tag{5.7}$$

---

[1] See Coccato et al. (2009) for a fully description of the smoothing technique.

Table 5.1: Amplitude and direction of rotation in 4 elliptical bins. Column 1: Major axis range four the four elliptical bins. Columns 2, 3 & 4: Fitted values $V_{sys}$, $V_{rot}$, and $PA_{kin}$ as obtained by fitting Eq.5.7 to the mean veloocity field.

| $\Delta R$ (kpc) | $V_{sys}$ ($kms^{-1}$) | $V_{rot}$ ($kms^{-1}$) | PA (deg) |
|---|---|---|---|
| $R \leq 45$ | 1238.3± 23.5 | 7.1±9.4 | – |
| $45 < R \leq 70$ | 1253.2± 20.5 | 7.5±14.6 | – |
| $70 < R \leq 90$ | 1255.3± 19.9 | 9.6±16.6 | – |
| $R > 90$ | 1265.3± 22.7 | 37.3±23.3 | -35.8±10.5 |

where, R is the major axis distance of each PN from the galaxy centre at a position angle, PA, on the sky, and with mean velocity $< V >$. The fitted values $V_{sys}$, $V_{rot}$, and $PA_{kin}$, represent the M87 systemic velocity, the amplitude of rotation, and the kinematic PA. To study possible kinematic decoupling we divide our PN sample in four different elliptical bins, and the amplitude of rotation is measured for each of the bins separately. In Table5.1 we list the results of the fitting.

As shown in Fig 5.2, in the first three bins the system is characterised by low rotation, consistent inside the uncertainties with no-rotation. For larger major axis distances, i.e. $R > 90$ kpc, a rotational component is observed with $V_{rot} = 38.3 \pm 22.4\,kms^{-1}$, and $PA_{kin} = -35.8^\circ \pm 10.5^\circ$. With the photometric major axis at $PA_{phot} = -25.6^\circ$ (Kormendy et al. 2009)[2], this result is consistent with no misalignment between photometric and kinematic axes. The fitted systemic velocities show variance within the uncertainties, hence no radial gradients towards the outer regions is measured, with values consistent with $V_{sys} = 1275 \pm 24\,kms^{-1}$ estimated by Longobardi et al. (2015b) from the whole PN sample. The uncertainties on the fitted variables are computed by means of Monte Carlo simulations as described in Coccato et al. (2009, 2013).

## 5.3 The kinematics of the M87 halo: ordered vs random motion

### 5.3.1 $\lambda_R$ parameter

Using the full two-dimensional kinematics information, Emsellem et al. (2007) introduced the $\lambda_R$ parameter as a proxy for the projected specific angular momentum, spectroscopically measured as:

$$\lambda_R = \frac{\sum_{i=1}^{N_p} F_i R_i | < V > - V_{sys}|}{\sum_{i=1} F_i R_i \sqrt{(< V_i > - V_{sys})^2 + < \sigma_i >^2}}, \tag{5.8}$$

where $F_i$ is the flux associated to the ith point, and $< V >$, and $< \sigma >$ are as in Eq.5.3 and Eq.5.4. The $\lambda(R)$ parameter measures the importance of rotation as function of the distance from the galaxy's centre. With a threshold of 0.1, galaxies are separated into:

---

[2] PA are measured with respect the north axis with the east to the left.

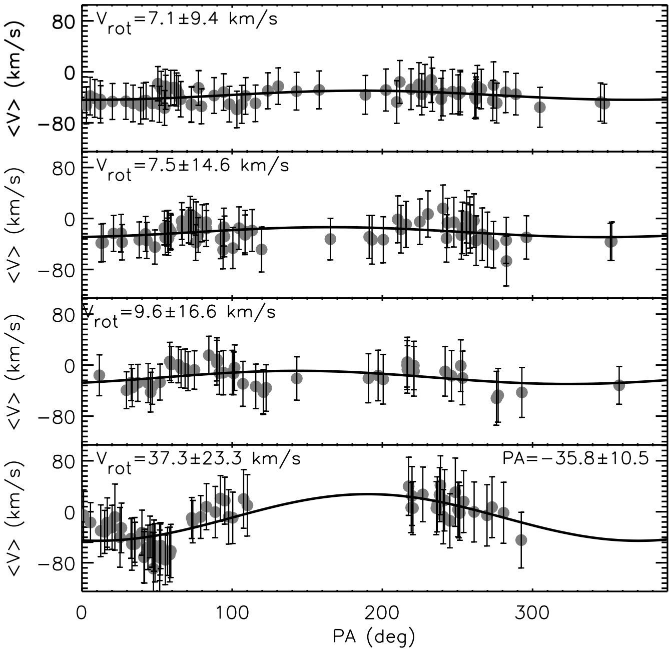

Figure 5.2: Mean LOS velocities subtracted of the galaxy systemic velocity $V_{sys} = 1275\,\mathrm{kms}^{-1}$ as function of the PA on the sky for different elliptical bins (see text). The continuous black line shows the best-fit model to the data (Eq.5.7), consistent with a system dominated by dispersion in the first three bins, while the last panel indicate an amplitude of $\sim 40 \pm 20\,\mathrm{kms}^{-1}$ and a kinematic major axis at P.A.=120°. The uncertainties on the fitted variables are computed by means of Monte Carlo simulations.

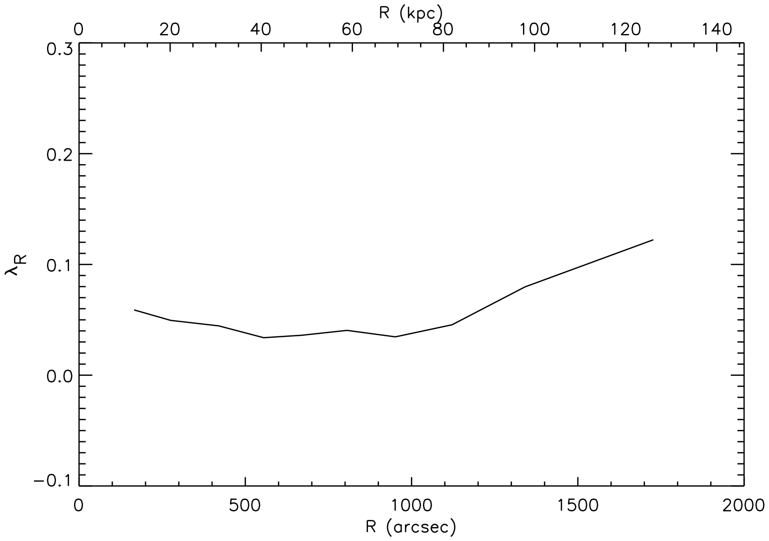

Figure 5.3: Radial $\lambda_R$ profile for the halo of M87 extracted from PNs kinematics. Its values increase for $R > 70$ kpc, crossing the fast rotator regime at $R \sim 110$ kpc.

> *fast rotators,* $\lambda(\mathrm{R}) > 0.1$: These are found to be systems with well aligned photometric and kinematic axis, nearly axisymmetric, with a rising $\lambda_{\mathrm{R}}$ profile;

> *slow rotators,* $\lambda(\mathrm{R}) < 0.1$: These are more massive systems, nearly round with a significant misalignment between photometric and kinematic axis, moderate degree of triaxiality, with a flat or decreasing $\lambda_{\mathrm{R}}$ profile.

We use the average two-dimensional velocity and velocity dispersion fields at the position of the PNs to compute the PN $\lambda_R$ profile in the surveyed area around M87. Following Coccato et al. (2009), when computing this parameter from the two-dimensional PN kinematics the weighting factor $\mathrm{F_i}$ is replaced by $1/c_R$, with $c_R$ the spatial completeness factor as in Longobardi et al. (2015a). As Coccato et al. (2009) states, this implicitly incorporates the weighting by the local stellar surface density. In Fig. 5.3 we show the $\lambda_R$ profile for major axis distance $20\,\mathrm{kpc} \lesssim \mathrm{R} \lesssim 200\,\mathrm{kpc}$. This is shown to be almost flat in the inner $\sim 70$ kpc, and then slowly increases to values of $\sim 0.13$.

### 5.3.2 Velocity dispersion profile of M87

We are now interested in studying the composite velocity dispersion profile for the halo of M87. In the next sections we are going to trace the M87 $\sigma$ profile covering the galaxy entirely, by using our new PN data and available absorption line and IFU data from the literature. Moreover by comparing the different techniques we investigate the effects of the Virgo IC component, and the need to account for the transition region between the galaxy halo and the Virgo ICL.

#### Effects from environment

In the area surveyed in this work, Longobardi et al. (2015a) showed that the M87 halo is surrounded by IC stars that represent a distinct dynamical component in terms of velocity distribution and parent stellar population. We now enquire what effect the IC population would have on measurements of LOSVD from luminosity weighted tracers when such kinematical decomposition is not applied.

In Fig. 5.4 we plot the projected phase-space distribution for both halo (red asterisks) and IC (blue asterisks) PNs. In the same figure we also show the LOSVD ’running average’, and ’running dispersion’[3] for both the halo only (black lines) and the total halo+IC (green lines) system. While the overall mean velocity is not affected by the IC component, it is clear that this population has an impact on the estimate of the dispersion. If halo and IC populations are not separated, the dispersion is overestimated, reaching, at its maximum, the Virgo sub-cluster A velocity dispersion $\sim 800\,\mathrm{kms^{-1}}$ (Binggeli et al. 1993; Conselice et al. 2001). Moreover, as shown by the black line in Fig. 5.4, the halo dispersion first slowly rises, and then declines, reaching its minimum at $R \sim 170\,\mathrm{kpc}$. This trend is statistically significant as it is observed

---

[3] This quantities represent the mean and the dispersion of sub-sequences of $n$ PNs from the full data-set. In our work $n = 25$.

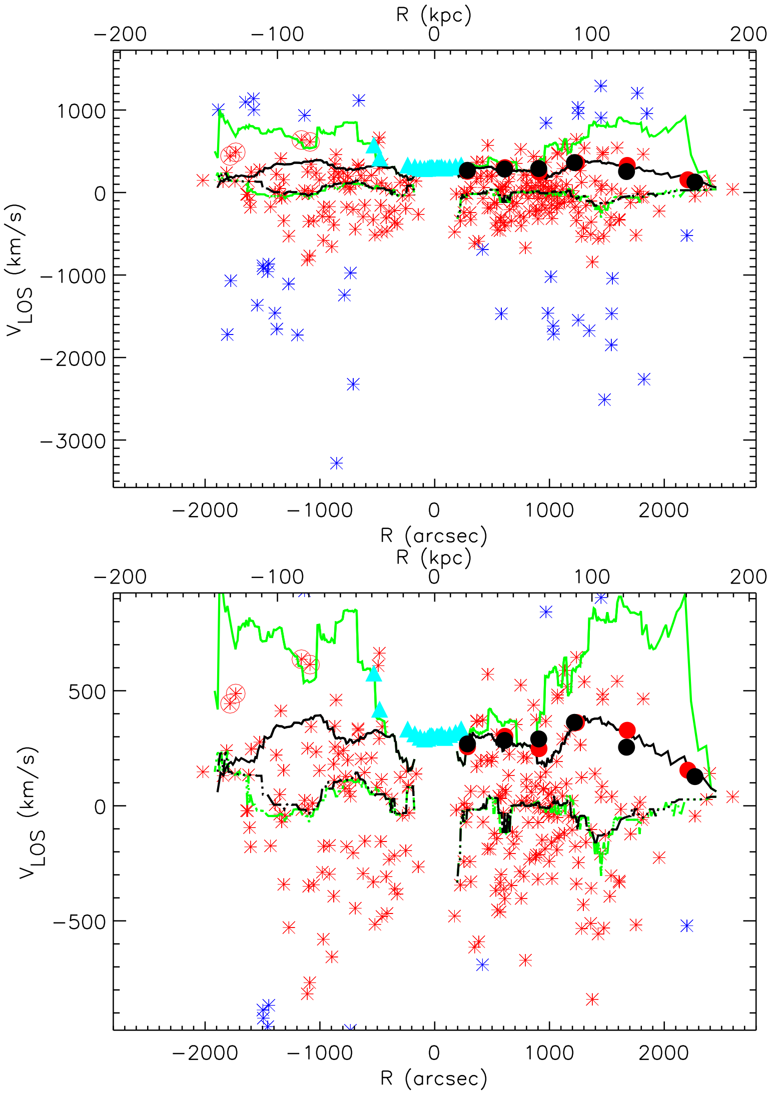

Figure 5.4: **Top-Panel:** Projected phase-space diagram showing $V_{\mathrm{LOS}}$ vs. major axis distance $R$ from the centre of M87, for all the spectroscopically confirmed PNs, both M87 halo (red asterisks) and IC component (blue asterisks) from Longobardi et al. (2015a). Asterisks in red circles are the four PNs identified as kinematical outliers in Sect.5.2.1. Black dashed-dot and black continuous lines depict the running average, and running dispersion computed from the 254 halo PNs. Red dots represent the robust estimate of the halo dispersion from Longobardi et al. (2015a), while black dots show the velocity dispersion when PN velocities are weighted by $\gamma_P$ (see text). They agree well, all showing a decline for major axis distances $R > 100\,\mathrm{kpc}$. Green dashed-dot and Green continuous lines represent the same running average, and running dispersion for the halo+IC component system. It is clear that the inclusion of the ICL component leads to larger $\sigma$ values (see text for more details). Cyan triangles are IFU velocity dispersion data from Murphy et al. (2011, 2014). IC light may impact the IFU kinematics. **Bottom-Panel**: Same as top panel with a narrower velocity range ± 1000 km/s centred on the systemic velocity of M87.

Table 5.2: Velocity dispersion estimates from the new PN sample in the outer region of M87. Column 1: Major axis distance. Columns 2, 3 & 4: Velocity dispersions and their uncertainties for the three different systems halo+IC component, M87 halo, and M87 smooth halo only (see text for more details).

| R<br>(kpc) | $\sigma$ halo+ICL<br>($\mathrm{kms}^{-1}$) | $\sigma$ robust halo<br>($\mathrm{kms}^{-1}$) | $\sigma$ smooth halo<br>($\mathrm{kms}^{-1}$) |
|---|---|---|---|
| 20 | 243.6± 69.5 | 256.7±33.1 | 269.1±34.7 |
| 45 | 358.5± 70.0 | 301.7±23.3 | 284.0±22.7 |
| 70 | 506.4± 57.5 | 248.3±26.5 | 290.6±32.1 |
| 90 | 691.8± 61.0 | 361.7±26.5 | 362.6±30.4 |
| 12 | 794.6± 67.8 | 328.1±37.1 | 254.6±36.7 |
| 170 | 512.7± 88.3 | 154.6±36.4 | 126.9±36.6 |

over several sub-sequences of the halo running dispersion. On the other hand, if we consider the halo+IC PNs together, the increase is steeper starting from smaller radii, and outer decline is caused by the outermost PNs.

In Sect. 5.2.1 we also pointed out the presence of substructures in the halo of M87. Hence, we now recompute the halo velocity dispersion by binning the PN velocity sample in elliptical annuli, and for each bin we determine a weighted estimate of the LOSV dispersion from the M87 systemic velocity,

$$\sigma = \frac{\sum_i (\mathrm{V_{LOS,i}} - \mathrm{V_{sys}})^2 \gamma_{P,i}}{\sum_i \gamma_{P,i}}, \tag{5.9}$$

where, $\gamma_{P,i}$ represents the ith PN probability to belong to the main halo component (see Sect. 5.2.1).

In Table5.2 we list the the PN velocity dispersion values for different radial bins and the different systems M87 halo+IC component, M87 halo, and M87 smooth halo only. The robust estimate of the halo dispersion computed by Longobardi et al. (2015a) and the dispersion values that come if each PN velocity is weighted by its probability to belong to the smooth halo component, agree well showing deviation at the major axis distances where the identified substructures have the highest density of tracers (see also Fig. 5.4).

### Overall trend of the halo $\sigma$ profile

The aim now is to construct a composite $\sigma$ profile by accounting for different tracers at different radii, hence tracing M87 stellar motion from the innermost regions out to R ∼ 175 kpc.

The random-motion profile of M87 is shown in Fig. 5.5, where the major axis distance is replaced with the average ellipse radius, $R_{\mathrm{avg}} = (ab)^{1/2}$ of the isophote[4]. At small distances ($R_{\mathrm{avg}} < 10$ kpc) absorption line measurements (van der Marel 1994b; Sembach & Tonry 1996; Emsellem et al. 2014)[5], show a falling velocity dispersion. As we move into the halo, the PN kinematics indicates that the velocity dispersion increases to a value $\sigma \sim 400\,\mathrm{kms}^{-1}$ out to $R_{\mathrm{avg}} \sim 100$ kpc, and for larger distances it steeply decreases and reaches its lowest value $\sigma \sim 100\,\mathrm{kms}^{-1}$ at $R_{\mathrm{avg}} \sim 150$ kpc.

---

[4] We have assumed an constant ellipticity of $e = 0.4$ (Kormendy et al. 2009).

[5] data from Sembach & Tonry (1996) have been corrected for the 7-10% offset from most other data set (but see Doherty et al. (2009) for more details).

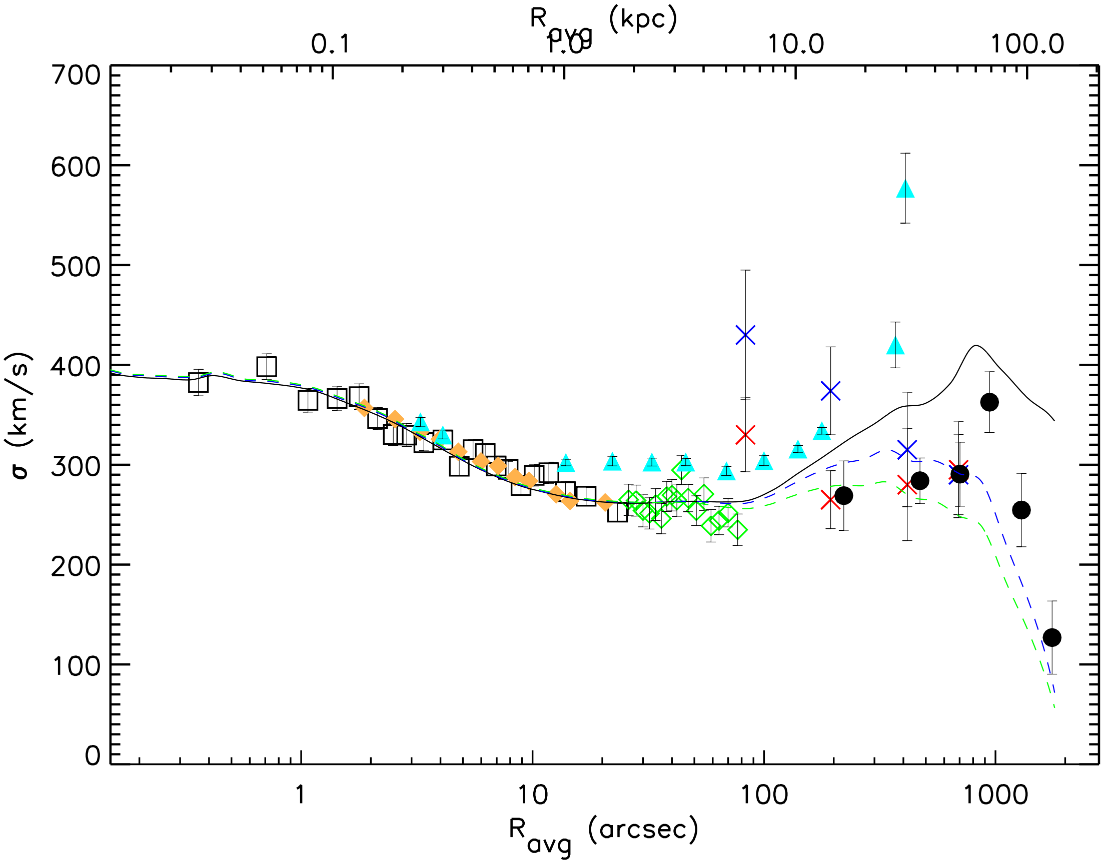

Figure 5.5: Velocity dispersion profile for the halo of M87 that combines data from absorption line spectra and discrete LOS velocity measurements for globular cluster and PNs. The inner 80 ″ are data from van der Marel (1994b) (squares) and from Sembach & Tonry (1996) (green diamonds). Cyan triangles are VIRUS-P data from Murphy et al. (2011), and the red and blue stars are globular cluster velocity dispersion data from Agnello et al. (2014). Filled dots represent velocity dispersion data for the halo PNs determined in this work.

In Fig.5.5 we also show VIRUS-P data from Murphy et al. (2011, 2014). These data overlap with the velocity dispersion from absorption line spectra (van der Marel 1994b; Sembach & Tonry 1996; Emsellem et al. 2014) resulting systematically higher. From beyond a few 100″ the reason might be the contamination by IC light (see Fig. 5.4). As shown by Fig.5.5 the ICL is contributing the most in the outer regions of the galaxy where the bound halo component starts becoming fainter.

For completeness we also show red and blue GC velocity dispersion data from Agnello et al. (2014) (red and blue stars, respectively). While the $\sigma$ values of the red GCs are in better agreement with those measured for the integrated light, blue GCs $\sigma$ value deviates strongly.

To better understand the observed velocity dispersion profile, we compare it with the predicted $\sigma$ profiles from spherical Jeans models by Doherty et al. (2009). They solved spherical Jeans equation assuming a total gravitational potential as determined by X-ray studies (Nulsen & Bohringer 1995), and with an orbital structure that becomes highly radially anisotropic ($\beta > 0.4$) in the outer halo (black continuous line in Fig.5.5). The observed small velocity dispersion values at $R \sim 175$ kpc are then reproduced under the hypothesis of a truncated halo (dashed lines in Fig.5.5). As shown in Fig.5.5, none of these models can simultaneously reproduce the increase followed by the sharp decline as traced by our data. As we are going to discuss in Sect. 5.4, this velocity dispersion profile might be reflecting the dynamical history of M87.

## 5.4 Discussion and Conclusion

In Sect.5.2 we presented the kinematics of the Virgo central galaxy M87. We used 250 PNs as kinematical tracers covering the outer halo of M87 from $\sim 20$ kpc to $\sim 170$ kpc along the major axis. The smoothed Gaussian velocity map showed that the system is not rotating in the inner regions, while for major axis distances, $R > 90$ kpc, the kinematics shows a small amount of ordered motion. This is also consistent with the measured $\lambda(R)$ profile that slowly grows to values $\sim$0.13 in the outermost bin.

We then enquire whether the observed kinematics reflects the galaxy halo formation history. The fact that M87 has a cD envelope is consistent with accretion phenomena dominating its outer mass assembly (Kormendy et al. 2009; Bender et al. 2014). In the case of M87, this has been recently proven by Longobardi et al. (2015b) who discovered an accretion event in the halo of M87 revealed as both kinemtaic and spatial substructure. This result shows that beyond $\sim 60$ kpc the M87 halo is still growing. Then the relatively higher importance of ordered motion in the outer regions can be interpreted as the streaming motion of material that has been recently accreted. From the observed velocities the accreted material is falling in behind M87, and in the North side it would have fallen along the LOS. Interestingly, the furthest PNs with bluer velocities are spatially associated with a previously identified tidal stream (Mihos et al. 2005; Romanowsky et al. 2012).

Together with the velocity we also give information on its second moment. As shown in Fig.5.5 the $\sigma$ profile is measured to increase between major axis distance 20 kpc $<$ R $<$ 90 kpc. In principle, this rise can be explained by the presence of a massive dark-matter halo (Murphy et al. 2014). However, the large radial coverage of this study shows that, after its first rise, the $\sigma$

profile sharply decreases to a value of $\sigma \sim 100\,\mathrm{kms}^{-1}$ at major-axis distances $R \sim 170$ kpc, making its dynamical interpretation more complex. When comparing the dispersion profile with previously published Jeans dynamical models by Doherty et al. (2009) it is clear that they cannot be representative of the observed data. Besides the poor match in the inner regions the strongest disagreement happens beyond 100 kpc where the observed steep decline makes these models unlikely, even when a truncation of the halo is considered.

In a pioneering paper by Dressler (1979) the rise of the second velocity moment measured in the cD galaxy in Abell2029 was interpret as a 'necessary' condition for the cD halo to be forming by accumulated debris from tidal interaction and dynamical friction during the halo formation processes. This interpretation would strengthen the argument of the ongoing assembling of the M87 halo. If the M87 kinematics reflects the cD halo growth through accretion events, the decrease of the $\sigma$ profile might result from a complex orbital distribution of the stars that cannot be represented by a spherical symmetric models under the assumption of dynamical equilibrium.

Future work is required that will focus on more sophisticated dynamical models. This will make it possible to constraint the orbital structure far in the outer region of the giant elliptical M87, tracing the transition from the smooth halo to the still forming and lumpy halo, and also to understand the interplay between DM content and stellar orbital distribution in the measured dispersion profile of the central cluster galaxy M87.

# Chapter 6

# Summary and Conclusion

One of the most fascinating questions in extragalactic astronomy is "How did galaxies form and evolve". According to the current theory of hierarchical formation and evolution of structures, galaxies grow by mergers and accretion of smaller subsystems. In this framework the outermost regions of galaxies, where dynamical times are longer, contain an enormous wealth of information, expected to preserve fossil records of these events in the form of long-lasting substructures imprinted in the phase space, star formation history and chemical enrichment. However, thus far detailed studies have been carried out only for very few isolated nearby galaxies (e.g McConnachie et al. 2009; Crnojević et al. 2013), and little is known about the physical properties of galaxy halos in galaxy clusters where dynamical histories may not be the same as isolated systems.

The work in this thesis is dedicated to this topic and studies the light and motions in the halo of the brightest cluster galaxy (BCG) in Virgo A, the giant elliptical M87, and its surrounding intracluster light (ICL).

The formation of BCG halos and ICL is tightly related to the morphological transformation of galaxies in clusters. In the hierarchical structure formation paradigm, accretion events are believed to play a predominant role in the formation of both the ICL and massive ellipticals (Murante et al. 2007; De Lucia & Blaizot 2007; Puchwein et al. 2010). The ICL, mainly formed by tidally stripped stars from satellite galaxies, can represent up to 50% of the optical light in a cluster, depending on the dynamical status and history of the hosting structure. On the other hand, accretion events are believed to be responsible for the growth of massive elliptical halos at relatively low redshift ($z < 2$; Oser et al. 2010). In dense environments, accretion is even more dramatic, such that at the centre of massive clusters, at the bottom of their potential well, the majority of stars are expected to be accreted (Laporte et al. 2013; Cooper et al. 2014).

When studying BCGs we might wonder whether any physical difference does exist between the central galaxy halo and the ICL. Observationally, we are able to identify the presence of accreted components by the excess of light on top of the extrapolation of the galaxy's inner profile (Zibetti et al. 2005; Gonzalez et al. 2007; D'Souza et al. 2014), by high Sèrsic indices ($n > 4$ Kormendy et al. 2009), by the variation in the ellipticity profile (Tal & van Dokkum 2011; D'Souza et al. 2014; Longobardi et al. 2015b), and through colour gradients. However, no differentiation between the BCG's halo and the ICL is usually possible and their photometric properties and colours are usually determined by treating them as a continuum.

But is this really the case? Does the BCG halo smoothly continue into the ICL? Is the extended halo (cD halo), observed around many BCGs, the central part of the cluster diffuse light component or is it part of the host galaxy, and hence not sharing the dynamics of the ICL? And if they are different components, do they form from the accretion of similar systems?

The Virgo cluster, the nearest large scale structure in the Universe, and its central galaxy M87 are prime targets to address the topic of galaxy/cluster formation and evolution, and to answer the questions raised above. Virgo is characterised by both spatial and kinematic substructures, with different subgroups possessing different morphological mixes of galaxies (Binggeli et al. 1987). Moreover, the evidence that many galaxies are presently falling towards the cluster core, as well as the presence of a complex network of extended tidal features revealed by deep photometric survey, suggest that Virgo core is not completely in equilibrium. Close to the dynamical centre of Virgo (Binggeli et al. 1987; Nulsen & Bohringer 1995; Mei et al. 2007), the giant elliptical galaxy M87, is a prime subject of investigation to understand the accretion histories of galaxies in dense environments. It has a cD halo, well described by a single Sèrsic fit with $n \sim 11$ (Kormendy et al. 2009), that extends out to $\sim 150$ kpc in radius, and down to 27 magarcsec$^{-2}$ in the V-band (optical light). The observed blue colour gradients towards its outskirts (Rudick et al. 2010), hence the inferred metallicity and age gradients (Liu et al. 2005; Montes et al. 2014), are consistent with a late build up of its halo, suggesting that here we can find a great deal of information about the physical mechanisms that govern the mass assembly in the Universe.

The most significant challenge to investigate galaxy halos far away from their centres is that these regions have a very low surface brightness, making it difficult for most of the traditional techniques to be successful. Planetary nebulas (PNs) are stars in the mass range between 1 and 8 $M\odot$ at the end of the AGB phase, before they end their lives as white dwarfs. They offer a unique tool to investigate these environments owing to their strong [OIII] emission line, whereby $\sim 15\%$ of the luminosity of the central star is re-emitted in the forbidden [OIII] line at $\lambda5007$ Å (Dopita et al. 1992). Several PN surveys in nearby clusters and out to 50-100 Mpc have shown that these tracers can be detected out to several hundreds of kpc and that they supply a great deal of information about their hosting system. The observed properties of the PN population, such as the $\alpha$-parameter, and the PN luminosity function (PNLF) correlate with the physical properties of the system they belong to, such as colour, metallicity, age, and merger history. Moreover, as a consequence of their strong emission line their line-of-sight velocity (LOSV) can be successfully measured making PNs valuable tracers of galaxy kinematics.

Initial studies of PNs in Virgo showed that their numbers varied over different fields (Aguerri et al. 2005), suggesting that the ICL is poorly mixed. Furthermore, recent research of a small sample of PNs around M87 found that by using their kinematics, they might be separable into components that are bound to either the potential of M87's halo or that of the cluster (Doherty et al. 2009).

The work in this thesis proves these initial hypotheses, by shedding light on the halo-ICL dichotomy, through the combined use of new large and extended photometric and spectroscopic PN samples. The photometric data was obtained as result of a wide and deep survey with the Suprime-Cam at the Subaru Telescope. From the photometry, PNs were identified using a set of sophisticated colour-magnitude selection criteria (Arnaboldi et al. 2002). Kinematic data of the PNs was acquired with the FLAMES spectrograph at the VLT telescope, representing a $\sim 15$ times larger sample than what was previously used (Doherty et al. 2009).

Together, these new surveys led to the acquirement of the most extended ($\sim 0.5\,\mathrm{deg}^2$ area centred on M87), deepest, and largest sample of PNs in the Virgo cluster core that allowed the study of the transition region between galaxy halo and IC component. This thesis used this wealth of data to come to the following conclusions:

1. **The BCG halo of M87 and the Virgo ICL are dynamically distinct components with different velocity and density distributions.**

   The kinematic study of the PN sample showed the coexistence of two dynamically distinct components, reflected in the bimodality of the LOSV distribution, which has strong asymmetric wings that make it deviate from the near-Gaussian distributions usually measured for early type galaxies (Gerhard 1993; Bender et al. 1994). Using a robust procedure we showed that the total velocity distribution splits into two Gaussian kinematic components, one that feels the potential of the galaxy ($\mathrm{V_{halo}} = 1275\,\mathrm{kms^{-1}}$, $\sigma_{\mathrm{halo}} \simeq 300\,\mathrm{kms^{-1}}$) and a broader one that reflects the cluster potential ($\mathrm{V_{ICL}} = 1000\,\mathrm{kms^{-1}}$, $\sigma_{\mathrm{ICL}} \simeq 900\,\mathrm{kms^{-1}}$). This allowed a robust separation of the two PN populations, leading to the identification of 243 PNs for the M87 halo and 44 ICPNs.

   The study of the PN number density profile showed that the halo PNs follow the galaxy surface brightness profile, with M87's light profile described by a $n = 11.8$ Sèrsic law, while the ICPNs are characterised by a much shallower power-law profile, $\mathrm{I_{ICL}} \propto \mathrm{R}^{\gamma}$ with $\gamma$ in the range [-0.34,-0.04]. We then concluded that halo and ICPNs have very different surface density distributions with the halo more centrally concentrated, but less extended than the free floating component.

   These results are consistent with recent cosmological hydro-dynamical simulations that showed that it is possible to separate the BCG halo and the ICL components when the particles' dynamical information is available (Dolag et al. 2010; Cui et al. 2014). Identifying simulated particles as either a halo or IC component, they find two distinct stellar populations in terms of kinematics, spatial distribution and physical properties. Other studies (Cooper et al. 2014) that do not adopt such a dynamical definition of the two components and study the BCG halo plus ICL system as a single entity, find double-Sèrsic surface density profiles in the centre of their simulated cluster, where the inner regions ($\mathrm{R} < 200\,\mathrm{kpc}$) are dominated by 'relaxed' accreted components, and at larger radii by 'unrelaxed' accreted components. It is likely that the distinct BCG and ICL components found in the hydro-dynamical simulations are related to the relaxed and unrelaxed accreted component found in the particle tagging analysis. Combining the results of this thesis with the theoretical work outlined above, leads to the following conclusion:

   - *The progenitors of the stars in the steeper Sèrsic (relaxed) component would be accreted from more massive systems at higher redshifts, while the stars in the shallower and more extended ICL (unrelaxed) component would come from the accretion of less massive systems at lower redshifts.*

This bimodality does not have to be representative of the dynamical history of every cluster. It is plausible to think that a more uniform distribution of progenitor masses would lead to a single dynamical BCG plus ICL system reflected in a smooth transition in kinematics and physical properties.

2. **M87's halo and Virgo's ICL have two different parent stellar populations, consistent with the halo being redder and more metal rich than the ICL.**

   Once I discovered that Virgo's BCG halo and ICL were two different dynamical components, I investigated their physical properties through the study of their $\alpha$-parameters and their PNLFs.

   The $\alpha$-parameter, that quantifies the stellar luminosity associated to a PN, is observed to correlate with the integrated (B-V) colour of the underlying stellar population. Bluer galaxies ((B-V) $< 0.8$) are characterised by an almost constant value of specific PN number, $\alpha \sim 3 \times 10^{-8}$ $\mathrm{N_{PN}L_{\odot,bol}^{-1}}$, while the spread increases for redder galaxies, spanning a range $10^{-9} - 6 \times 10^{-8}$ $\mathrm{N_{PN}L_{\odot,bol}^{-1}}$. The reddest objects with the lowest $\alpha$-parameters are associated with the older and more metal rich systems as a correlation does exist between $\alpha$ and the far (FUV-V) colour (Buzzoni et al. 2006)

   From the analysis of both the photometric and spectroscopically confirmed PN samples we find that:

   - *Halo and IC PNs have different $\alpha-parameters$. We find $\alpha_{\mathrm{halo}} = 1.06\times10^{-8}$ $N_{\mathrm{PN}}L_{\odot,\mathrm{bol}}^{-1}$ and $\alpha_{\mathrm{ICL}} = 2.72\times10^{-8}$ $N_{\mathrm{PN}}L_{\odot,\mathrm{bol}}^{-1}$*[1].

   This result comes from the analysis of the total PN surface density profile that is seen to flatten and deviate from the galaxy light profile at large radii. The physical parameter that links a PN population to the luminosity of its parent stars is the PN specific number, and in this thesis it has been shown that a discrepancy between the PN number density and the light profile reflects a transition between different stellar systems characterised by different $\alpha$ values. By defining a two component photometric model I showed that the measured PN density profile is consistent with the surface-brightness profile at large radii if the ICL stellar components contribute $\sim 3$ times more PNs per unit luminosity than the halo. The gradient in $\alpha$ is then tracing the known gradient towards bluer colours at large radii (Rudick et al. 2010), due to the increased contribution of ICL at large distances and its lower metallicity as compared to the halo population (Williams et al. 2007; Liu et al. 2005; Montes et al. 2014).

   The PNLF depicts the number of PNs as a function of magnitude in a given galaxy system. It is often empirically described via a truncated exponential formula (Ciardullo et al. 1989) that reproduces the high mass cutoff observed for the PN central stars in nearby galaxies, and models the fading of a uniformly expanding nebula ionised by an unevolving central star. However, in the last ten years, deeper observations have shown that the PNLF slope is not the same for all of the different Hubble types, but that it correlates with the star formation history of the parent stellar population. Steeper slopes are observed in older stellar populations and flat or slowly decreasing slopes in younger systems (Ciardullo et al. 2004; Ciardullo 2010).

---

[1] These values come from the analysis of the spectroscopically followed-up sample. As we discuss in Chapt. 3 these values of the $\alpha$-parameter are consistent with those previously obtained from the photometric study.

The depth of the survey presented in this thesis allowed a detailed study of the shape of the PNLF for both M87's halo and the Virgo IC component. I discovered that:

- *Both the halo and IC PNLFs are steeper than the standard analytical function. Moreover, the ICPNLF shows an overall shallower gradient and there is a dip present at ~1-1.5 mag fainter than the bright cutoff.*

The steepening is consistent with older stellar populations that have a higher fraction of low mass core PNs. The dip, instead, is an evolutionary feature that is observed in luminosity functions of star forming systems such as the SMC (Jacoby & De Marco 2002), LMC (Reid & Parker 2010), M33 (Ciardullo et al. 2004), and NGC6822 (Hernández-Martínez & Peña 2009). One interpretation is that the dip is the result of a superposition of faint and brighter PN populations coming from older and younger stellar parent systems respectively (Rodríguez-González et al. 2014). Under this assumption we speculated that the position of the dip with respect to the bright cutoff could then reflect the relative importance of the two populations of stars, such that the older and more metal rich systems would show the dip moving towards brighter magnitudes. This could explain the dip observed in the ICPN population of Virgo.

Even though a solid theoretical understanding has not been reached yet, the presence of the dip in the ICPNLF, but not in the halo PNLF provides additional evidence that the halo and ICL are two different stellar populations.

After showing the relation between the cD halo and ICL, the question I addressed next, was whether the cD halo of M87 can be considered as a smooth dynamical component or whether it shows signatures of accretion events.

3. **The M87 cD halo is still growing through the accretion of smaller systems as predicted by hierarchical galaxy evolution models.**

This finding is based on the synergy between PN kinematics and deep V/B band photometry. The accretion event was first identified as a kinematic substructure in the PN velocity phase space that showed a chevron like (V-shaped) feature as the result of a not complete phase-mixing of a disrupted satellite. From theoretical simulations (e.g. Bullock & Johnston 2005) the chevron describes the orbits of the satellite, and its edge traces the distance where the disrupted stars reach the end of their radial excursion and slow to a halt before they reverse their motion. As a consequence of the wrapping of the satellite orbits, an enhancement of the stellar density is revealed in the form of spatially extended low-surface brightness feature. For the first time this feature has been observationally confirmed by this work. At the distance at which I measured the edge of the chevron the analysis of the deep V-band image showed the presence of a ‘crown’ shaped substructure, that was unknown before this study. This structure causes an increase in surface brightness by $\gtrsim$ 60%. The crown represents the densest region of the entire substructure that extends $\sim$ 50 kpc along the major axis, where we also observe a variation in the ellipticity profile and colour gradient. These results show that,

- *This accretion event has caused an important modification of the outer halo of M87 in the last Gyr.*

The event is consistent with a progenitor galaxy with $L = 2.8 \pm 1.0 \times 10^9 L_{\odot,V}$, a colour of $(B - V) = 0.75 \pm 0.05$, and a stellar mass of $M = 6.4 \pm 2.3 \times 10^9 M_\odot$.

In addition, the overall halo PN kinematics also suggest that the growth of M87 is still ongoing. As a consequence of the large radial extension of our survey we were able to see that the halo is dominated by random motion closer to the centre, while it shows a small amount of rotation, $V_{rot} = 37.3 \pm 23.3\,\mathrm{kms}^{-1}$, for major axis distances $R > 90$ kpc. The kinematic decoupling is also supported by the $\lambda(R)$ parameter, a proxy of the angular momentum, that increases to $\lambda(R) = 0.13$ at large radii.

For the first time M87’s velocity dispersion profile has been traced out ~200 kpc along the major axis. This showed that as we move into the halo the velocity dispersion increases to a value $\sigma \sim 400\,\mathrm{kms}^{-1}$ and then sharply declines to a value $\sigma \sim 100\,\mathrm{kms}^{-1}$. The presence of ordered motion in the outer halo has been interpreted as the presence of accreted material of which we are tracing its streaming motion. If what we are measuring is the result of the hierarchical assembling of the M87 halo, then the shape of the sigma profile will be reflecting a complex orbital distribution of the stars. When comparing the dispersion profile with previously published dynamical models by Doherty et al. (2009) it is clear that the orbital distribution of the stars in the outer halo of M87 cannot be represented by spherical symmetric models under the assumption of dynamical equilibrium.

Thanks to this work we can now claim that:

- *Beyond ~ 60 kpc M87’s halo is still assembling, and its kinematics reflect the dynamical complexity of a system still growing.*

## 6.1 Future Work

To understand the Virgo cluster as whole, a study involving different regions and physical properties must be carried out. In the framework of “galaxy evolution in high density environments”, the study of the bright giant elliptical galaxy M49, logically follows and complements the one carried out for M87. M49 is at the centre of the Virgo sub-cluster B that is now falling towards M87. Hence, it represents a structure in a phase prior to cluster formation, being less processed than M87. In addition, the outer regions of this galaxy show a radial gradient in colour (Mihos et al. 2013), believed to be the result of a strong gradient in metallicity, where the bluer colours are associated with metal poor populations.

Using PN data from the M49 PN Suprime-Cam survey we are going to extract a catalogue of ~500 PNs covering the galaxy halo out to ~70 kpc (see Fig. 1.8). By following the same work flow as for M87, I can model the PN density as function of radii and determine whether M49's halo blends into the ICL. Furthermore, with the spectroscopic follow-up of this data the study of the projected phase-space will prove whether the observed metal-poor component in the outer region of M49 indeed belongs to the galaxy halo or is, in fact, a part of the ICL.

This study will be an important step to constrain the accretion history of galaxies and diffuse stellar component in quite a different regime, making it possible to draw conclusions on the role of the environment in galaxy evolution.

# Appendix A

# Spectroscopically confirmed emission line objects in the outer region of M87: the catalogue

In Chapter3 I presented the PN spectroscopic survey carried out with the FLAMES spectrograph on the VLT-UT2 telescope in the GIRAFFE+MEDUSA mode.

The final sample of emission line objects consisted of 380 sources, of which 287 were classified as PNs (243 bound to the M87 halo, and 44 to the IC component), and the remaining as background emission line galaxies, either as Ly$\alpha$ or as [OII] emitters. Based the shape of the line profile of the strongest emission. The extracted spectra fall into these categories:

- PN spectra: the [OIII]$\lambda$5007Å emission of a PN is characterised by a narrow and symmetric line shape and very low continuum. In high S/N spectra, we detected the redshifted [OIII] $\lambda$4959/5007Å doublet. Typical S/N ratios for the spectroscopically confirmed PN [OIII]]$\lambda$5007Å cover a range of $2.5 \leq S/N \leq 8.5$ per resolution element.

- Ly$\alpha$ spectra: the emission line of a Ly$\alpha$ emitter has a broader and more asymmetric line profile, characterised by a steep drop-off at bluer wavelengths. Such a signature comes from the forest absorption bluewards of Ly$\alpha$: the symmetric emission line is truncated below the object redshift by Ly$\alpha$ scattering in the intergalactic medium.

- [OII] spectra: the [OII]$\lambda$3727Å emitters are characterised by the redshifted, resolved and broad emission lines of the oxygen doublet at $\lambda$3726-3729Å.

In what follows I list the characteristics of the spectroscopically confirmed emission line objects in the outer regions of M87, followed by their FLAMES spectra.

Table A.1: **Spectroscopically confirmed halo PNs**

Column 1: PN ID. Column 2 & 3 Right Ascension and Declination. Columns 4: Redshifted [OIII]$\lambda$5007 Å emission wavelength. Columns 5: Line-of-sight velocity. Column 6: $\lambda$5007 magnitude.

| **Class Halo** | **ID** | **R. A.** (deg) | **Dec.** (deg) | $\lambda_{5007}$ (Å) | $\mathbf{V}_{\mathrm{LOS}}$ (kms$^{-1}$) | $m_{5007}$ |
|---|---|---|---|---|---|---|
| | M87_PN_1 | 187.71854 | 12.353678 | 5023.9 | 1009.6 | 26.2 |
| | M87_PN_2 | 187.72142 | 12.348808 | 5030.6 | 1413.4 | 27.1 |
| | M87_PN_3 | 187.6765 | 12.427306 | 5020.3 | 795.7 | 27.1 |
| | M87_PN_4 | 187.71867 | 12.427481 | 5028.0 | 1256.5 | 27.0 |
| | M87_PN_5 | 187.71025 | 12.335025 | 5027.8 | 1243.8 | 27.1 |
| | M87_PN_6 | 187.66475 | 12.393191 | 5022.5 | 930.5 | 27.4 |
| | M87_PN_7 | 187.75 | 12.356303 | 5029.7 | 1362.5 | 27.4 |
| | M87_PN_8 | 187.71446 | 12.331519 | 5029.6 | 1355.9 | 26.9 |
| | M87_PN_9 | 187.7148 | 12.327861 | 5030.8 | 1425.4 | 26.7 |
| | M87_PN_10 | 187.75357 | 12.384075 | 5025.0 | 1080.3 | 27.5 |
| | M87_PN_11 | 187.72763 | 12.435656 | 5024.2 | 1032.3 | 27.1 |
| | M87_PN_12 | 187.71429 | 12.448464 | 5028.5 | 1285.2 | 27.7 |
| | M87_PN_13 | 187.65375 | 12.402114 | 5027.1 | 1204.3 | 27.4 |
| | M87_PN_14 | 187.65349 | 12.438325 | 5028.1 | 1264.8 | 26.8 |
| | M87_PN_15 | 187.74701 | 12.324327 | 5027.6 | 1233.1 | 27.6 |
| | M87_PN_16 | 187.69196 | 12.464794 | 5028.0 | 1258.2 | 26.6 |
| | M87_PN_17 | 187.692 | 12.327072 | 5030.3 | 1398.4 | 26.6 |
| | M87_PN_18 | 187.64667 | 12.438114 | 5024.2 | 1032.3 | 26.9 |
| | M87_PN_19 | 187.64583 | 12.404033 | 5029.3 | 1338.5 | 26.5 |
| | M87_PN_20 | 187.64426 | 12.43172 | 5022.8 | 944.9 | 27.0 |
| | M87_PN_21 | 187.76553 | 12.330517 | 5021.9 | 891.5 | 26.7 |
| | M87_PN_22 | 187.701 | 12.309298 | 5022.2 | 913.7 | 26.6 |
| | M87_PN_23 | 187.72328 | 12.464052 | 5018.0 | 660.9 | 27.2 |
| | M87_PN_24 | 187.69734 | 12.31117 | 5024.6 | 1057.5 | 26.3 |
| | M87_PN_25 | 187.67549 | 12.487284 | 5034.4 | 1643.5 | 26.7 |
| | M87_PN_26 | 187.67545 | 12.487333 | 5034.4 | 1641.1 | 26.7 |
| | M87_PN_27 | 187.63622 | 12.450075 | 5031.1 | 1444.6 | 27.8 |
| | M87_PN_28 | 187.71776 | 12.295794 | 5028.8 | 1305.0 | 27.0 |
| | M87_PN_29 | 187.63087 | 12.418137 | 5018.4 | 684.2 | 27.1 |
| | M87_PN_30 | 187.769 | 12.416172 | 5024.4 | 1042.5 | 27.2 |
| | M87_PN_31 | 187.64154 | 12.480819 | 5031.6 | 1473.3 | 27.2 |
| | M87_PN_32 | 187.75346 | 12.284417 | 5020.5 | 807.1 | 27.6 |
| | M87_PN_33 | 187.63612 | 12.372925 | 5034.5 | 1647.7 | 27.4 |
| | M87_PN_34 | 187.65637 | 12.49852 | 5027.1 | 1204.3 | 27.3 |
| | M87_PN_35 | 187.78429 | 12.316503 | 5023.1 | 967.1 | 27.7 |

**Table A.1 – *continued on next page***

**Table A.1** – ***continued from previous page***

| **Class** | **ID** | **R. A.** | **Dec.** | $\lambda_{5007}$ | $V_{\mathrm{LOS}}$ | $m_{5007}$ |
|---|---|---|---|---|---|---|
| **Halo** | | (deg) | (deg) | (Å) | ($\mathrm{kms}^{-1}$) | |
| | M87_PN_36 | 187.62196 | 12.436973 | 5029.3 | 1335.5 | 27.9 |
| | M87_PN_37 | 187.67717 | 12.308206 | 5029.1 | 1325.3 | 27.5 |
| | M87_PN_38 | 187.64845 | 12.506208 | 5031.6 | 1472.1 | 27.0 |
| | M87_PN_39 | 187.78178 | 12.292065 | 5034.0 | 1618.3 | 26.6 |
| | M87_PN_40 | 187.72438 | 12.272491 | 5020.2 | 793.9 | 26.8 |
| | M87_PN_41 | 187.75412 | 12.461741 | 5037.8 | 1846.6 | 27.8 |
| | M87_PN_42 | 187.76045 | 12.45325 | 5025.2 | 1088.1 | 26.9 |
| | M87_PN_43 | 187.79688 | 12.354792 | 5030.2 | 1389.5 | 27.0 |
| | M87_PN_44 | 187.77242 | 12.277689 | 5025.7 | 1119.8 | 28.3 |
| | M87_PN_45 | 187.65471 | 12.318883 | 5039.4 | 1938.3 | 26.7 |
| | M87_PN_46 | 187.61842 | 12.481863 | 5025.1 | 1086.3 | 27.2 |
| | M87_PN_47 | 187.79218 | 12.29672 | 5033.1 | 1566.8 | 28.4 |
| | M87_PN_48 | 187.80283 | 12.337646 | 5038.4 | 1883.8 | 26.6 |
| | M87_PN_49 | 187.63242 | 12.51103 | 5031.8 | 1485.3 | 27.1 |
| | M87_PN_50 | 187.80504 | 12.331863 | 5029.6 | 1354.7 | 26.7 |
| | M87_PN_51 | 187.60896 | 12.400066 | 5026.3 | 1154.6 | 27.3 |
| | M87_PN_52 | 187.75212 | 12.254531 | 5019.7 | 759.7 | 26.8 |
| | M87_PN_53 | 187.63338 | 12.521892 | 5022.1 | 906.5 | 27.7 |
| | M87_PN_54 | 187.6973 | 12.265911 | 5022.8 | 944.3 | 28.0 |
| | M87_PN_55 | 187.60376 | 12.406055 | 5033.5 | 1584.8 | 27.7 |
| | M87_PN_56 | 187.61412 | 12.371403 | 5025.9 | 1132.4 | 26.8 |
| | M87_PN_57 | 187.61455 | 12.508245 | 5020.7 | 822.6 | 27.6 |
| | M87_PN_58 | 187.79842 | 12.273658 | 5031.8 | 1482.9 | 26.7 |
| | M87_PN_59 | 187.70084 | 12.529319 | 5029.0 | 1317.0 | 26.6 |
| | M87_PN_60 | 187.71599 | 12.523736 | 5020.6 | 813.7 | 27.8 |
| | M87_PN_61 | 187.67212 | 12.540608 | 5028.9 | 1309.2 | 27.1 |
| | M87_PN_62 | 187.60587 | 12.509553 | 5023.3 | 976.0 | 26.8 |
| | M87_PN_63 | 187.61391 | 12.521308 | 5028.8 | 1306.8 | 26.9 |
| | M87_PN_64 | 187.74133 | 12.508833 | 5032.7 | 1542.3 | 27.2 |
| | M87_PN_65 | 187.61249 | 12.524708 | 5029.5 | 1345.7 | 27.0 |
| | M87_PN_66 | 187.78853 | 12.452441 | 5027.8 | 1243.8 | 27.5 |
| | M87_PN_67 | 187.66463 | 12.548965 | 5022.2 | 912.5 | 27.9 |
| | M87_PN_68 | 187.69612 | 12.248731 | 5025.7 | 1121.6 | 27.3 |
| | M87_PN_69 | 187.65488 | 12.551717 | 5021.5 | 871.2 | 27.6 |
| | M87_PN_70 | 187.82254 | 12.368733 | 5030.7 | 1419.4 | 26.9 |
| | M87_PN_71 | 187.58463 | 12.436636 | 5029.3 | 1337.9 | 26.9 |
| | M87_PN_72 | 187.6765 | 12.259089 | 5023.4 | 980.2 | 26.9 |
| | M87_PN_73 | 187.74112 | 12.223494 | 5031.7 | 1478.7 | 27.9 |

**Table A.1** – ***continued on next page***

**Table A.1** – ***continued from previous page***

| **Class** | **ID** | **R. A.** | **Dec.** | $\lambda_{5007}$ | $V_{\rm LOS}$ | $m_{5007}$ |
|---|---|---|---|---|---|---|
| **Halo** | | (deg) | (deg) | (Å) | (kms$^{-1}$) | |
| | M87_PN_74 | 187.58263 | 12.418517 | 5030.5 | 1406.8 | 26.6 |
| | M87_PN_75 | 187.71788 | 12.542045 | 5032.0 | 1499.1 | 27.0 |
| | M87_PN_76 | 187.60596 | 12.542306 | 5024.8 | 1067.7 | 27.6 |
| | M87_PN_77 | 187.76228 | 12.217158 | 5033.1 | 1563.2 | 26.8 |
| | M87_PN_78 | 187.7168 | 12.547031 | 5022.5 | 928.7 | 28.1 |
| | M87_PN_79 | 187.836 | 12.300025 | 5033.8 | 1604.5 | 27.0 |
| | M87_PN_80 | 187.83604 | 12.29999 | 5033.9 | 1610.0 | 27.0 |
| | M87_PN_81 | 187.58588 | 12.523852 | 5026.4 | 1161.2 | 27.2 |
| | M87_PN_82 | 187.73055 | 12.213985 | 5030.1 | 1386.5 | 26.9 |
| | M87_PN_83 | 187.79697 | 12.219478 | 5020.9 | 829.8 | 27.0 |
| | M87_PN_84 | 187.59454 | 12.54544 | 5028.3 | 1276.8 | 27.4 |
| | M87_PN_85 | 187.78378 | 12.207553 | 5024.9 | 1070.1 | 27.6 |
| | M87_PN_86 | 187.65805 | 12.578116 | 5034.2 | 1627.9 | 27.8 |
| | M87_PN_87 | 187.57146 | 12.510631 | 5026.1 | 1142.6 | 27.1 |
| | M87_PN_88 | 187.84933 | 12.338711 | 5029.0 | 1316.4 | 28.3 |
| | M87_PN_89 | 187.75557 | 12.53547 | 5023.5 | 988.6 | 26.9 |
| | M87_PN_90 | 187.83025 | 12.422917 | 5029.3 | 1337.9 | 27.8 |
| | M87_PN_91 | 187.66051 | 12.587555 | 5037.0 | 1799.3 | 27.6 |
| | M87_PN_92 | 187.68069 | 12.584475 | 5021.6 | 872.4 | 28.0 |
| | M87_PN_93 | 187.855 | 12.306561 | 5031.6 | 1473.3 | 27.8 |
| | M87_PN_94 | 187.58549 | 12.561605 | 5028.6 | 1296.0 | 27.1 |
| | M87_PN_95 | 187.76854 | 12.189089 | 5025.3 | 1097.7 | 27.5 |
| | M87_PN_96 | 187.58896 | 12.570811 | 5031.8 | 1487.7 | 27.9 |
| | M87_PN_97 | 187.55318 | 12.466286 | 5023.2 | 968.8 | 27.9 |
| | M87_PN_98 | 187.81583 | 12.203706 | 5030.4 | 1402.7 | 27.6 |
| | M87_PN_99 | 187.63855 | 12.254711 | 5029.5 | 1349.9 | 28.2 |
| | M87_PN_100 | 187.7135 | 12.579017 | 5017.1 | 604.0 | 27.3 |
| | M87_PN_101 | 187.73825 | 12.562828 | 5028.3 | 1274.4 | 27.8 |
| | M87_PN_102 | 187.668 | 12.223264 | 5030.0 | 1378.1 | 27.7 |
| | M87_PN_103 | 187.75078 | 12.183056 | 5032.3 | 1514.7 | 27.8 |
| | M87_PN_104 | 187.61554 | 12.59678 | 5029.7 | 1357.7 | 26.6 |
| | M87_PN_105 | 187.67867 | 12.596952 | 5028.6 | 1297.2 | 27.8 |
| | M87_PN_106 | 187.63174 | 12.601384 | 5031.7 | 1482.3 | 27.1 |
| | M87_PN_107 | 187.55359 | 12.530583 | 5027.1 | 1202.5 | 27.5 |
| | M87_PN_108 | 187.56238 | 12.370578 | 5024.4 | 1043.2 | 27.3 |
| | M87_PN_109 | 187.76219 | 12.170587 | 5032.0 | 1500.9 | 27.8 |
| | M87_PN_110 | 187.66653 | 12.610456 | 5029.3 | 1333.7 | 27.3 |
| | M87_PN_111 | 187.74268 | 12.168542 | 5036.0 | 1734.6 | 26.9 |

**Table A.1** – ***continued on next page***

**Table A.1** – ***continued from previous page***

| **Class** | **ID** | **R. A.** | **Dec.** | $\lambda_{5007}$ | $V_{\mathrm{LOS}}$ | $m_{5007}$ |
|---|---|---|---|---|---|---|
| **Halo** | | (deg) | (deg) | (Å) | (kms$^{-1}$) | |
| | M87_PN_112 | 187.77457 | 12.547217 | 5035.6 | 1712.4 | 27.0 |
| | M87_PN_113 | 187.55492 | 12.371822 | 5028.5 | 1288.2 | 27.5 |
| | M87_PN_114 | 187.86629 | 12.235381 | 5032.5 | 1530.8 | 28.1 |
| | M87_PN_115 | 187.76562 | 12.162514 | 5034.0 | 1620.7 | 26.5 |
| | M87_PN_116 | 187.85783 | 12.212745 | 5030.1 | 1383.5 | 27.0 |
| | M87_PN_117 | 187.72325 | 12.594389 | 5024.5 | 1049.7 | 28.2 |
| | M87_PN_118 | 187.76471 | 12.561822 | 5029.7 | 1360.7 | 27.6 |
| | M87_PN_119 | 187.81938 | 12.17152 | 5021.7 | 882.0 | 27.4 |
| | M87_PN_120 | 187.70667 | 12.177028 | 5031.3 | 1456.0 | 27.7 |
| | M87_PN_121 | 187.79008 | 12.536309 | 5024.7 | 1060.5 | 28.1 |
| | M87_PN_122 | 187.57721 | 12.602594 | 5034.5 | 1648.9 | 26.8 |
| | M87_PN_123 | 187.72063 | 12.166717 | 5017.3 | 618.3 | 27.9 |
| | M87_PN_124 | 187.75479 | 12.576086 | 5023.0 | 955.7 | 26.7 |
| | M87_PN_125 | 187.53233 | 12.523955 | 5027.1 | 1202.5 | 27.9 |
| | M87_PN_126 | 187.52795 | 12.476007 | 5028.2 | 1268.4 | 27.5 |
| | M87_PN_127 | 187.62663 | 12.629797 | 5024.7 | 1062.9 | 28.0 |
| | M87_PN_128 | 187.88586 | 12.279984 | 5025.4 | 1103.1 | 27.3 |
| | M87_PN_129 | 187.88188 | 12.35132 | 5023.3 | 977.8 | 27.2 |
| | M87_PN_130 | 187.60016 | 12.626612 | 5028.1 | 1264.8 | 27.5 |
| | M87_PN_131 | 187.56351 | 12.602736 | 5030.4 | 1399.6 | 27.3 |
| | M87_PN_132 | 187.52612 | 12.435 | 5025.8 | 1126.4 | 26.8 |
| | M87_PN_133 | 187.56679 | 12.615659 | 5029.5 | 1347.5 | 27.0 |
| | M87_PN_134 | 187.56683 | 12.615723 | 5029.5 | 1349.9 | 27.0 |
| | M87_PN_135 | 187.54329 | 12.593988 | 5025.1 | 1087.5 | 27.5 |
| | M87_PN_136 | 187.53159 | 12.57248 | 5028.1 | 1261.8 | 28.0 |
| | M87_PN_137 | 187.81898 | 12.144147 | 5025.3 | 1098.3 | 27.5 |
| | M87_PN_138 | 187.53217 | 12.383675 | 5034.4 | 1642.3 | 26.9 |
| | M87_PN_139 | 187.74707 | 12.5995 | 5030.7 | 1421.2 | 26.8 |
| | M87_PN_140 | 187.67867 | 12.171842 | 5018.6 | 695.0 | 27.4 |
| | M87_PN_141 | 187.78987 | 12.561939 | 5027.8 | 1245.0 | 27.3 |
| | M87_PN_142 | 187.89728 | 12.321417 | 5023.5 | 986.2 | 27.1 |
| | M87_PN_143 | 187.56284 | 12.627603 | 5029.1 | 1322.3 | 27.9 |
| | M87_PN_144 | 187.71182 | 12.629397 | 5027.5 | 1228.9 | 28.9 |
| | M87_PN_145 | 187.58109 | 12.642333 | 5024.2 | 1033.5 | 26.8 |
| | M87_PN_146 | 187.90108 | 12.250764 | 5030.8 | 1427.8 | 27.0 |
| | M87_PN_147 | 187.63174 | 12.658133 | 5029.2 | 1331.3 | 27.6 |
| | M87_PN_148 | 187.84654 | 12.494901 | 5025.6 | 1117.4 | 27.2 |
| | M87_PN_149 | 187.80566 | 12.555256 | 5028.5 | 1285.8 | 27.3 |

**Table A.1** – ***continued on next page***

**Table A.1** – ***continued from previous page***

| **Class**<br>**Halo** | **ID** | **R. A.** (deg) | **Dec.** (deg) | $\lambda_{5007}$ (Å) | $V_{\mathrm{LOS}}$ ($\mathrm{kms}^{-1}$) | $m_{5007}$ |
|---|---|---|---|---|---|---|
| | M87_PN_150 | 187.67996 | 12.650602 | 5023.0 | 958.7 | 27.2 |
| | M87_PN_151 | 187.79596 | 12.119917 | 5032.2 | 1509.3 | 26.6 |
| | M87_PN_152 | 187.50137 | 12.504559 | 5027.6 | 1237.3 | 27.5 |
| | M87_PN_153 | 187.4995 | 12.520833 | 5029.6 | 1354.7 | 27.9 |
| | M87_PN_154 | 187.91083 | 12.243276 | 5022.5 | 931.7 | 27.5 |
| | M87_PN_155 | 187.77237 | 12.601711 | 5031.5 | 1467.4 | 27.6 |
| | M87_PN_156 | 187.54788 | 12.642034 | 5025.1 | 1083.3 | 27.6 |
| | M87_PN_157 | 187.6805 | 12.147114 | 5028.5 | 1287.0 | 26.6 |
| | M87_PN_158 | 187.74821 | 12.623484 | 5027.4 | 1224.1 | 26.8 |
| | M87_PN_159 | 187.72412 | 12.640761 | 5036.3 | 1756.7 | 27.0 |
| | M87_PN_160 | 187.81525 | 12.558512 | 5026.0 | 1136.0 | 27.0 |
| | M87_PN_161 | 187.91071 | 12.217841 | 5034.0 | 1618.3 | 27.7 |
| | M87_PN_162 | 187.64453 | 12.169842 | 5038.5 | 1888.6 | 28.2 |
| | M87_PN_163 | 187.70483 | 12.655974 | 5026.1 | 1146.8 | 27.0 |
| | M87_PN_164 | 187.62062 | 12.192317 | 5015.5 | 506.3 | 26.8 |
| | M87_PN_165 | 187.85475 | 12.121581 | 5022.4 | 925.1 | 27.8 |
| | M87_PN_166 | 187.91983 | 12.32702 | 5028.0 | 1259.4 | 27.9 |
| | M87_PN_167 | 187.79561 | 12.09998 | 5032.5 | 1524.9 | 27.2 |
| | M87_PN_168 | 187.91716 | 12.352389 | 5014.6 | 457.8 | 27.3 |
| | M87_PN_169 | 187.49037 | 12.550709 | 5029.0 | 1317.6 | 27.1 |
| | M87_PN_170 | 187.60054 | 12.682834 | 5033.1 | 1565.0 | 27.1 |
| | M87_PN_171 | 187.58842 | 12.68442 | 5026.3 | 1155.8 | 27.6 |
| | M87_PN_172 | 187.92584 | 12.231791 | 5028.7 | 1299.0 | 27.6 |
| | M87_PN_173 | 187.5735 | 12.680756 | 5038.1 | 1863.4 | 28.2 |
| | M87_PN_174 | 187.70483 | 12.670115 | 5029.9 | 1370.3 | 28.3 |
| | M87_PN_175 | 187.492 | 12.592972 | 5036.9 | 1792.1 | 27.9 |
| | M87_PN_176 | 187.92587 | 12.205524 | 5028.0 | 1258.2 | 27.8 |
| | M87_PN_177 | 187.63396 | 12.160333 | 5038.9 | 1911.9 | 27.4 |
| | M87_PN_178 | 187.4832 | 12.435522 | 5027.5 | 1231.3 | 27.2 |
| | M87_PN_179 | 187.48976 | 12.607314 | 5033.7 | 1599.2 | 27.6 |
| | M87_PN_180 | 187.75937 | 12.646813 | 5026.5 | 1169.6 | 27.7 |
| | M87_PN_181 | 187.47113 | 12.542601 | 5028.6 | 1297.2 | 28.0 |
| | M87_PN_182 | 187.48364 | 12.610003 | 5027.4 | 1223.5 | 27.1 |
| | M87_PN_183 | 187.60538 | 12.712627 | 5025.3 | 1098.3 | 26.3 |
| | M87_PN_184 | 187.47575 | 12.413355 | 5022.6 | 935.3 | 27.7 |
| | M87_PN_185 | 187.717 | 12.685208 | 5039.0 | 1920.3 | 27.3 |
| | M87_PN_186 | 187.47876 | 12.626014 | 5024.2 | 1028.2 | 27.8 |
| | M87_PN_187 | 187.66397 | 12.716441 | 5032.7 | 1539.2 | 27.8 |

**Table A.1** – ***continued on next page***

**Table A.1** – ***continued from previous page***

| **Class** | **ID** | **R. A.** | **Dec.** | $\lambda_{5007}$ | $V_{\rm LOS}$ | $m_{5007}$ |
|---|---|---|---|---|---|---|
| **Halo** | | (deg) | (deg) | (Å) | (kms$^{-1}$) | |
| | M87_PN_188 | 187.82054 | 12.058084 | 5019.5 | 746.0 | 27.0 |
| | M87_PN_189 | 187.60562 | 12.727547 | 5030.3 | 1397.8 | 27.6 |
| | M87_PN_190 | 187.63954 | 12.725058 | 5019.4 | 741.8 | 26.6 |
| | M87_PN_191 | 187.45192 | 12.550039 | 5021.1 | 844.8 | 27.3 |
| | M87_PN_192 | 187.45309 | 12.466088 | 5037.3 | 1813.7 | 28.2 |
| | M87_PN_193 | 187.95657 | 12.192297 | 5027.5 | 1230.7 | 28.4 |
| | M87_PN_194 | 187.89075 | 12.072683 | 5022.6 | 933.5 | 27.7 |
| | M87_PN_195 | 187.91302 | 12.092864 | 5030.9 | 1429.6 | 27.1 |
| | M87_PN_196 | 187.46063 | 12.621375 | 5025.6 | 1116.2 | 28.0 |
| | M87_PN_197 | 187.86838 | 12.053639 | 5027.1 | 1204.9 | 27.1 |
| | M87_PN_198 | 187.94867 | 12.138441 | 5035.2 | 1687.2 | 26.4 |
| | M87_PN_199 | 187.90854 | 12.075106 | 5027.7 | 1239.1 | 27.3 |
| | M87_PN_200 | 187.91579 | 12.08227 | 5029.1 | 1323.5 | 27.3 |
| | M87_PN_201 | 187.49701 | 12.704686 | 5019.8 | 763.9 | 26.9 |
| | M87_PN_202 | 187.44539 | 12.603756 | 5026.6 | 1172.0 | 27.6 |
| | M87_PN_203 | 187.47684 | 12.681309 | 5022.3 | 916.7 | 27.4 |
| | M87_PN_204 | 187.73454 | 12.708111 | 5014.2 | 433.8 | 26.8 |
| | M87_PN_205 | 187.83412 | 12.029766 | 5032.0 | 1495.5 | 27.7 |
| | M87_PN_206 | 187.83983 | 12.028106 | 5028.4 | 1279.8 | 27.1 |
| | M87_PN_207 | 187.43625 | 12.462292 | 5030.6 | 1414.0 | 26.9 |
| | M87_PN_208 | 187.48013 | 12.711756 | 5019.0 | 717.8 | 28.5 |
| | M87_PN_209 | 187.97899 | 12.165408 | 5025.4 | 1100.7 | 27.4 |
| | M87_PN_210 | 187.42368 | 12.491617 | 5024.8 | 1065.3 | 27.5 |
| | M87_PN_211 | 187.42351 | 12.586188 | 5028.9 | 1312.8 | 28.1 |
| | M87_PN_212 | 187.76479 | 12.707466 | 5029.7 | 1358.3 | 26.8 |
| | M87_PN_213 | 187.44417 | 12.674233 | 5036.0 | 1737.6 | 27.2 |
| | M87_PN_214 | 187.44412 | 12.67427 | 5036.4 | 1759.7 | 27.2 |
| | M87_PN_215 | 187.41846 | 12.587622 | 5019.4 | 744.2 | 26.5 |
| | M87_PN_216 | 187.45351 | 12.703153 | 5026.1 | 1146.2 | 27.2 |
| | M87_PN_217 | 187.93163 | 12.031044 | 5032.9 | 1551.8 | 26.6 |
| | M87_PN_218 | 187.44855 | 12.71427 | 5021.7 | 881.4 | 27.0 |
| | M87_PN_219 | 187.41434 | 12.640644 | 5023.2 | 971.2 | 28.1 |
| | M87_PN_220 | 187.48088 | 12.758375 | 5028.9 | 1314.6 | 27.4 |
| | M87_PN_221 | 187.75465 | 12.747416 | 5037.3 | 1816.1 | 27.5 |
| | M87_PN_222 | 187.58246 | 12.097236 | 5032.4 | 1521.9 | 27.0 |
| | M87_PN_223 | 187.9259 | 11.998703 | 5025.3 | 1096.5 | 27.3 |
| | M87_PN_224 | 187.40204 | 12.654916 | 5022.8 | 947.9 | 27.6 |
| | M87_PN_225 | 187.46695 | 12.77063 | 5022.7 | 942.5 | 27.5 |

**Table A.1** – ***continued on next page***

**Table A.1 –** ***continued from previous page***

| **Class** | **ID** | **R. A.** | **Dec.** | $\lambda_{5007}$ | $V_{\rm LOS}$ | $m_{5007}$ |
|---|---|---|---|---|---|---|
| **Halo** | | (deg) | (deg) | (Å) | (kms$^{-1}$) | |
| | M87_PN_226 | 187.63937 | 12.042292 | 5026.7 | 1180.4 | 27.5 |
| | M87_PN_227 | 187.70917 | 11.995761 | 5030.5 | 1409.2 | 27.8 |
| | M87_PN_228 | 187.69672 | 12.789561 | 5028.0 | 1260.0 | 28.8 |
| | M87_PN_229 | 187.68613 | 12.006248 | 5027.9 | 1252.9 | 28.3 |
| | M87_PN_230 | 187.77524 | 11.966839 | 5027.9 | 1254.0 | 27.1 |
| | M87_PN_231 | 187.37001 | 12.5527 | 5026.2 | 1152.2 | 28.2 |
| | M87_PN_232 | 187.61038 | 12.035954 | 5036.4 | 1762.7 | 27.4 |
| | M87_PN_233 | 188.04268 | 12.13988 | 5030.6 | 1412.2 | 27.5 |
| | M87_PN_234 | 187.36578 | 12.491344 | 5019.6 | 757.3 | 26.9 |
| | M87_PN_235 | 187.35971 | 12.612737 | 5028.0 | 1260.0 | 27.9 |
| | M87_PN_236 | 187.60538 | 12.027788 | 5035.7 | 1718.4 | 27.2 |
| | M87_PN_237 | 187.37892 | 12.396855 | 5028.5 | 1290.6 | 29.2 |
| | M87_PN_238 | 187.821 | 12.746442 | 5027.3 | 1214.5 | 28.3 |
| | M87_PN_239 | 188.05318 | 12.110403 | 5032.3 | 1515.3 | 29.0 |
| | M87_PN_240 | 187.35805 | 12.466258 | 5036.0 | 1739.3 | 26.7 |
| | M87_PN_241 | 187.84816 | 11.906125 | 5030.5 | 1405.6 | 27.1 |
| | M87_PN_242 | 187.84491 | 12.762709 | 5024.5 | 1049.7 | 27.8 |
| | M87_PN_243 | 187.91779 | 11.867352 | 5030.7 | 1422.4 | 27.6 |

Figure A.1: **Spectra of single confirmed halo PNs**. Red vertical lines mark the position of the two oxygen lines at their redshifted wavelengths. Spectra have been smoothed to 0.015 nm per pixel. The PN ID is specified as legend.

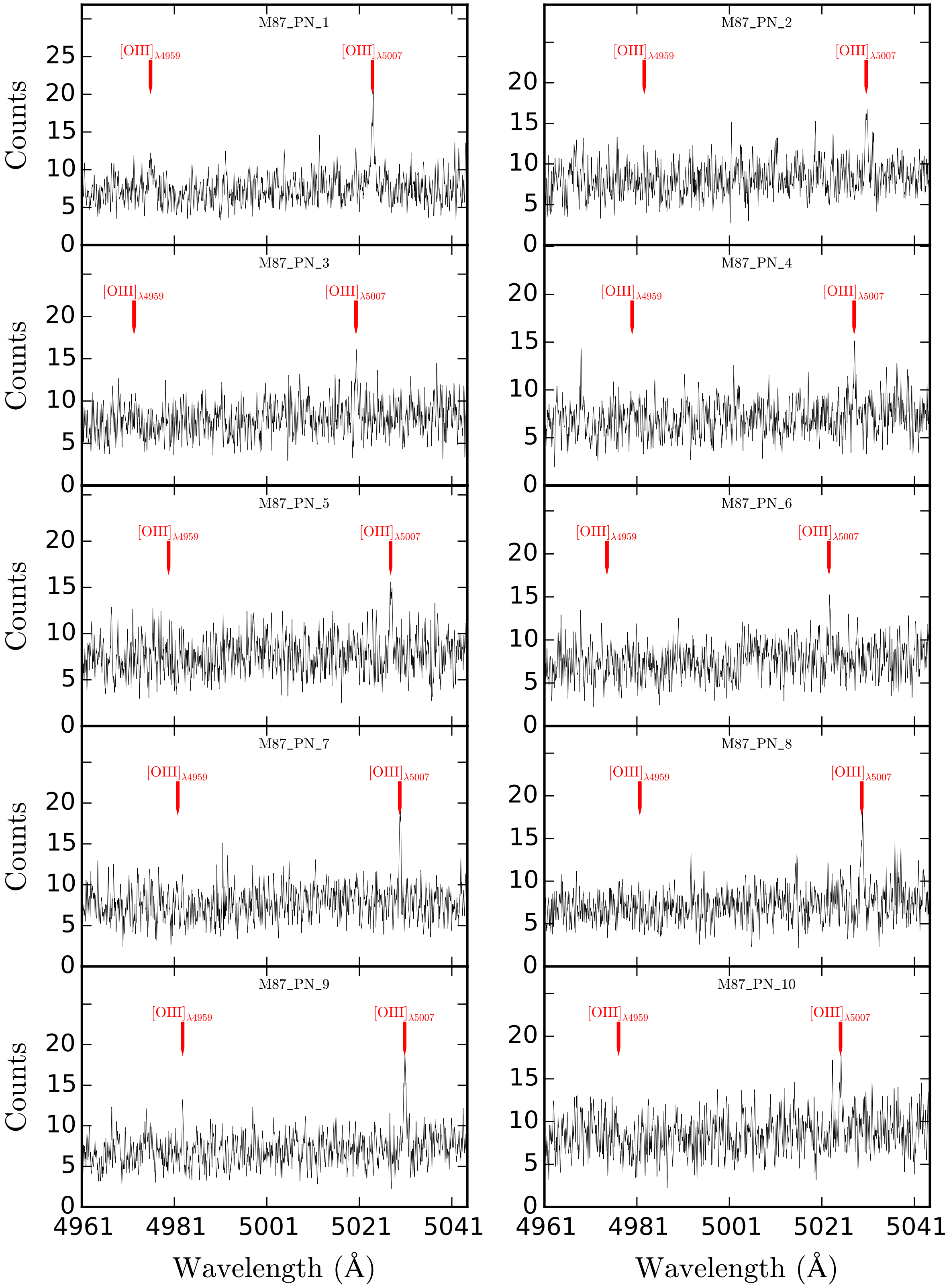

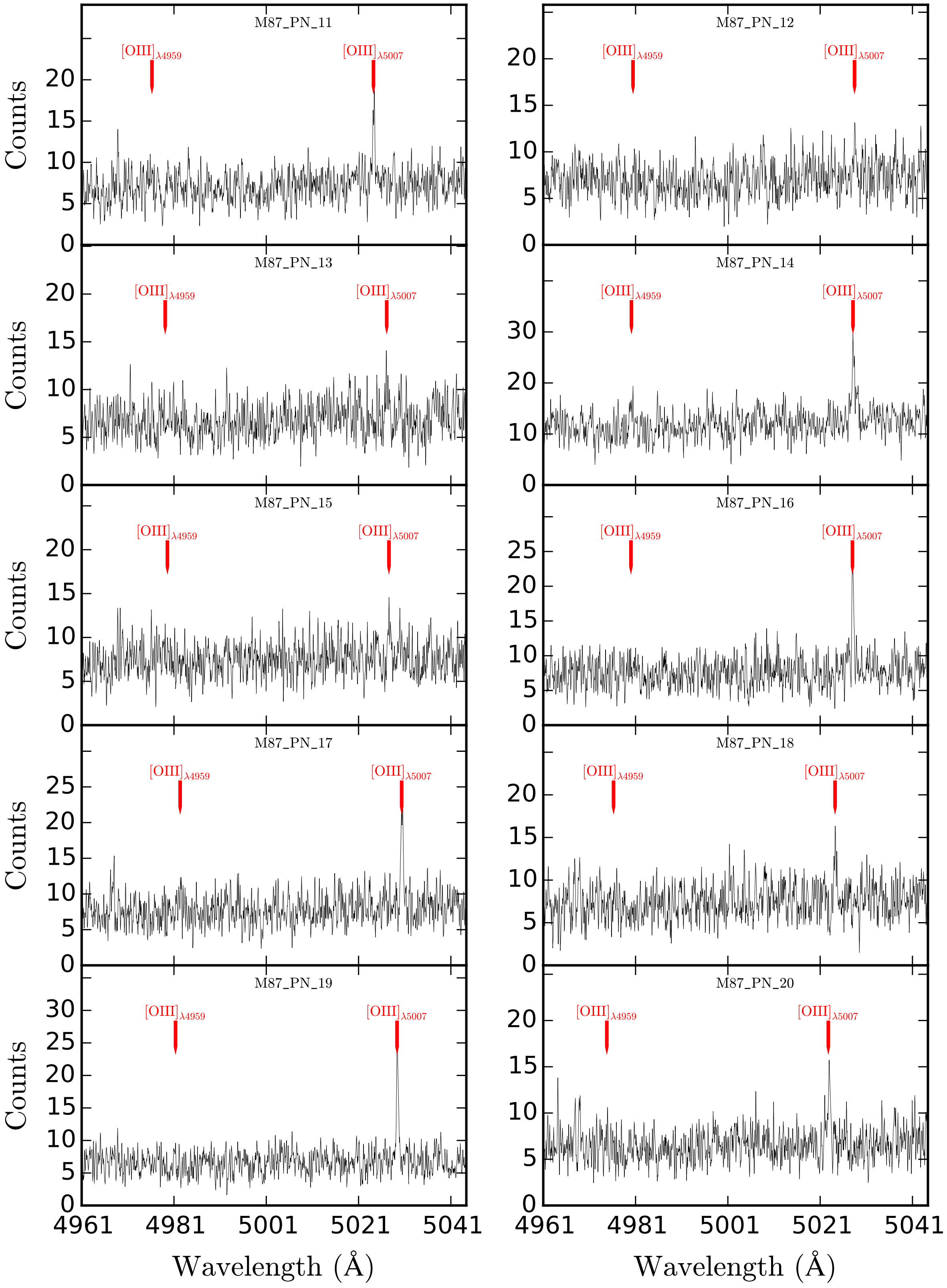
M87_PN_11
M87_PN_12
M87_PN_13
M87_PN_14
M87_PN_15
M87_PN_16
M87_PN_17
M87_PN_18
M87_PN_19
M87_PN_20
[OIII]$_{\lambda 4959}$
[OIII]$_{\lambda 5007}$
Counts
Wavelength (Å)
4961
4981
5001
5021
5041
0
5
10
15
20
25
30

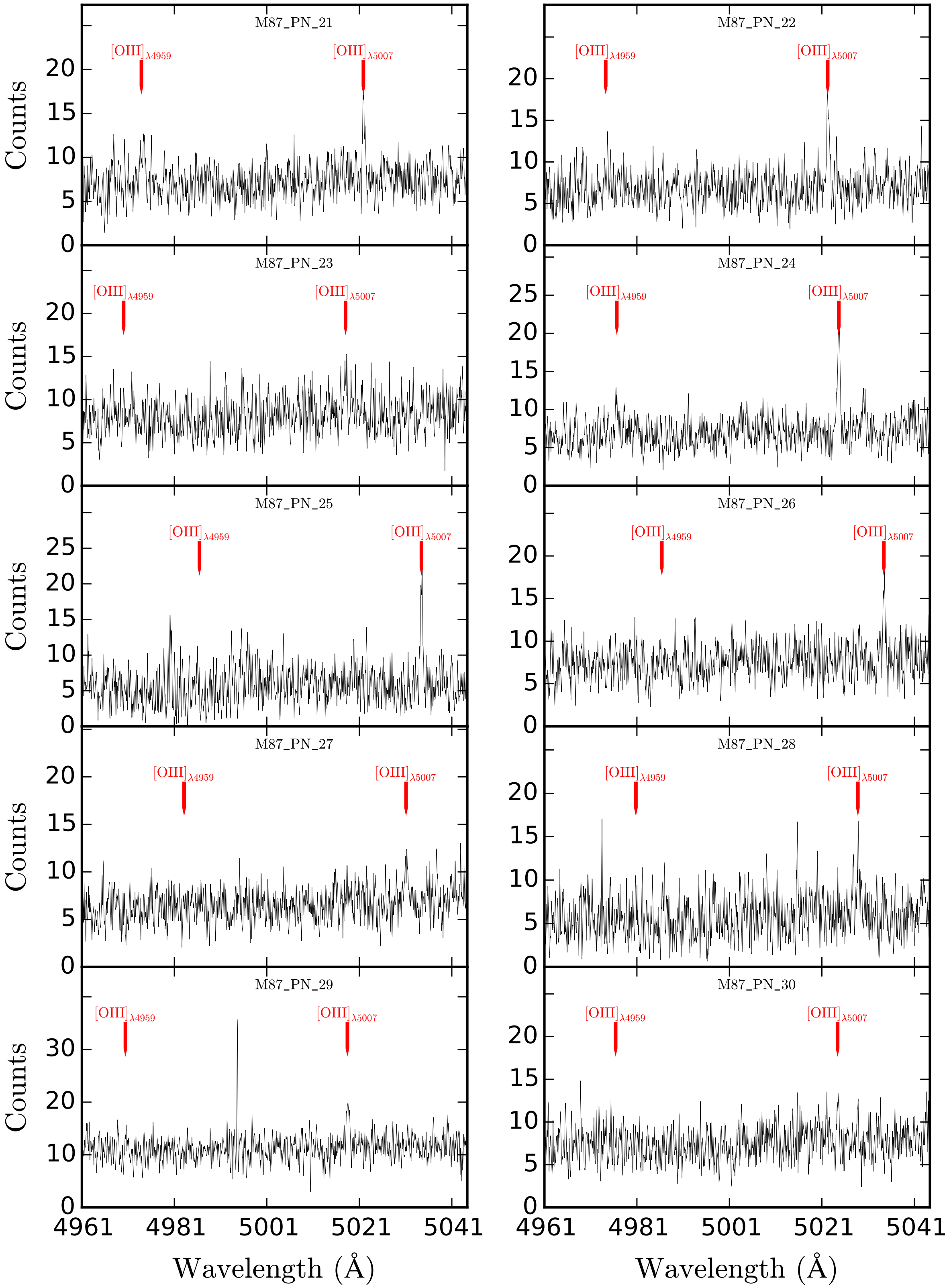
M87_PN_21
M87_PN_22
M87_PN_23
M87_PN_24
M87_PN_25
M87_PN_26
M87_PN_27
M87_PN_28
M87_PN_29
M87_PN_30
[OIII]$_{\lambda4959}$
[OIII]$_{\lambda5007}$
Counts
Wavelength (Å)
4961
4981
5001
5021
5041
0
5
10
15
20
25
30

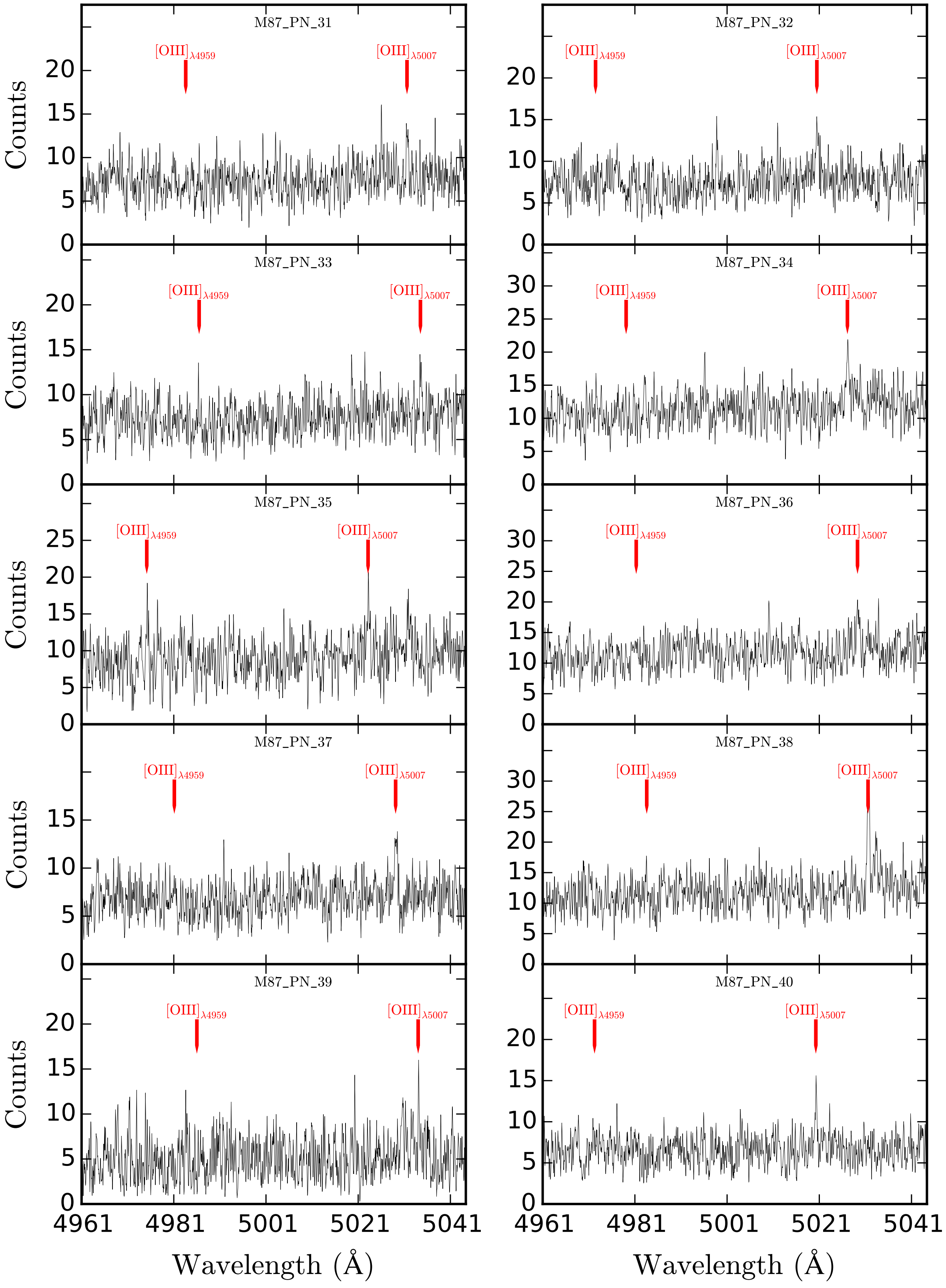
M87_PN_31
M87_PN_32
M87_PN_33
M87_PN_34
M87_PN_35
M87_PN_36
M87_PN_37
M87_PN_38
M87_PN_39
M87_PN_40
[OIII]$_{\lambda4959}$
[OIII]$_{\lambda5007}$
Counts
0
5
10
15
20
25
30
4961
4981
5001
5021
5041
Wavelength (Å)

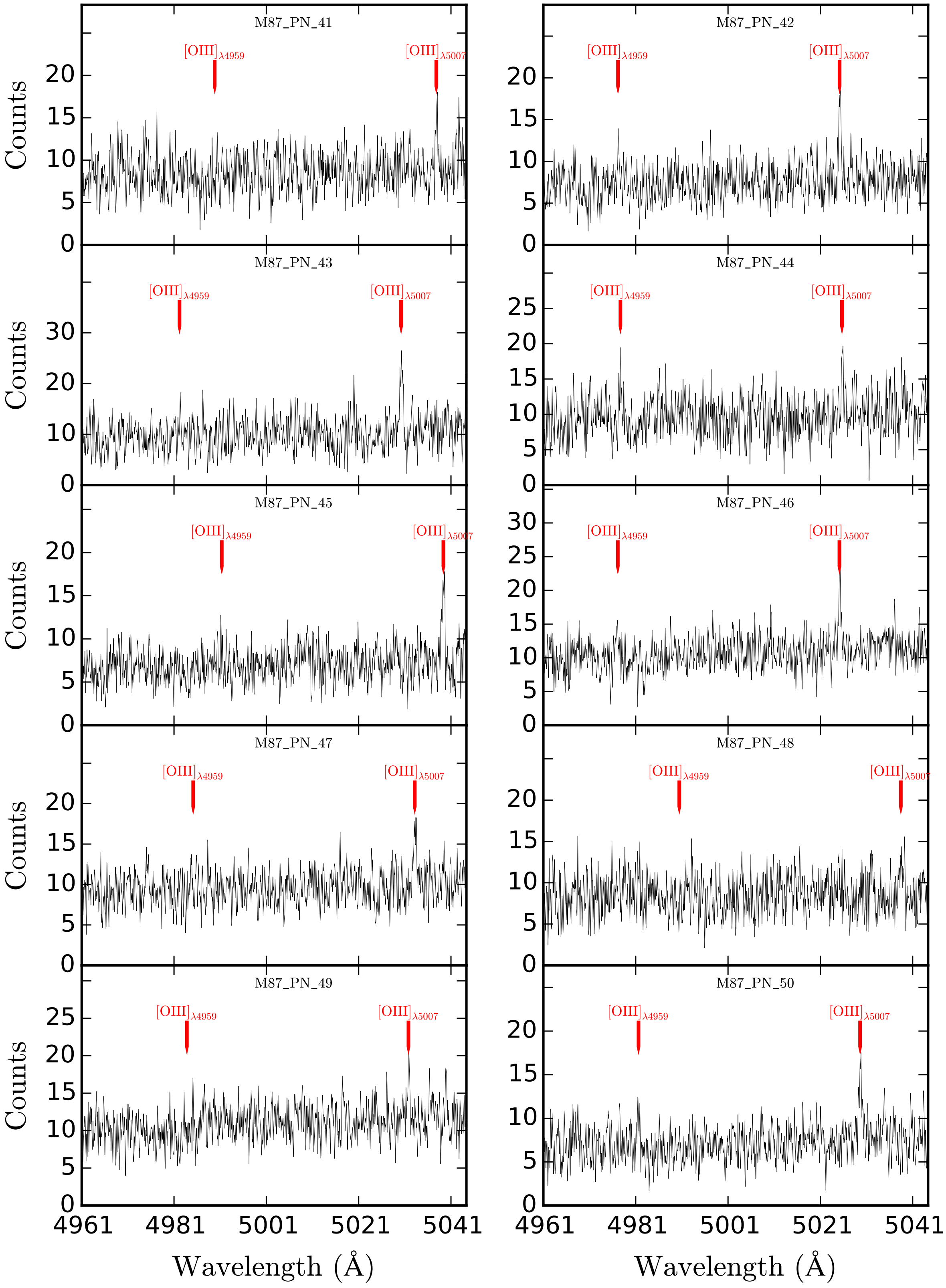
M87_PN_41
M87_PN_42
M87_PN_43
M87_PN_44
M87_PN_45
M87_PN_46
M87_PN_47
M87_PN_48
M87_PN_49
M87_PN_50
[OIII]$_{\lambda 4959}$
[OIII]$_{\lambda 5007}$
Counts
Wavelength (Å)
4961
4981
5001
5021
5041
0
5
10
15
20
25
30

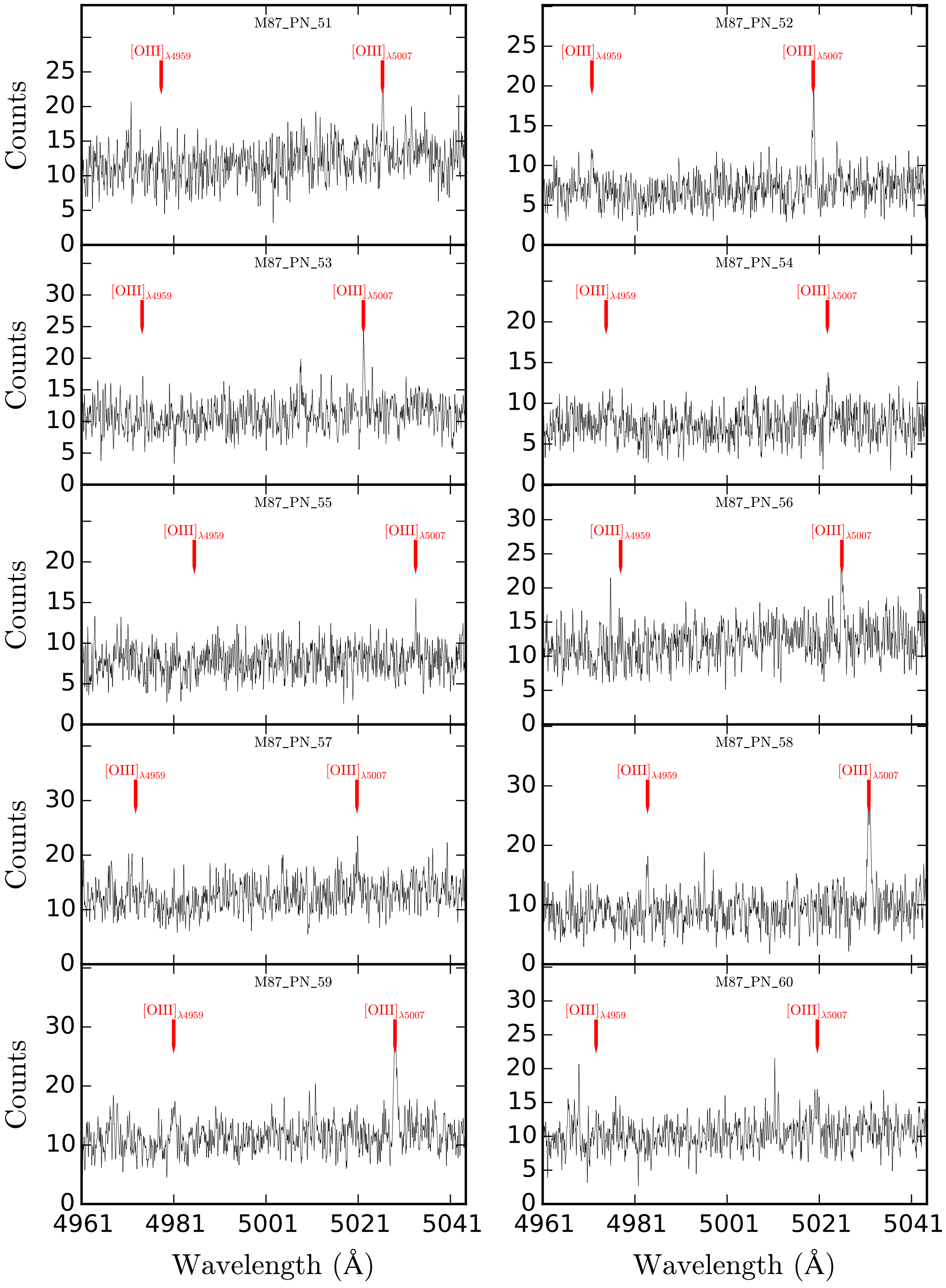
M87_PN_51
M87_PN_52
M87_PN_53
M87_PN_54
M87_PN_55
M87_PN_56
M87_PN_57
M87_PN_58
M87_PN_59
M87_PN_60
[OIII]λ4959
[OIII]λ5007
Counts
Wavelength (Å)
4961
4981
5001
5021
5041
0
5
10
15
20
25
30

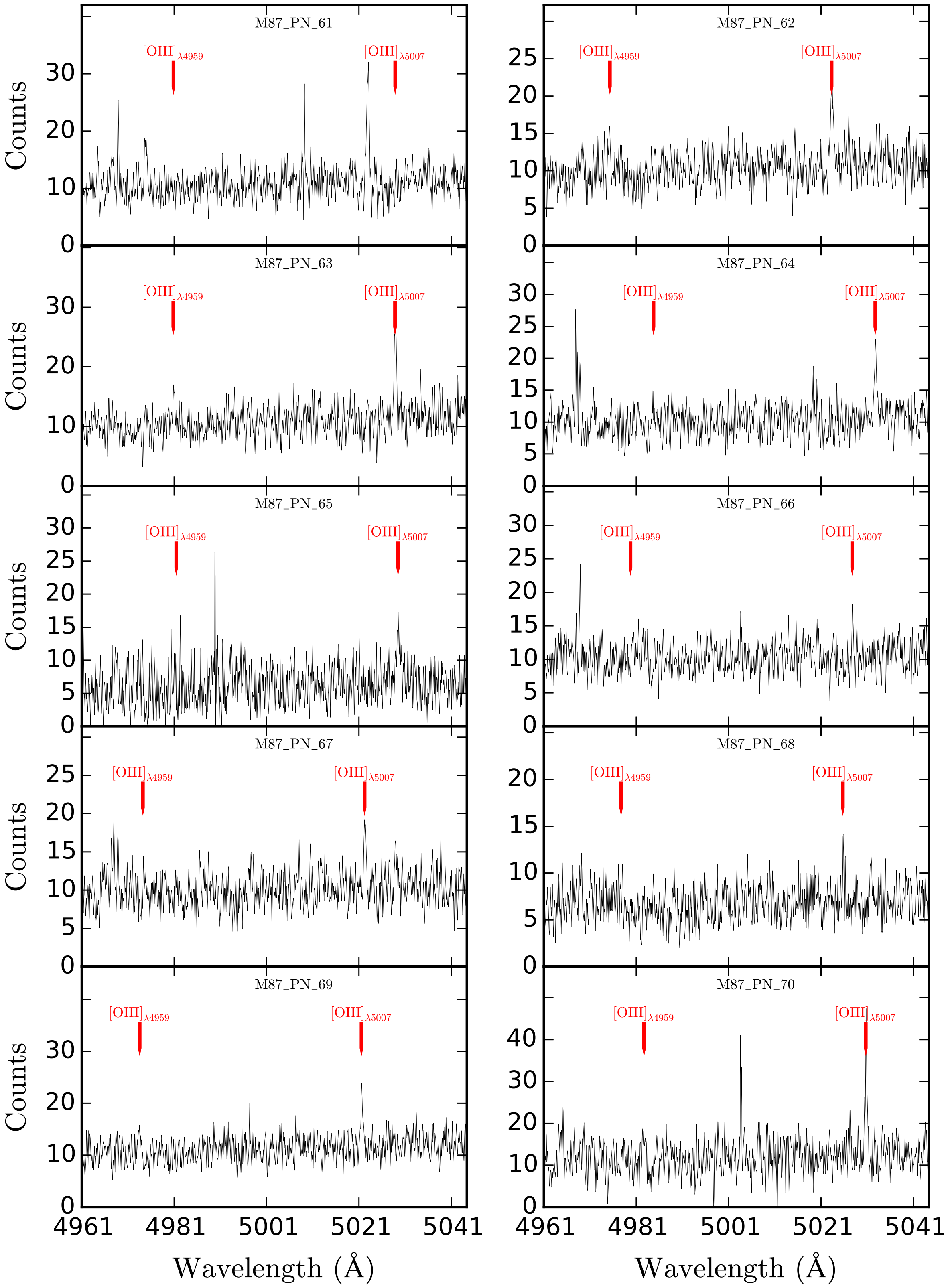
M87_PN_61
M87_PN_62
M87_PN_63
M87_PN_64
M87_PN_65
M87_PN_66
M87_PN_67
M87_PN_68
M87_PN_69
M87_PN_70
[OIII]$_{\lambda4959}$
[OIII]$_{\lambda5007}$
Counts
0
5
10
15
20
25
30
40
4961
4981
5001
5021
5041
Wavelength (Å)

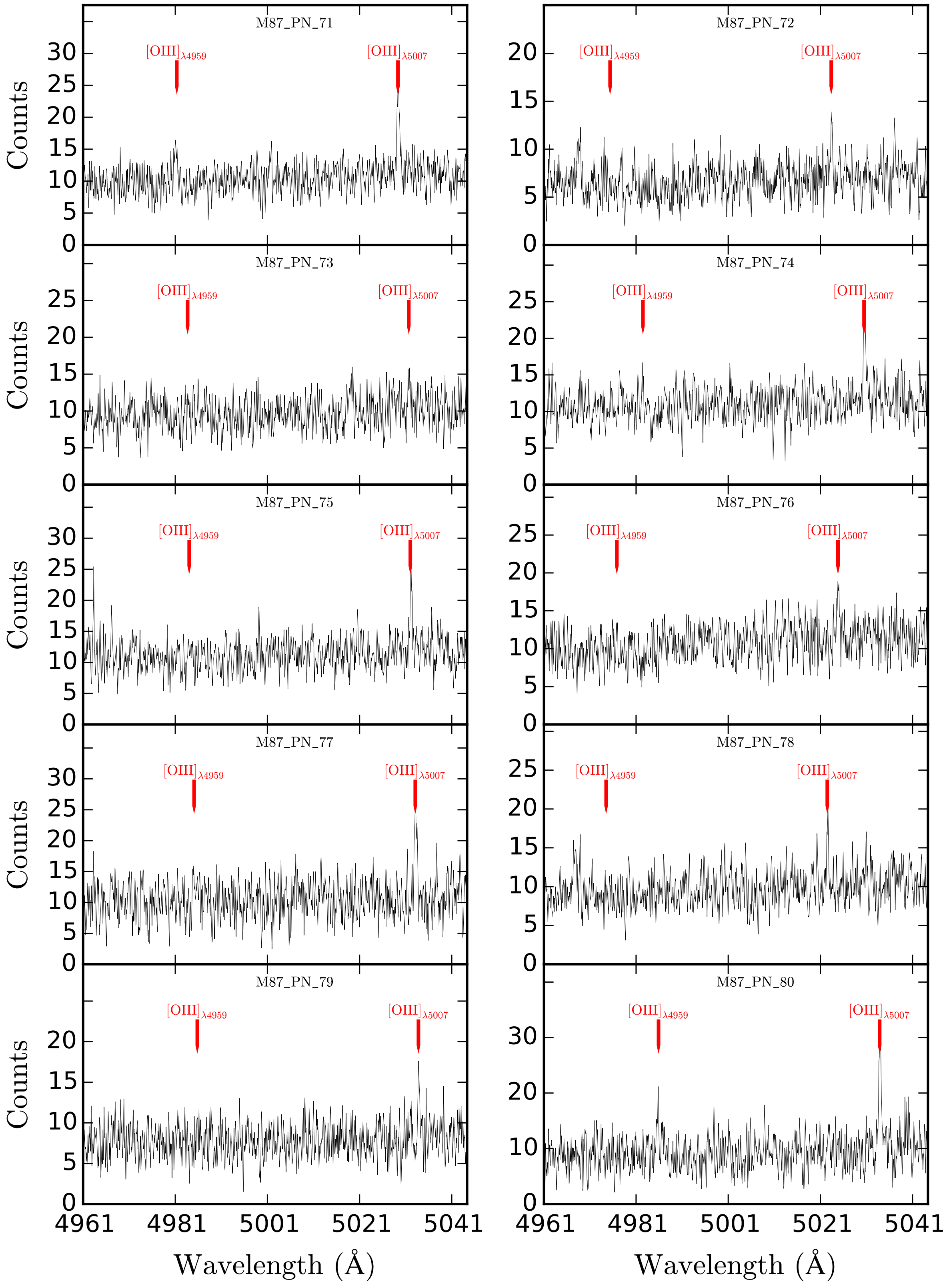
M87_PN_71
M87_PN_72
M87_PN_73
M87_PN_74
M87_PN_75
M87_PN_76
M87_PN_77
M87_PN_78
M87_PN_79
M87_PN_80
[OIII]λ4959
[OIII]λ5007
Counts
Wavelength (Å)
4961
4981
5001
5021
5041

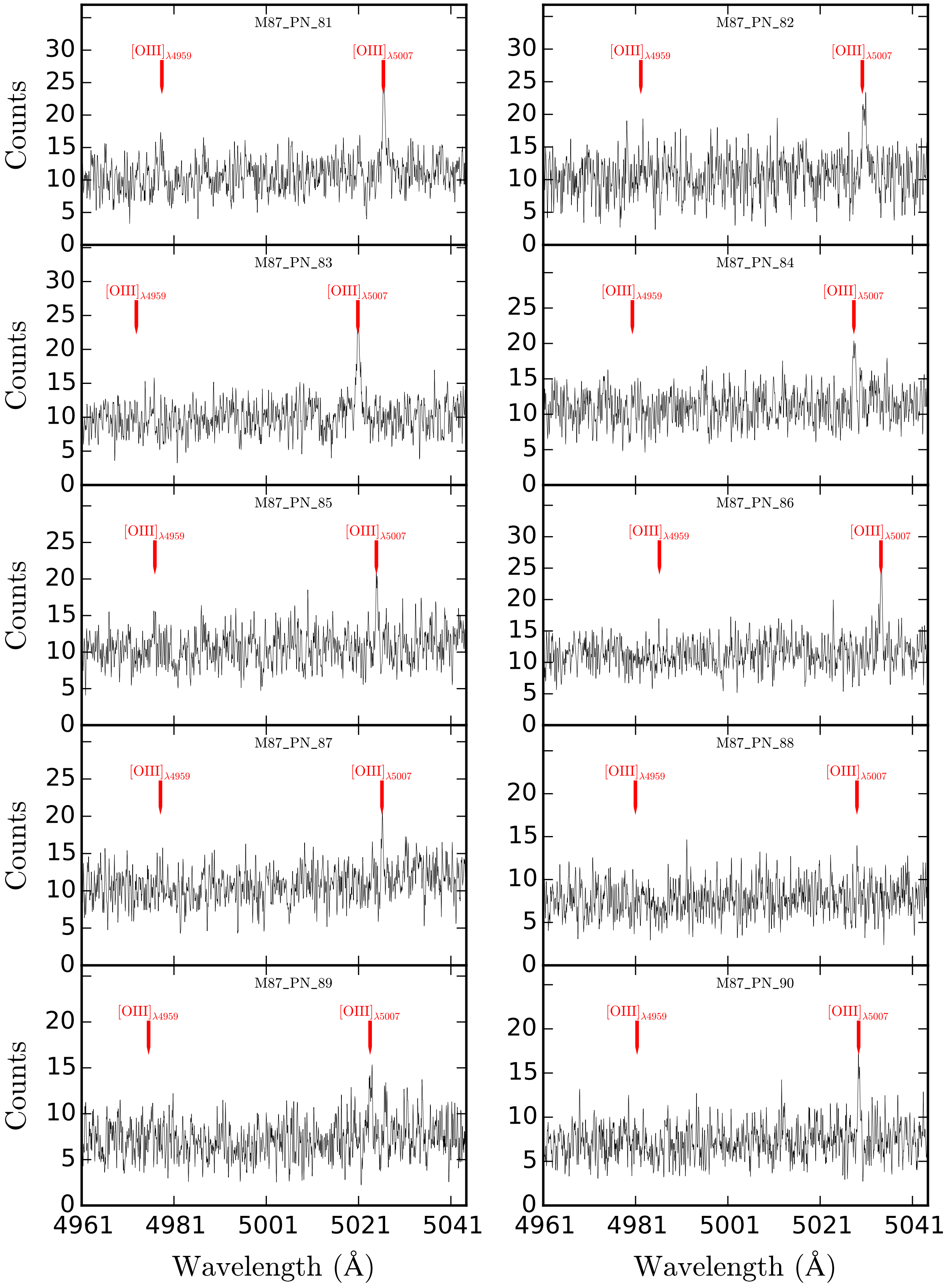
M87_PN_81
M87_PN_82
M87_PN_83
M87_PN_84
M87_PN_85
M87_PN_86
M87_PN_87
M87_PN_88
M87_PN_89
M87_PN_90
[OIII]$_{\lambda 4959}$
[OIII]$_{\lambda 5007}$
Counts
0
5
10
15
20
25
30
4961
4981
5001
5021
5041
Wavelength (Å)

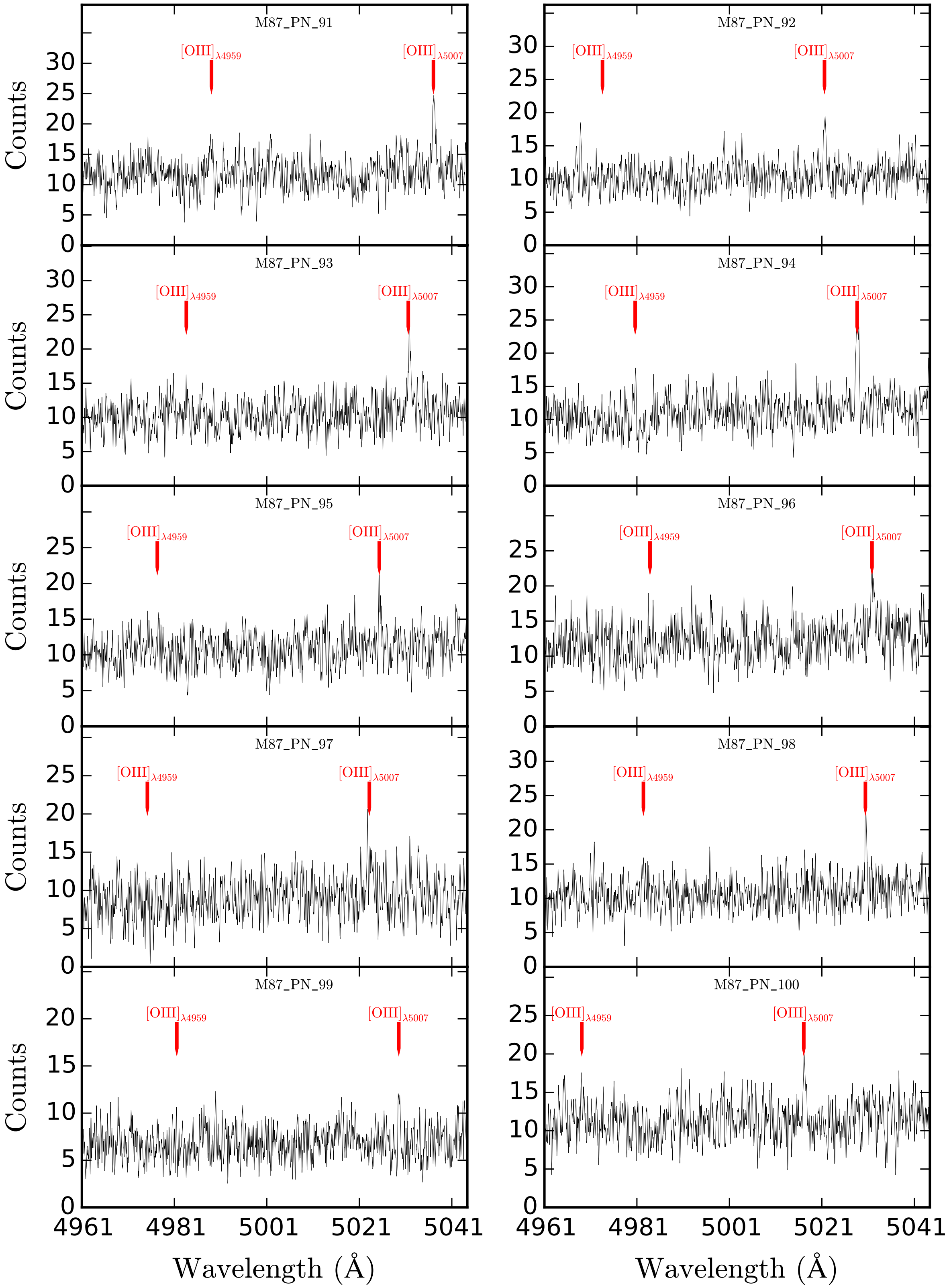
M87_PN_91
M87_PN_92
M87_PN_93
M87_PN_94
M87_PN_95
M87_PN_96
M87_PN_97
M87_PN_98
M87_PN_99
M87_PN_100
[OIII]λ4959
[OIII]λ5007
Counts
Wavelength (Å)
4961
4981
5001
5021
5041
0
5
10
15
20
25
30

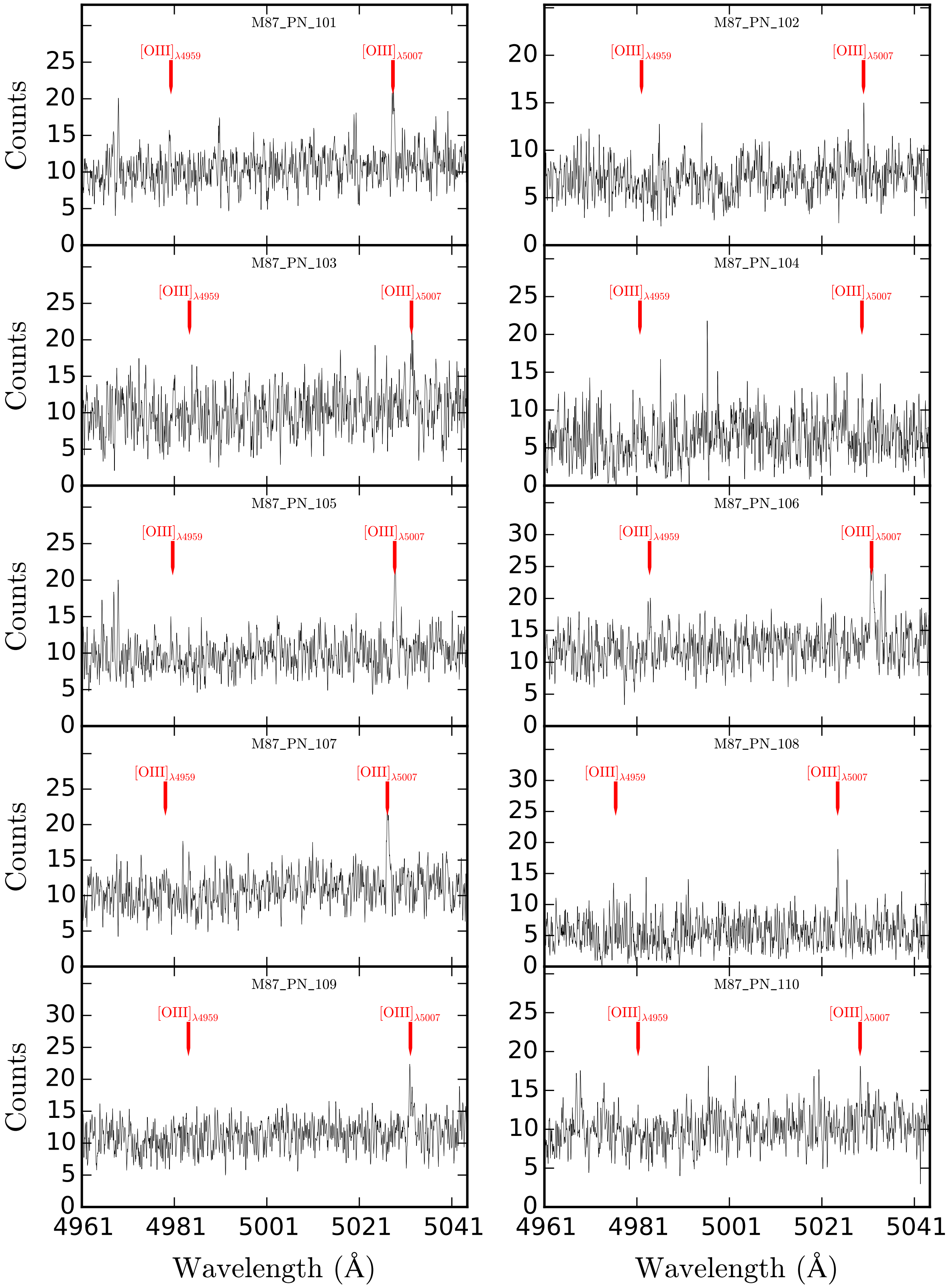
M87_PN_101
M87_PN_102
M87_PN_103
M87_PN_104
M87_PN_105
M87_PN_106
M87_PN_107
M87_PN_108
M87_PN_109
M87_PN_110
[OIII]$_{\lambda4959}$
[OIII]$_{\lambda5007}$
Counts
0
5
10
15
20
25
30
4961
4981
5001
5021
5041
Wavelength (Å)

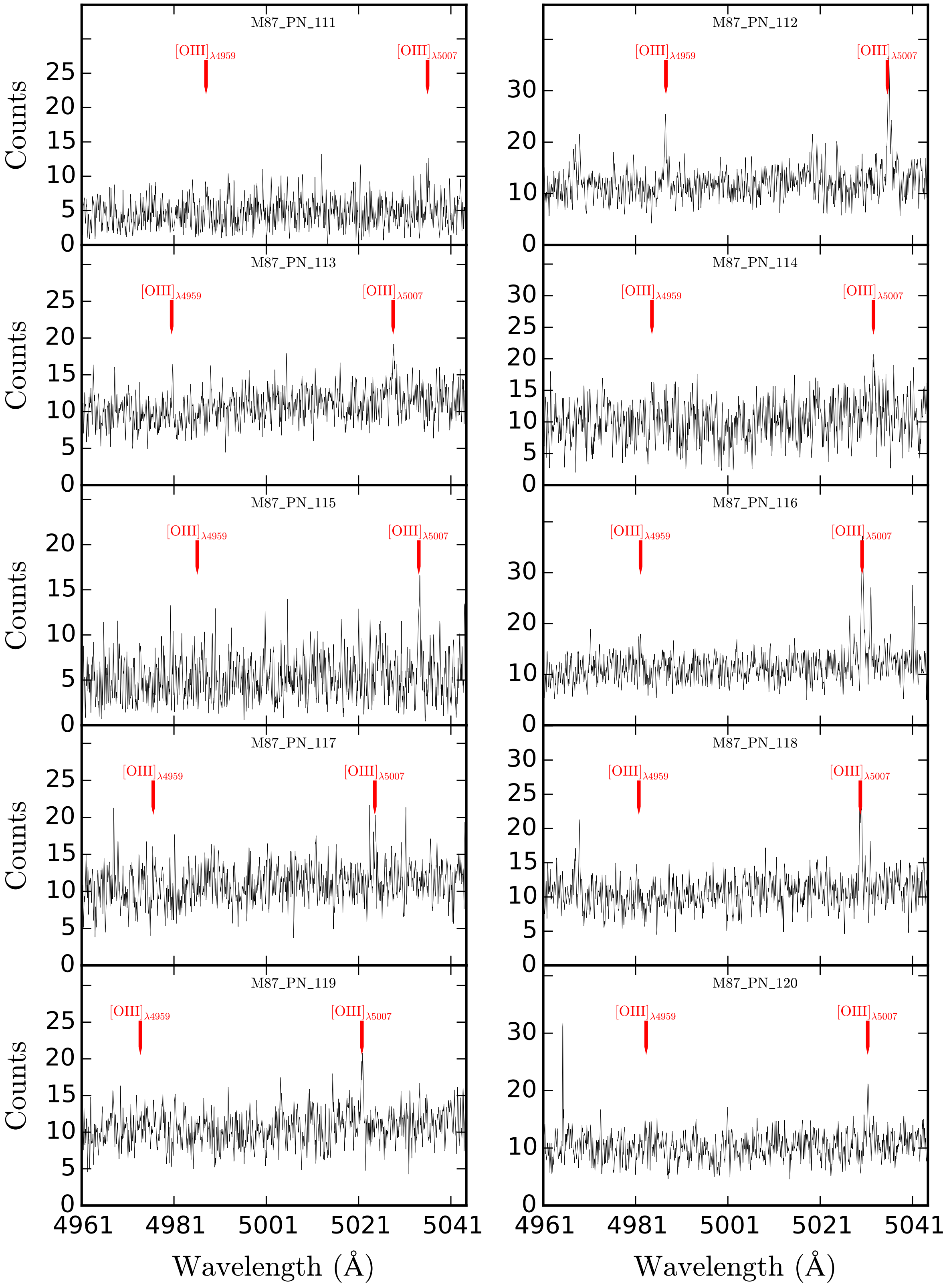
M87_PN_111
M87_PN_112
M87_PN_113
M87_PN_114
M87_PN_115
M87_PN_116
M87_PN_117
M87_PN_118
M87_PN_119
M87_PN_120
[OIII]$_{\lambda4959}$
[OIII]$_{\lambda5007}$
Counts
0
5
10
15
20
25
30
4961
4981
5001
5021
5041
Wavelength (Å)

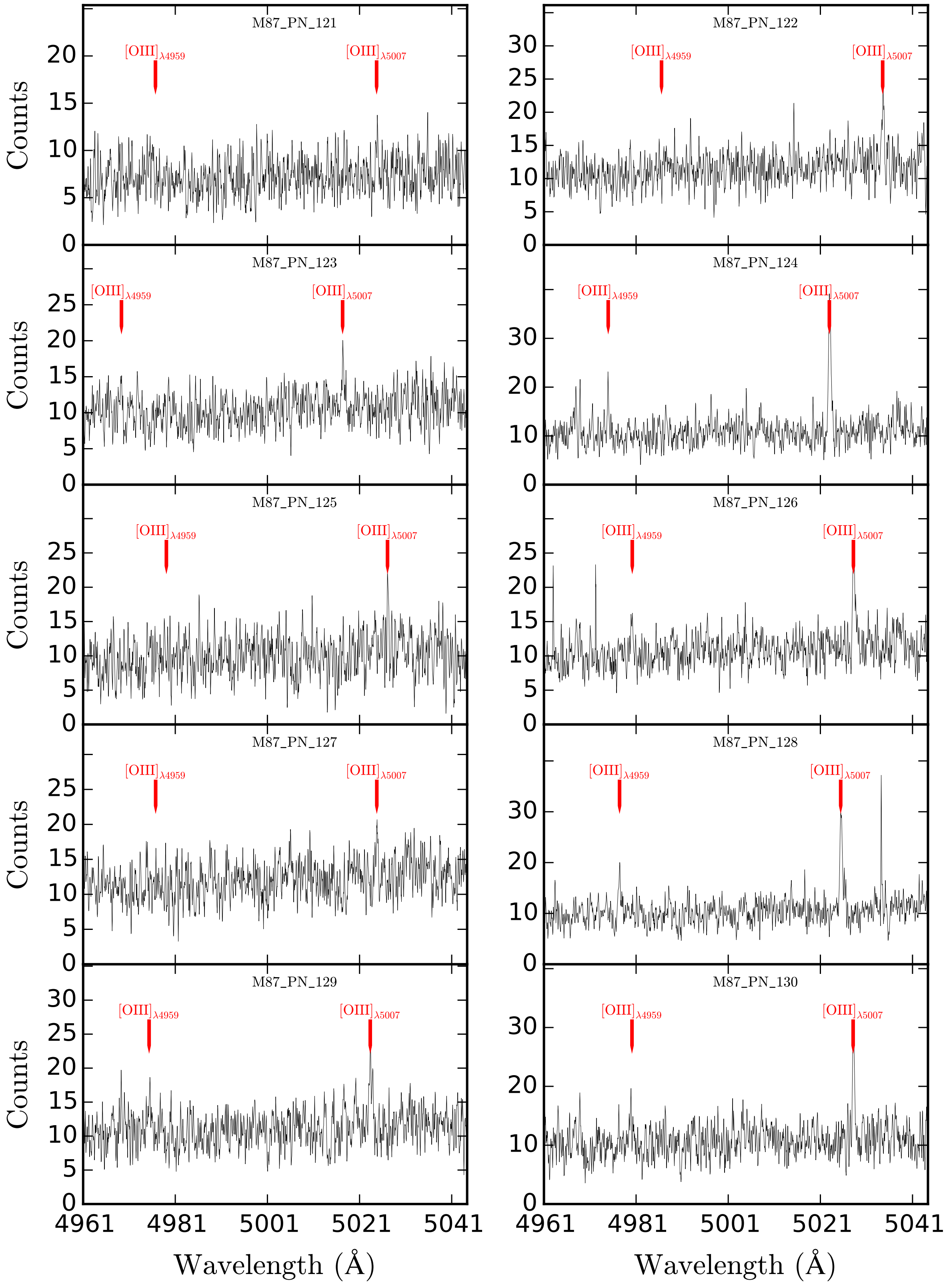
M87_PN_121
M87_PN_122
M87_PN_123
M87_PN_124
M87_PN_125
M87_PN_126
M87_PN_127
M87_PN_128
M87_PN_129
M87_PN_130
[OIII]$_{\lambda4959}$
[OIII]$_{\lambda5007}$
Counts
Wavelength (Å)
4961
4981
5001
5021
5041
0
5
10
15
20
25
30

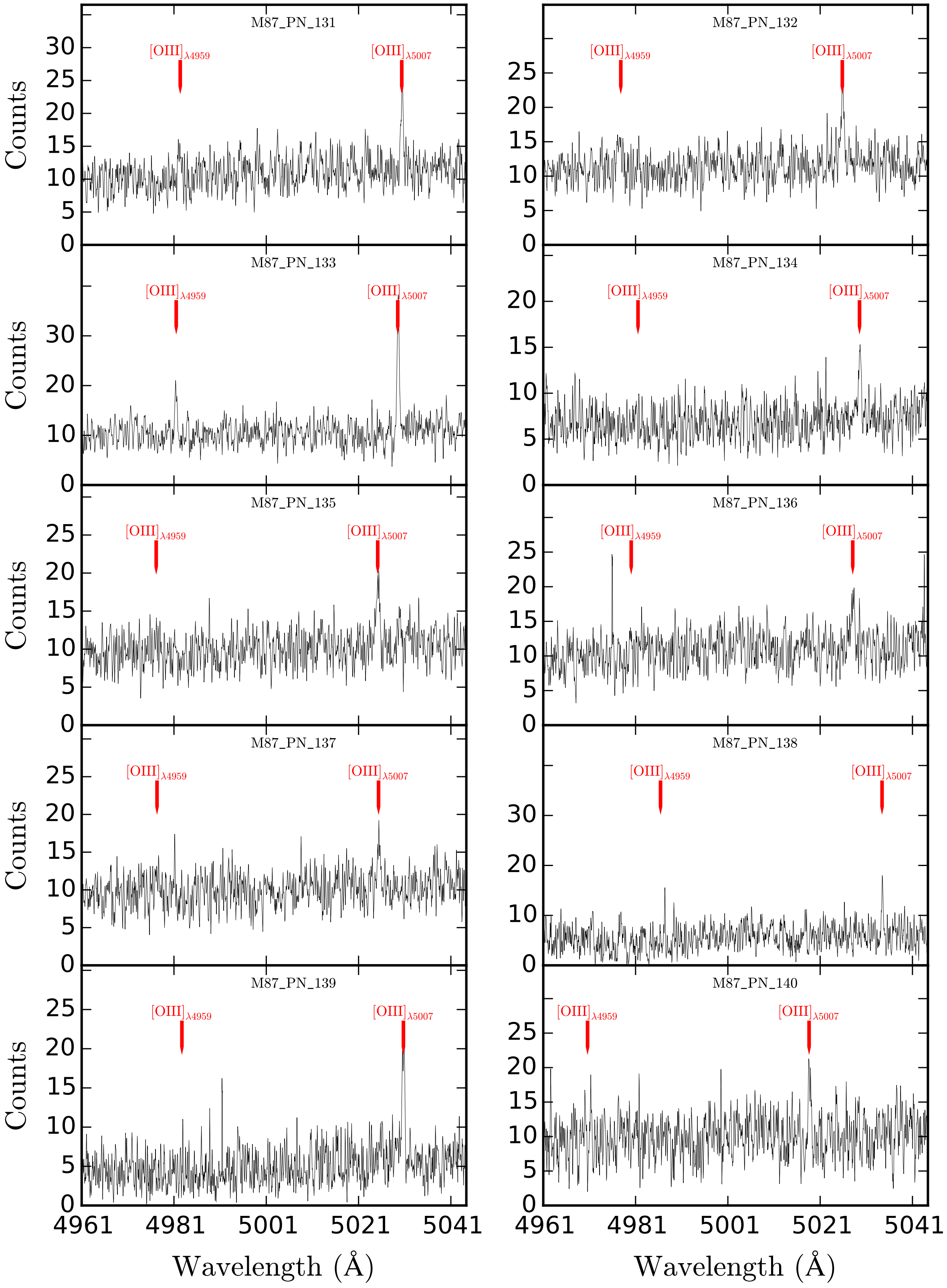
M87_PN_131
M87_PN_132
M87_PN_133
M87_PN_134
M87_PN_135
M87_PN_136
M87_PN_137
M87_PN_138
M87_PN_139
M87_PN_140
[OIII]$_{\lambda4959}$
[OIII]$_{\lambda5007}$
Counts
0
5
10
15
20
25
30
4961
4981
5001
5021
5041
Wavelength (Å)

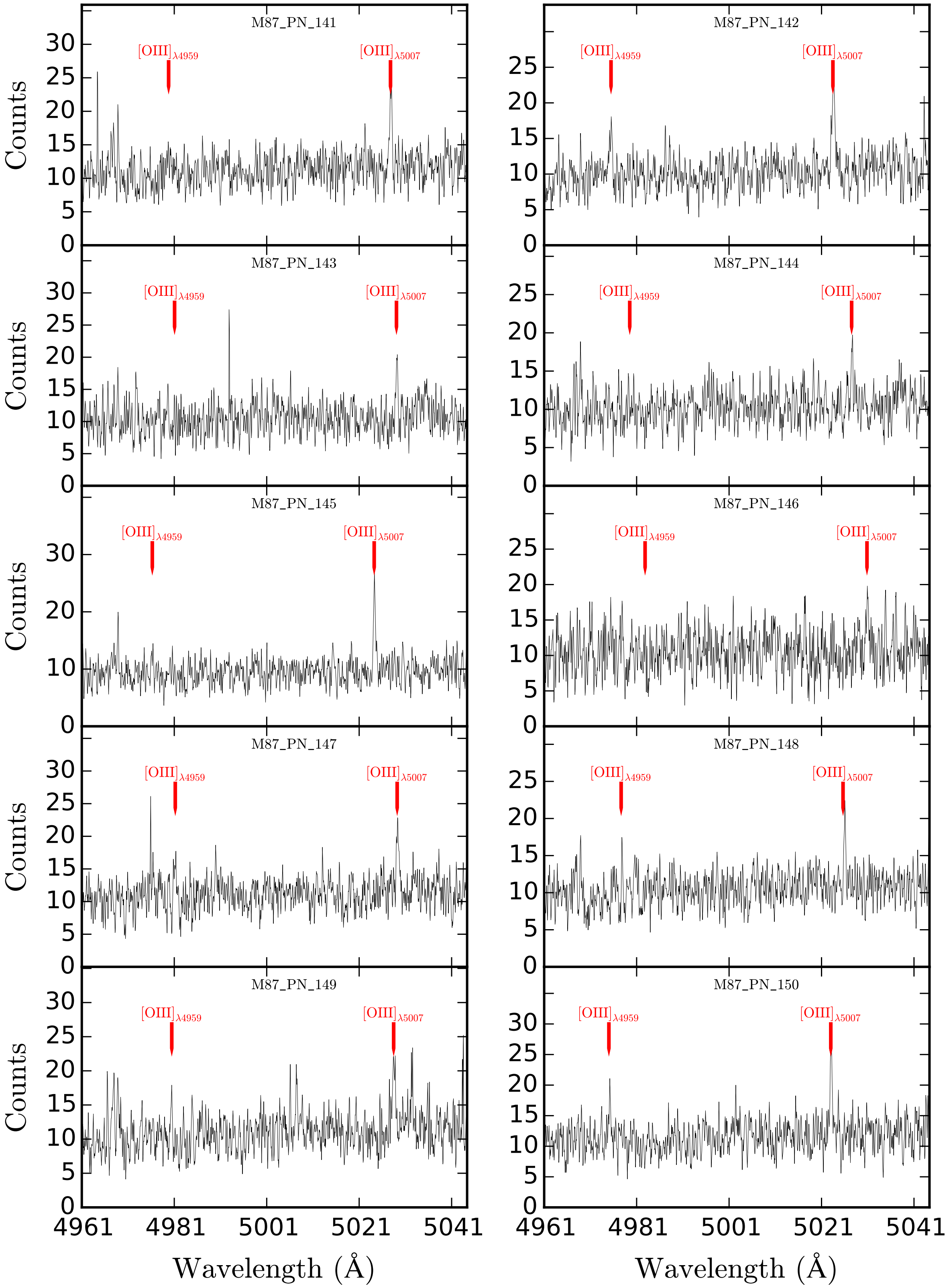
M87_PN_141
M87_PN_142
M87_PN_143
M87_PN_144
M87_PN_145
M87_PN_146
M87_PN_147
M87_PN_148
M87_PN_149
M87_PN_150
[OIII]$_{\lambda4959}$
[OIII]$_{\lambda5007}$
Counts
0
5
10
15
20
25
30
4961
4981
5001
5021
5041
Wavelength (Å)

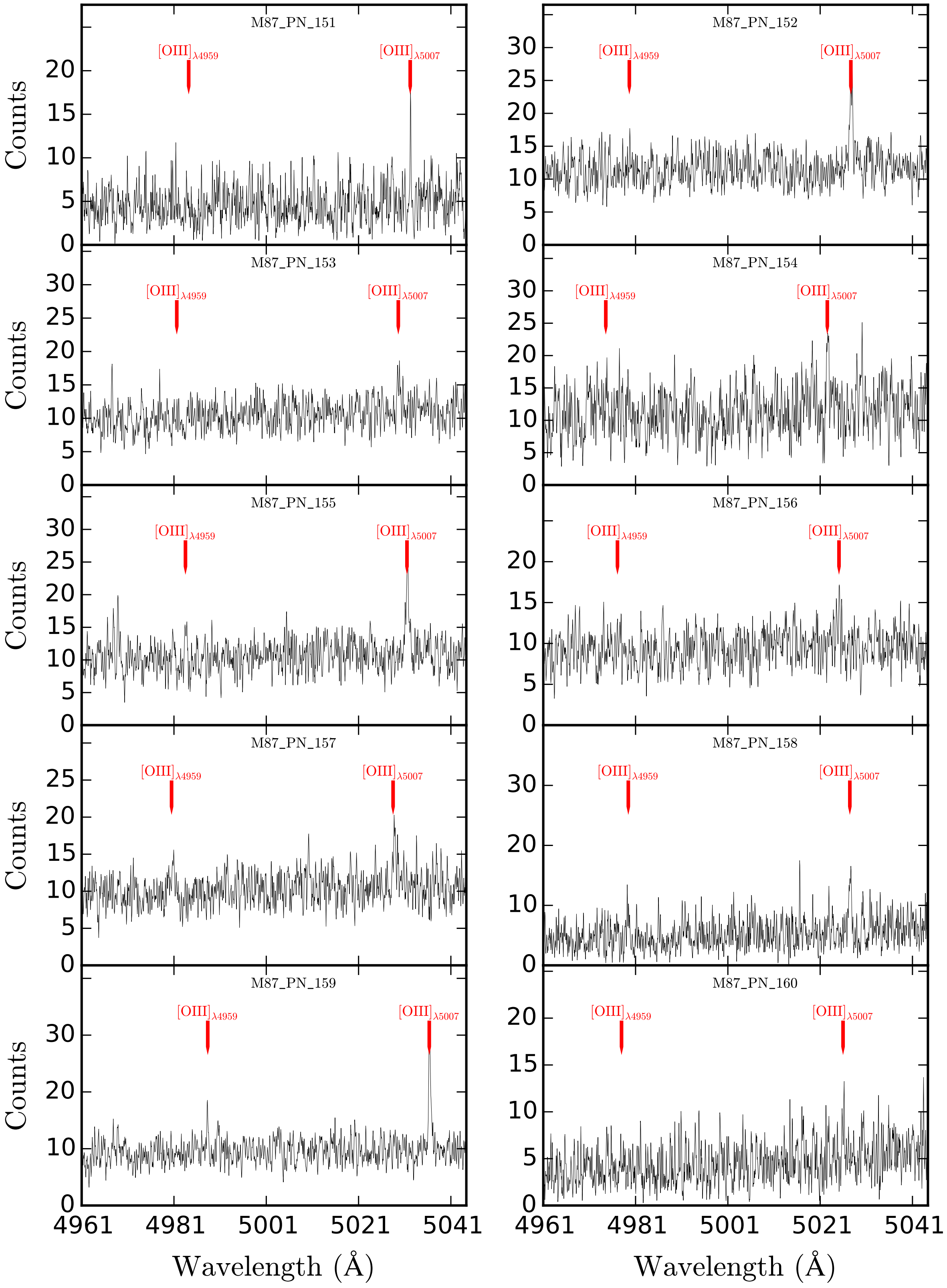
M87_PN_151
M87_PN_152
M87_PN_153
M87_PN_154
M87_PN_155
M87_PN_156
M87_PN_157
M87_PN_158
M87_PN_159
M87_PN_160
[OIII]λ4959
[OIII]λ5007
Counts
Wavelength (Å)
4961
4981
5001
5021
5041

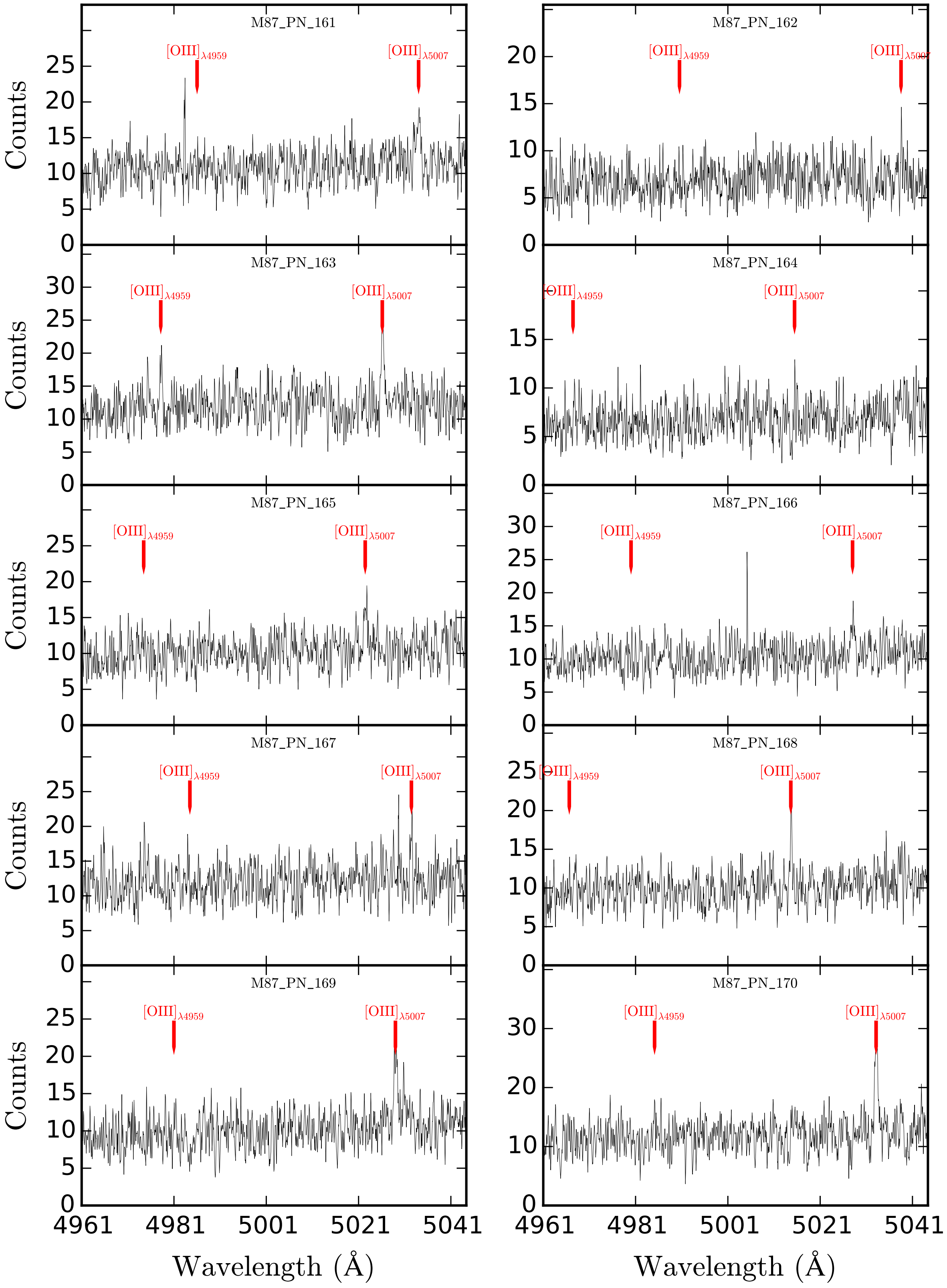
M87_PN_161
M87_PN_162
M87_PN_163
M87_PN_164
M87_PN_165
M87_PN_166
M87_PN_167
M87_PN_168
M87_PN_169
M87_PN_170
[OIII]$_{\lambda 4959}$
[OIII]$_{\lambda 5007}$
Counts
Wavelength (Å)
4961
4981
5001
5021
5041
0
5
10
15
20
25
30

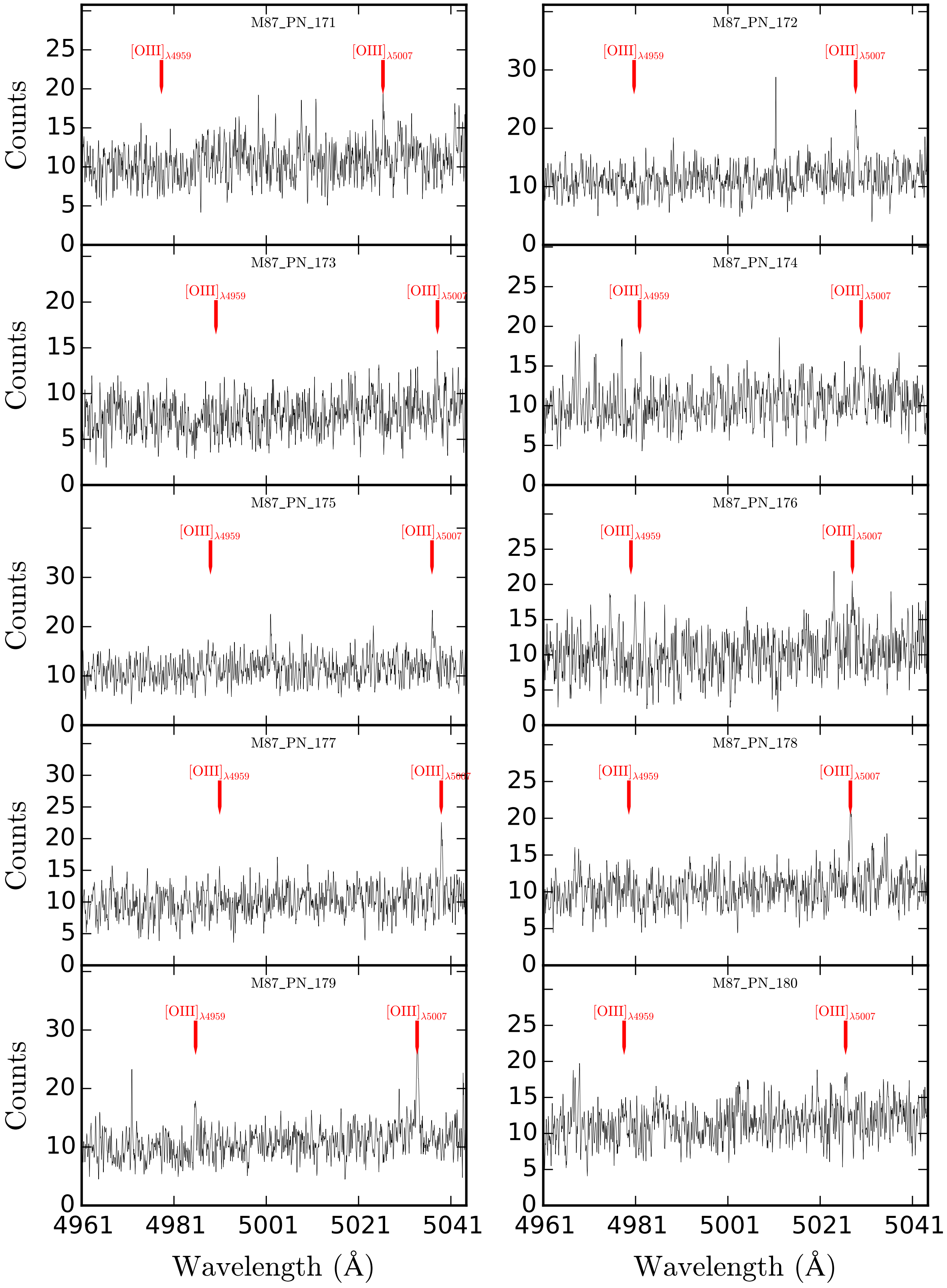
M87_PN_171
M87_PN_172
M87_PN_173
M87_PN_174
M87_PN_175
M87_PN_176
M87_PN_177
M87_PN_178
M87_PN_179
M87_PN_180
[OIII]$_{\lambda4959}$
[OIII]$_{\lambda5007}$
Counts
0
5
10
15
20
25
30
4961
4981
5001
5021
5041
Wavelength (Å)

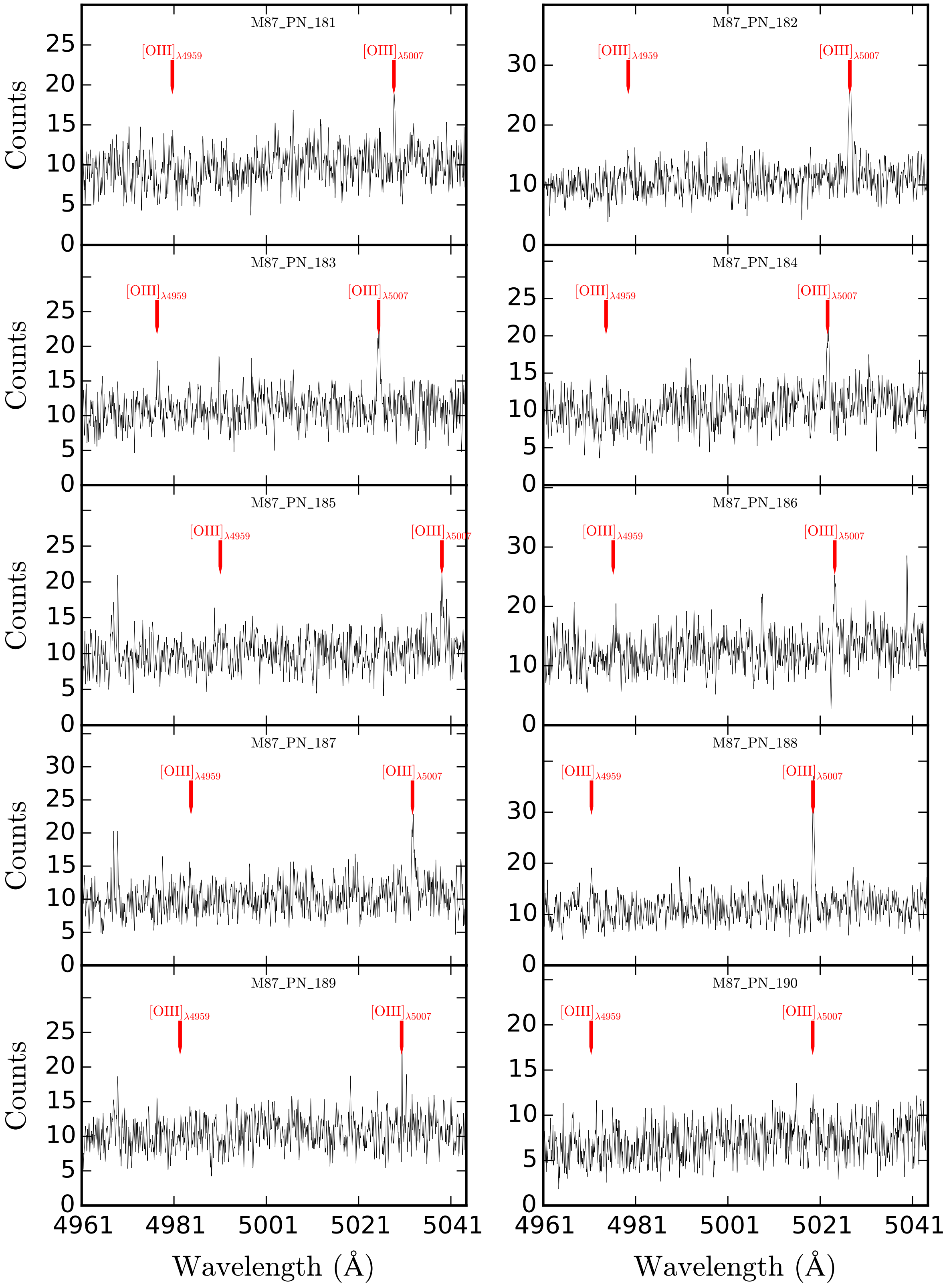
M87_PN_181
M87_PN_182
M87_PN_183
M87_PN_184
M87_PN_185
M87_PN_186
M87_PN_187
M87_PN_188
M87_PN_189
M87_PN_190
[OIII]$_{\lambda4959}$
[OIII]$_{\lambda5007}$
Counts
Wavelength (Å)
4961
4981
5001
5021
5041

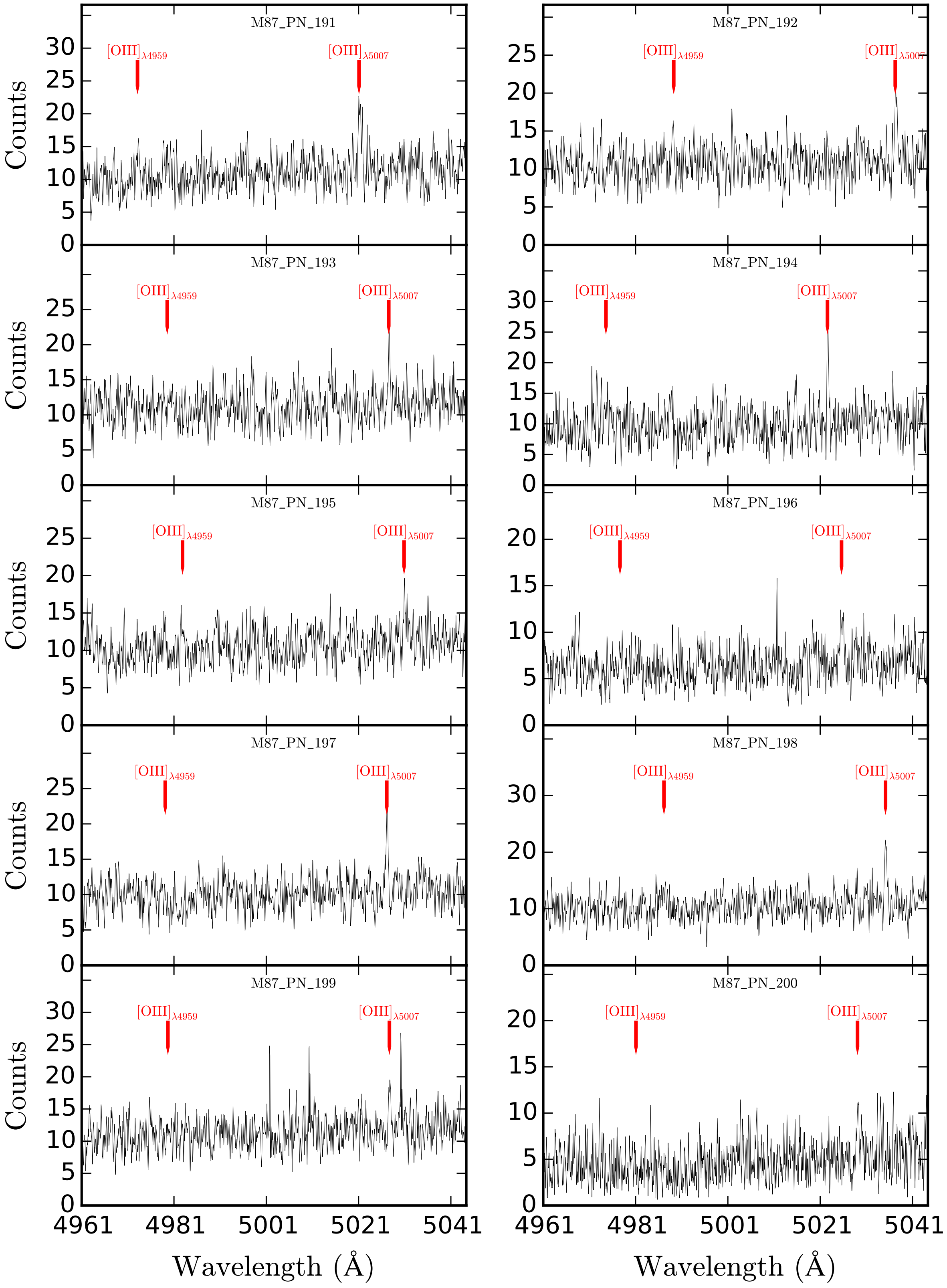
M87_PN_191
M87_PN_192
M87_PN_193
M87_PN_194
M87_PN_195
M87_PN_196
M87_PN_197
M87_PN_198
M87_PN_199
M87_PN_200
[OIII]λ4959
[OIII]λ5007
Counts
0
5
10
15
20
25
30
4961
4981
5001
5021
5041
Wavelength (Å)

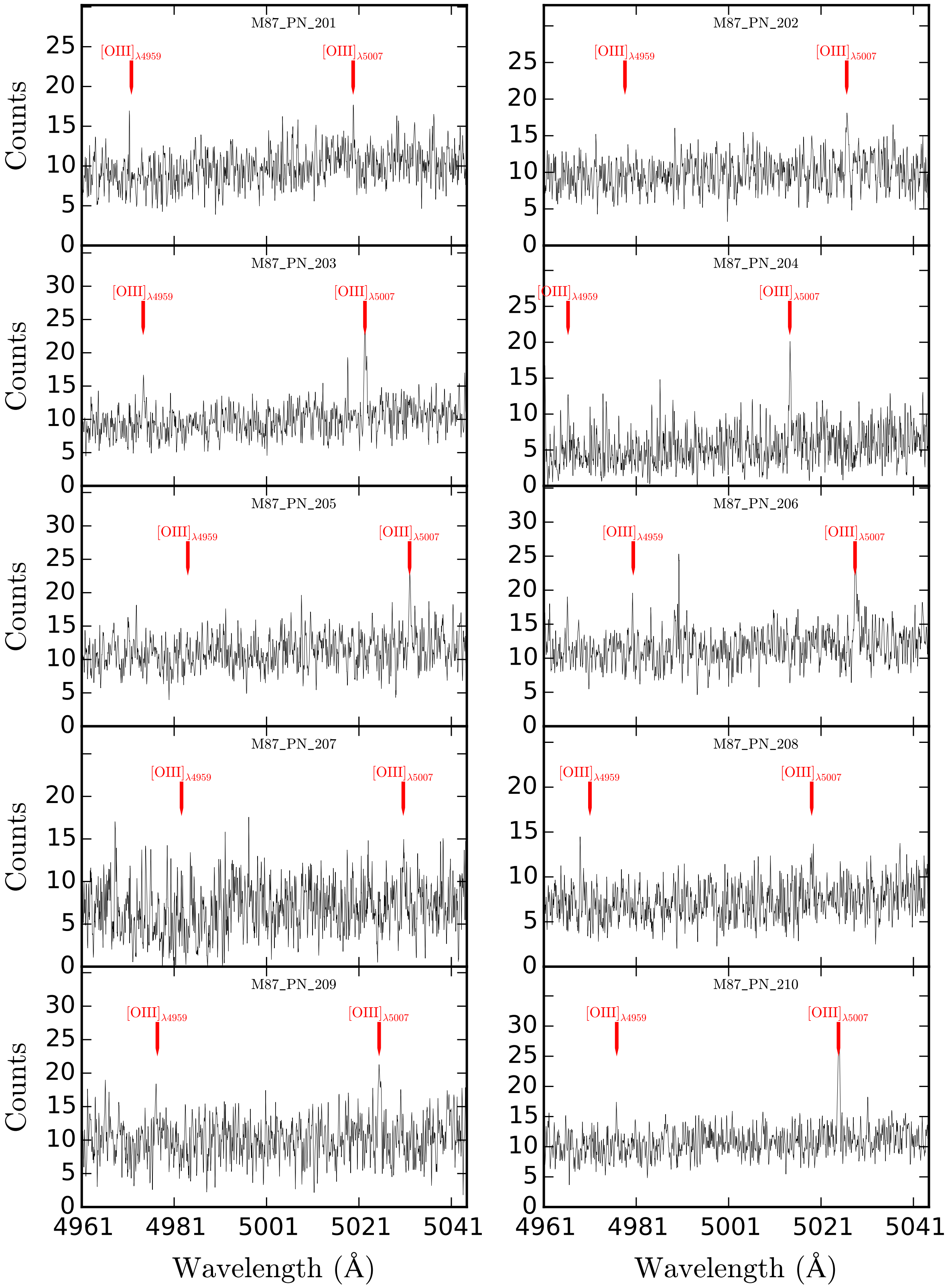
M87_PN_201
M87_PN_202
M87_PN_203
M87_PN_204
M87_PN_205
M87_PN_206
M87_PN_207
M87_PN_208
M87_PN_209
M87_PN_210
[OIII]$_{\lambda4959}$
[OIII]$_{\lambda5007}$
Counts
0
5
10
15
20
25
30
4961
4981
5001
5021
5041
Wavelength (Å)

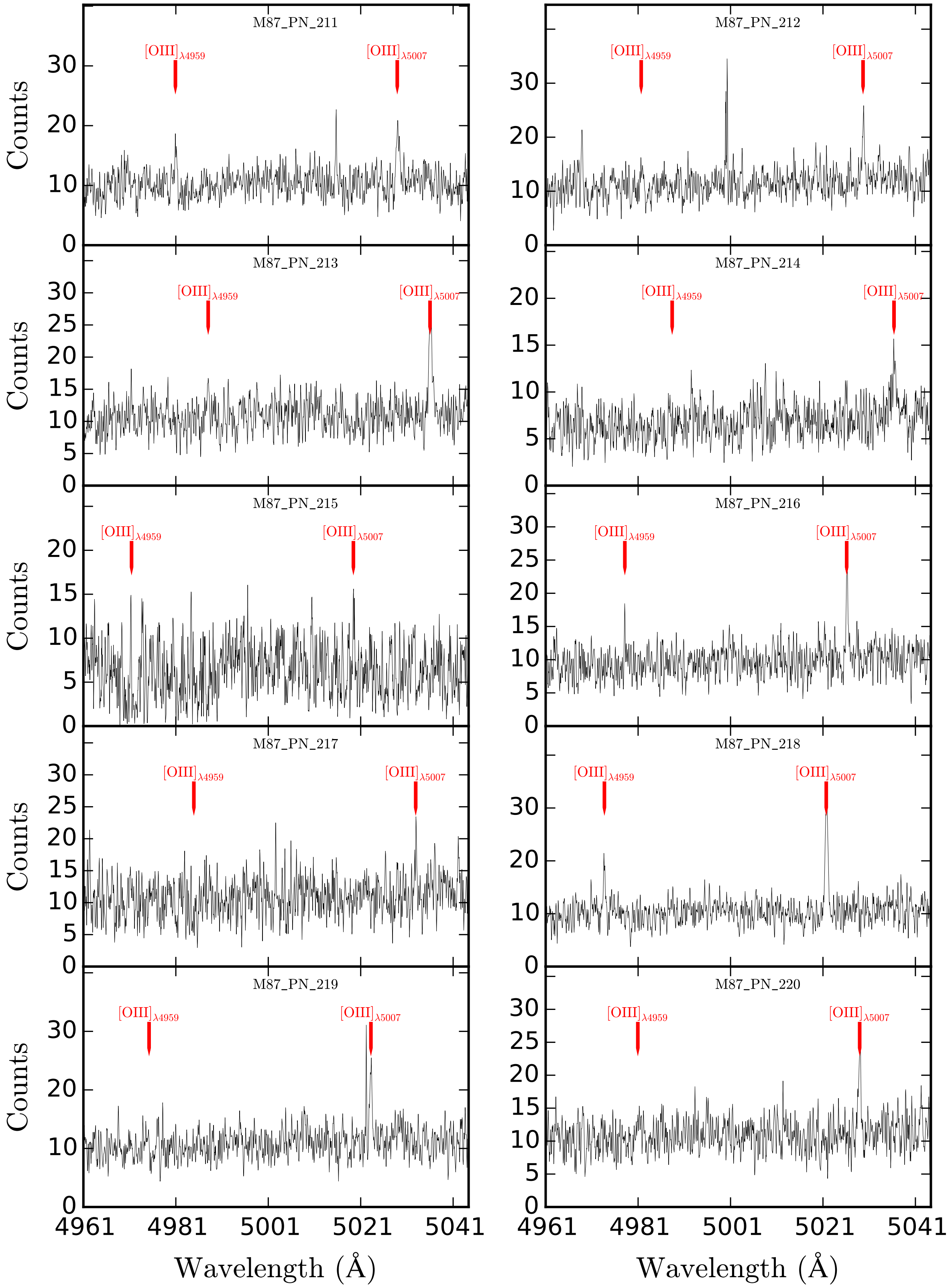
M87_PN_211
M87_PN_212
M87_PN_213
M87_PN_214
M87_PN_215
M87_PN_216
M87_PN_217
M87_PN_218
M87_PN_219
M87_PN_220
[OIII]$_{\lambda4959}$
[OIII]$_{\lambda5007}$
Counts
0
5
10
15
20
25
30
4961
4981
5001
5021
5041
Wavelength (Å)

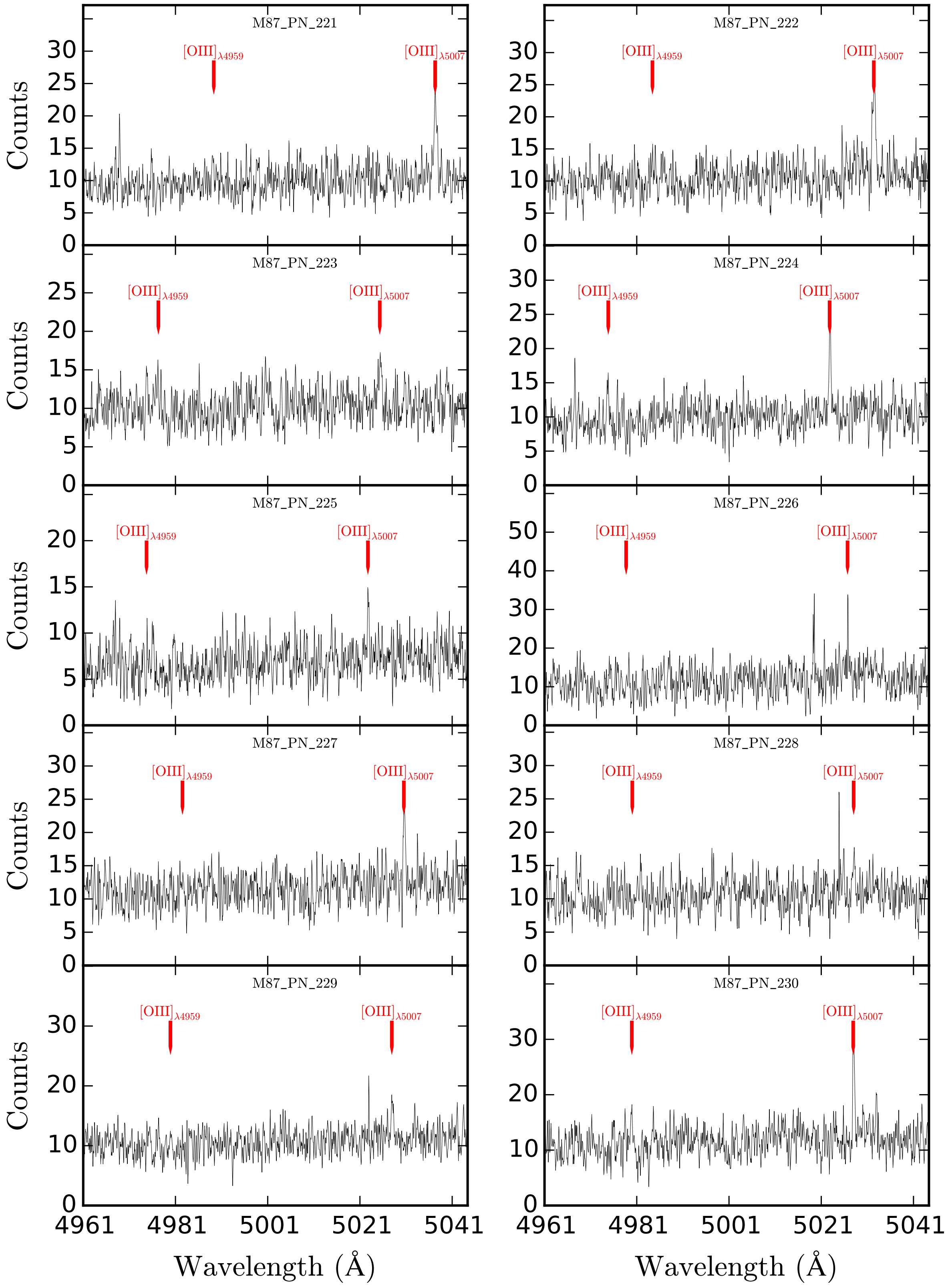
M87_PN_221
M87_PN_222
M87_PN_223
M87_PN_224
M87_PN_225
M87_PN_226
M87_PN_227
M87_PN_228
M87_PN_229
M87_PN_230
[OIII]$_{\lambda 4959}$
[OIII]$_{\lambda 5007}$
Counts
4961
4981
5001
5021
5041
Wavelength (Å)

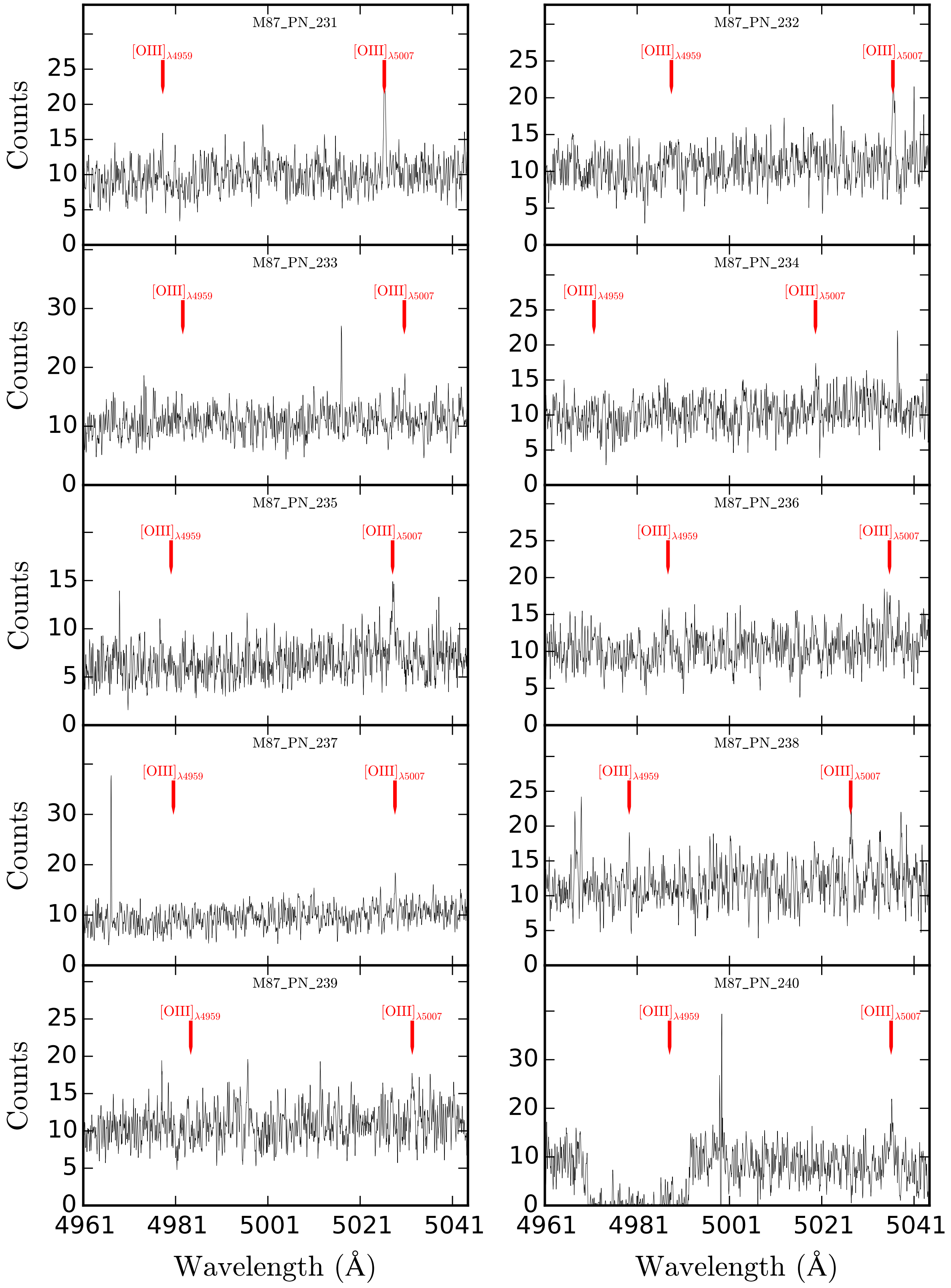
M87_PN_231
M87_PN_232
M87_PN_233
M87_PN_234
M87_PN_235
M87_PN_236
M87_PN_237
M87_PN_238
M87_PN_239
M87_PN_240
[OIII]$_{\lambda4959}$
[OIII]$_{\lambda5007}$
Counts
Wavelength (Å)
4961
4981
5001
5021
5041
0
5
10
15
20
25
30

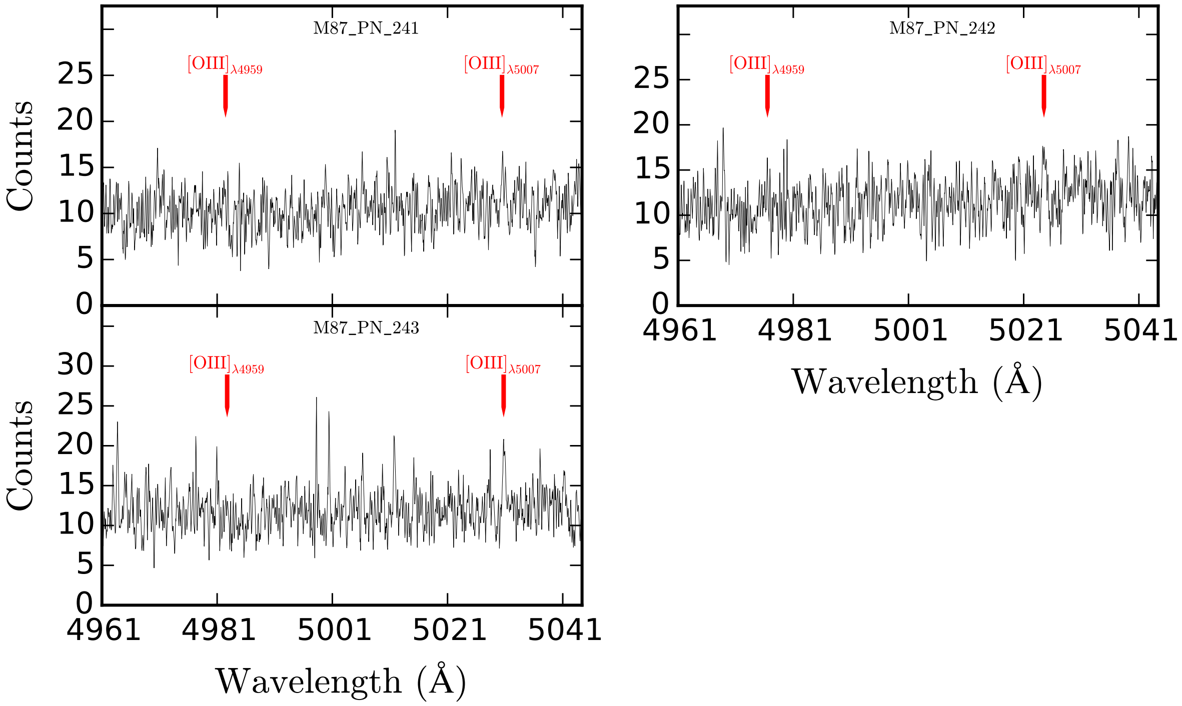
M87_PN_241
M87_PN_242
M87_PN_243
[OIII]$_{\lambda4959}$
[OIII]$_{\lambda5007}$
Counts
0
5
10
15
20
25
30
4961
4981
5001
5021
5041
Wavelength (Å)

Table A.2: **Spectroscopically confirmed ICL PNs**

Column 1: PN ID. Column 2 & 3 Right Ascension and Declination. Columns 4: Redshifted [OIII]$\lambda$5007 Å emission wavelength. Columns 5: Line-of-sight velocity. Column 6: $\lambda$5007 magnitude.

| **Class ICL** | **ID** | **R. A.** (deg) | **Dec.** (deg) | $\lambda_{5007}$ (Å) | **V**$_{\rm LOS}$ (kms$^{-1}$) | $m_{5007}$ |
|---|---|---|---|---|---|---|
| | M87_PN_1 | 187.60788 | 12.513958 | 5003.8 | -194.7 | 28.9 |
| | M87_PN_2 | 187.72371 | 12.222947 | 5046.9 | 2390.6 | 27.7 |
| | M87_PN_3 | 187.66525 | 12.24715 | 4989.5 | -1048.5 | 27.7 |
| | M87_PN_4 | 187.8313 | 12.238 | 5012.0 | 299.6 | 28.1 |
| | M87_PN_5 | 187.84641 | 12.399469 | 5007.5 | 31.2 | 26.6 |
| | M87_PN_6 | 187.81367 | 12.176325 | 4973.5 | -2005.4 | 26.3 |
| | M87_PN_7 | 187.68179 | 12.641177 | 5003.9 | -187.5 | 27.0 |
| | M87_PN_8 | 187.84549 | 12.495178 | 5011.2 | 254.6 | 26.9 |
| | M87_PN_9 | 187.58751 | 12.655169 | 5001.3 | -343.9 | 26.8 |
| | M87_PN_10 | 187.52283 | 12.596066 | 4999.6 | -441.0 | 27.2 |
| | M87_PN_11 | 187.66025 | 12.129625 | 4999.5 | -452.4 | 27.9 |
| | M87_PN_12 | 187.81166 | 12.6105 | 5045.5 | 2306.8 | 27.1 |
| | M87_PN_13 | 187.86038 | 12.54835 | 5002.5 | -272.0 | 28.7 |
| | M87_PN_14 | 187.94128 | 12.163738 | 5009.8 | 166.6 | 27.4 |
| | M87_PN_15 | 187.66005 | 12.736664 | 5000.3 | -399.6 | 27.0 |
| | M87_PN_16 | 187.91887 | 12.07867 | 4957.8 | -2949.1 | 29.6 |
| | M87_PN_17 | 187.93182 | 12.090827 | 5000.7 | -379.3 | 28.3 |
| | M87_PN_18 | 187.8652 | 12.034039 | 5003.9 | -186.3 | 28.4 |
| | M87_PN_19 | 187.45238 | 12.68155 | 5049.8 | 2516.5 | 28.5 |
| | M87_PN_20 | 187.82779 | 12.655069 | 4986.4 | -1235.5 | 27.7 |
| | M87_PN_21 | 187.40538 | 12.593377 | 4997.4 | -572.8 | 27.1 |
| | M87_PN_22 | 187.40443 | 12.500341 | 5003.8 | -193.5 | 27.8 |
| | M87_PN_23 | 187.93179 | 12.023661 | 5005.5 | -91.1 | 26.9 |
| | M87_PN_24 | 187.427 | 12.381725 | 5010.9 | 234.3 | 32.0 |
| | M87_PN_25 | 187.97299 | 12.059444 | 5045.0 | 2277.4 | 26.9 |
| | M87_PN_26 | 187.64313 | 12.047909 | 5047.3 | 2412.8 | 26.6 |
| | M87_PN_27 | 187.94991 | 12.001811 | 5046.6 | 2371.5 | 28.9 |
| | M87_PN_28 | 187.79286 | 12.761614 | 5048.4 | 2479.3 | 27.7 |
| | M87_PN_29 | 187.75504 | 11.938739 | 5010.4 | 205.5 | 27.2 |
| | M87_PN_30 | 188.05862 | 12.250364 | 4953.1 | -3227.7 | 27.6 |
| | M87_PN_31 | 188.0551 | 12.126984 | 4999.5 | -446.4 | 28.8 |
| | M87_PN_32 | 187.34676 | 12.564989 | 4990.5 | -988.0 | 28.8 |
| | M87_PN_33 | 187.34317 | 12.615492 | 5044.2 | 2231.9 | 29.9 |
| | M87_PN_34 | 187.94716 | 11.919353 | 5045.0 | 2279.2 | 26.2 |
| | M87_PN_35 | 188.12738 | 12.256375 | 4949.2 | -3462.6 | 28.6 |

**Table A.2 – *continued on next page***

**Table A.2** – ***continued from previous page***

| **Class**<br>**ICL** | **ID** | **R. A.** (deg) | **Dec.** (deg) | $\lambda_{5007}$ (Å) | $V_{\rm LOS}$ (kms$^{-1}$) | $m_{5007}$ |
|---|---|---|---|---|---|---|
| | M87_PN_36 | 187.98628 | 12.186553 | 5013.8 | 408.0 | 26.4 |
| | M87_PN_37 | 187.54721 | 12.603345 | 5042.3 | 2117.4 | 27.7 |
| | M87_PN_38 | 187.99559 | 12.174933 | 5013.5 | 387.7 | 27.9 |
| | M87_PN_39 | 187.65266 | 12.495434 | 5016.8 | 584.2 | 27.0 |
| | M87_PN_40 | 187.75159 | 12.715092 | 5043.4 | 2179.7 | 28.1 |
| | M87_PN_41 | 187.99199 | 12.160833 | 5012.9 | 352.3 | 27.1 |
| | M87_PN_42 | 187.90837 | 12.170931 | 5043.9 | 2209.1 | 26.6 |
| | M87_PN_43 | 187.55525 | 12.708831 | 5044.2 | 2231.3 | 27.9 |
| | M87_PN_44 | 187.98462 | 12.166172 | 5012.3 | 315.1 | 26.8 |

Figure A.2: **Spectra of single confirmed IC PNs**.
Red vertical lines mark the position of the two oxygen lines at their redshifted wavelengths. Spectra have been smoothed to 0.015 nm per pixel. The PN ID is specified as legend.

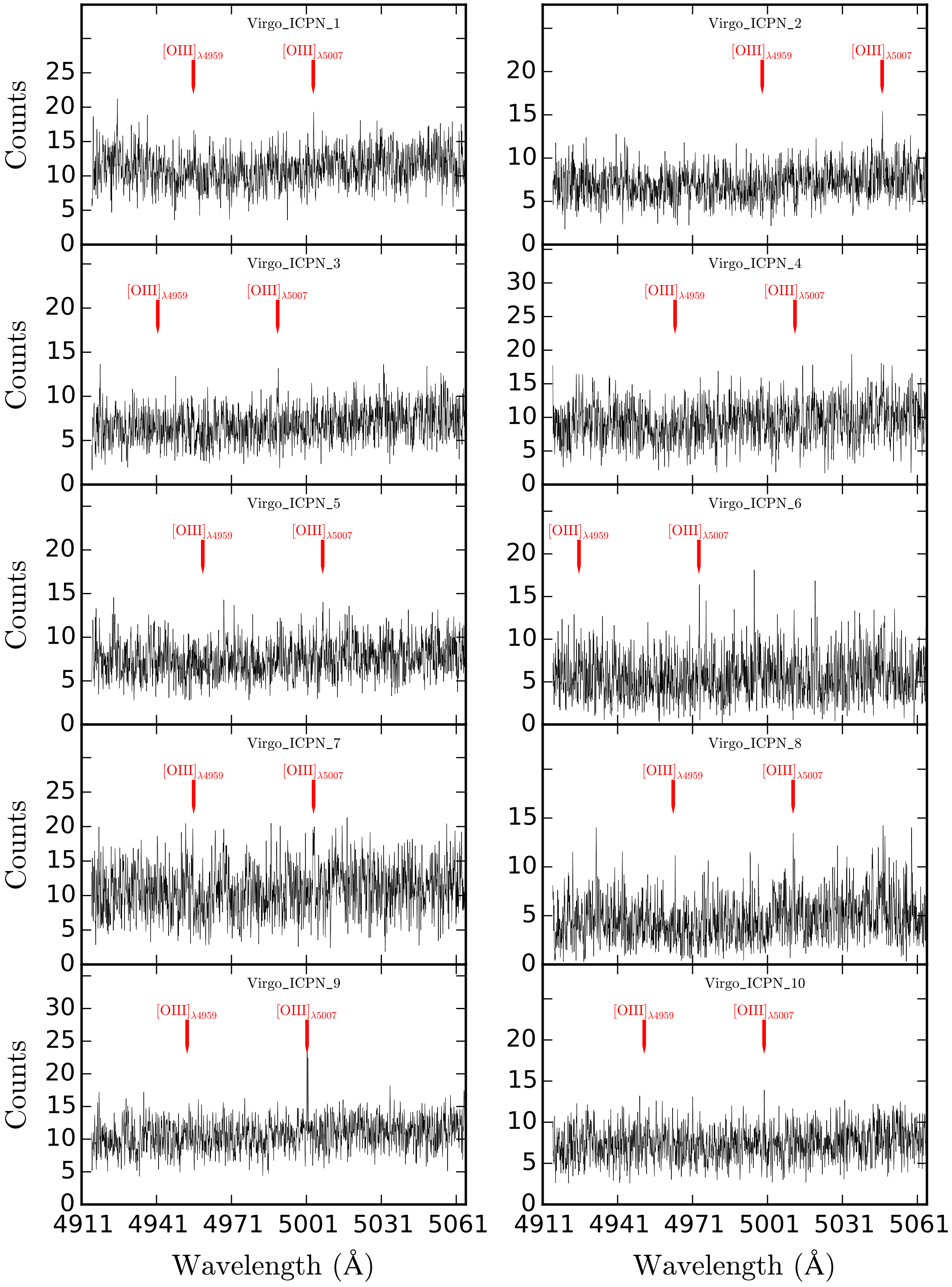

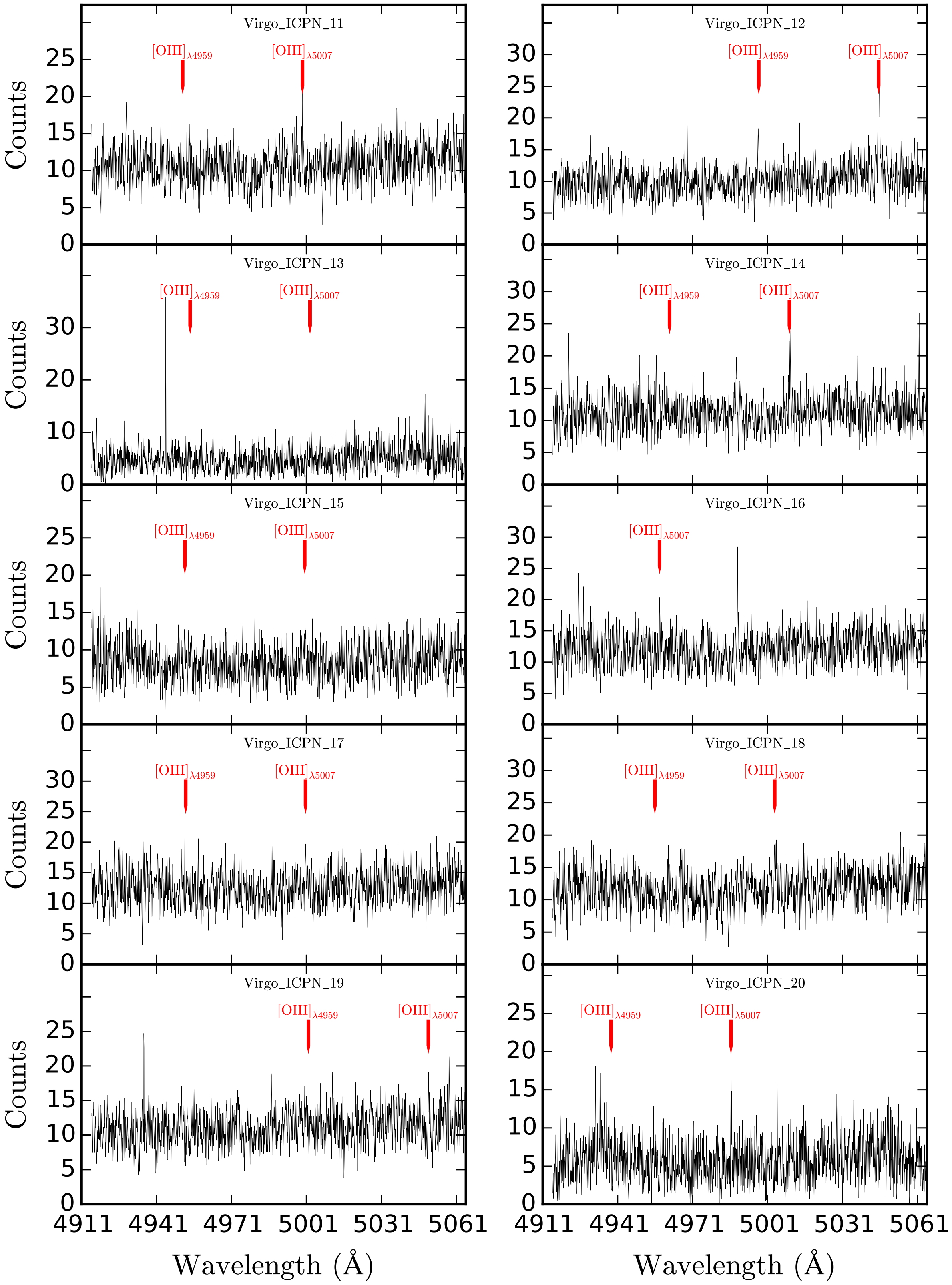
Virgo_ICPN_11
Virgo_ICPN_12
Virgo_ICPN_13
Virgo_ICPN_14
Virgo_ICPN_15
Virgo_ICPN_16
Virgo_ICPN_17
Virgo_ICPN_18
Virgo_ICPN_19
Virgo_ICPN_20
[OIII]λ4959
[OIII]λ5007
Counts
Wavelength (Å)
4911
4941
4971
5001
5031
5061
0
5
10
15
20
25
30

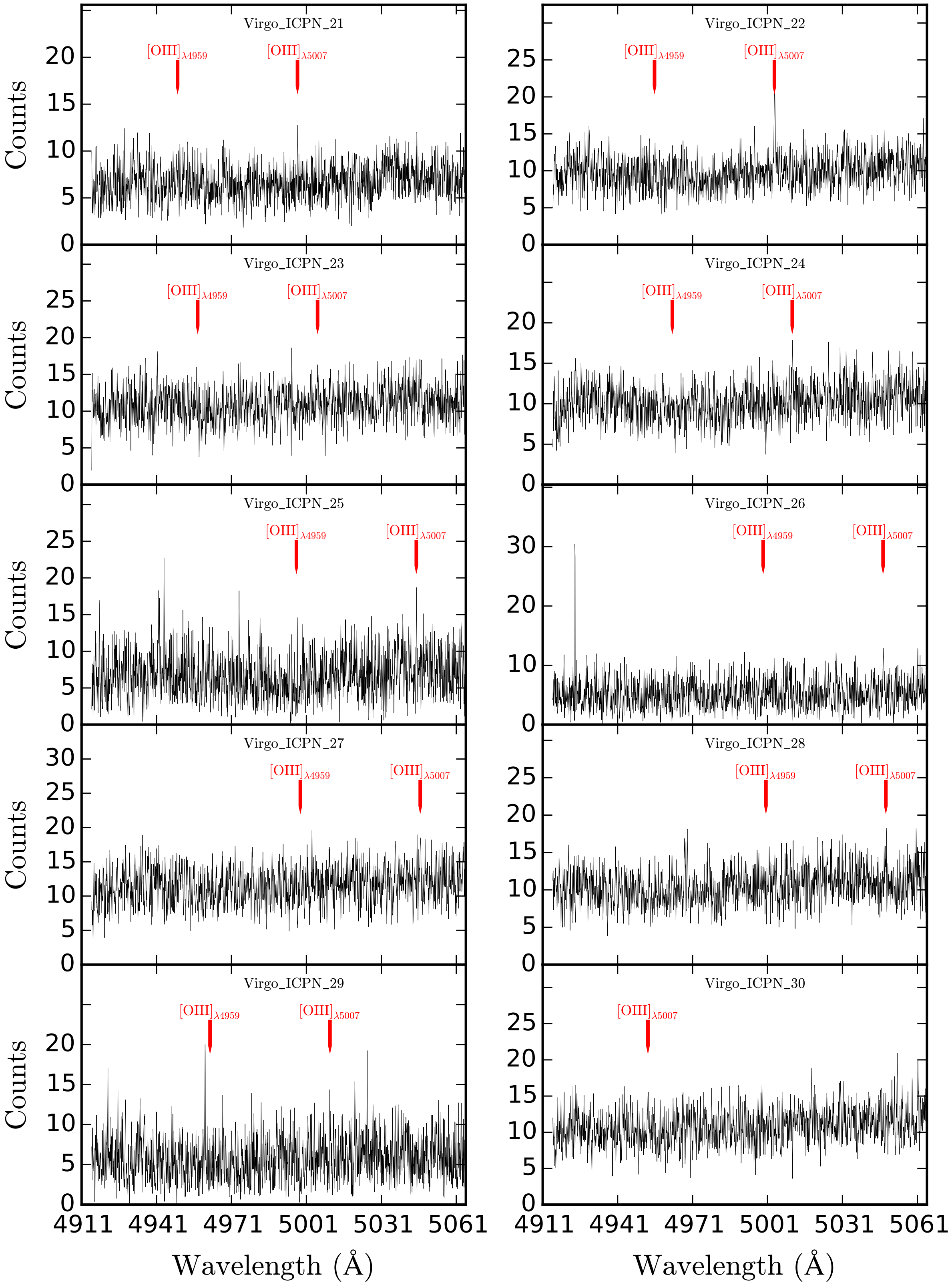
Virgo_ICPN_21
[OIII]$_{\lambda 4959}$
[OIII]$_{\lambda 5007}$
Virgo_ICPN_22
[OIII]$_{\lambda 4959}$
[OIII]$_{\lambda 5007}$
Virgo_ICPN_23
[OIII]$_{\lambda 4959}$
[OIII]$_{\lambda 5007}$
Virgo_ICPN_24
[OIII]$_{\lambda 4959}$
[OIII]$_{\lambda 5007}$
Virgo_ICPN_25
[OIII]$_{\lambda 4959}$
[OIII]$_{\lambda 5007}$
Virgo_ICPN_26
[OIII]$_{\lambda 4959}$
[OIII]$_{\lambda 5007}$
Virgo_ICPN_27
[OIII]$_{\lambda 4959}$
[OIII]$_{\lambda 5007}$
Virgo_ICPN_28
[OIII]$_{\lambda 4959}$
[OIII]$_{\lambda 5007}$
Virgo_ICPN_29
[OIII]$_{\lambda 4959}$
[OIII]$_{\lambda 5007}$
Virgo_ICPN_30
[OIII]$_{\lambda 5007}$
Counts
0 5 10 15 20 25 30
4911 4941 4971 5001 5031 5061
Wavelength (Å)

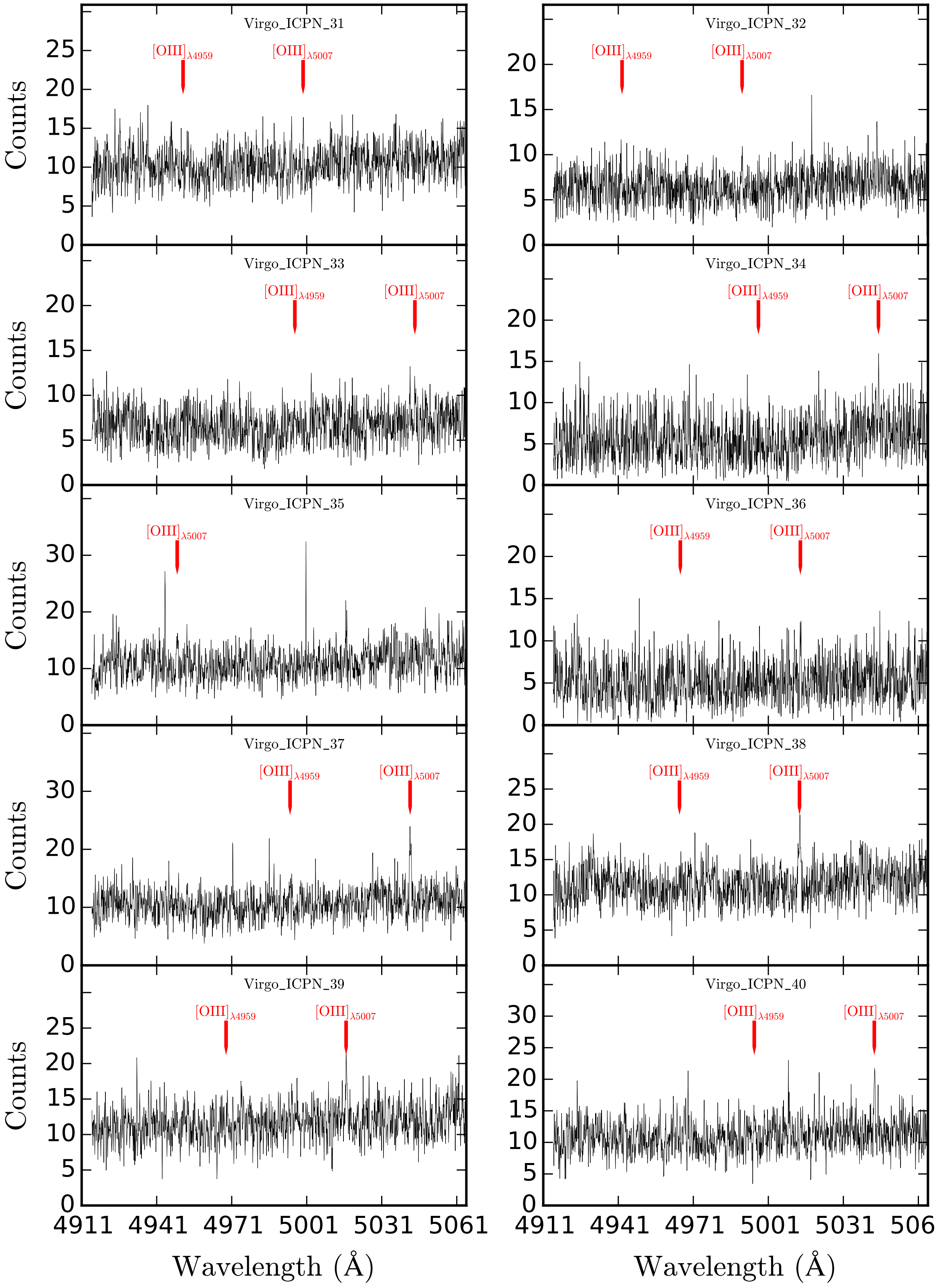
Virgo_ICPN_31
Virgo_ICPN_32
Virgo_ICPN_33
Virgo_ICPN_34
Virgo_ICPN_35
Virgo_ICPN_36
Virgo_ICPN_37
Virgo_ICPN_38
Virgo_ICPN_39
Virgo_ICPN_40
[OIII]$_{\lambda 4959}$
[OIII]$_{\lambda 5007}$
Counts
Wavelength (Å)
4911
4941
4971
5001
5031
5061
0
5
10
15
20
25
30

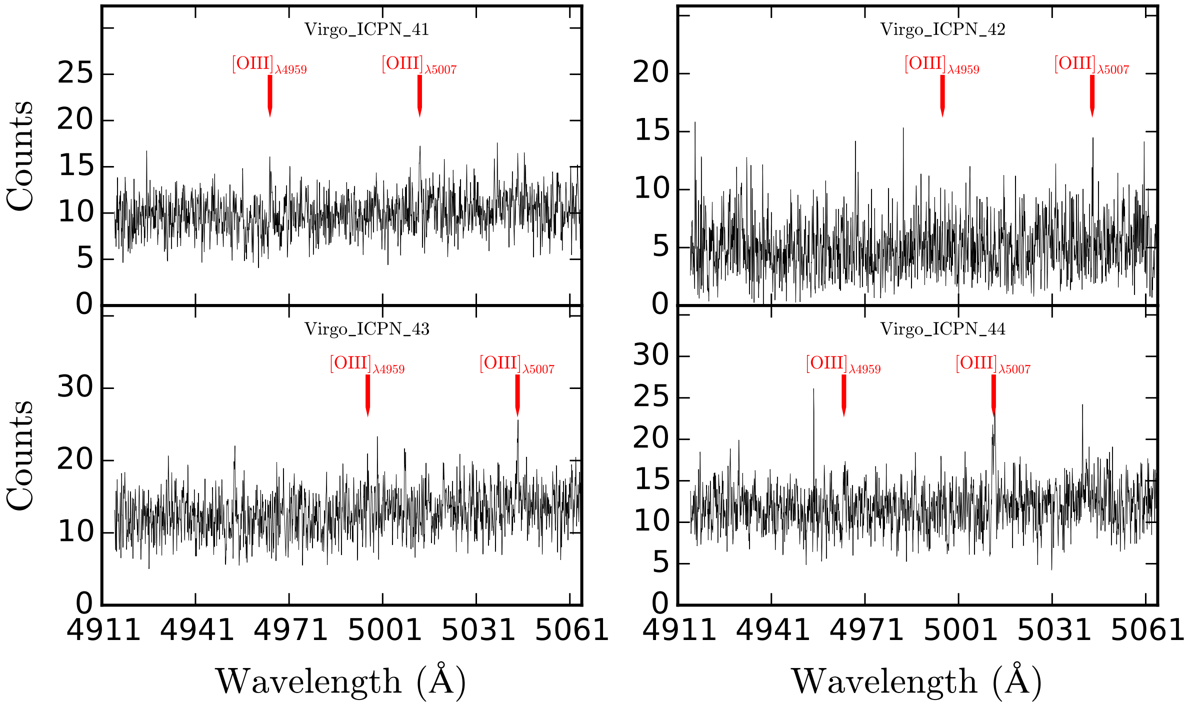
Virgo_ICPN_41
Virgo_ICPN_42
Virgo_ICPN_43
Virgo_ICPN_44
[OIII]$_{\lambda4959}$
[OIII]$_{\lambda5007}$
Counts
Wavelength (Å)
4911
4941
4971
5001
5031
5061
0
5
10
15
20
25
30

Table A.3: **Spectroscopically confirmed *Lyα* emitters at $z$ ~3.1**
Column 1: ID. Column 2 & 3 Right Ascension and Declination. Column 4: Redshift. Columns 5: Redshifted [OIII]$\lambda$1216 Å emission wavelength. Columns 5: $\lambda$5007 magnitude.

| **Class** | **ID** | **R. A.** | **Dec.** | Redshift | $\lambda_{5007}$ | $m_{5007}$ |
|---|---|---|---|---|---|---|
| *Lyα* | | (deg) | (deg) | | (Å) | |
| | Lyα_1 | 187.67258 | 12.549342 | 3.14432 | 5038.1 | 27.8 |
| | Lyα_2 | 187.84953 | 12.647509 | 3.11678 | 5004.6 | 27.4 |
| | Lyα_3 | 187.69124 | 12.649667 | 3.12861 | 5019.0 | 29.3 |
| | Lyα_4 | 187.69096 | 12.696572 | 3.14377 | 5037.5 | 28.4 |
| | Lyα_5 | 187.86641 | 12.781892 | 3.11582 | 5003.5 | 27.4 |
| | Lyα_6 | 187.59647 | 12.709186 | 3.1515 | 5046.9 | 26.9 |
| | Lyα_7 | 187.8192 | 12.566897 | 3.14093 | 5034.0 | 27.8 |
| | Lyα_8 | 188.00946 | 11.998261 | 3.14868 | 5043.4 | 25.5 |
| | Lyα_9 | 187.87482 | 11.815558 | 3.11487 | 5002.3 | 26.9 |
| | Lyα_10 | 187.88995 | 12.023433 | 3.14093 | 5034.0 | 25.4 |
| | Lyα_11 | 187.85225 | 12.091519 | 3.1327 | 5024.0 | 26.7 |
| | Lyα_12 | 187.81604 | 12.071353 | 3.13928 | 5032.0 | 26.8 |
| | Lyα_13 | 188.03113 | 12.131422 | 3.14833 | 5043.0 | 25.9 |
| | Lyα_14 | 187.8425 | 12.374389 | 3.14418 | 5037.9 | 25.2 |
| | Lyα_15 | 187.69975 | 11.960897 | 3.11049 | 4997.0 | 26.8 |
| | Lyα_16 | 187.53949 | 12.008178 | 3.10802 | 4994.0 | 25.6 |
| | Lyα_17 | 187.79596 | 12.119917 | 3.1393 | 5032.0 | 26.6 |
| | Lyα_18 | 187.73183 | 11.945514 | 3.10347 | 4988.5 | 25.6 |
| | Lyα_19 | 187.77354 | 12.553534 | 3.11936 | 5007.8 | 26.4 |
| | Lyα_20 | 187.56787 | 12.658097 | 3.15293 | 5048.6 | 26.9 |
| | Lyα_21 | 187.66513 | 12.667778 | 3.12019 | 5008.8 | 26.7 |
| | Lyα_22 | 187.85234 | 12.747059 | 3.10634 | 4992.0 | 26.7 |
| | Lyα_23 | 187.71971 | 12.583138 | 3.15211 | 5047.6 | 26.6 |
| | Lyα_24 | 187.64426 | 12.43172 | 3.1515 | 5046.9 | 26.8 |
| | Lyα_25 | 187.45554 | 12.472574 | 3.10067 | 4985.1 | 25.5 |
| | Lyα_26 | 187.7155 | 12.542981 | 3.12175 | 5010.7 | 26.0 |
| | Lyα_27 | 187.46738 | 12.70948 | 3.14202 | 5035.3 | 25.8 |
| | Lyα_28 | 187.47063 | 12.710722 | 3.14209 | 5035.4 | 25.7 |
| | Lyα_29 | 187.53072 | 12.371803 | 3.14066 | 5033.7 | 26.4 |
| | Lyα_30 | 187.68837 | 12.488842 | 3.12005 | 5008.6 | 26.8 |
| | Lyα_31 | 187.55872 | 12.646553 | 3.1264 | 5016.3 | 26.8 |
| | Lyα_32 | 187.56154 | 12.390031 | 3.13322 | 5024.6 | 19.9 |
| | Lyα_33 | 187.52184 | 12.414778 | 3.11839 | 5006.6 | 27.0 |
| | Lyα_34 | 187.4295 | 12.490428 | 3.13714 | 5029.4 | 27.8 |
| | Lyα_35 | 187.57762 | 12.543864 | 3.11296 | 5000.0 | 27.2 |

**Table A.3 – *continued on next page***

**Table A.3** – ***continued from previous page***

| **Class**<br>*Lyα* | **ID** | **R. A.**<br>(deg) | **Dec.**<br>(deg) | Redshift | $\lambda_{5007}$<br>(Å) | $m_{5007}$ |
|---|---|---|---|---|---|---|
| | Lyα_36 | 187.4836 | 12.568211 | 3.1508 | 5046.0 | 28.2 |
| | Lyα_37 | 187.73013 | 12.601284 | 3.12118 | 5010.0 | 27.5 |
| | Lyα_38 | 187.69925 | 12.609317 | 3.15491 | 5051.0 | 27.7 |
| | Lyα_39 | 187.38728 | 12.623231 | 3.11296 | 5000.0 | 27.6 |
| | Lyα_40 | 187.49046 | 12.689183 | 3.13151 | 5022.6 | 27.4 |
| | Lyα_41 | 187.4511 | 12.457389 | 3.1127 | 4999.7 | 27.2 |
| | Lyα_42 | 187.64691 | 12.486684 | 3.13216 | 5023.3 | 28.8 |
| | Lyα_43 | 187.59888 | 12.492583 | 3.14039 | 5033.4 | 28.0 |
| | Lyα_44 | 187.43051 | 12.529531 | 3.13887 | 5031.5 | 27.9 |
| | Lyα_45 | 187.46063 | 12.621375 | 3.13369 | 5025.2 | 27.4 |
| | Lyα_46 | 187.61537 | 12.404722 | 3.13001 | 5020.7 | 27.3 |
| | Lyα_47 | 187.89978 | 11.89645 | 3.14429 | 5038.1 | 27.8 |
| | Lyα_48 | 187.68533 | 12.036498 | 3.12109 | 5009.9 | 28.0 |
| | Lyα_49 | 187.8954 | 12.003422 | 3.13718 | 5029.4 | 27.3 |
| | Lyα_50 | 188.05159 | 12.086108 | 3.14297 | 5036.5 | 27.0 |
| | Lyα_51 | 187.9259 | 11.998703 | 3.13354 | 5025.0 | 27.1 |
| | Lyα_52 | 187.96204 | 12.130745 | 3.13263 | 5023.9 | 27.4 |
| | Lyα_53 | 187.93182 | 12.090827 | 3.15108 | 5046.3 | 28.6 |
| | Lyα_54 | 187.90945 | 12.250206 | 3.13523 | 5027.1 | 27.9 |
| | Lyα_55 | 187.86713 | 12.175658 | 3.13667 | 5028.8 | 27.3 |
| | Lyα_56 | 187.79904 | 12.203711 | 3.13848 | 5031.0 | 28.1 |
| | Lyα_57 | 187.75833 | 12.14363 | 3.1411 | 5034.2 | 27.7 |
| | Lyα_58 | 187.78929 | 12.239847 | 3.13603 | 5028.1 | 27.7 |
| | Lyα_59 | 187.81137 | 12.312161 | 3.1062 | 4991.8 | 27.1 |
| | Lyα_60 | 187.89137 | 12.184967 | 3.1292 | 5019.8 | 27.3 |
| | Lyα_61 | 187.90495 | 12.195108 | 3.13006 | 5020.8 | 27.8 |
| | Lyα_62 | 187.96451 | 12.340789 | 3.10226 | 4987.0 | 27.2 |
| | Lyα_63 | 187.9325 | 12.257183 | 3.14929 | 5044.2 | 29.0 |
| | Lyα_64 | 187.79953 | 12.109692 | 3.11071 | 4997.3 | 27.1 |
| | Lyα_65 | 187.59383 | 12.064636 | 3.14157 | 5034.8 | 28.0 |
| | Lyα_66 | 187.89728 | 12.321417 | 3.13231 | 5023.5 | 26.9 |
| | Lyα_67 | 187.80203 | 12.220386 | 3.1084 | 4994.5 | 27.2 |
| | Lyα_68 | 187.79837 | 12.273514 | 3.13846 | 5031.0 | 26.6 |
| | Lyα_69 | 187.478 | 12.738325 | 3.12896 | 5019.4 | 27.4 |
| | Lyα_70 | 187.59647 | 12.709186 | 3.14997 | 5045.0 | 26.9 |

Figure A.3: **Spectra of single confirmed Ly$\alpha$ emitters at $z$ ~3.1**. Red vertical lines mark the position of the Ly$\alpha$ $\lambda$1216 Å at its redshifted wavelengths. Spectra have been smoothed to 0.015 nm per pixel. The Ly$\alpha$ ID is specified as legend.

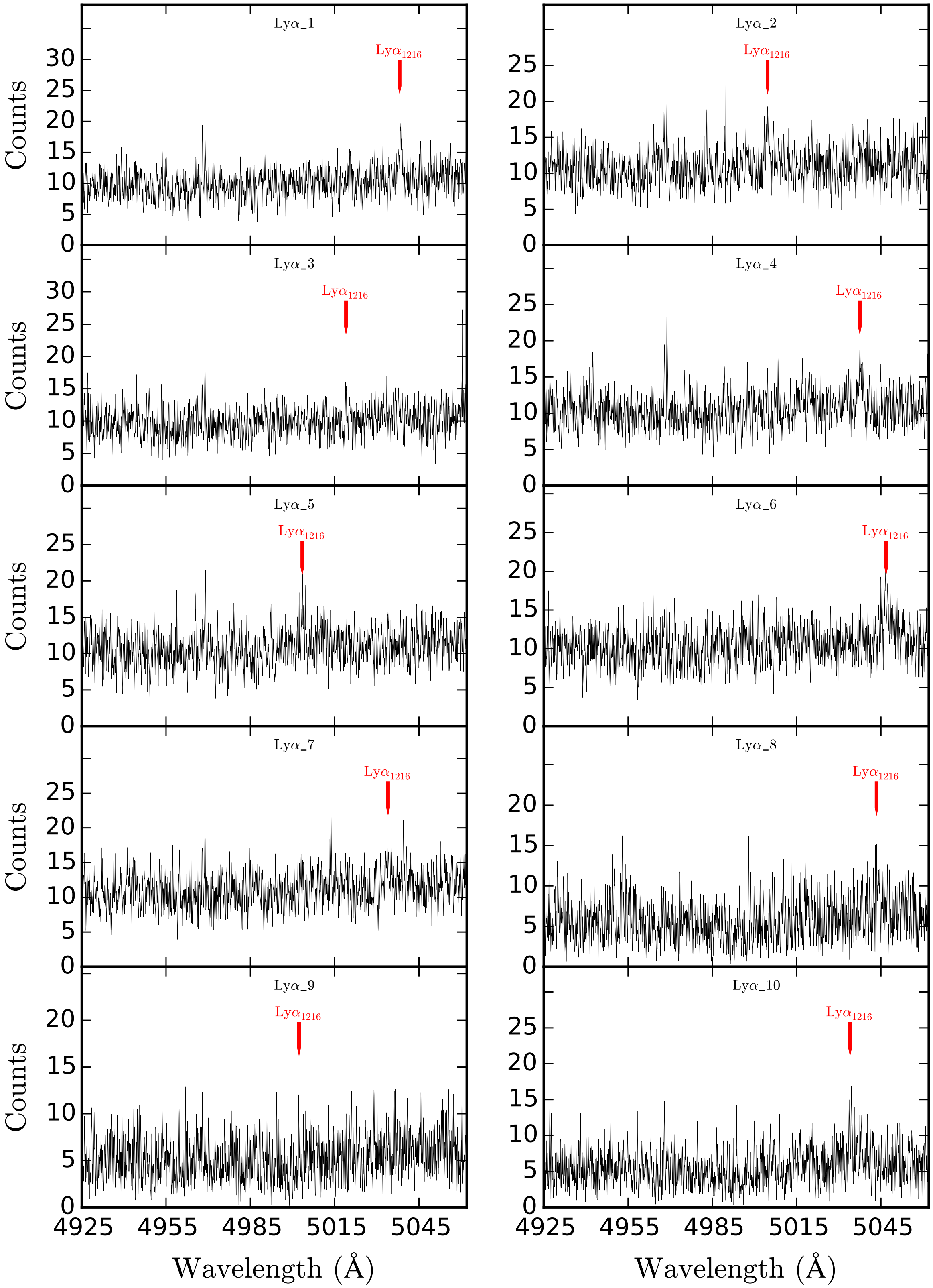

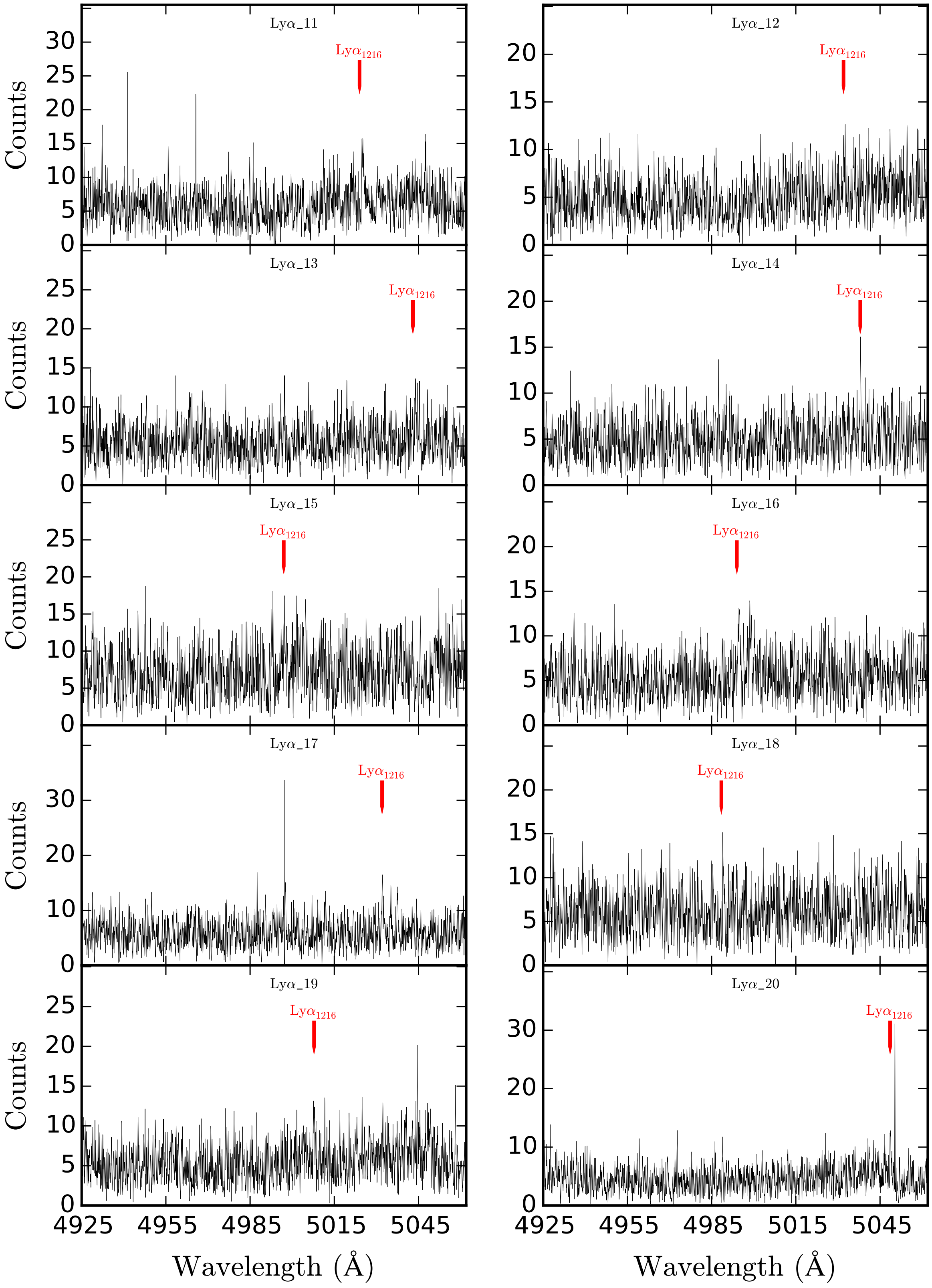
Lyα_11
Lyα_12
Lyα_13
Lyα_14
Lyα_15
Lyα_16
Lyα_17
Lyα_18
Lyα_19
Lyα_20
$Ly\alpha_{1216}$
Counts
0
5
10
15
20
25
30
4925
4955
4985
5015
5045
Wavelength (Å)

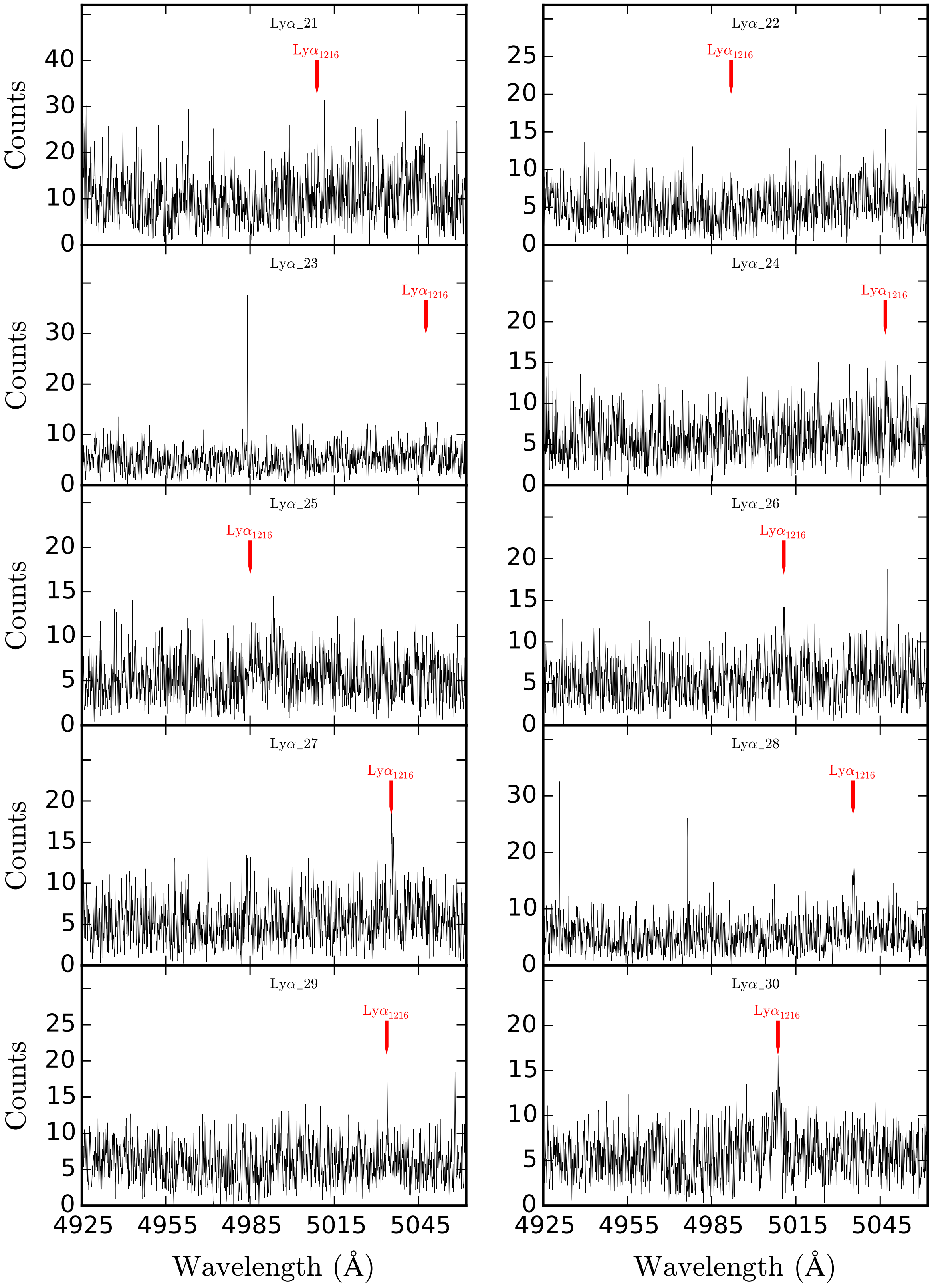
Lyα_21
Lyα_22
Lyα_23
Lyα_24
Lyα_25
Lyα_26
Lyα_27
Lyα_28
Lyα_29
Lyα_30
Lyα1216
Counts
Wavelength (Å)
4925
4955
4985
5015
5045
0
5
10
15
20
25
30
40

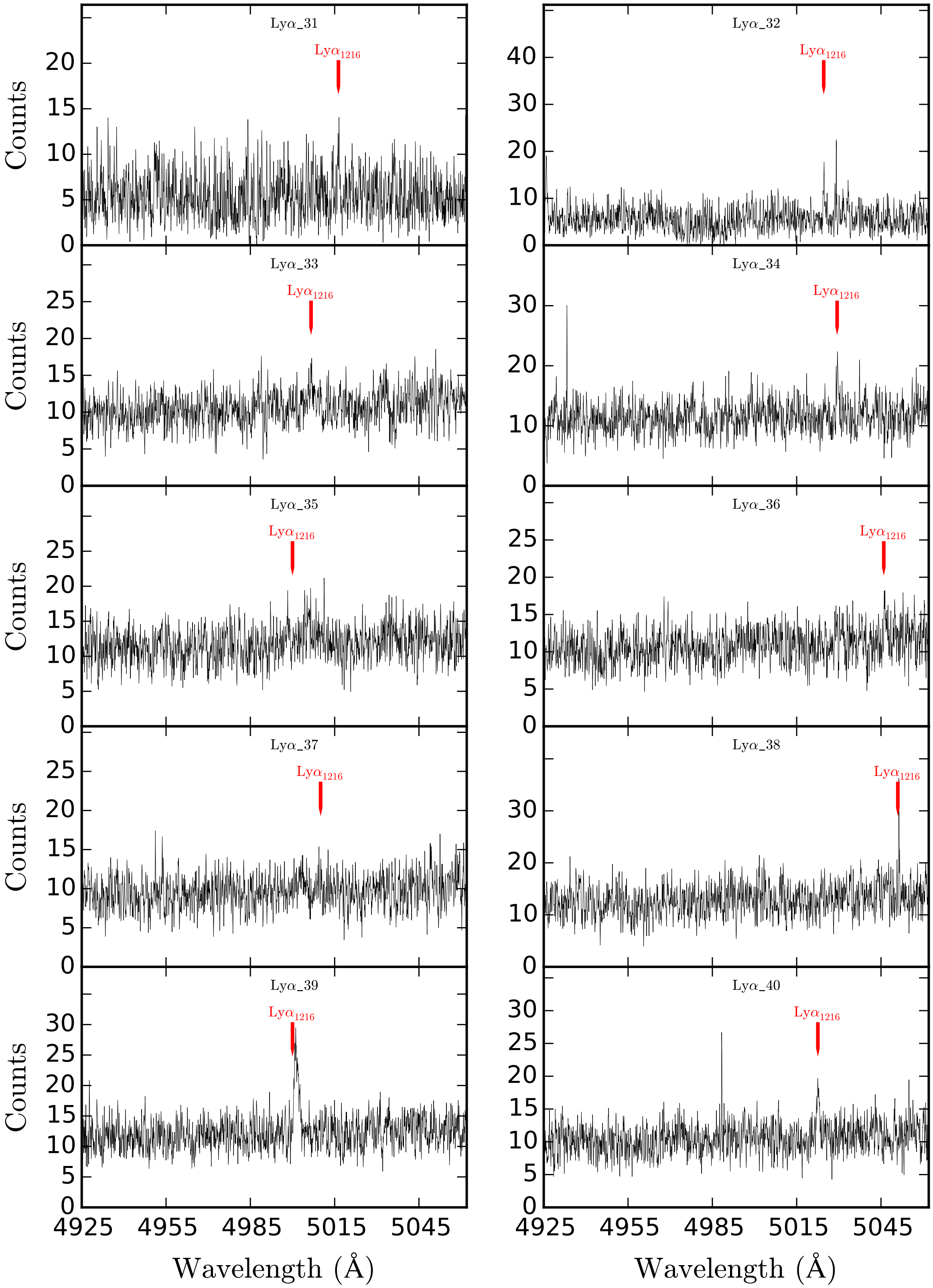
Lyα_31
Lyα$_{1216}$
Lyα_32
Lyα$_{1216}$
Lyα_33
Lyα$_{1216}$
Lyα_34
Lyα$_{1216}$
Lyα_35
Lyα$_{1216}$
Lyα_36
Lyα$_{1216}$
Lyα_37
Lyα$_{1216}$
Lyα_38
Lyα$_{1216}$
Lyα_39
Lyα$_{1216}$
Lyα_40
Lyα$_{1216}$
Counts
Counts
Counts
Counts
Counts
0
5
10
15
20
25
30
40
4925
4955
4985
5015
5045
Wavelength (Å)
Wavelength (Å)

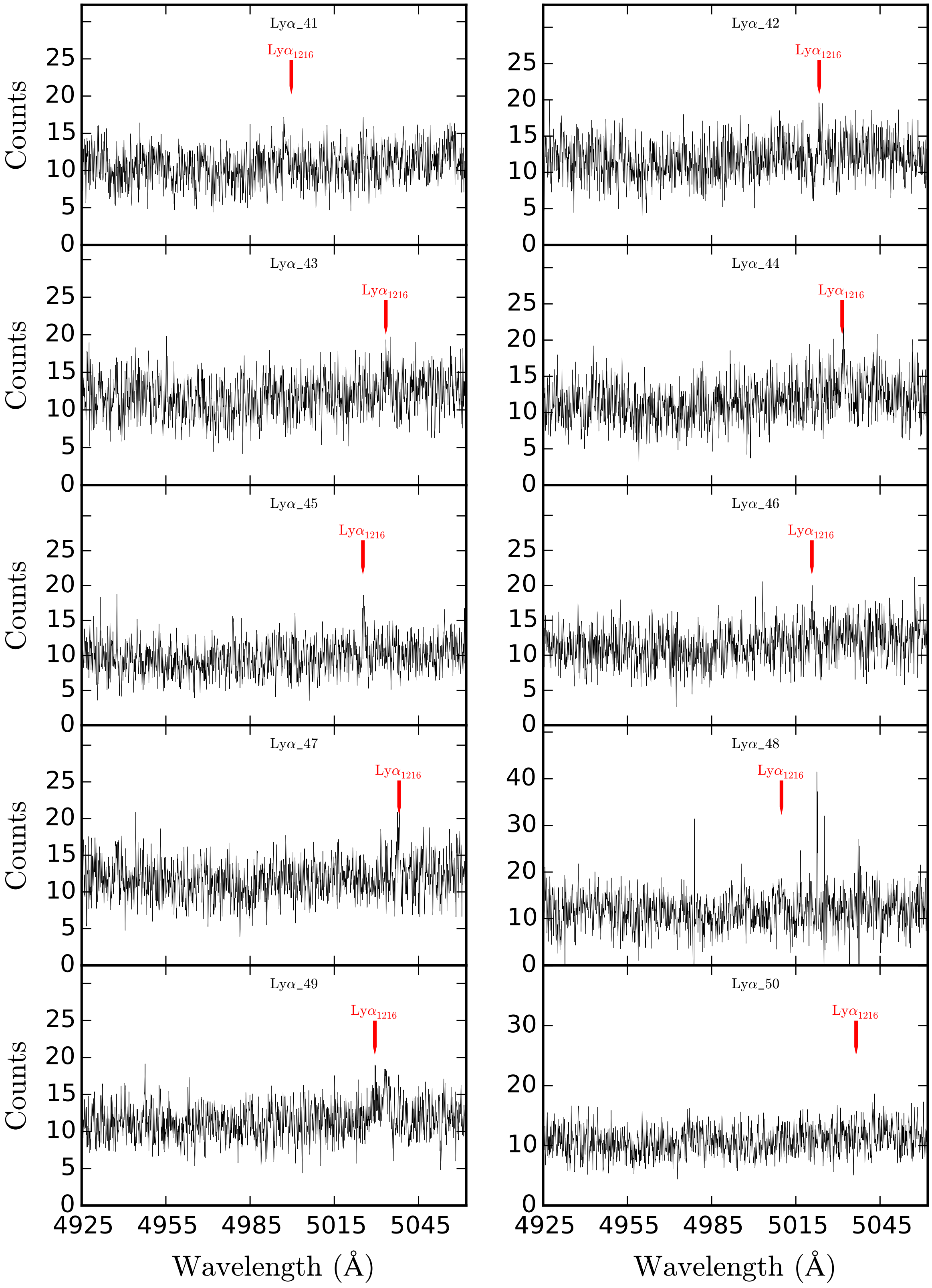
Lyα_41
Lyα_42
Lyα_43
Lyα_44
Lyα_45
Lyα_46
Lyα_47
Lyα_48
Lyα_49
Lyα_50
$\mathrm{Ly}\alpha_{1216}$
Counts
0
5
10
15
20
25
30
40
4925
4955
4985
5015
5045
Wavelength (Å)

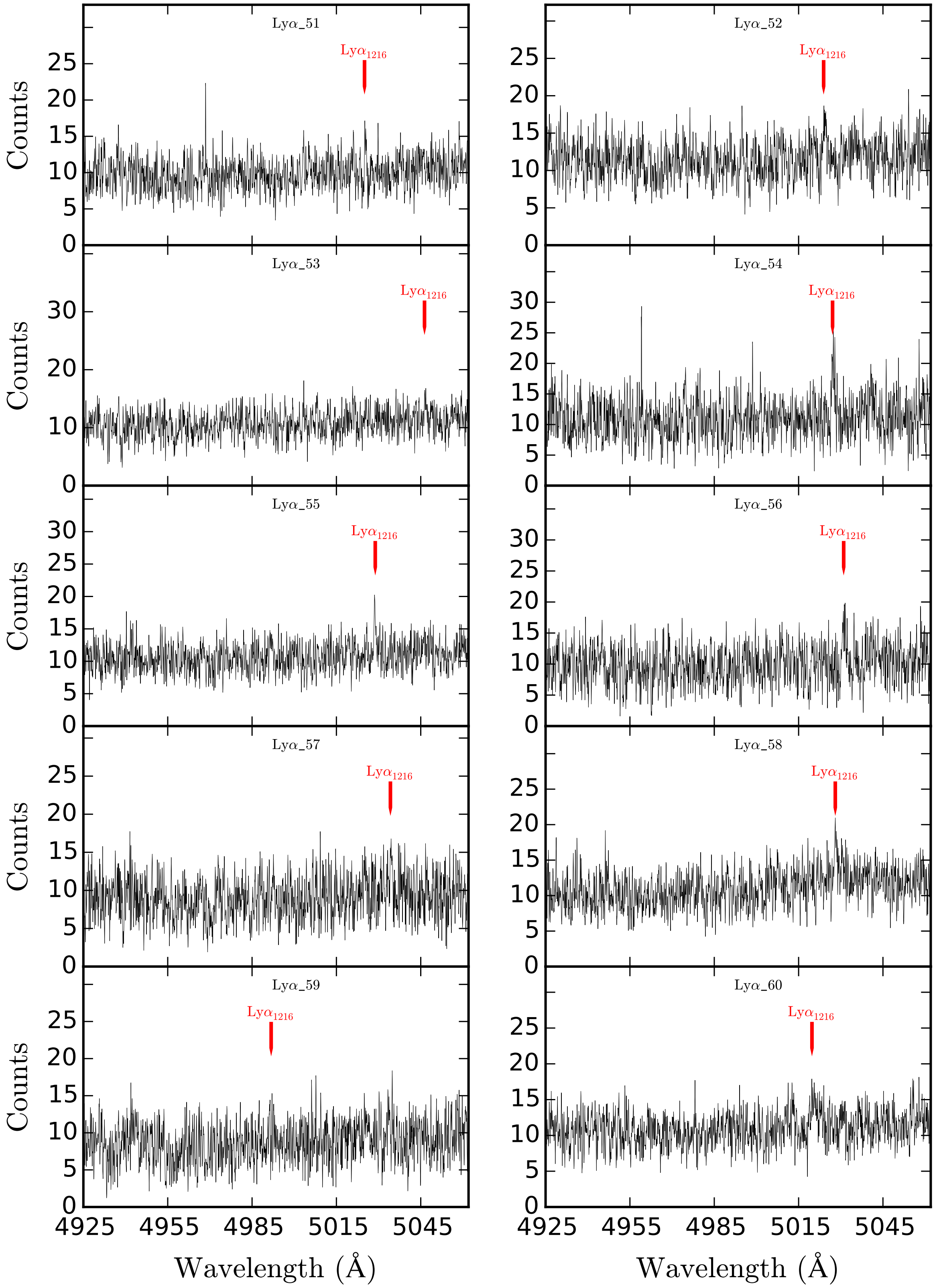
Lyα_51
Lyα_52
Lyα_53
Lyα_54
Lyα_55
Lyα_56
Lyα_57
Lyα_58
Lyα_59
Lyα_60
Lyα1216
Counts
0
5
10
15
20
25
30
4925
4955
4985
5015
5045
Wavelength (Å)

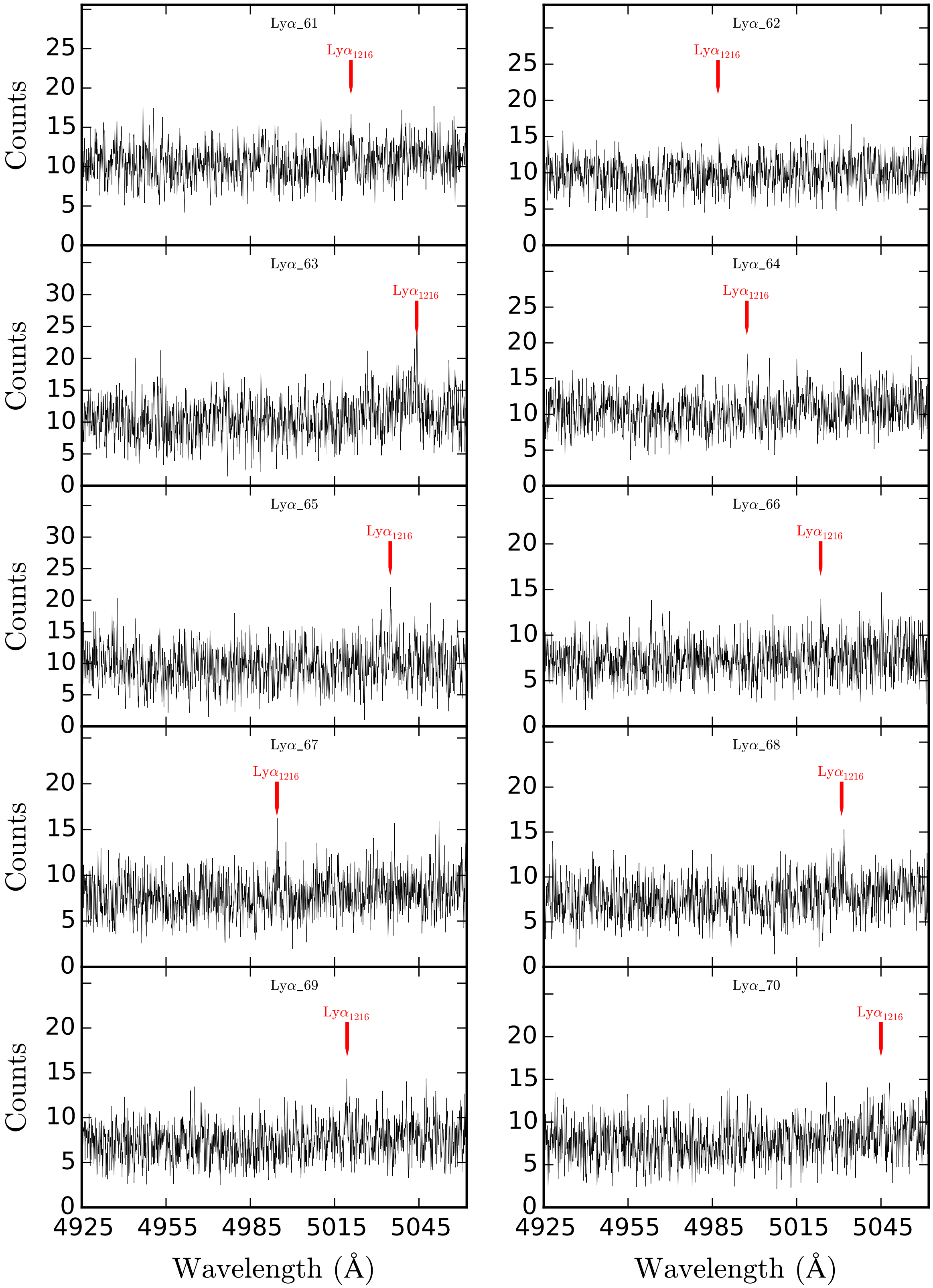
Lyα_61
Lyα_62
Lyα_63
Lyα_64
Lyα_65
Lyα_66
Lyα_67
Lyα_68
Lyα_69
Lyα_70
Lyα$_{1216}$
Counts
Wavelength (Å)
4925
4955
4985
5015
5045

Table A.4: **Spectroscopically confirmed [OII] emitters at $z$ ∼0.34**
Column 1: ID. Column 2 & 3 Right Ascension and Declination. Column 4: Redshift. Columns 5: Redshifted [OIII]$\lambda$3728 Å emission wavelength. Columns 5: $\lambda$5007 magnitude.

| **Class** OII | **ID** | **R. A.** (deg) | **Dec.** (deg) | Redshift | $\lambda_{5007}$ (Å) | $m_{5007}$ |
|---|---|---|---|---|---|---|
| | OII_1 | 187.82095 | 12.719233 | 0.349238 | 5031.0 | 29.3 |
| | OII_2 | 187.85286 | 12.745406 | 0.349447 | 5031.7 | 28.0 |
| | OII_3 | 187.79796 | 12.625875 | 0.349785 | 5033.0 | 27.3 |
| | OII_4 | 187.9883 | 12.030364 | 0.353004 | 5045.0 | 24.4 |
| | OII_5 | 187.87633 | 12.066151 | 0.344421 | 5013.0 | 25.0 |
| | OII_6 | 187.722 | 11.903913 | 0.343616 | 5010.0 | 23.6 |
| | OII_7 | 187.75787 | 12.036751 | 0.350322 | 5035.0 | 25.3 |
| | OII_8 | 188.00171 | 12.161158 | 0.344957 | 5015.0 | 25.2 |
| | OII_9 | 187.71547 | 12.021386 | 0.345762 | 5018.0 | 24.2 |
| | OII_10 | 187.7155 | 12.542981 | 0.34309 | 5008.0 | 26.0 |
| | OII_11 | 187.8745 | 12.552559 | 0.345365 | 5016.5 | 25.9 |
| | OII_12 | 187.82129 | 12.760753 | 0.34812 | 5024.8 | 25.6 |
| | OII_13 | 187.79437 | 12.587527 | 0.351695 | 5040.1 | 25.2 |
| | OII_14 | 187.37054 | 12.386814 | 0.338879 | 4991.3 | 26.5 |
| | OII_15 | 187.50554 | 12.389667 | 0.332881 | 4968.0 | 27.7 |
| | OII_16 | 187.45033 | 12.423719 | 0.351049 | 5037.7 | 27.6 |
| | OII_17 | 187.48845 | 12.488989 | 0.339029 | 4992.9 | 27.2 |
| | OII_18 | 187.35992 | 12.527152 | 0.353951 | 5048.5 | 27.1 |
| | OII_19 | 187.3735 | 12.610031 | 0.353801 | 5048.0 | 28.7 |
| | OII_20 | 187.39134 | 12.411733 | 0.353541 | 5047.0 | 27.3 |
| | OII_21 | 187.52553 | 12.682273 | 0.349262 | 5031.1 | 27.1 |
| | OII_22 | 187.77737 | 11.973433 | 0.35121 | 5038.3 | 27.4 |
| | OII_23 | 187.77171 | 12.002422 | 0.353809 | 5048.0 | 27.9 |
| | OII_24 | 187.74509 | 12.024236 | 0.353157 | 5045.6 | 27.4 |
| | OII_25 | 187.71638 | 12.023791 | 0.350966 | 5034.4 | 27.0 |
| | OII_26 | 187.97829 | 12.172136 | 0.344689 | 5014.0 | 27.5 |
| | OII_27 | 187.81276 | 11.876198 | 0.354614 | 5051.0 | 27.3 |
| | OII_28 | 187.74466 | 12.138375 | 0.337039 | 4985.5 | 27.0 |
| | OII_29 | 187.58833 | 12.026625 | 0.350024 | 5031.9 | 27.8 |
| | OII_30 | 187.73676 | 11.981005 | 0.34849 | 5028.2 | 26.9 |
| | OII_31 | 187.71638 | 12.300692 | 0.349321 | 5029.3 | 27.3 |
| | OII_32 | 187.8082 | 12.290309 | 0.352736 | 5044.0 | 27.7 |
| | OII_33 | 187.76678 | 12.364878 | 0.351931 | 5043.0 | 27.6 |
| | OII_34 | 187.7298 | 12.312523 | 0.351395 | 5039.0 | 27.3 |
| | OII_35 | 187.61617 | 12.788303 | 0.338519 | 4991.5 | 28.3 |

Figure A.4: **Spectra of single confirmed [OII] emitters at $z$ ~0.34**. Red vertical lines mark the position of the central wavelength between the two redshifetd [OII] $\lambda$3726/3729 Å emission lines. Spectra have been smoothed to 0.015 nm per pixel. The PN ID is specified as legend.

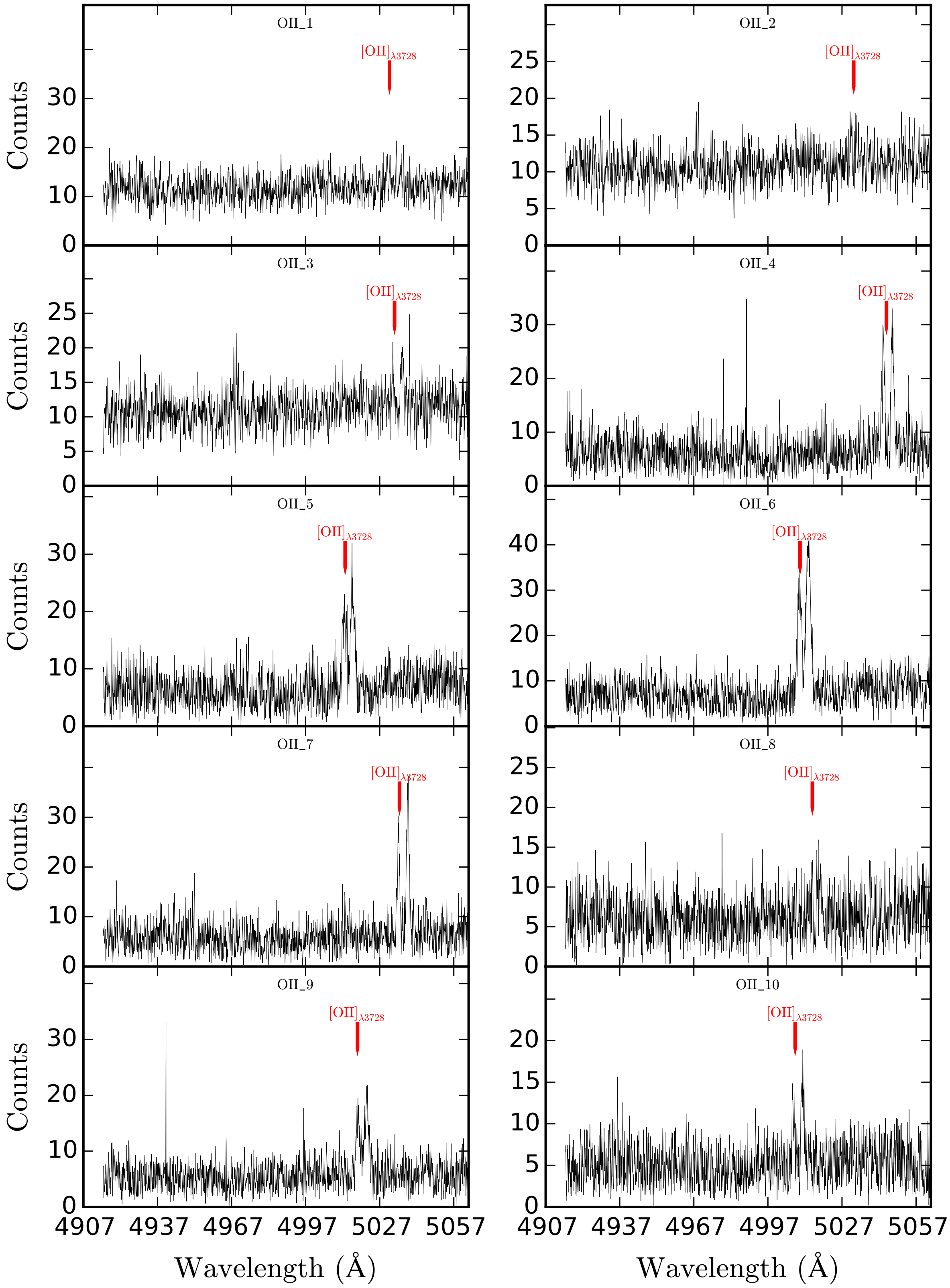

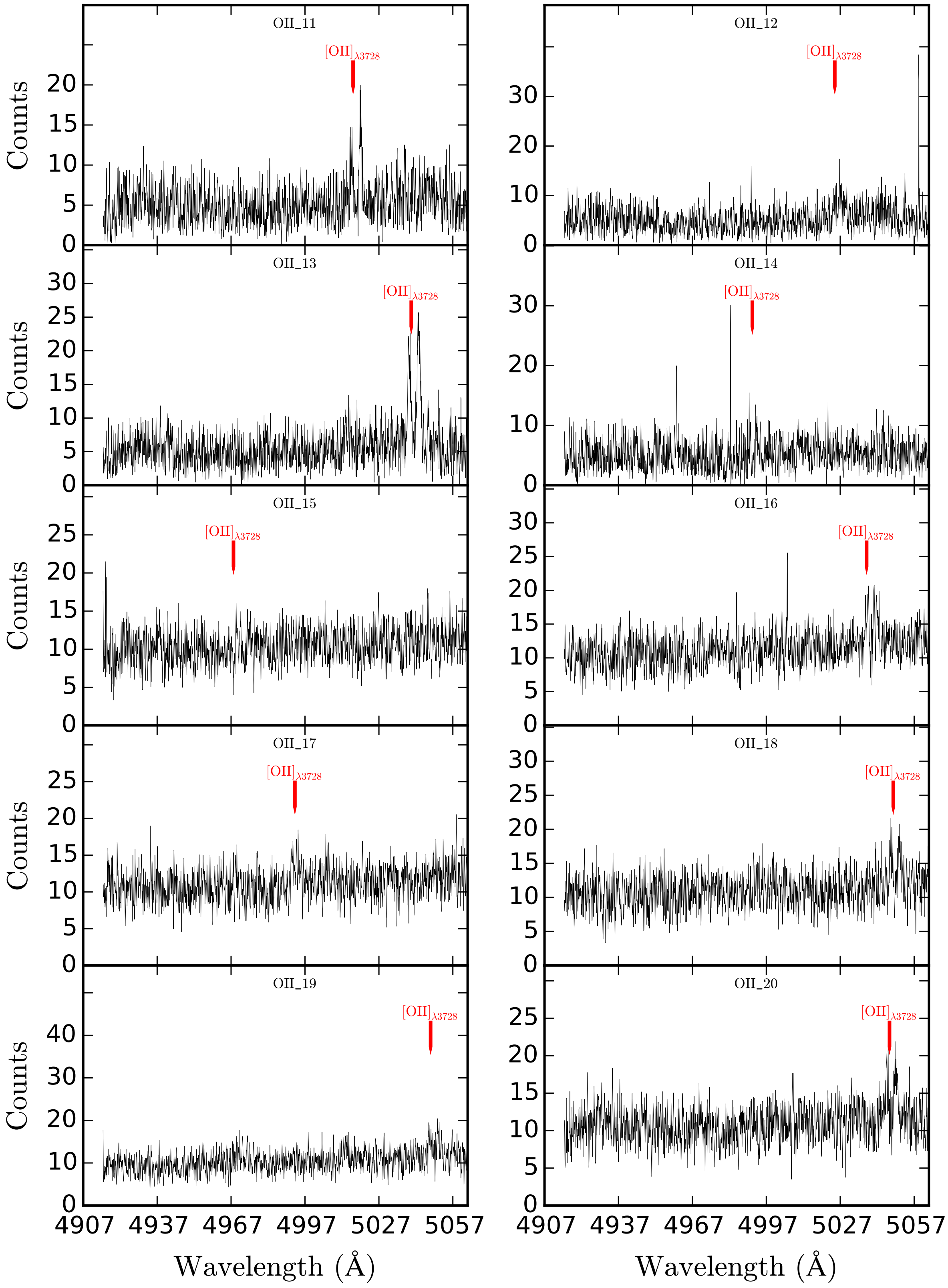
OII_11
OII_12
OII_13
OII_14
OII_15
OII_16
OII_17
OII_18
OII_19
OII_20
$[\text{OII}]_{\lambda3728}$
Counts
0
5
10
15
20
25
30
40
4907
4937
4967
4997
5027
5057
Wavelength (Å)

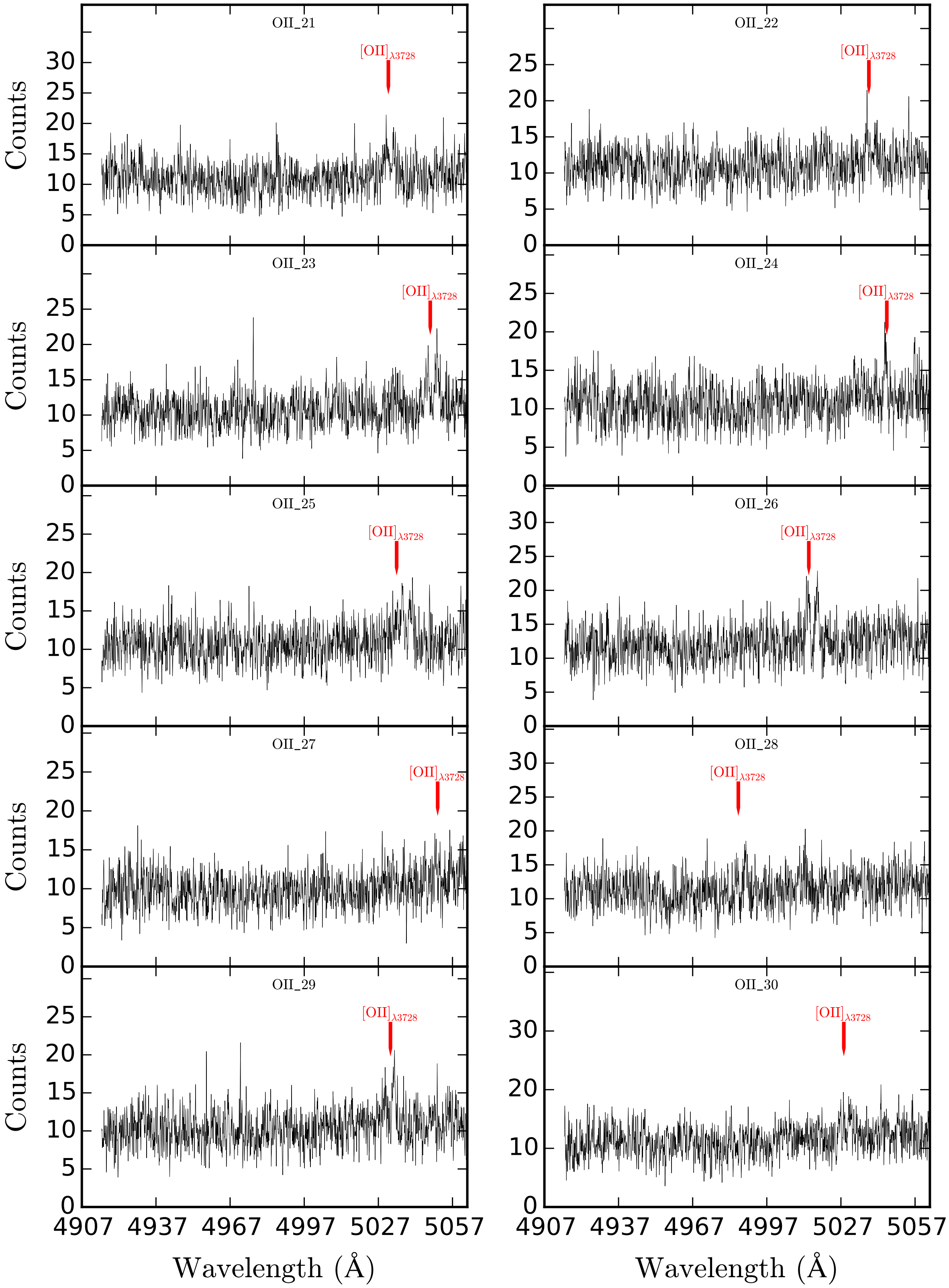
OII_21
OII_22
OII_23
OII_24
OII_25
OII_26
OII_27
OII_28
OII_29
OII_30
[OII]$_{\lambda3728}$
Counts
Wavelength (Å)
4907
4937
4967
4997
5027
5057
0
5
10
15
20
25
30

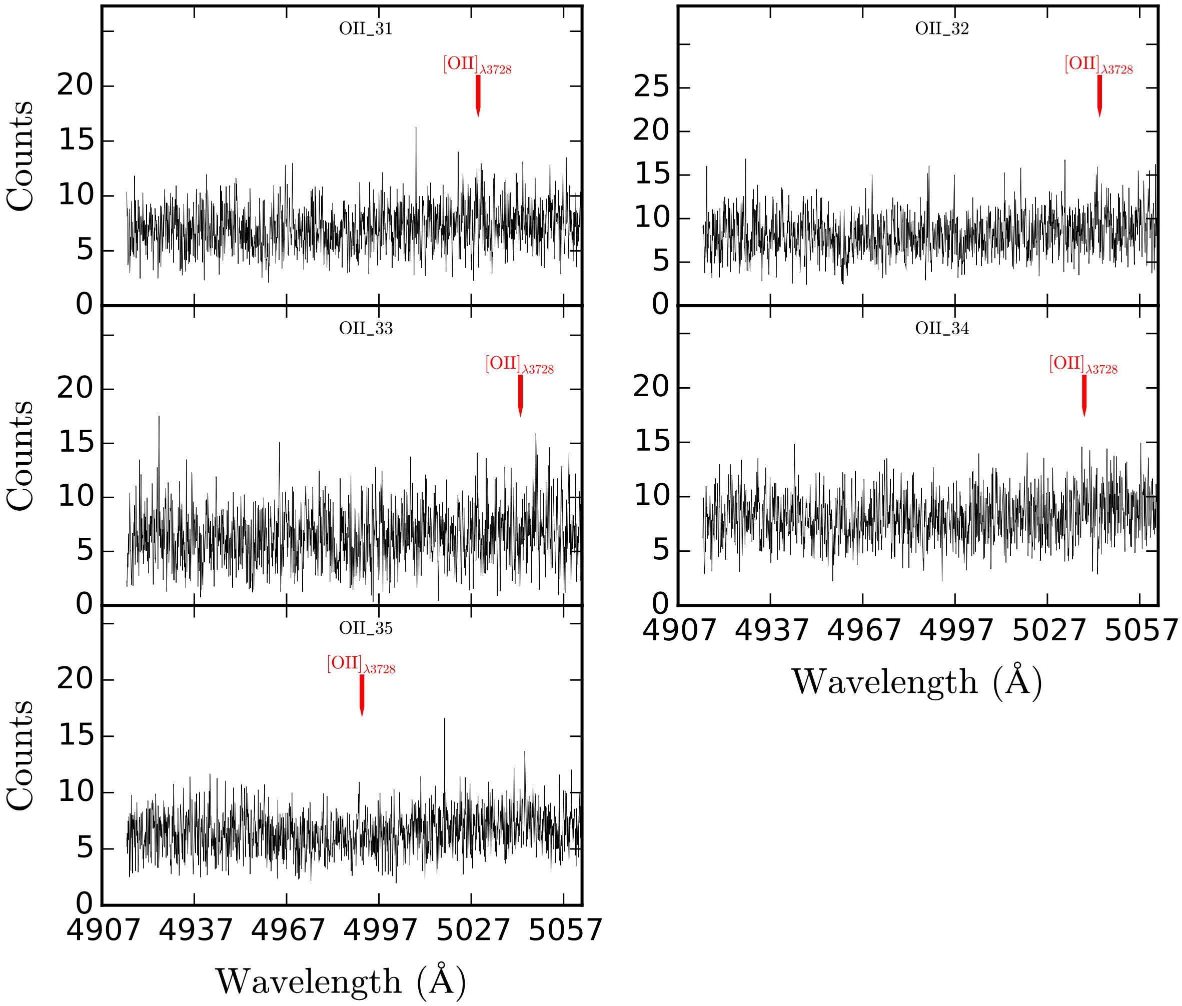
OII_31
OII_32
OII_33
OII_34
OII_35
[OII]$_{\lambda3728}$
Counts
0
5
10
15
20
25
4907
4937
4967
4997
5027
5057
Wavelength (Å)

# Bibliography

1999, The Observatory, 119, 296

Abadi, M. G., Navarro, J. F., & Steinmetz, M. 2006, MNRAS, 365, 747

Abadi, M. G., Navarro, J. F., Steinmetz, M., & Eke, V. R. 2003, ApJ, 591, 499

Abell, G. O. 1958, ApJS, 3, 211

Adami, C., Biviano, A., Durret, F., & Mazure, A. 2005, A&A, 443, 17

Adelman-McCarthy, J. K. & et al. 2009, VizieR Online Data Catalog, 2294, 0

Agnello, A., Evans, N. W., Romanowsky, A. J., & Brodie, J. P. 2014, ArXiv e-prints

Aguerri, J. A. L., Gerhard, O. E., Arnaboldi, M., et al. 2005, AJ, 129, 2585

Arnaboldi, M., Aguerri, J. A. L., Napolitano, N. R., et al. 2002, AJ, 123, 760

Arnaboldi, M., Freeman, K. C., Gerhard, O., et al. 1998, ApJ, 507, 759

Arnaboldi, M., Freeman, K. C., Mendez, R. H., et al. 1996, ApJ, 472, 145

Arnaboldi, M., Freeman, K. C., Okamura, S., et al. 2003, AJ, 125, 514

Arnaboldi, M., Gerhard, O., Aguerri, J. A. L., et al. 2004, ApJ, 614, L33

Arnaboldi, M., Ventimiglia, G., Iodice, E., Gerhard, O., & Coccato, L. 2012, A&A, 545, A37

Bahcall, N. A. 1996, ArXiv Astrophysics e-prints

Bautz, L. P. & Morgan, W. W. 1970, ApJ, 162, L149

Behroozi, P. S., Wechsler, R. H., & Conroy, C. 2013, ApJ, 770, 57

Bender, R. 1988, A&A, 193, L7

Bender, R., Burstein, D., & Faber, S. M. 1992, ApJ, 399, 462

Bender, R., Kormendy, J., Cornell, M. E., & Fisher, D. B. 2014, ArXiv e-prints

Bender, R., Saglia, R. P., & Gerhard, O. E. 1994, MNRAS, 269, 785

Bender, R., Surma, P., Doebereiner, S., Moellenhoff, C., & Madejsky, R. 1989, A&A, 217, 35

Bernardi, M., Hyde, J. B., Sheth, R. K., Miller, C. J., & Nichol, R. C. 2007, AJ, 133, 1741

Bernstein, G. M., Nichol, R. C., Tyson, J. A., Ulmer, M. P., & Wittman, D. 1995, AJ, 110, 1507

Bernstein, J. P. & Bhavsar, S. P. 2001, MNRAS, 322, 625

Bertin, E. & Arnouts, S. 1996, A&AS, 117, 393

Best, P. N. 2007, in Astronomical Society of the Pacific Conference Series, Vol. 379, Cosmic Frontiers, ed. N. Metcalfe & T. Shanks, 213

Binggeli, B., Popescu, C. C., & Tammann, G. A. 1993, A&AS, 98, 275

Binggeli, B., Sandage, A., & Tammann, G. A. 1988, ARA&A, 26, 509

Binggeli, B., Tammann, G. A., & Sandage, A. 1987, AJ, 94, 251

Bird, S., Harris, W. E., Blakeslee, J. P., & Flynn, C. 2010, A&A, 524, A71

Bournaud, F., Jog, C. J., & Combes, F. 2005, A&A, 437, 69

Boylan-Kolchin, M., Ma, C.-P., & Quataert, E. 2008, MNRAS, 383, 93

Bryan, G. L. 2000, ApJ, 544, L1

Bullock, J. S. & Johnston, K. V. 2005, ApJ, 635, 931

Burke, C., Collins, C. A., Stott, J. P., & Hilton, M. 2012, MNRAS, 425, 2058

Buton, C., Copin, Y., Aldering, G., et al. 2013, A&A, 549, A8

Buzzoni, A., Arnaboldi, M., & Corradi, R. L. M. 2006, MNRAS, 368, 877

Caldwell, N., Strader, J., Romanowsky, A. J., et al. 2014, ApJ, 787, L11

Caon, N., Capaccioli, M., & D'Onofrio, M. 1993, MNRAS, 265, 1013

Capaccioli, M. & Caon, N. 1989, in European Southern Observatory Conference and Workshop Proceedings, Vol. 31, ESO/ST-ECF Data Analysis Workshop, ed. P. J. Grosbøl, F. Murtagh, & R. H. Warmels, 107–126

Cappellari, M., Bacon, R., Bureau, M., et al. 2006, MNRAS, 366, 1126

Cappellari, M., Emsellem, E., Krajnovi'c, D., et al. 2011, mnras, 413, 813

Cardelli, J. A., Clayton, G. C., & Mathis, J. S. 1989, ApJ, 345, 245

Castro-Rodríguez, N., Aguerri, J. A. L., Arnaboldi, M., et al. 2003, A&A, 405, 803

Castro-Rodríguez, N., Arnaboldi, M., Aguerri, J. A. L., et al. 2009, A&A, 507, 621

Churazov, E., Forman, W., Vikhlinin, A., et al. 2008a, MNRAS, 388, 1062

Churazov, E., Forman, W., Vikhlinin, A., et al. 2008b, MNRAS, 388, 1062

Churazov, E., Tremaine, S., Forman, W., et al. 2010, MNRAS, 404, 1165

Ciardullo, R. 2010, PASA, 27, 149

Ciardullo, R., Durrell, P. R., Laychak, M. B., et al. 2004, ApJ, 614, 167

Ciardullo, R., Feldmeier, J. J., Jacoby, G. H., et al. 2002, ApJ, 577, 31

Ciardullo, R., Jacoby, G. H., Feldmeier, J. J., & Bartlett, R. E. 1998, ApJ, 492, 62

Ciardullo, R., Jacoby, G. H., Ford, H. C., & Neill, J. D. 1989, ApJ, 339, 53

Ciotti, L. 1991, A&A, 249, 99

Coccato, L., Arnaboldi, M., & Gerhard, O. 2013, MNRAS, 436, 1322

Coccato, L., Arnaboldi, M., Gerhard, O., et al. 2010, A&A, 519, A95

Coccato, L., Gerhard, O., Arnaboldi, M., et al. 2009, MNRAS, 394, 1249

Cole, S., Lacey, C. G., Baugh, C. M., & Frenk, C. S. 2000, MNRAS, 319, 168

Colless, M., Ellis, R. S., Taylor, K., & Hook, R. N. 1990, MNRAS, 244, 408

Conroy, C., Wechsler, R. H., & Kravtsov, A. V. 2007, ApJ, 668, 826

Conselice, C. J., Gallagher, III, J. S., & Wyse, R. F. G. 2001, ApJ, 559, 791

Contini, E., De Lucia, G., Villalobos, Á., & Borgani, S. 2014, MNRAS, 437, 3787

Cooper, A. P., Gao, L., Guo, Q., et al. 2014, ArXiv e-prints

Cortesi, A., Arnaboldi, M., Coccato, L., et al. 2013, A&A, 549, A115

Côté, P., McLaughlin, D. E., Hanes, D. A., et al. 2001, ApJ, 559, 828

Crnojević, D., Ferguson, A. M. N., Irwin, M. J., et al. 2013, MNRAS, 432, 832

Cui, W., Murante, G., Monaco, P., et al. 2014, MNRAS, 437, 816

Da Rocha, C., Ziegler, B. L., & Mendes de Oliveira, C. 2008, MNRAS, 388, 1433

D'Abrusco, R., Fabbiano, G., & Zezas, A. 2015, ArXiv e-prints

Das, P., Gerhard, O., Churazov, E., & Zhuravleva, I. 2010, MNRAS, 409, 1362

De Lucia, G. & Blaizot, J. 2007, MNRAS, 375, 2

De Lucia, G., Springel, V., White, S. D. M., Croton, D., & Kauffmann, G. 2006, MNRAS, 366, 499

De Lucia, G., Weinmann, S., Poggianti, B. M., Aragón-Salamanca, A., & Zaritsky, D. 2012, MNRAS, 423, 1277

de Vaucouleurs, G. 1948, Annales d'Astrophysique, 11, 247

Desroches, L.-B., Quataert, E., Ma, C.-P., & West, A. A. 2007, MNRAS, 377, 402

Doherty, M., Arnaboldi, M., Das, P., et al. 2009, A&A, 502, 771

Dolag, K., Murante, G., & Borgani, S. 2010, MNRAS, 405, 1544

Dopita, M. A., Jacoby, G. H., & Vassiliadis, E. 1992, ApJ, 389, 27

Douglas, N. G., Arnaboldi, M., Freeman, K. C., et al. 2002, PASP, 114, 1234

Dressler, A. 1978, ApJ, 223, 765

Dressler, A. 1979, ApJ, 231, 659

Dressler, A. 1980, ApJ, 236, 351

Dressler, A., Faber, S. M., Burstein, D., et al. 1987, ApJ, 313, L37

Dressler, A. & Gunn, J. E. 1983, ApJ, 270, 7

D'Souza, R., Kauffman, G., Wang, J., & Vegetti, S. 2014, MNRAS, 443, 1433

Duc, P.-A., Cuillandre, J.-C., Karabal, E., et al. 2015, MNRAS, 446, 120

Durrell, P. R., Ciardullo, R., Feldmeier, J. J., Jacoby, G. H., & Sigurdsson, S. 2002, ApJ, 570, 119

Durrell, P. R., Côté, P., Peng, E. W., et al. 2014, ArXiv e-prints

Emsellem, E., Cappellari, M., Krajnović, D., et al. 2007, MNRAS, 379, 401

Emsellem, E., Cappellari, M., Peletier, R. F., et al. 2004, MNRAS, 352, 721

Emsellem, E., Krajnović, D., & Sarzi, M. 2014, MNRAS, 445, L79

Faber, S. M., ed. 1987, Nearly normal galaxies: From the Planck time to the present; Proceedings of the Eighth Santa Cruz Summer Workshop in Astronomy and Astrophysics, Santa Cruz, CA, July 21-Aug. 1, 1986

Faber, S. M. & Jackson, R. E. 1976, ApJ, 204, 668

Faber, S. M., Tremaine, S., Ajhar, E. A., et al. 1997, AJ, 114, 1771

Feldmeier, J. J., Ciardullo, R., & Jacoby, G. H. 1998, ApJ, 503, 109

Feldmeier, J. J., Ciardullo, R., Jacoby, G. H., & Durrell, P. R. 2003, ApJS, 145, 65

Feldmeier, J. J., Ciardullo, R., Jacoby, G. H., & Durrell, P. R. 2004a, ApJ, 615, 196

Feldmeier, J. J., Mihos, J. C., Morrison, H. L., et al. 2004b, ApJ, 609, 617

Feldmeier, J. J., Mihos, J. C., Morrison, H. L., Rodney, S. A., & Harding, P. 2002, ApJ, 575, 779

Ferguson, A. M. N., Gallagher, J. S., & Wyse, R. F. G. 1998, AJ, 116, 673

Forman, W., Jones, C., & Tucker, W. 1985, ApJ, 293, 102

Forte, J. C., Vega, E. I., & Faifer, F. 2012, MNRAS, 421, 635

Gal-Yam, A., Maoz, D., Guhathakurta, P., & Filippenko, A. V. 2003, AJ, 125, 1087

Gallagher, III, J. S. & Ostriker, J. P. 1972, AJ, 77, 288

Gawiser, E., Francke, H., Lai, K., et al. 2007, ApJ, 671, 278

Gebhardt, K., Adams, J., Richstone, D., et al. 2011, ApJ, 729, 119

Gerhard, O., Arnaboldi, M., Freeman, K. C., et al. 2005, ApJ, 621, L93

Gerhard, O., Arnaboldi, M., Freeman, K. C., et al. 2007, A&A, 468, 815

Gerhard, O., Kronawitter, A., Saglia, R. P., & Bender, R. 2001, AJ, 121, 1936

Gerhard, O. E. 1993, MNRAS, 265, 213

Gnedin, O. Y. 2003, ApJ, 589, 752

Gonzalez, A. H., Sivanandam, S., Zabludoff, A. I., & Zaritsky, D. 2013, ApJ, 778, 14

Gonzalez, A. H., Zabludoff, A. I., & Zaritsky, D. 2005, ApJ, 618, 195

Gonzalez, A. H., Zabludoff, A. I., Zaritsky, D., & Dalcanton, J. J. 2000, ApJ, 536, 561

Gonzalez, A. H., Zaritsky, D., & Zabludoff, A. I. 2007, ApJ, 666, 147

Gregg, M. D. & West, M. J. 1998a, Nature, 396, 549

Gregg, M. D. & West, M. J. 1998b, Nature, 396, 549

Gronwall, C., Ciardullo, R., Hickey, T., et al. 2007, ApJ, 667, 79

Guennou, L., Adami, C., Da Rocha, C., et al. 2012, A&A, 537, A64

Gunn, J. E. & Gott, III, J. R. 1972, ApJ, 176, 1

Hammer, F., Flores, H., Lilly, S. J., et al. 1997, ApJ, 481, 49

Harris, W. E., Harris, G. L. H., & Alessi, M. 2013, ApJ, 772, 82

Henize, K. G. & Westerlund, B. E. 1963, ApJ, 137, 747

Hernández-Martínez, L. & Peña, M. 2009, A&A, 495, 447

Hernquist, L. & Barnes, J. E. 1991, Nature, 354, 210

Hernquist, L. & Spergel, D. N. 1992, ApJ, 399, L117

Hernquist, L., Spergel, D. N., & Heyl, J. S. 1993, ApJ, 416, 415

Hibbard, J. E. & Mihos, J. C. 1995, AJ, 110, 140

Hoffman, L., Cox, T. J., Dutta, S., & Hernquist, L. 2010, ApJ, 723, 818

Hogg, D. W. 1999, ArXiv Astrophysics e-prints

Hogg, D. W., Cohen, J. G., Blandford, R., & Pahre, M. A. 1998, ApJ, 504, 622

Hopkins, P. F., Somerville, R. S., Cox, T. J., et al. 2009, MNRAS, 397, 802

Hui, X., Ford, H. C., Ciardullo, R., & Jacoby, G. H. 1993, ApJ, 414, 463

Hui, X., Ford, H. C., Freeman, K. C., & Dopita, M. A. 1995, ApJ, 449, 592

Humphrey, P. J., Buote, D. A., Gastaldello, F., et al. 2006, ApJ, 646, 899

Jacoby, G. H. 1989, ApJ, 339, 39

Jacoby, G. H., Africano, J. L., & Quigley, R. J. 1987, PASP, 99, 672

Jacoby, G. H., Ciardullo, R., & Ford, H. C. 1990, ApJ, 356, 332

Jacoby, G. H. & De Marco, O. 2002, AJ, 123, 269

Janowiecki, S., Mihos, J. C., Harding, P., et al. 2010, ApJ, 715, 972

Kelson, D. D., Zabludoff, A. I., Williams, K. A., et al. 2002, ApJ, 576, 720

Komatsu, E., Smith, K. M., Dunkley, J., et al. 2011, ApJS, 192, 18

Koopmans, L. V. E., Treu, T., Bolton, A. S., Burles, S., & Moustakas, L. A. 2006, ApJ, 649, 599

Kormendy, J. 1977, ApJ, 218, 333

Kormendy, J. & Bender, R. 1996, ApJ, 464, L119

Kormendy, J., Fisher, D. B., Cornell, M. E., & Bender, R. 2009, ApJS, 182, 216

Krick, J. E. & Bernstein, R. A. 2007, AJ, 134, 466

Laporte, C. F. P., White, S. D. M., Naab, T., & Gao, L. 2013, MNRAS, 435, 901

Larson, R. B. 1974, MNRAS, 166, 585

Lidman, C., Suherli, J., Muzzin, A., et al. 2012, MNRAS, 427, 550

Lin, Y.-T., Mohr, J. J., & Stanford, S. A. 2003, ApJ, 591, 749

Lin, Y.-T., Mohr, J. J., & Stanford, S. A. 2004, ApJ, 610, 745

Liu, Y., Zhou, X., Ma, J., et al. 2005, AJ, 129, 2628

Longobardi, A., Arnaboldi, M., Gerhard, O., et al. 2013, A&A, 558, A42

Longobardi, A., Arnaboldi, M., Gerhard, O., & Hanuschik, R. 2015a, ArXiv e-prints

Longobardi, A., Arnaboldi, M., Gerhard, O., & Mihos, J. C. 2015b, ArXiv e-prints

Longobardi et al. 2015, A&A, in prep.

Loubser, S. I. & Sánchez-Blázquez, P. 2012, MNRAS, 425, 841

Lynden-Bell, D. 1967, MNRAS, 136, 101

MacKay, D. J. 2003, Information theory, inference, and learning algorithms, Vol. 7 (Citeseer)

Magrini, L., Leisy, P., Corradi, R. L. M., et al. 2005, A&A, 443, 115

Mahdavi, A., Hoekstra, H., Babul, A., & Henry, J. P. 2008, MNRAS, 384, 1567

Malin, D. F. & Carter, D. 1980, Nature, 285, 643

Markwardt, C. B. 2009, in Astronomical Society of the Pacific Conference Series, Vol. 411, Astronomical Data Analysis Software and Systems XVIII, ed. D. A. Bohlender, D. Durand, & P. Dowler, 251

Mathieu, A., Merrifield, M. R., & Kuijken, K. 2002, MNRAS, 330, 251

Matthews, T. A., Morgan, W. W., & Schmidt, M. 1964, ApJ, 140, 35

Mayer, L., Mastropietro, C., Wadsley, J., Stadel, J., & Moore, B. 2006, MNRAS, 369, 1021

McConnachie, A. W., Irwin, M. J., Ibata, R. A., et al. 2009, Nature, 461, 66

McGaugh, S. S. & Schombert, J. M. 2014, AJ, 148, 77

McNeil, E. K., Arnaboldi, M., Freeman, K. C., et al. 2010, A&A, 518, A44

McNeil-Moylan, E. K., Freeman, K. C., Arnaboldi, M., & Gerhard, O. E. 2012, A&A, 539, A11

Mei, S., Blakeslee, J. P., Côté, P., et al. 2007, ApJ, 655, 144

Melnick, J. & Sargent, W. L. W. 1977, ApJ, 215, 401

Méndez, R. H., Kudritzki, R. P., Ciardullo, R., & Jacoby, G. H. 1993, A&A, 275, 534

Méndez, R. H., Riffeser, A., Kudritzki, R.-P., et al. 2001, ApJ, 563, 135

Méndez, R. H., Teodorescu, A. M., Schönberner, D., Jacob, R., & Steffen, M. 2008, ApJ, 681, 325

Merrett, H. R., Merrifield, M. R., Douglas, N. G., et al. 2006, MNRAS, 369, 120

Merritt, D. 1984, ApJ, 276, 26

Merritt, D. 1985, ApJ, 289, 18

Mihos, J. C. 2004, in IAU Symposium, Vol. 217, Recycling Intergalactic and Interstellar Matter, ed. P.-A. Duc, J. Braine, & E. Brinks, 390

Mihos, J. C., Harding, P., Feldmeier, J., & Morrison, H. 2005, ApJ, 631, L41

Mihos, J. C., Harding, P., Rudick, C. S., & Feldmeier, J. J. 2013, ApJ, 764, L20

Mihos, J. C. & Hernquist, L. 1996, ApJ, 464, 641

Mihos et al. 2015, Journal, in prep.

Miyazaki, S., Komiyama, Y., Sekiguchi, M., et al. 2002, PASJ, 54, 833

Montes, M., Trujillo, I., Prieto, M. A., & Acosta-Pulido, J. A. 2014, MNRAS, 439, 990

Moore, B., Katz, N., Lake, G., Dressler, A., & Oemler, A. 1996, Nature, 379, 613

Moore, B., Lake, G., & Katz, N. 1998, ApJ, 495, 139

Moore, B., Quinn, T., Governato, F., Stadel, J., & Lake, G. 1999, MNRAS, 310, 1147

Murante, G., Arnaboldi, M., Gerhard, O., et al. 2004, ApJ, 607, L83

Murante, G., Giovalli, M., Gerhard, O., et al. 2007, MNRAS, 377, 2

Murphy, J. D., Gebhardt, K., & Adams, J. J. 2011, ApJ, 729, 129

Murphy, J. D., Gebhardt, K., & Cradit, M. 2014, ApJ, 785, 143

Naab, T., Johansson, P. H., & Ostriker, J. P. 2009, ApJ, 699, L178

Naab, T., Khochfar, S., & Burkert, A. 2006, ApJ, 636, L81

Nagino, R. & Matsushita, K. 2009, A&A, 501, 157

Napolitano, N. R., Pannella, M., Arnaboldi, M., et al. 2003, ApJ, 594, 172

Navarro, J. F., Frenk, C. S., & White, S. D. M. 1996, ApJ, 462, 563

Navarro, J. F., Frenk, C. S., & White, S. D. M. 1997, ApJ, 490, 493

Nulsen, P. E. J. & Bohringer, H. 1995, MNRAS, 274, 1093

Oegerle, W. R. & Hill, J. M. 2001, AJ, 122, 2858

Oemler, Jr., A. 1974, ApJ, 194, 1

Oser, L., Ostriker, J. P., Naab, T., Johansson, P. H., & Burkert, A. 2010, ApJ, 725, 2312

Ostriker, J. P. & Tremaine, S. D. 1975, ApJ, 202, L113

Pedregosa, F., Varoquaux, G., Gramfort, A., et al. 2011, Journal of Machine Learning Research, 12, 2825

Peebles, P. J. E. 1993, Principles of Physical Cosmology

Peimbert, M. 1990, RMXAA, 20, 119

Peletier, R. F., Davies, R. L., Illingworth, G. D., Davis, L. E., & Cawson, M. 1990, AJ, 100, 1091

Peng, E. W., Ford, H. C., & Freeman, K. C. 2004, ApJ, 602, 685

Pérez-Montero, E. & Díaz, A. I. 2003, MNRAS, 346, 105

Pota, V., Forbes, D. A., Romanowsky, A. J., et al. 2013, MNRAS, 428, 389

Pratt, G. W. 2006, ArXiv Astrophysics e-prints

Presotto, V., Girardi, M., Nonino, M., et al. 2014, A&A, 565, A126

Puchwein, E., Springel, V., Sijacki, D., & Dolag, K. 2010, MNRAS, 406, 936

Purcell, C. W., Bullock, J. S., & Zentner, A. R. 2007, ApJ, 666, 20

Quinn, P. J. 1984, ApJ, 279, 596

Rafferty, D. A., McNamara, B. R., & Nulsen, P. E. J. 2008, ApJ, 687, 899

Read, J. I., Wilkinson, M. I., Evans, N. W., Gilmore, G., & Kleyna, J. T. 2006a, MNRAS, 366, 429

Read, J. I., Wilkinson, M. I., Evans, N. W., Gilmore, G., & Kleyna, J. T. 2006b, MNRAS, 366, 429

Reid, W. A. & Parker, Q. A. 2010, MNRAS, 405, 1349

Renzini, A. & Buzzoni, A. 1986, in Astrophysics and Space Science Library, Vol. 122, Spectral Evolution of Galaxies, ed. C. Chiosi & A. Renzini, 195–231

Rhee, G. F. R. N. & Latour, H. J. 1991, A&A, 243, 38

Richtler, T., Dirsch, B., Gebhardt, K., et al. 2004, AJ, 127, 2094

Robertson, B., Bullock, J. S., Cox, T. J., et al. 2006, ApJ, 645, 986

Rodríguez-González, A., Hernández-Martínez, L., Esquivel, A., et al. 2014, ArXiv e-prints

Romanowsky, A. J., Strader, J., Brodie, J. P., et al. 2012, ApJ, 748, 29

Rood, H. J. & Sastry, G. N. 1971, PASP, 83, 313

Royer, F., Blecha, A., North, P., et al. 2002, in Society of Photo-Optical Instrumentation Engineers (SPIE) Conference Series, Vol. 4847, Astronomical Data Analysis II, ed. J.-L. Starck & F. D. Murtagh, 184–194

Rudick, C. S., Mihos, J. C., Frey, L. H., & McBride, C. K. 2009, ApJ, 699, 1518

Rudick, C. S., Mihos, J. C., Harding, P., et al. 2010, ApJ, 720, 569

Rudick, C. S., Mihos, J. C., & McBride, C. 2006, ApJ, 648, 936

Saglia, R. P., Fabricius, M., Bender, R., et al. 2010, A&A, 509, A61

Sargent, W. L. W., Young, P. J., Lynds, C. R., et al. 1978, ApJ, 221, 731

Schechter, P. 1976, ApJ, 203, 297

Schönberner, D., Jacob, R., Sandin, C., & Steffen, M. 2010, A&A, 523, A86

Schönberner, D., Jacob, R., & Steffen, M. 2005, A&A, 441, 573

Schuberth, Y., Richtler, T., Hilker, M., et al. 2010, A&A, 513, A52

Seigar, M. S., Graham, A. W., & Jerjen, H. 2007, MNRAS, 378, 1575

Sembach, K. R. & Tonry, J. L. 1996, AJ, 112, 797

Sérsic, J. L. 1963, Boletin de la Asociacion Argentina de Astronomia La Plata Argentina, 6, 41

Somerville, R. S., Barden, M., Rix, H.-W., et al. 2008, ApJ, 672, 776

Somerville, R. S., Lee, K., Ferguson, H. C., et al. 2004, ApJ, 600, L171

Springel, V. & Hernquist, L. 2005, ApJ, 622, L9

Strader, J., Romanowsky, A. J., Brodie, J. P., et al. 2011, ApJS, 197, 33

Taffoni, G., Mayer, L., Colpi, M., & Governato, F. 2003, MNRAS, 341, 434

Tal, T. & van Dokkum, P. G. 2011, ApJ, 731, 89

Tal, T., van Dokkum, P. G., Nelan, J., & Bezanson, R. 2009, AJ, 138, 1417

Tamura, N., Kobayashi, C., Arimoto, N., Kodama, T., & Ohta, K. 2000, AJ, 119, 2134

Tamura, N., Sharples, R. M., Arimoto, N., et al. 2006, MNRAS, 373, 601

Tegmark, M., Strauss, M. A., Blanton, M. R., et al. 2004, Phys. Rev. D, 69, 103501

Teplitz, H. I., Malkan, M. A., Steidel, C. C., et al. 2000, ApJ, 542, 18

Theuns, T. & Warren, S. J. 1997a, MNRAS, 284, L11

Theuns, T. & Warren, S. J. 1997b, MNRAS, 284, L11

Thomas, D., Maraston, C., Bender, R., & Mendes de Oliveira, C. 2005, ApJ, 621, 673

Thomas, J., Saglia, R. P., Bender, R., et al. 2007a, MNRAS, 382, 657

Thomas, J., Saglia, R. P., Bender, R., et al. 2007b, MNRAS, 382, 657

Toledo, I., Melnick, J., Selman, F., et al. 2011, MNRAS, 414, 602

Toomre, A. & Toomre, J. 1972, ApJ, 178, 623

Tremaine, S., Henon, M., & Lynden-Bell, D. 1986, MNRAS, 219, 285

Trentham, N. & Mobasher, B. 1998, MNRAS, 293, 53

Trujillo, I., Ferreras, I., & de La Rosa, I. G. 2011, MNRAS, 415, 3903

van Albada, T. S. 1982, MNRAS, 201, 939

van der Marel, R. P. 1994a, MNRAS, 270, 271

van der Marel, R. P. 1994b, MNRAS, 270, 271

van Dokkum, P. G. 2001, PASP, 113, 1420

van Dokkum, P. G., Abraham, R., & Merritt, A. 2014, ApJ, 782, L24

van Dokkum, P. G., Whitaker, K. E., Brammer, G., et al. 2010, ApJ, 709, 1018

Ventimiglia, G., Arnaboldi, M., & Gerhard, O. 2011, A&A, 528, A24+

Ventimiglia, G., Gerhard, O., Arnaboldi, M., & Coccato, L. 2010, A&A, 520, L9

Vikhlinin, A., Markevitch, M., Murray, S. S., et al. 2005, ApJ, 628, 655

Vílchez-Gómez, R. 1999, in Astronomical Society of the Pacific Conference Series, Vol. 170, The Low Surface Brightness Universe, ed. J. I. Davies, C. Impey, & S. Phillips, 349

von der Linden, A., Best, P. N., Kauffmann, G., & White, S. D. M. 2007, MNRAS, 379, 867

Walsh, J. L., Barth, A. J., Ho, L. C., & Sarzi, M. 2013, ApJ, 770, 86

Watson, D. F., Berlind, A. A., & Zentner, A. R. 2012, ApJ, 754, 90

Watson, D. F. & Conroy, C. 2013, ApJ, 772, 139

Weil, M. L., Bland-Hawthorn, J., & Malin, D. F. 1997, ApJ, 490, 664

Weiss, A. & Ferguson, J. W. 2009, A&A, 508, 1343

White, P. M., Bothun, G., Guerrero, M. A., West, M. J., & Barkhouse, W. A. 2003, ApJ, 585, 739

White, S. D. M. & Rees, M. J. 1978, MNRAS, 183, 341

Williams, B. F., Ciardullo, R., Durrell, P. R., et al. 2007, ApJ, 656, 756

Willman, B., Governato, F., Wadsley, J., & Quinn, T. 2004, MNRAS, 355, 159

Yan, H., Hathi, N. P., & Windhorst, R. A. 2008, ApJ, 675, 136

Yoshida, M., Yagi, M., Okamura, S., et al. 2002, ApJ, 567, 118

Zabludoff, A. I., Huchra, J. P., & Geller, M. J. 1990, ApJS, 74, 1

Zhang, H.-X., Peng, E. W., Côté, P., et al. 2015, ApJ, 802, 30

Zhang, Y.-Y., Finoguenov, A., Böhringer, H., et al. 2007, A&A, 467, 437

Zhu, L., Long, R. J., Mao, S., et al. 2014, ArXiv e-prints

Zibetti, S., White, S. D. M., Schneider, D. P., & Brinkmann, J. 2005, MNRAS, 358, 949

Zwicky, F. 1937, ApJ, 86, 217

Zwicky, F. 1952, PASP, 64, 242

Zwicky, F., Herzog, E., Wild, P., Karpowicz, M., & Kowal, C. T. 1961, Catalogue of galaxies and of clusters of galaxies, Vol. I

# Acknowledgements

It has now been four years since I started my PhD. Many things changed, I changed. So, I would like to thank all the people that accompanied me during this time.

First, I want to thank my supervisor, Ortwin, and my co-supervisor, Magda. You both allowed me to live this adventure, believing in my potentialities. During these years you pushed me when I wasn’t feeling strong enough, you told me off when you thought it was the case, encouraged me when the only thing I needed was a wise opinion. During these years you made me stronger, allowing me, now, to be what I will be.

A big ‘thank you’ goes to my group and friends: Lodo, Giulia, Inma, Lucia, Chris, Matthieau, Mattias, Sotiris, Isabella, Angeles, Claudia, Anna, and Laura. Each of you helped me to proceed in these years, maybe with a laugh, a gaze (not sure it is actually the right word, but wordreference suggests it so...), a chat, or a nice going out, even though this resulted in having fever for four days... Seriously, guys, thanks a lot.

Next are Iolanda, Giulia, and Viky. You are like sisters for me . You always knew when to say the right thing in the right time. You were there, always, and I know you will always be.

A thanks goes to Mariabs and Guido. I am firmly convinced that without you both I wouldn’t be where I am now.

Now, it’s your turn, Bhaskar. It’s funny, if this acknowledgements would have been written two years ago, they would have been different. However, now I know I need to thank you. You supported me like I was your sister, you made me see things with a different prospective, and for sure, if now I am more patient, I owe it to you!!!

I also want to thank Anne and Ged. Speaking with you it is one of my favourite things, you always made me feel like family, and always, always, cheered me up.

For sure in these acknowledgements my family deserves a special place. Mamma, Papá, Ambra, Guido, and Giorgia, these four years abroad made me realise how lucky I am in having you. Mamma, Papá, you always believed in me, you inspired me, and made the way to get here the smoothest possible. Ambra and Giorgia, you are for me examples of determination and sweetness. I will always look up to you, but please stop getting angry at me because I don’t have balance on my phone!

Finally, the person without which I could not be able to go through these years, is my partner, Jonny. It is amazing how well you understand me, how caring you can be. Before I met you, I wasn’t able to really say what I was feeling, and now look where I am, writing cheesy things in my thesis. Seriously though, without your support everything would have been so much harder (even just coping with Dark-ages Bhaskar).

To conclude these long acknowledgements, as I have written at the beginning of this thesis, with ‘ hope, faith, and a little bit of luck’, nothing is impossible. Well, I believe my luck was meeting all of you during this journey!